FRIEDRICH-SCHILLER-
UNIVERSITÄT
JENA

Tailoring the Interface of Magnetic Nano-Composites

Dissertation

(kumulativ)

zur Erlangung des akademischen Grades

doctor rerum naturalium (Dr. rer. nat.)

vorgelegt dem Rat der Chemisch-Geowissenschaftlichen Fakultät der

Friedrich-Schiller-Universität Jena

von M. Sc. Philip Biehl

geboren am 16.09.1989 in Göttingen

Gutachter:

1. Prof. Dr. Felix H. Schacher, Jena (Friedrich Schiller Universität Jena)

2. Prof. Dr. Thomas Heinze, Jena (Friedrich Schiller Universität Jena)

Tag der öffentlichen Verteidigung: 28.09.2020

Table of Contents

1. Introduction

Parts of this chapter have been published in **P2)** P. Biehl, M. von der Lühe, S. Dutz, F. H. Schacher, *Polymers* **2018**, *10*, *91.*

About 60 years ago Richard Feynman gave his famous lecture entitled 'There's Plenty of Room at the Bottom' in which he gave an outlook on how nanotechnology could develop and how our society and daily life would be influenced by its use.[1] Since this inspiring talk our society has experienced radical technical changes and with the ongoing digital revolution at the end of the 20th century it is clear that the world as we know it nowadays is not thinkable without manipulations at the nano-scale. In addition to the effects on our digital society, we find artificial nanostructures in almost every part of our daily life, from cosmetic applications (titanium dioxide nanoparticles in sunscreens),[2] various food applications[3-5] to extremely robust and lightweight components for technical applications.[6] Several nanomaterials were already used way before the term 'nano-technology' was established (mainly as pigments).[2] However, the scientific analysis of nanomaterials, the knowledge about the fundamental scientific processes which cause nano-effects, and the tailored synthesis of artificial nanomaterials are a product of the 20th century.[7] With the introduction of new artificial nanomaterials in our daily life also the threat of nanotechnology on our environment and our health currently raises much attention, which is recently discussed most prominently in the context of micro/nano-plastics.[8] Despite the widespread use of nanomaterials in various fields, nanoscience has not yet delivered on all its initial promises, especially for its introduction into the biomedical field.[9] However, compared to the great potential nanoscience has shown in other fields, its introduction into medicine still bears tremendous potential in the context of drug delivery systems (DDS), diagnostics and treatment of multiple diseases.

Nanomaterials can be described as a class of materials which feature "characteristic physical and chemical properties different from the bulk as a consequence of having at least one spatial dimension in the size range of 1–1000 nm."[10] This definition already shows that nanomaterials are not simply described by a size range but require special features which arise due to the nanoscale. The special features arising for nanoparticles originate from mainly two physical effects: One is the quantization of the electronic states, which is relevant for optical and magnetic features, which depend strongly on size, and the other is the higher surface to volume ratio compared to bulk materials, which is very important for the interesting thermal, mechanical and chemical properties of nanoparticles.[11] Hereby a 'true' nano-effect is observed, when the arising feature is not just continuously scalable with the size (like surface area) but occurs suddenly and can be understood by use of classical quantum mechanics.[2] As already mentioned the definition 'nanomaterial' is size and material dependent, as different materials exhibit nano related properties at an individual length scale. For instance, iron oxide particles exhibit a single domain per particle up to a diameter of 128 nm, while the single-domain size for iron particles must be below 15 nm in order to show this effect.[12] The message though is that the challenge of nano-chemistry is to understand how the properties of nanomaterials scale with physical dimension as different properties scale in distinct ways with size.[10]

Colloidal nanoparticles describe a material class at a length scale close to the molecular level. This makes them highly interesting from a physicochemical point of view as they represent a bridge between the molecular scale and the length scale of bulk materials.[7, 10] Materials in this size range show properties which remind of molecular properties like 'solubility' and precipitation, properties which remind of bulk materials like specific surface areas, and individual properties which are not known for either of the two classes like plasmon resonance or super-para-magnetism.[10, 13-14] Structures on a comparable length scale like artificial nanoparticles can be found in any biological system in the form of proteins, DNA, or viruses.[7]

The final properties of a nanoparticles are determined by its chemical composition, its geometry (size and shape), and its surface properties which are determined by the respective molecules employed to coat their surface (chapter 1.2).[15] Each parameter affects the properties of the final material and can be used to tune them in a desired way. There are basically two approaches to create nanostructures:

bottom-up (or chemical pathway) and top-down processing (mechanical pathway).[10] The bottom up method uses molecular precursors to synthesize nanoscopic structures, whereas the top down method uses bulk materials which are fabricated to nano-sized objects by e.g. mechanical forces.[10] The energy to produce nanoparticles with these techniques differs a lot and surprisingly less energy is demanded for the majority of top down approaches which are thus often more sustainable (typical reaction enthalpies cannot compete with the direct mechanical creation of surface energy).[2] However, this method requires complex mechanical equipment for the synthesis of a limited variation of nanostructures and is by far less established in academics. In the following, reference is made to the bottom up approach as method of choice.

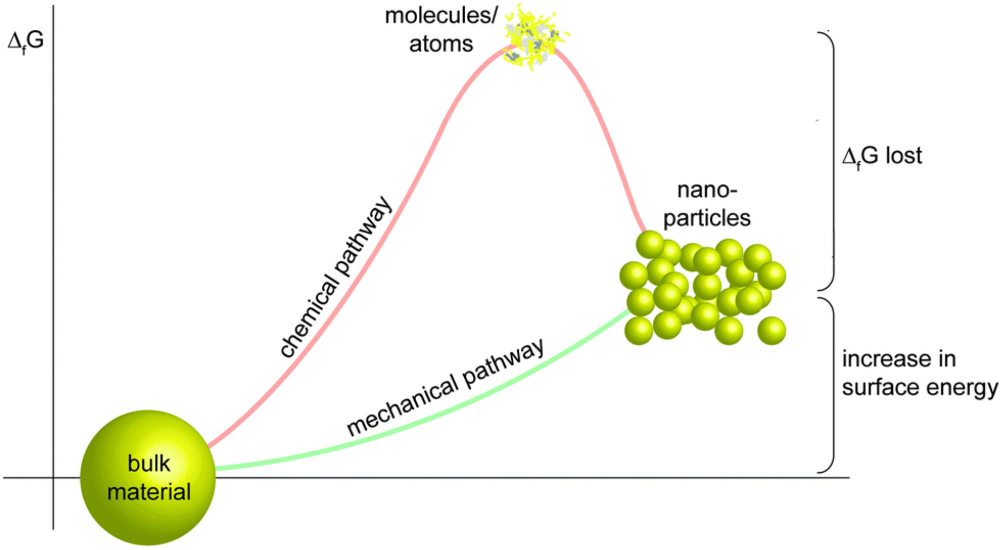

Figure 1: Energy profile (Gibbs free energy) along chemical or mechanical nanoparticle preparation. The chemical pathway suffers from an a priori unnecessary diminution step (high intermediate ΔG) since the atomic/ionic or molecular intermediates are then again combined to intermediate size particles. For the majority of the constituents, their local state in a nanomaterial resembles the one in the bulk. Reprinted from [Chem. Soc. Rev. 2015, 44, 5793-5805] with permission of The Royal Society of Chemistry.[2]

Reaching defined structures by bottom up approach at magnitudes of nanometers is just possible by using scientific phenomena that allow a spontaneous organization of molecules into specific structures defining the composition, the size and shape of materials in the nanometer range.[16] The understanding of these fundamental driving forces allows a tailored design of various new and exciting nano-structures which will enter into various fields of science and shows that even nowadays there is still plenty room at the bottom.

1.1. Magnetic Nanoparticles

As mentioned in the previous chapter the biomedical research area represents a field in nano-science with great potential. Magnetic nanoparticles (MNP) are highly interesting candidates for a possible implementation in this area as this class of colloidal nanoparticles can perform multiple tasks of interest at the same time (magnetic resonance imaging (MRI)), magnetically guided drug delivery, hyperthermia treatment) (Figure 2A).[13]

The materials for the magnetic core can be of diverse composition like elemental metals (Co, Fe, and Ni), Alloys (e.g. CoPt, FePt, FeNi, or FeCo), and Oxides (mainly different iron oxides and some mixed oxides like cobalt-ferrites).[17] However, for biomedical applications iron oxides have shown the most promising properties, such as their magnetic properties (ferro/ferri-magnetic behavior), excellent biodegradability, good stability against oxidation and most importantly their low toxicity.[12] The success of iron oxide is also reflected in the nanoparticles approved for clinical use, all of which use MNP based on iron oxide (see below).

The benefit of this material class lays in the possibility of an external manipulation of these particles by magnetic fields. While magnetic bulk materials exhibit a hysteresis when an external magnetic field is applied, magnets on the nanoscale lose their magnetic memory due to Brownian molecular motion, an effect known as superparamagnetism.[12] This allows the manipulation of these particles with external magnets without the threat of a subsequent (magnetically induced) particle aggregation, which is crucial for applications inside a bloodstream where nanoparticle size has tremendous influence on toxicity.[12, 18-19]

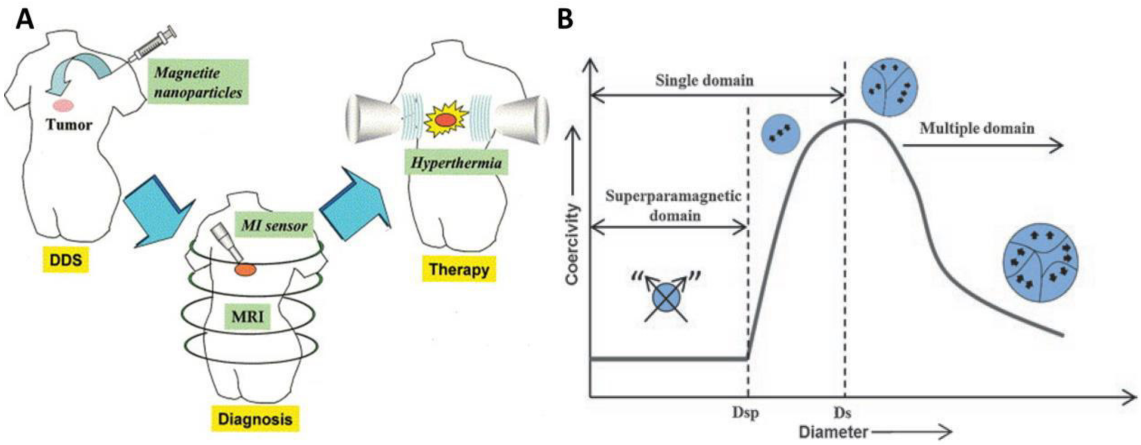

Figure 2: A) Graphical representation of biomedical applications for magnetic nanoparticles. Reprinted from [J Biosci Bioeng 2005, 100, 1-11.] with permission of Elsevier.[20] B) Graphical representation of size dependent magnetic properties at the nanoscale. Reprinted from [Springer International Publishing, Cham, 2019, pp. 245-276] with permission of Springer Nature.[21]

The magnetic properties of MNP depend on the one hand on the applied material but are on the other hand significantly determined by the particle size. Figure 2B illustrates schematically how the coercivity changes with particle size. The downscaling makes the materials shift from a multi-domain regime over single-domain regime to the superparamagnetic regime. The two size regimes are determined by D_s for diameter of single domain and D_{sp} for diameter of superparamagnetism.[21] Large particles with magnetic properties exhibit a multi-domain structure, where each domain consists of a segment with uniform magnetization which is separated by Bloch walls. If the particle size is decrease below D_s it gets energetically unfavorable for the system to maintain Bloch walls which leads to particles which exhibit a single domain. The D_s is mainly determined by various anisotropic energy terms.[12] Since a particle with uniform magnetization exhibits no domain walls the magnetization will be reversed by spin rotation, leading to very high coercivity. A further decrease of the particle size below D_s results in particles which exhibit superparamagnetic behavior. The particles are thus so small, that the thermal energy of the surrounding is sufficient to rapidly flip the magnetization of the particle.[13] The system starts to behave like a small paramagnet. As a consequence the system shows no remaining hysteresis.[12] Furthermore, the coercivity (H_c) and the remanent magnetization (M_r) of the system takes on values of zero. However, the system can still respond to external magnetic fields with a relatively large saturated magnetization M_s.[22]

As mentioned above, MNP are favorable for mainly three applications in the biomedical field: drug delivery, contrast agents, and hyperthermia transmitters. Even though all these applications can be addressed by MNP, the use of tailored MNP is beneficial as each of these applications requires a different magnetic response of the nanoparticles.[23] For instance, a contrast agent requires a powerful enhancement of the proton relaxation times T1 and T2 which increases with an enhanced surface-to-volume ratios (thus a reduced nanoparticles size corresponds to stronger MR-contrast),[24] while an application as hyperthermia transmitter should primary allow a sufficient heat generation, which benefits from a certain magnetic hysteresis achievable by using larger magnetic cores.[25] In terms of MR-contrast agents it was shown that the core sizes of MNP have a major impact on the relaxivity properties which could be seen in the variation of the core diameter between 4 to 20 nm and a corresponding reduction in saturation magnetization which reduced the T_2 relaxation capabilities tremendously.[26] This investigation showed that indeed there is a qualitative trend between core diameter and its potential application as contrast agent, which goes beyond the superparamagnetic properties.

However, the heat generation by MNP is discussed in several publications in detail.[27-30] It can be said briefly that superparamagnetic nanoparticles are not favorable for heat generation. Rather particles in the size range of single domain particles or above the superparamagnetic domain range should be preferred.[30] In case of iron oxide MNP it was shown, that monodisperse particles larger than 20 nm are more effective in heat induction. However, larger diameters seemed not to increase the heat generation significantly further.[30] Another way to generate particles with good heating capability is to produce cluster-like magnetic nanoparticles. Instead of the individual behavior, the collective behavior of the magnetic particles is utilized, which shows a “superferrimagnetic” behavior due to the exchange interaction between the individual particles, even though all particles inside are of superparamagnetic size.[25, 31-33] A main drawback with MNP which increase in size is their tendency for agglomeration, as the existence of a remanent magnetization leads to magnetic attraction between the nanoparticles. Hence, a proper surface functionalization which preserves the colloidal properties of the particles is of particular importance for such systems.

Commercial MNP for medical application are already approved on different levels. For instance, NanoTherm® (MagForce, Germany) is designed for heat mediated cancer treatment and until today the first nano-pharmaca for the treatment of glioblastoma (aggressive brain tumor). It is alredy approved in Europe, and under clinical trial in the USA.[34] Feraheme® (ferumoxytol, AMAG Pharmaceuticals), Lumiren®, Feridex IV®, and Combidex® and GastroMARK represent three FDA approved nanoparticle systems on the basis of iron oxide which have been designed as targeted MRI contrast agents. However, today just Feraheme is still in use, while the other two were withdrawn from the market for reasons that remain unclear.[24, 35]

1.2. Polyzwitterions/Polyampholytes@MNP

As already mentioned in the previous section, the fascinating properties of nanomaterials in general and MNP in particular are only accessible through intelligent surface chemistry. Surface ligands play a key role in synthesizing nanomaterials and equipping them with interesting synergistic properties. The strength of the nanomaterial research field lies in its interdisciplinary nature and the possibility to work with building blocks which merge properties of different disciplines.[9] Surface ligands can either be implemented during the synthesis process itself or later on by ligand exchange techniques (postsynthetic modification).[15] Both approaches have benefits and drawbacks. The synthesis process of robust and crystalline NPs is guided by the choice and amount of surface ligand leading to a defined size and shape of the final nanoparticle.[36] Furthermore, surface ligands also regulate solubility of the nanoparticles and enrich them with additional properties. The choice of the surface ligand depends on many different parameters like the environment for the desired application, the aimed morphology of the nanoparticles, or the need for a chemical modification of the ligand shell.[37]

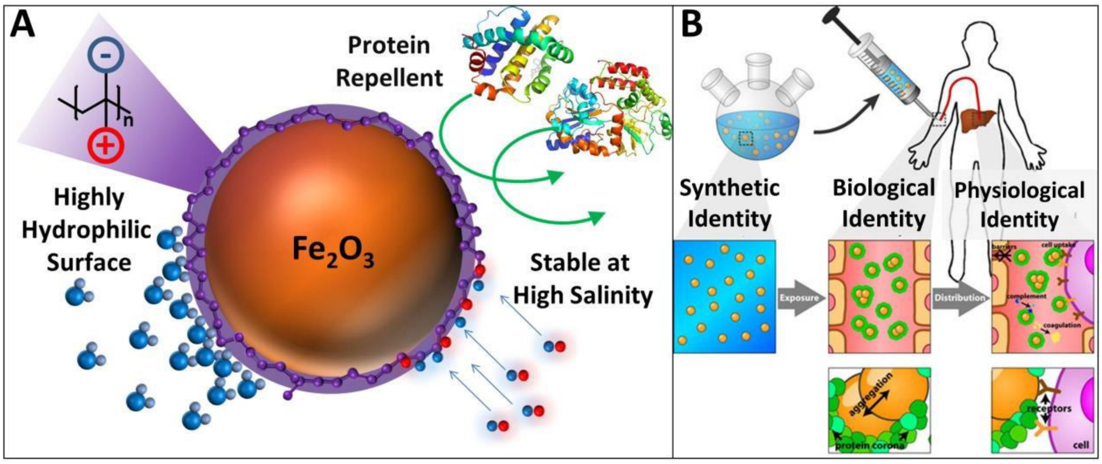

Figure 3: A) Graphical representation of properties deriving from zwitterionic coatings; B) graphical representation of nanoparticle interactions with biological fluids that determine synthetic and biological identity, and furthermore physiological response. Reprinted from[Chemical Society Reviews 2012, 41, 2780-2799] with permission of The Royal Society of Chemistry.[38]

In the field of biomedical applications the requirements on a sufficient ligand are very demanding as materials are exposed to a biological environment with proteins and other biomolecules which tend to interact with surfaces. A crucial parameter here is the formation of a protein corona around nanoparticles, which can alter the properties of colloidal systems in an unwanted way.[38-40] When nanoparticles enter a biological system the present proteins can alter their (surface)-properties leading to undesired interactions with their surroundings.[19, 38] While the synthetic identity of nanoparticles is determined as their properties after synthesis, their biological identity is determined as their properties upon interactions with a biological environment (Figure 3B).[38] As a consequence of this the particles can aggregate, loose a specific ligand function or trigger an immune response which results in severe health problems.[41] It is thus mandatory to suppress the formation of a protein corona. One way to tackle this issue is the application of polyzwitterions as surface ligands. As the surface of proteins and cells is of zwitterionic nature (amino acids, phosphatidylcholine head groups) polyzwitterions represent in some cases a biomimicing in other cases a bioinspired approach to aim these surface properties.[42] There are several examples of zwitterionic structures in biological systems which take on various tasks like dynamic separation as cell wall, charged building blocks in proteins or osmolyte in marine fish[43](Figure 4). Polyzwitterions can be described as a subclass of polyelectrolytes and contain in each repeat unit equal amounts of positive and negative charged groups, giving them a high charge density while at the same time being electrostatically neutral overall.[44] Their antifouling properties are interpreted to arise from their properties of combining high charge density with overall electrostatic neutrality, their high hydrophilicity, binding large amounts of water by hydrogen-bonding, which gives them a sterically demanding 'balloon' of water, and a high chain flexibility.[45]

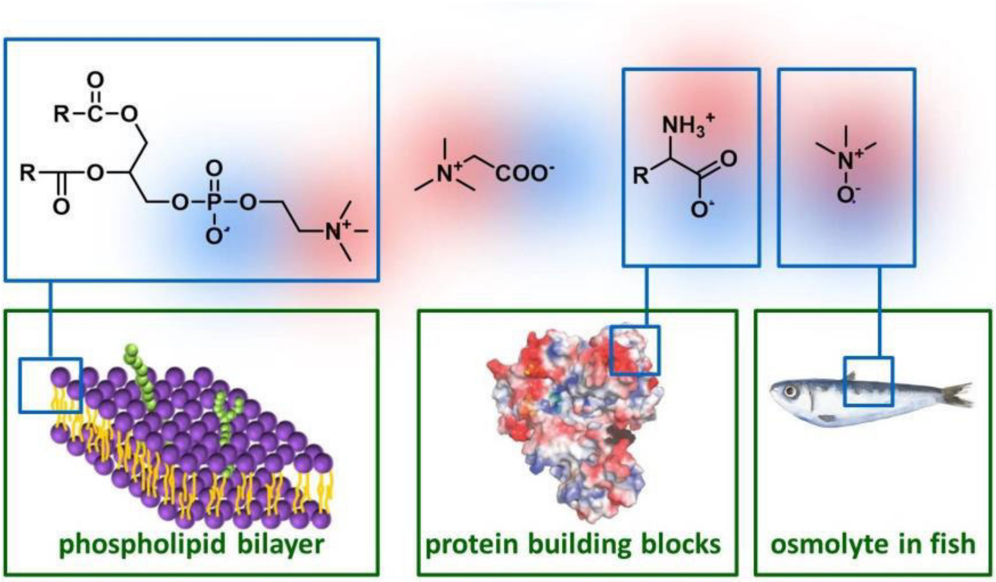

Figure 4: Examples of naturally occurring zwitterionic compounds: general structure of the phosphatidylcholine head group in lipids, betaine, general structure of α-aminoacids, trimethylamine oxide.

Besides their antifouling properties polyzwitterions exhibit additional interesting features as their solubility usually is increased under saline conditions, which is in contrast to most hydrophilic polymers. This property stems from the anti-polyelectrolyte behavior - polymer solubility, the solution viscosity and the swelling of polymer network increase with added salts.[46] An explanation for this exceptional behavior can be found in the unique charge distribution along these polymers. The oppositely charged functional groups lead to attractive electrostatic (inter and intramolecular) and dipole-dipole interactions leading to a relatively collapsed polymer (Figure 5). The addition of salt leads to a reduction of these attractive interactions as the Debye length is reduced by an increasing ionic strength. In consequence the polymer chains start stretching upon addition of salt and by that an increased solubility and solution viscosity is observable.[47] This antipolyelectrolyte effect sets polyzwitterions apart from common polyelectrolytes which tend to aggregate upon addition of salt, as their solubility depends on the repulsive forces between their charged groups. Due to a strong cationic or anionic charge, common polyelectrolytes are also much more susceptible to interactions with charged molecules in their environment than polyzwitterions.

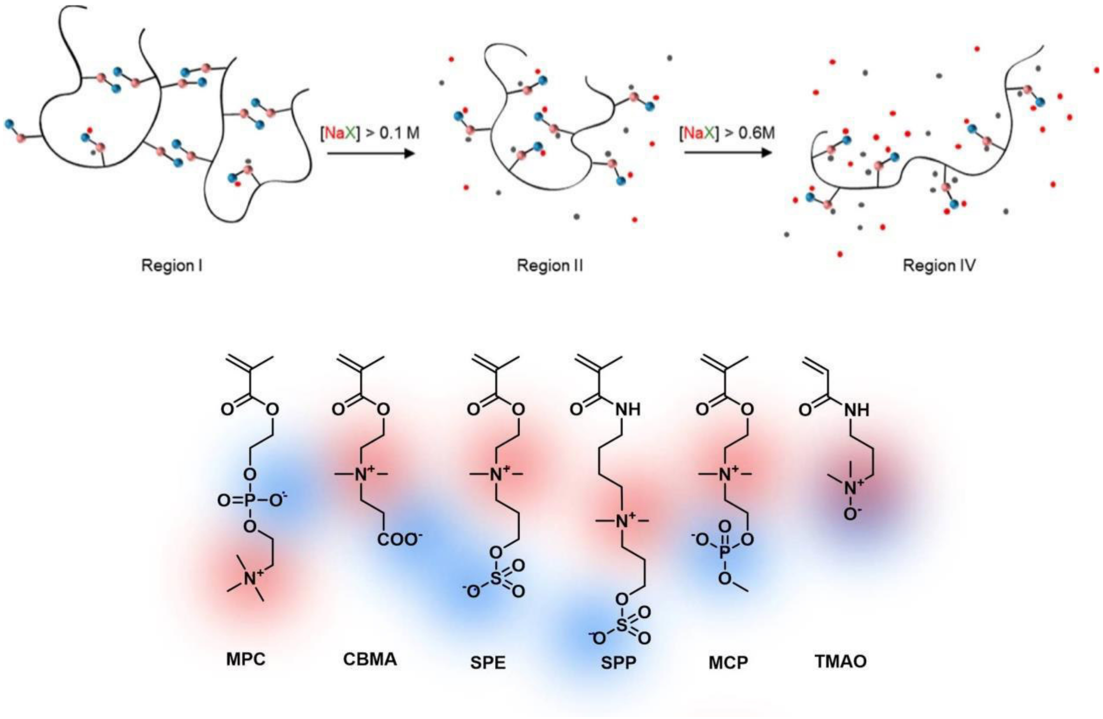

Figure 5: Upper row - schematic representation of ion and zwitterion pairing as a function of salt concentration. Reprinted from [Macromolecules 2017, 50, 4454-4464] with permission of American Chemical Society.[46] Lower row - frequently used monomers for synthesizing polyzwitterions: phosphorylcholine methacrylate (MPC), carboxybetaine methacrylate (CBMA), sulfobetaine methacrylate (SPE), sulfobetaine methacrylamide (SPP), 2-(methacryloyloxy) ethyl choline phosphate (MCP), and dimethylaminopropylacrylamide-*N*-oxide (TMAO).

Most polyzwitterionic structures found in literature show permanent charge over a broad pH range by using strong acids on the one side, like sulfate or phosphonic acid groups and quaternary amines as functional groups on the other side. The quaternization of the amine often leads to increased solubility of the resulting polymer, since H bonds between the amine and its counterpart are suppressed. A few typical examples of monomers frequently implemented in polymers are shown in Figure 5. As can be seen the functionalities vary from poly(phosphobetaine)s[48] over poly(sulfobetaine)s[48] to poly(carbobetaine)s.[48] An exception represents TMAO as a relatively new class of polyzwitterions. It is recently the polyzwitterion with the lowest distance between anionic and cationic charge and mimics trimethylaminoxid, an osmolyte in the cells in marine fish and stabilizer for proteins. The short distance between the charges is supposed to enhance the nonfouling property of this material.[43] However, as already mentioned all here shown monomers exhibit both charged groups successively in one side group and most chargeable groups exhibit a permanent charge over a broad pH range. Other examples of polyzwitterions are rather rare.

Beside homo-polymers there are several examples where oppositely charged monomers are incorporated in copolymers like poly(4-vinylpyridine-*co*-acrylic acid),[49-50] poly(*N,N*-dimethylaminoethyl methacrylate-*co*-methacrylic acid),[51] or poly(sodium styrene sulfonate-*co*-4-vinylpyridine).[52] However, even though these polymers consist of oppositely charged moieties they are not determined as polyzwitterions but as polyampholytes since the charged groups are not attached at the same repetitive unit and are thus not necessarily in charge-balance.[53]

As a result of the permanently charged groups in most polyzwitterions there is a limited influence of pH on the net charge of these polymers. When functional groups with weak pK_a and respective pK_b values are used, the overall charge becomes pH dependent and switchable from negative charge at high pH to positive charge at low pH, with a zwitterionic charge in an intermediate pH range. There is an ongoing discussion whether these materials are still considered as polyzwitterions or rather as polyampholytes as till now the definition of a polyzwitterion includes a permanent charge of both groups at the same time over a broad pH range.[54] In general these materials are rather described as annealed polyampholytes (‘acid-base monomers that are ionized depending on the pH of the solution’[55]) and are referred to below as polyampholytes or weak polyzwitterions. At different pH values, these polyampholytes can present polyanionic, polyzwitterionic, or polycationic character (Figure 6),[56] which enables thus a complete reversal of net charge. This pH-responsive behavior is of considerable interest for coating materials. Interactions with charged molecules can change upon an external pH trigger which opens the possibility to make use of naturally occurring pH fluctuations.[55, 57] A very prominent and important change in pH can be observed in the environment of cancer tissue. It has been shown that the pH within cancer cells can be as low as 5–5.5 while healthy cells typically exhibit a pH value of

7.4.[58] This renders the use of weak polyzwitterionic or polyampholytic coatings as pH sensitive DDS highly interesting.

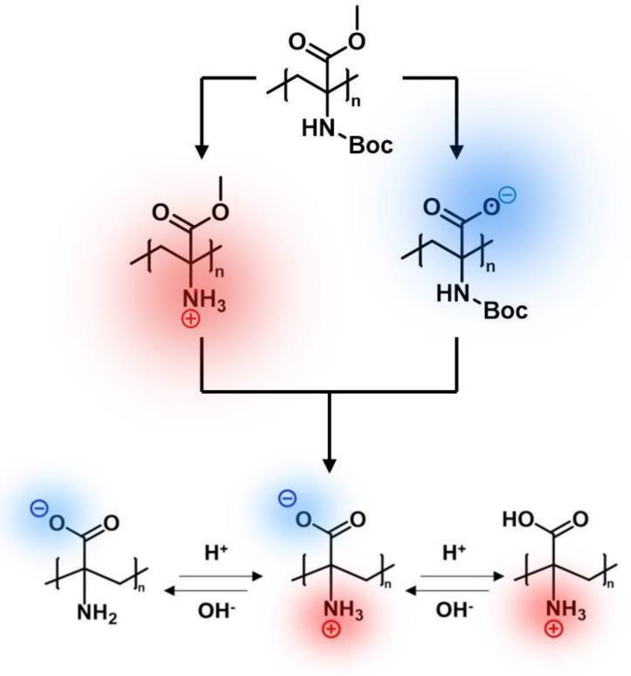

Figure 6: Different deprotection routes of poly(*tert*-butoxycarbonylamino methylacrylate) (P*t*BAMA) resulting in either a polyanion, a polycation, or a weak polyzwitterion (poly(dehydroalanine) (PDha)) allowing a subsequent pH dependent charge adjustment.[56]

While polyzwitterions represent an interesting coating material for MNP there are multiple ways of connecting these two building blocks which can roughly be divided into three basic attachment methods: ligand attachment, weak interactions, and covalent binding, whereby the latter case can be further subdivided into different grafting approaches (Figure 7).[17] While covalent attachment is often achieved by silane chemistry (chapter 1.3), a functionalization based on ligand attachment or weak interactions makes use of either electrostatic, van der Waals interactions, or hydrogen bonding.[17] The great benefit for these latter cases lays in the self-controlled surface complexation of the magnetic core by respective ligands which provides the particles with a rather thin polymer layer and leads to a changed surface functionality while at the same time just a limited amount of non-magnetic material is attached, preserving the magnetic properties.[18] The applied ligands bind either by customized end groups or by functional pendant groups along the polymer. Typical anchoring groups are hereby various catechol derivatives,[59-61] carboxylates[62] or phosphonates[63] (Figure 7). The different anchoring groups described here vary in strength towards iron oxide nanoparticles whereby catechol ligands with a very high complexation constant, as in the case of mimosine as ligand, can even lead to the removal of Fe^{3+}-ions and thus a gradual disruption of the nanoparticles over time.[64] Hence, an anchoring mechanism via a pendant group allows another interesting binding possibility as also ligands with lower binding affinity can lead to a very stable binding due to the multiple binding sites which immobilize the macromolecule.[50, 65-66]

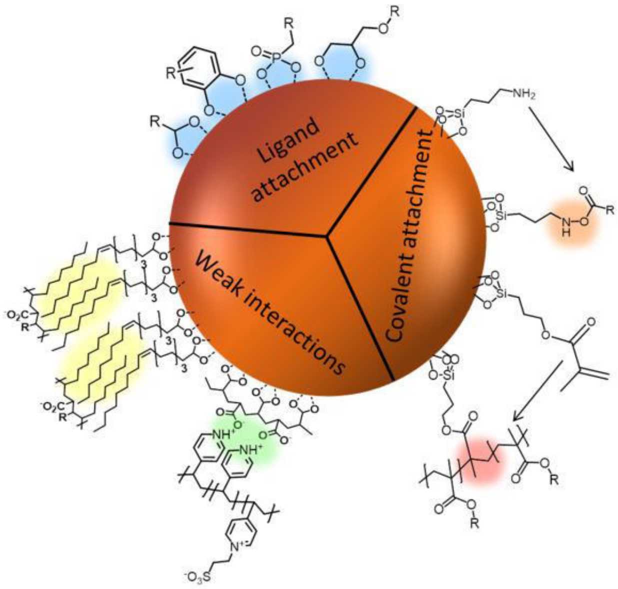

Figure 7: Schematic representation of applied immobilization techniques for polyzwitterions at the surface of MNP. Reprinted from [Polymers 2018, 10, 91].

There are manifold examples of polyzwitterions which were bound to MNP. A good overview is given in the review article by Biehl *et al.*[17] Among various polymers the most frequently used polyzwitterions like P(MPC)[67-68], P(CBMA)[69-70], P(SPE)[71] have all been applied as surface ligand. The field of application for the resulting particles was in these cases most often located in the biomedical section, with the surface coating having the task of acting as a protein-repellent layer.

The application of weak polyzwitterions as surface coating for magnetic nanoparticles is a rather unexplored field. PDha as one example was used as surface coating for MNP by von der Lühe *et al.*[65] The precursor P*t*BAMA allowed a relatively selective deprotection of the orthogonal protective groups which led in the one case to a polyelectrolyte with only positive charge or in the other case to a polyanion. The pendent groups of the polymer were carboxylic acids on the one side, which allowed a sufficient anchoring at the particle surface, while the basic groups consisted of primary amines. The functionalization of MNP was only successful for the polyanion and the fully deprotected polymer PDha showing the importance of the free carboxylic acid as anchoring group. The functional groups allowed subsequently the pH dependent adjustment of surface charge, ranging from negative surface charge at high pH values to positive surface charge at low pH values.[72]

1.3. Silane-Based Covalent Coating of MNP

A covalent attachment of the surface ligands has several benefits. Most important to mention the resistance of ligands towards external influences like salinity, pH or ligand exchange processes makes a covalent attachment attractive. As mentioned before the most prominent way for a covalent attachment is the use of silane groups. Functionalization with silane-based surface ligands in general is probably the most explored coating technique in the field of colloidal metal oxide nanoparticles.[73-78]

The silane groups used for functionalization open a facile way to install a broad variety of functional groups, ranging from thiols over amines to vinyl moieties by commercially available molecular precursors (Figure 8).

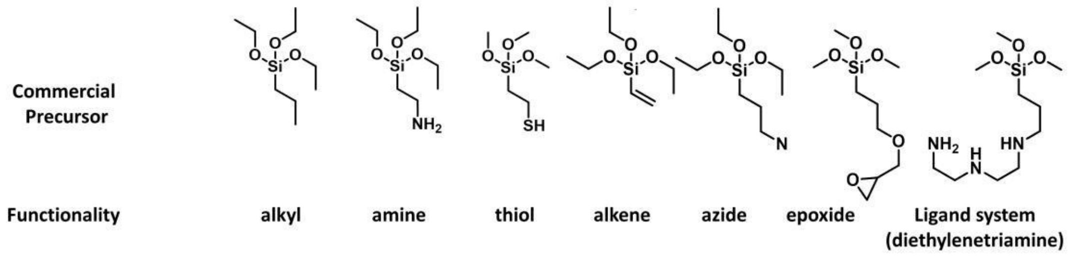

Figure 8: Structures of selected commercially available molecular precursors for silanization from left to right: triethoxy-propylsilane; 3-amino-propyltriethoxysilane; (3-mercaptopropyl)trimethoxysilane (MPTS); triethoxyvinylsilane; 3-azidopropyltriethoxysilane; (3-glycidyloxypropyl)trimethoxysilane; N^1-(3-trimethoxysilylpropyl)diethylenetriamine.

The sol gel chemistry as privileging choice for a silane-based coating of MNPMNP goes back to the late 1960s, when Stöber and co-workers developed a process for synthesizing narrow dispersed silica nanoparticles which was named after him the ‘Stöber process’.[79] Thus the most frequently used silane for functionalization of MNP is indeed tetraethoxysilane (TEOS) which provides a silica shell as surface layer and results in well water dispersible biocompatible magnetic colloids.[73-75] However, more versatile precursors allow the implementation of functional groups. The implementation of silane coupling agents as precursors for sol gel reactions were in particular explored by Schmidt *et al.* in the mid-1980^s and inaugurated the integration of organic chemistry in sol gel chemistry.[80-81] The great benefit of silane-chemistry today lays in the broad variety of precursors which are commercially available.[76, 78, 82-85] The different functionalities allow the access to either desired surface properties or to a further functionalization by other molecules. Thus silanes represent a bridge between an inorganic nanoparticle surface and common organic or macromolecular chemistry. Once the functional groups are applied to the nanoparticle surface they hold the possibility for either being used as desired functionality,[86] for further transformation of the functional groups into other desirable substituents,[78] or as coupling agent to attach other (macro-)molecules.[82-83, 87-88]

The covalent attachment of polymers to nanoparticles by silane chemistry can be achieved by grafting-to, grafting-from, or grafting-through approaches (Figure 9). In any case a suitable binding motif is mandatory for a successful grafting. Either the polymer is attached to a silane-group and subsequently grafted onto a surface,[89] or the surface is first coated with functional silane-groups which enable a subsequent anchoring of the respective ligand.[90] A ‘grafting from’ processing usually allows higher grafting densities, as the formation of macromolecules appears by addition of single monomer units which are more likely to add to the outer sphere of the forming shell than it would be the case for macromolecules which are entropically hindered to add to an already slightly covered surface.[91] Further is the formation of densely grafted polymers at a surface accompanied by stretching of the polymer chains leading to even larger radii of gyration compared to the equivalent free polymer in solution.[92-93]

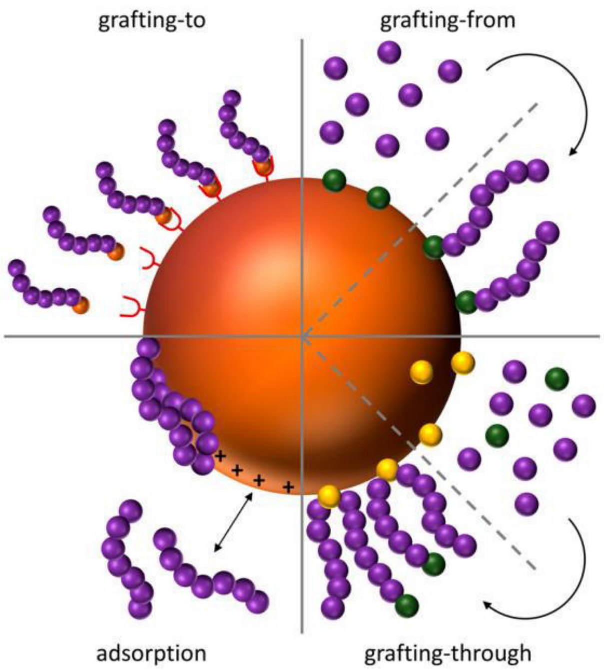

Figure 9: Schematic representation of different grafting methods of polymers to nanoparticle surfaces. Reprinted from [Polymers 2018, 10, 91].

The "grafting to" process, on the other hand, enables each building block (polymer and nanoparticle) to be adjusted before they are merged in one hybrid material. In general the decision on the grafting method usually underlays a variety of factors like functional groups along the polymer, interplay of solution properties of nano-colloid and polymer, and post-polymerization reactions which might affect the nanoparticle stability and hence it is difficult to prefer one grafting method in general.

The grafting through approach as a hybrid of both methods discussed before allows the formation of polymer chains at MNP while at the same time obtaining polymers in solution which can be used for further characterization. There are several publications which describe radical chain-transfer reactions for the formation of polymer coatings at surfaces.[88, 94-98] Most of these publications use silica as starting material, either as glass plate or as particle,[94, 96-98] and just a few investigate MNP.[88, 95]

Despite the great potential in the field of silane coatings, the synthesis of core shell particles is a demanding process. The crucial point is the generation of evenly coated nanoparticles with a desired thickness of silica/silane shell while at the same time nanoparticle aggregation and subsequent enclosure of several nanoparticles in one silica shell has to be avoided. This can be challenging especially in case of MNP. Very thick silane coatings can lead to an unwanted lack of magnetic response of the resulting nanoparticles (either separation issues or, effects on R2 relaxivity).[99-100] The coating process is subject to several factors, the most important of which are the following parameters: the ratio of silane to nanoparticles, the solvent, the pH value, the temperature and the stirring procedure. Furthermore, each type of silane is subjected to different hydrolysis rates, which depend on the respective functional group and the length of the alkyl spacer between the silane-organo-functionality and the silicon atom and the type of alkoxy groups (methyl or ethyl).[101-102] All these aspects have influence on the coating with silanes, which makes it necessary to encounter several parameters and careful adjustment of the reaction parameters in order to obtain the desired results.

1.4. Outline

The introduction of nanomaterials into our society has already happened on manifold levels and will continue within the next decades. While the size limit of matter comes to a physical limit as we experience during the last years overriding Moore's law[103], the development of nanomaterials by using various building blocks still remains a promising way for further development in this scientific field. The synergistic properties arising from the smart combination of building blocks are an attractive approach to find new and valuable nanomaterials to tackle current problems. Hereby a special role is given to interfacial processes as an understanding of the underlying forces and interactions is mandatory for a successful production, application and save handling of artificial nanomaterials. Among various nanomaterials, magnetic nanoparticles represent a material class with broad applicability which is ascribed to their unique property to act as a responsive system to a force which is barely found at higher magnitudes in our environment and represents thus a selective stimulus for various tasks. The surface modifications of MNP represent the key element towards a successful implementation of these materials in respective task areas, which range from support material for catalytic applications in organic solvents [104-105] to heat mediators in medical treatments.[25, 28, 106] Well designed and stable nano-colloids which maintain their initial/chemical identity under these various environments require a tailored surface design which in addition to an adaption to their surrounding can equip the resulting hybrid material with exiting new features. The interplay with surrounding molecules and the particle surface is hereby of particular interest as an individual designed surface can alter interactions in a desired way. This can mean desired and strong interactions to pollutants[107] or catalysts, the avoidance of unwanted interactions with proteins in biological media,[18] or a temporary binding to drugs which release under specific external trigger.[20, 108] All these processes are determined by physicochemical processes at the interface of the MNP and its surrounding.

The aim of this work is the variation of surface properties by polymers and the subsequent investigation of interactions with solvents and potential host molecules with the resulting colloidal nano-hybrid-materials.

The scope of this work hereby includes different synthetic surface modification methods to immobilize desired macromolecules at MNP (namely silane chemistry and ligand binding methods). The coating materials vary from various extensively used polymers to highly exceptional polyampholytic polymers featuring pH responsive properties. Subsequently, these systems are investigated towards their solution properties in terms of surface potential, colloidal stability and pH response. The pH responsive surface coatings allow further to switch the overall surface charge and in interplay with various charged moieties a magnetically guided transport. The interactions of charged molecules and nanoparticles with different polyampholytic shells is extensively examined with a focus on aspects like surrounding pH, charge and charge density of the cargo, and loading capacities, giving insights in fundamental interfacial processes.

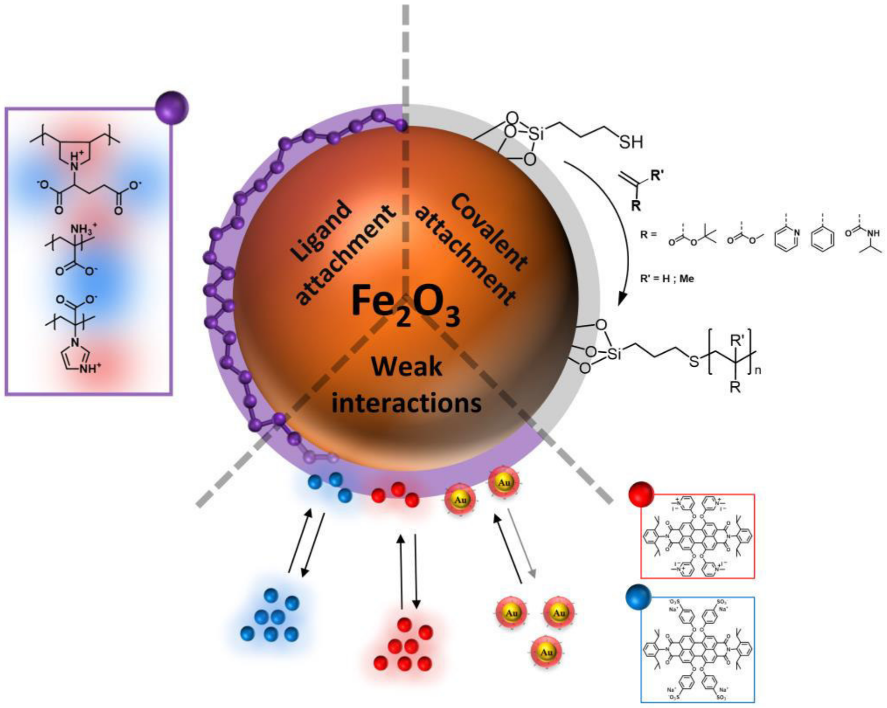

Figure 10: Schematic illustration of surface functionalization techniques used in this thesis and investigations of interactions between the resulting surfaces and different materials.

The thesis will be divided into mainly three sections which cover the synthesis and investigation of different polyampholytes/weak polyzwitterions, the surface modification of MNP with different surface ligands, and finally the investigation of potential interactions between these hybrid nanoparticles and varying charged species ranging from dye molecules to gold nanoparticles.

2. Polyampholytes

Parts of this chapter have been published in **P4)** J. H. Kruse, P. Biehl, F. H. Schacher, *Macromol. Rapid Commun.* **2019**, *40*, 1800857; **P6)** P. Biehl, P. Wiemuth, J. G. Lopez, M.-C. Barth, A. Weidner, S. Dutz, K. Peneva, F. H. Schacher, *Langmuir* **2020**, *36,* 6095–6105.

Polyzwitterions as a subclass of polyelectrolytes exhibit exiting properties in solution (high hydration state[109], antipolyelectrolyte effect[44], antifouling properties[110]) and differ thus strongly from polyelectrolytes which exhibit only anionic or cationic charge. If the charge bearing moieties are replaced by weak acidic and basic groups the charge-based interactions with their surroundings become highly fascinating as pH becomes a key element in the overall charge of the resulting polyampholytes. One fundamental part of this thesis is the preparation of defined and responsive surface properties at MNP. The synthesis of various polyampholytes which allow an application as versatile coating material for iron oxide nanoparticles is described in the following chapter.

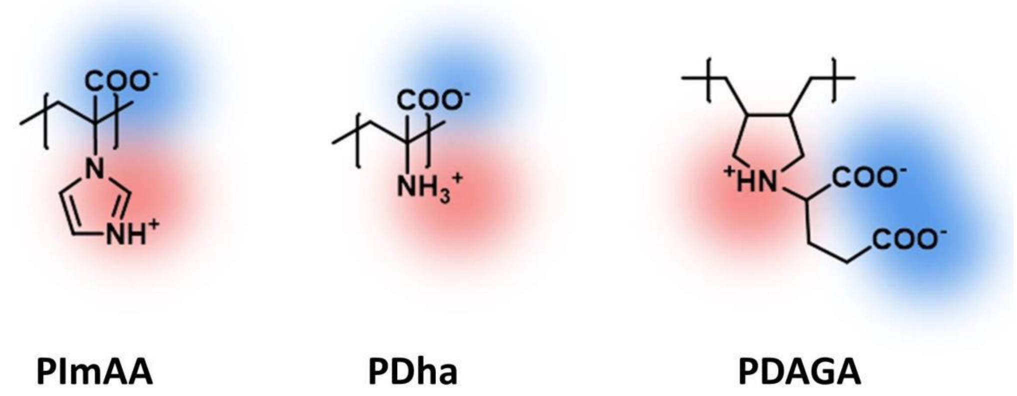

Figure 11: Structure of weak polyampholytes used in this work, shown in their charged state: poly(2-(imidazol-1-yl)acrylic acid) (PImAA), poly(dehydroalanine) (PDha), poly(*N,N*-diallylglutamate) (PDAGA).

2.1. Polymer Synthesis

The monomers for the respective polyampholytes shown in Figure 11 were synthesized according to protocols by Günther *et al.* (*tert*-butoxycarbonylamino methacrylate (*t*BAMA)),[56] Rössel *et al.* (ethyl 2-(imidazole-1-yl)acrylate (EImA)),[111] and Jamiu *et al.* (*N,N*-diallylglutamate (DAGA))[112].

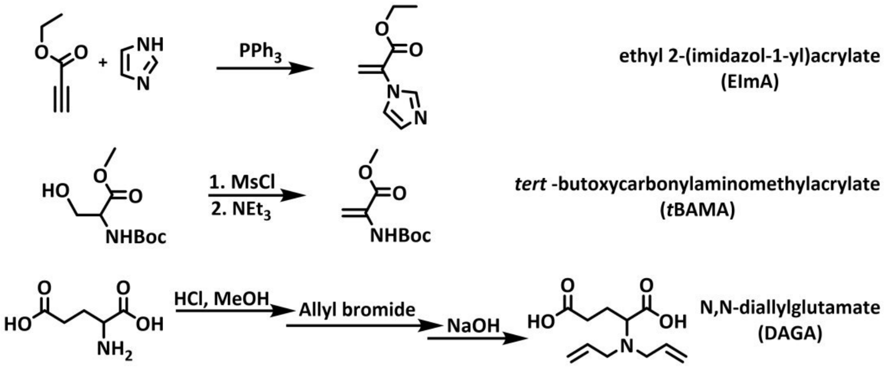

Scheme 1: Synthetic path ways of EImAA, *t*BAMA, and DAGA.

All monomers were obtained as crude products and purified either via column chromatography (EImA and *t*BAMA) or distillation (DAGA). While EImA and *t*BAMA were obtained as viscous liquids DAGA was obtained as a white powder. The ^{1}H-NMR-Spectra in Figure 12 show all expected signals of the purified monomers.

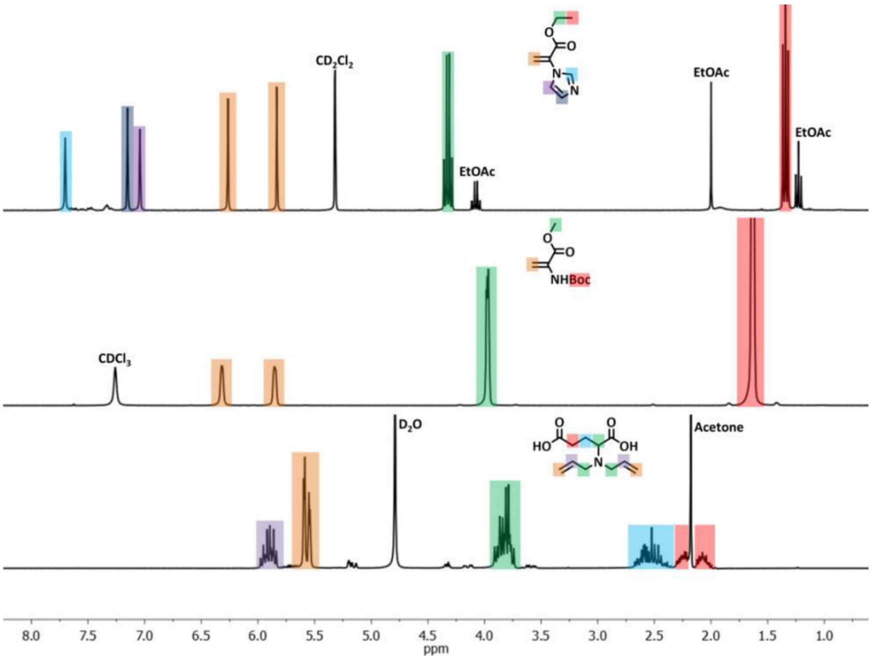

Figure 12: ^{1}H-NMR spectrum of EImA in CD$_2$Cl$_2$, *t*BAMA in CDCl$_3$, and DAGA in D$_2$O. EImA showing signals at δ = 7.70, 1H, δ = 7.15 ppm, 1H, δ = 7.04 ppm, δ = 6.26 ppm, 1H, δ = 5.83 ppm, 1H, δ = 4.32 ppm, 2H, δ = 1.34 ppm, 3H; *t*BAMA showing signals at δ = 6.31 ppm, 1H, δ = 5.86 ppm, 1H, δ = 3.97 ppm, 3H, and δ = 1.63 ppm, 1H; DAGA showing signals at δ = 5.91 ppm, 2H, δ = 5.57 ppm, 4H, δ = 3.84 ppm, 5H, δ = 2.55 ppm, 2H, δ = 2.24 ppm, 1H, and δ = 2.08 ppm, 1H.

The monomers were subsequently used for polymerization. EImA was polymerized using anionic polymerization while in case of DAGA free radical polymerization (FRP) was applied using ammonium persulfate (APS) as initiator in water. *t*BAMA was either polymerized by FRP with (2,4,6-trimethylbenzoyl)diphenylphosphine oxide (TPO) as initiator and nitroxide mediated polymerization (NMP). Table 1 shows exemplary reaction conditions and molecular weights obtained from SEC (size-exclusion calorimetry) measurements for the respective polymers. As can be seen the anionic polymerization of EImA results in lower molar masses and a moderate dispersity. Furthermore allows the NMP for *t*BAMA an acceptable reproducibility for the polymerization with moderate dispersities (in best case 1.6) and satisfying yields (up to 78%), whereas the FRP of *t*BAMA reduces the yield to 40%. The FRP of DAGA led to a water soluble polyelectrolyte with quite broad dispersity and yield around 50%.

Table 1: Molecular characteristics of the used polyampholytes as determined by SEC measurements.

Polymer	Polymerization method	Batch size	Solvent	Initiator	nitroxide	Yield [%]	$\overline{M}_n$ [g mol^{-1}]	$\overline{M}_w$ [g mol^{-1}]	*Đ*
PEImA	Anionic	3 g	THF 7,2 ml	KO*t*Bu	-		3,000^{a}	4,800^{a}	1.6^{a}
P*t*BAMA	FRP	3 g	Dioxan 3 ml	TPO 29 mg	-	40,2	24,350^{a}	51,550^{a}	2.1^{a}
P*t*BAMA	NMP	1 g	Dioxan 2 ml	blocbuilder 47 mg	SG1 23 mg	78,5	21,800^{a}	43,684^{a}	2.0^{a}
P*t*BAMA	NMP	1 g	Dioxan 2 ml	blocbuilder 47 mg	SG1 23 mg	78,0	29,400^{a}	50,900^{a}	1.7^{a}
P*t*BAMA	NMP	1.286 g	Dioxan 2.8 ml	blocbuilder 60 mg	SG1 30 mg	71,0	14,620^{a}	59,690^{a}	4.1^{a}
P*t*BAMA	NMP	2 g	Dioxan 4 ml	blocbuilder 94 mg	SG1 46 mg	75,1	19,847^{a}	32,163^{a}	1.6^{a}
PDAGA	FRP	1.4 g	H_2O 0.5 ml	APS 133 mg	-	47	2,100^{b}	8,100^{b}	3.8^{b}

a) Determined by SEC using $CHCl_3$ as eluent and calibrated against PMMA standards; b) Determined by SEC using 0,1 M Na_2HPO_4/0,05% NaN_3 pH 9 as eluent and calibrated against PAA standards; c) Determined by SEC using DMAc/LiCl SEC as eluent and calibrated against PMMA standards.

In case of PEImA and P*t*BAMA a subsequent deprotection was necessary in order to obtain a polyampholyte. Figure 13A shows the deprotection of both polymers and the final polyampholytes PImAA and PDha respectively. The final molecular weight was again investigated by SEC measurements. Exemplary the characteristics of each polyampholyte are shown in Table 2.

Table 2: Molecular characteristics of the used polyampholytes as determined by SEC measurements.

Sample	$\bar{M}_n$ [g mol^{-1}]	$\bar{M}_w$ [g mol^{-1}]	*Đ*
PImAA	2,700^a	3,800^a	1.4^a
PDha	13,700^b	27,300^b	2.0^b
PDAGA	2,100^a	8,100^a	3.8^a

a) Determined by SEC using 0,1 M Na_2HPO_4/0,05% NaN_3 pH 9 as eluent and calibrated against PAA standards; b) Determined by SEC using DMAc/LiCl SEC as eluent and calibrated against PMMA standards.

The dispersities are relatively broad while the molar mass of the final polymers varies between 2 kg mol^{-1} and 14 kg mol^{-1}.The respective SEC elution curves are shown in Figure 13B-D. The unprotected polymers were later on used for the functionalization of MNP discussed in chapter3.2.

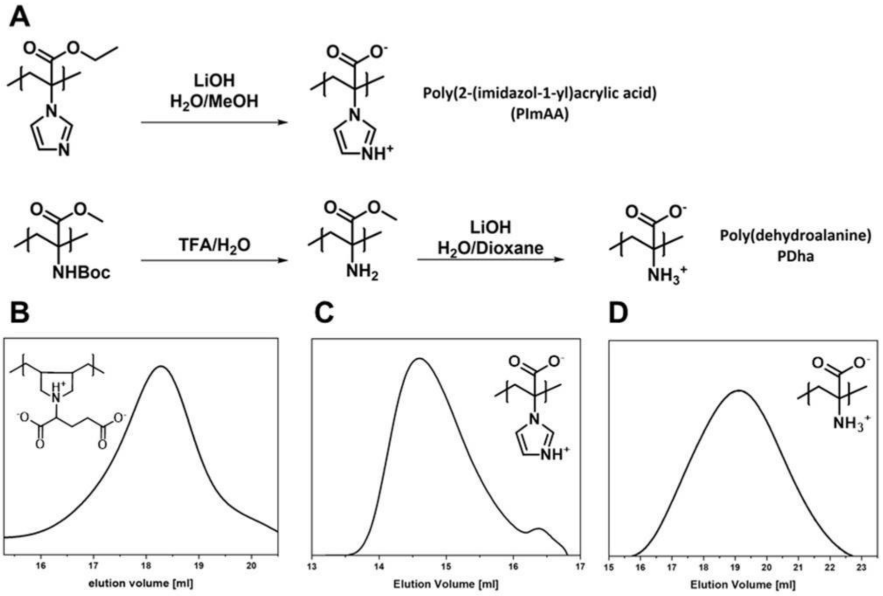

Figure 13: A) Synthetic path for the deprotection of PEImA to PImAA, and P*t*BAMA to PDha, and SEC elution traces of the used polyampholytes B) PDAGA (0,1 M Na_2HPO_4/0,05% NaN_3 pH 9, PAA calibration), C) PImAA (0,1 M Na_2HPO_4/0,05% NaN_3 pH 9, PAA calibration), D) PDha (DMAc/LiCl SEC, PMMA calibration).

2.2. Charge of Polyampholytes

As all of the synthesized polyampholytes are supposed to show a pH-dependent change in their net charge the investigation of their pH depending properties was important. All polyampholytes were dissolved under basic conditions and subsequently titrated with 0.1 N hydrochloric acid. The titration curves of the respective polyampholytes are shown in Figure 14. The deviations of these curves allow a rough estimation of the respective overall charge along the polymer. The inflection points at lower HCl volume can be assigned to the respective amines of the polymers (imidazole, primary amine and tertiary amine), while the inflection point at higher HCl volume marks the point where the carboxylic acid groups become protonated. The saddle points in between approximately depict the isoelectric point (IEP) of the respective polyampholyte.

The pK_a values for the amine and the carboxylic acid in PImAA are thus roughly localized at pH 10.5 and 4.2, respectively. The IEP which results from the titration is around 7.4. For PDha the pK_a values can be determined to 8.2 for the amine and 4.4 for the carboxylic acid and the IEP is located around 6.3. PDAGA, however, shows a pK_a value of 7.7 for the amine and 3.5 for the carboxylic acids resulting in an IEP of 5.6. It is noteworthy that the two carboxylic acids in PDAGA show protonation equilibria which are apparently too close to one another to be separated by the accuracy of the instrumental setup. In general it has to be noted that the information about the pH dependent solution properties, generated by titrations are difficult to be interpreted as precipitation of all polymers during the titration occurred which affect the protonation behaviour of the functional groups.

The pH range in which the respective polyampholytes precipitated are shown as gray areas in Figure 14A-C. PImAA precipitated between a pH of 6.9 and 2.0 while it was soluble outside this pH range. In case of PDha a precipitation below 5.5 was observable when the polymer was slowly titrated. If the titration speed was increased the precipitation occurred also at higher pH levels. However, PDha did not dissolve again if the pH was lowered further as in case of PImAA but stayed insoluble. In the case of PDAGA a miscibility gap between pH 3.0 and 1.9 was observed.

It is likely that the solution gap of all polyampholytes here indicates charge neutrality along the polymer, which leads to a collapsed polymer conformation. As PImAA and PDAGA dissolve again below a certain pH value it is likely that the respective degree of protonation of the carboxylic acid groups is responsible for this behavior. The lack of a lower pH value for the dissolving of precipitated PDha can be related to kinetic hindrance of the protonation of the amine. Of all polyampholytes discussed here PDha shows the highest density of functional groups which might explain strong intramolecular electrostatic interactions.

However, the occurrence of the upper pH value for a precipitation matches very well the in chapter 3.2 discussed isoelectric points of the resulting hybrid particles coated with the respective polyampholytes.

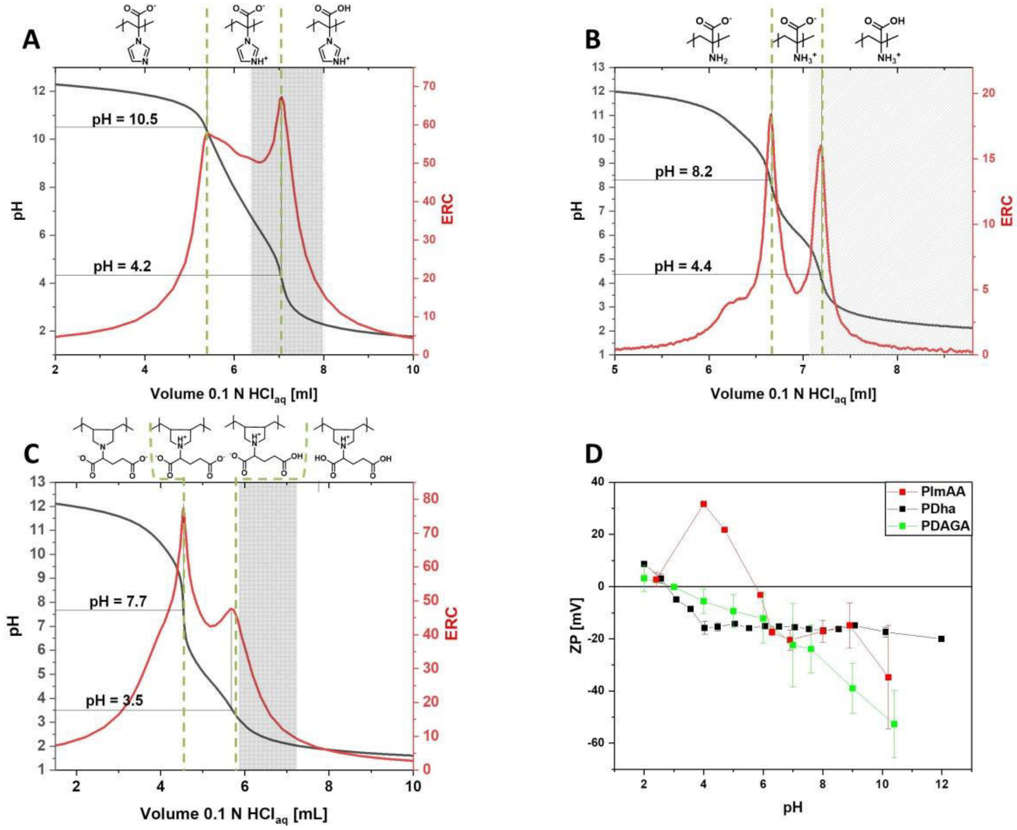

Figure 14: A) Titration curve of PImAA (5 g/L in 6 ml of 0.1 M NaOH) with 0.1 M HCl (black) and the first derivative (red); B) Titration curve of PDha (5 g/L in 6 ml of 0.1 M NaOH) with 0.1 M HCl (black) and the first derivative (red), green lines show the approximate range of zwitterionic charge; C) Titration curve of PDAGA (5 g/L in 6 ml of 0.1 M NaOH) with 0.1 M HCl (black) and the first derivative (red); D) Zeta potential measurements at varying pH of: PImAA (red), PDha (black), and PDAGA (green).

Zeta potential measurements in Figure 14D show the surface potentials for all three polyampholytes at different pH values. Since zeta potential measurements are based on the estimate that spherical colloids are present, the results shown here only roughly reflect the solution behaviour of free polymers in solution. It can be seen, that PImAA exhibits the steepest slope of a changing electrophoretic mobility while PDha and PDAGA change rather moderately. In case of PImAA and PDAGA, the measured isoelectric points determined by zeta potential measurements are in good agreement with the beginning precipitation observed in the titration studies (IEP(PImAA) = 6.0; IEP(PDAGA) = 3.0).

2.3.Variation of Protective Groups

As already described above, PDha is a polyampholyte with excellent inherent properties resulting from its high charge density and its repeating unit, which combines both an amine and a carboxylic acid in a confined space. Both functional groups represent weak chargeable groups and allow thus a pH dependent charge control along the backbone. The polymerization of PDha requires protective groups for both, the amine and the carboxyl functionality, which makes a subsequent deprotection necessary. As shown in in chapter 2 *t*BAMA offers one opportunity as polymerizable monomer and is so far the most studied monomer for the final synthesis of PDha.[56, 113-115] It was observed that the deprotection of the initially thought orthogonal protective groups (*tert*-butyloxycarbonyl (BOC) and methyl ester) results in partial cleavage of the respective other protective group.[72, 114] However, a complete deprotection of both protective groups within one step was also not realizable. This led to the investigation of alternative protecting groups. As shown in Scheme 2 desired properties of the protecting groups would be either an orthogonal way of cleavage or even simultaneous cleavage in one step.

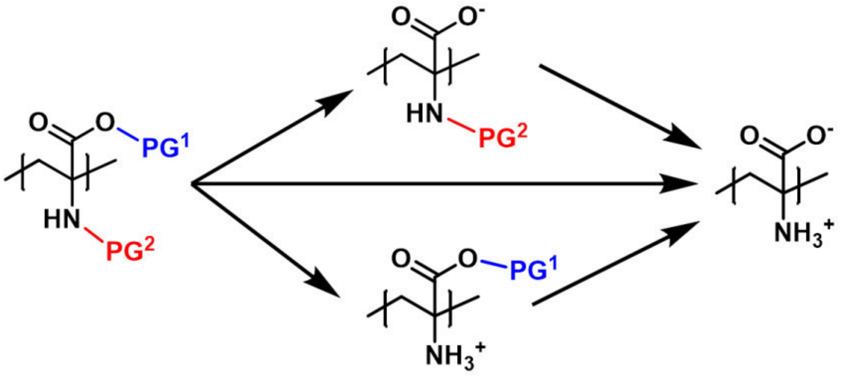

Scheme 2: Overview of deprotection steps with either orthogonal protective groups PG^1 and PG^2, or simultaneously cleavable protective groups leading to PDha.

We synthesized two alternatives to *t*BAMA: 2-*tert*-butoxycarbonylaminoacrylate (*t*BABA), bearing with a *tert*-butyloxycarbonyl at the amine and a benzyl ester at the carboxyl group, and methyl 2-benzyloxycarbonylaminoacrylate (BOMA), bearing a carboxybenzyl (Cbz) group at the amine and a methyl ester at the carboxyl group. The monomers were each synthesized in a two-step procedure as shown in Figure 15.

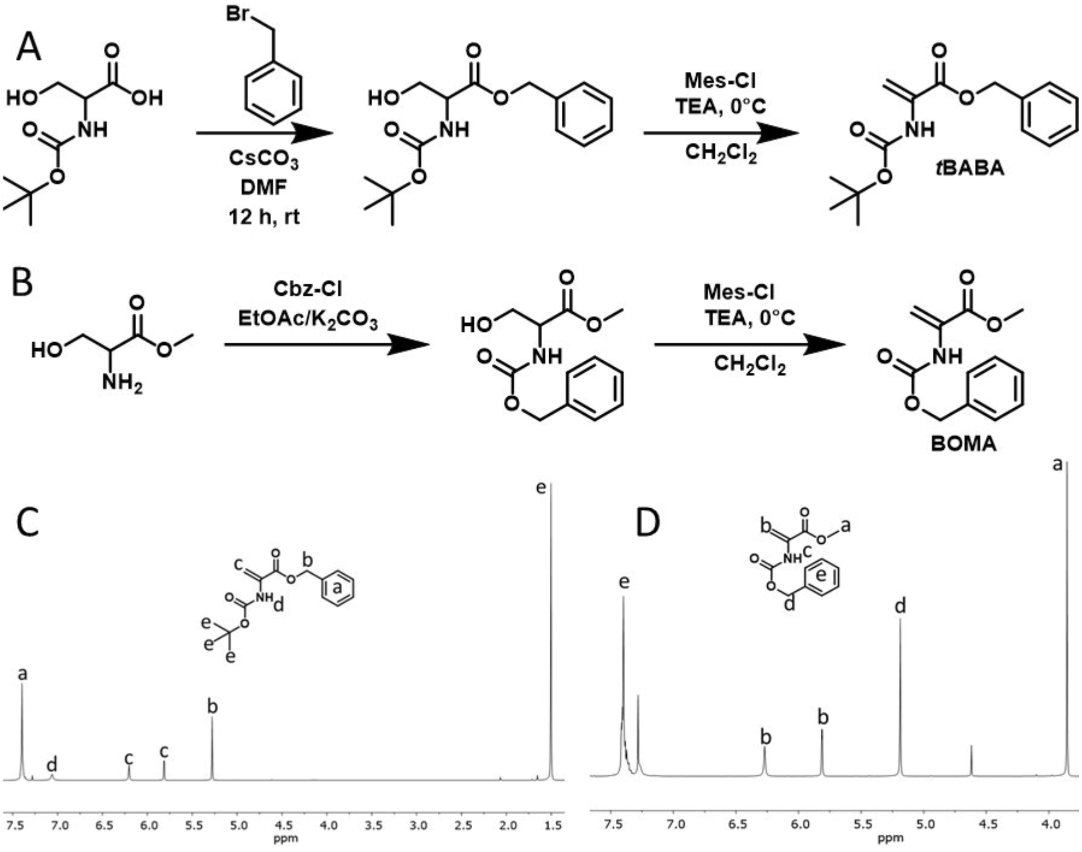

Figure 15: A) Synthesis of *t*BABA, B) synthesis of BOMA, C) ^{1}H-NMR of *t*BABA (300 MHz, $CDCl_3$), D) ^{1}H-NMR of BOMA (300 MHz, $CDCl_3$). Reprinted from [Macromol. Rapid Commun. 2019, 40, 1800857] with permission of John Wiley and Sons.

The synthesized monomers were subsequently polymerized using FRP at room temperature (RT) and TPO as photo-initiator. The polymerizations gave yields between 53% (PBOMA) and 62% (P*t*BABA) with dispersities between 1.5 and 2. The molar masses of the resulting polymers were adjustable between 13 000 and 18 000 g mol^{-1} for P*t*BABA and 15 000 and 50 000 g mol^{-1} respectively.

After polymerization different deprotection routs were examined (Scheme 3). The deprotection of P*t*BABA was first tried using trifluoroacetic acid (TFA) in dichloromethane to cleave the BOC protecting group. Surprisingly this approach led to a direct cleavage of both protecting groups resulting in PDha. Consequently we applied a milder method to achieve orthogonal deprotection. Thus the BOC group was cleaved using $SiCl_4$ in phenol resulting in a selective deprotection of the amine. The remaining benzyl ester can subsequently be removed using TFA as described before. For a first deprotection of the carboxylic acid we applied alkaline deprotection methodology using lithium hydroxide similar to the deprotection procedure described for P*t*BAMA. This resulted in a selective and complete removal of the benzyl ester while the BOC group remained unchanged. SEC was used to confirm the polymeric character of P*t*BABA at each deprotection step.

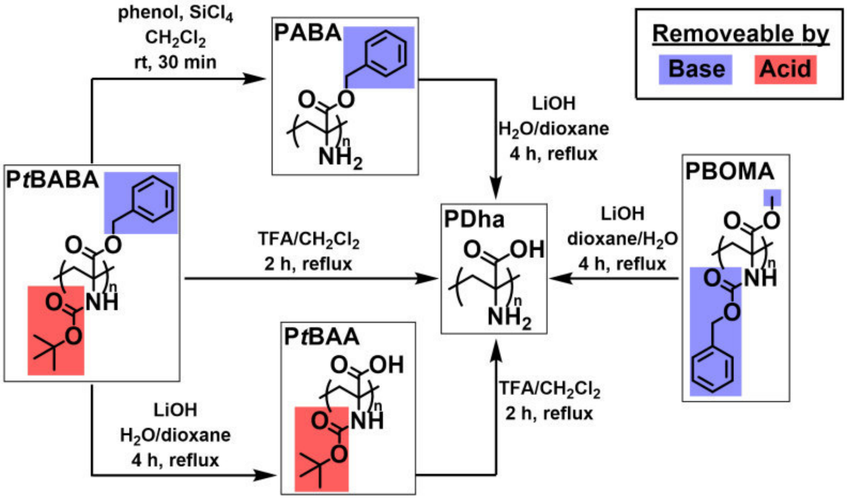

Scheme 3: Overview of the deprotection steps of P*t*BABA and PBOMA and their deprotection products poly(benzyl aminoacrylate) (PABA), poly(*tert*-butoxycarbonylaminoacrylate) (P*t*BAA) and polydehydroalanine (PDha).

PBOMA on the other hand could be fully deprotected within one step using alkaline conditions in a mixture of dioxane and water. Herewith we present two deprotection methods which enable the generation of PDha in one step under either acidic or alkaline conditions which can be very interesting for the introduction of the respective monomers into (block-) copolymers, or other polymer-based materials. The variation of different protecting groups in general broadens the platform of monomers for the general preparation of PDha-based materials.

3. Surface Functionalization of MNP

Parts of this chapter have been published in **P1)** M. Billing, C. Gräfe, A. Saal, P. Biehl, J. Clement, S. Dutz, S. Weidner, F. Schacher, *Macromol. Rapid Commun.* **2017**, *38*, 1600637; **P5)** P. Biehl, F. H. Schacher, *Surfaces* **2020***, 3, 116-131*; **P6)** P. Biehl, P. Wiemuth, J. G. Lopez, M.-C. Barth, A. Weidner, S. Dutz, K. Peneva, F. H. Schacher, *Langmuir* **2020**, *36,* 6095–6105**.**

The tailored surface functionalization of MNP will be discussed in the following section. In the first part ligand attachment of polyampholytes will be presented, while later on a two-step approach with silanization and subsequent grafting through immobilization of various polymers will be discussed. All particles were thoroughly investigated towards their solution properties including overall hydrodynamic size, (pH dependent) surface potential, and shell thickness.

3.1. Pristine Magnetic Nanoparticles

The particles were provided by the workgroup of Silvio Dutz and synthesized by the coprecipitation of a Fe^{2+}/Fe^{3+}-solution as described in 2011,[106, 116] resulting in final particles of about 20-50 nm in radius (dynamic light scattering (DLS) in Figure 16B), which were composed of primary cores with a radius of about 5 nm (X-ray diffraction, TEM) leading to so called multicore magnetic nanoparticles (MCNP). This particle size is just below the single domain radius of iron oxides (D_s (Fe_3O_4) =128 nm).[12] This results in associated magnetic properties which are favorable for an application aiming for heat generation (as discussed in chapter 1.1) like in the field of hyperthermia or any strategy aiming for rapid magnetic separation.[30] The increased diameter further leads to a stronger tendency of the particles to aggregate due to magnetic interactions.

Prior to an application of a polyampholytic shell the MCNP were investigated towards their particle size and shape (DLS and TEM), and their thermal properties (thermogravimetric analysis (TGA)). The results can be seen in Figure 16. TGA under synthetic air revealed that between 30 and 100 °C a slightly varying mass loss occurs which is related to attached water, subsequently an increasing mass around 200 °C was observable due to incomplete oxidation of iron oxides (iron (II) to iron (III)) and furthermore an additional mass loss of about 1-2% at higher temperatures was ascribed to unreacted carbonates which are involved in the synthesis process. All of the samples examined showed a good reproducibility of the different batches concerning their thermal properties is given. Exemplary TEM micrographs for the particles are shown in Figure 16B-E. The inorganic (multi-)core character is clearly visible and the diameter of the aggregates is about 100 nm. As the TEM micrographs were obtained from dry state samples the aggregation state might differ from solution.

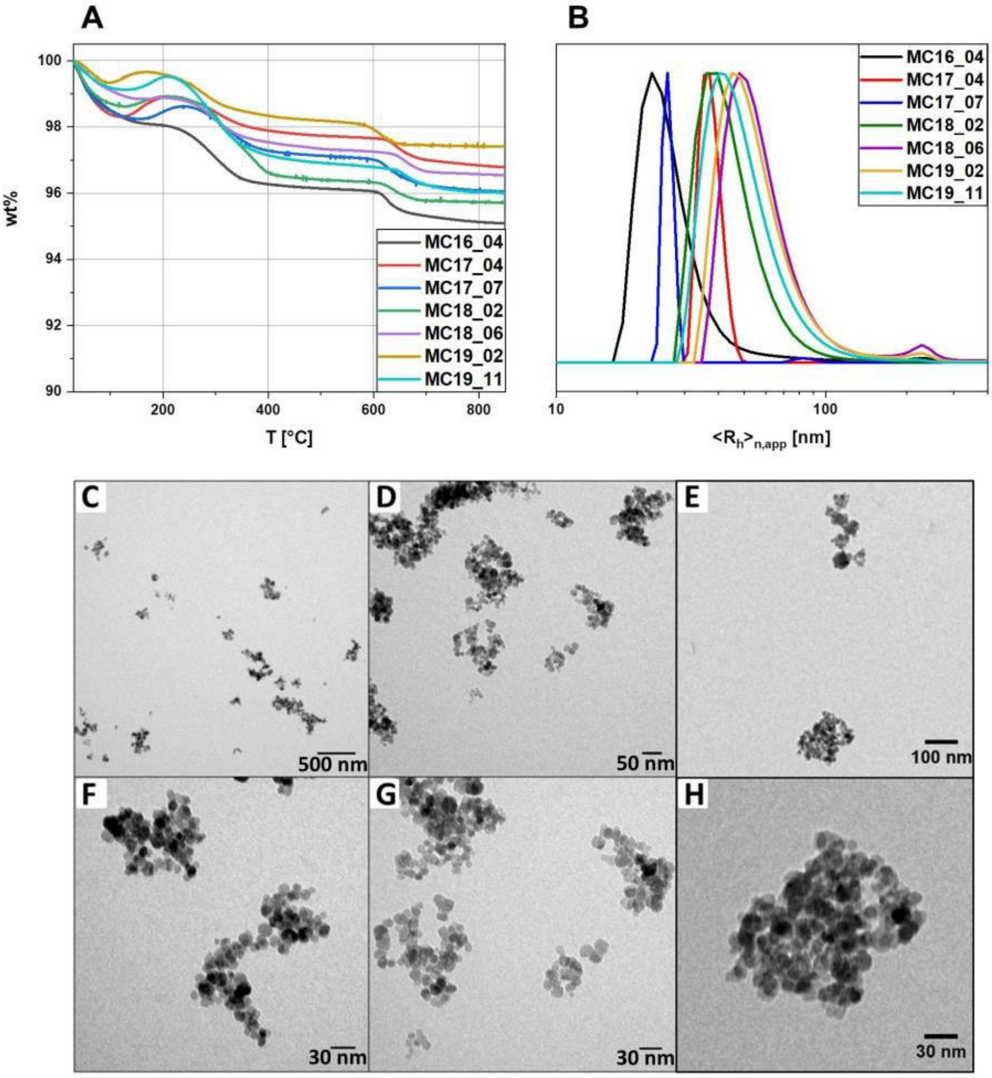

Figure 16: A) Thermograms of different batches pristine MCNP; B) Number-weighted DLS CONTIN plots of different batches of pristine MCNP; C)-G) exemplary TEM micrographs of pristine MCNP.

3.2. Polyampholytes@MNP

The pristine MCNP were subsequently coated using the three different polyampholytes discussed in chapter 2.1 (PImAA, PDha, and PDAGA). The carboxylic acids which are present as pendant group in each polymer acted as ligands to bind the polymers effectively to the nanoparticles. The particles were subsequently analyzed using DLS, Zetasizer, TGA, and TEM and compared to the pristine MCNP.

The coating process was similar for all polymers. In a first step the respective polymer was dissolved in water and subsequently the MCNP were added to the solution. The suspension was constantly treated with ultra-sonication and mechanical stirring. The formed polymeric shell was quantified using TGA measurements (Figure 17E). As the polyampholytes exhibit different solution properties each polymer was dissolved under different conditions. PImAA and PDha were first dissolved under basic conditions and subsequently titrated with diluted hydrochloric acid to pH values close to neutral pH. As mentioned earlier both polymers start precipitating around pH 6-7. The adjustment of the pH is crucial as it was observed that a successful adsorption requires at least pH values below pH = 10. We observed that the quantity of adsorbed PImAA increased with lower pH value for coating (approximately 3 weight percent (wt.%) at pH = 8, about 8 wt.% at pH = 7). In case of PDha the solution was adjusted to a pH of 7 resulting in a shell of 10 wt.% polymer. Dissolving PDAGA required 10 wt.% sodium chloride (referred to the amount of polymer). This resulting solution had a pH value around 5 and led to PDAGA@MCNP with a polymer content of 8 wt.%.

The particles were characterized using TEM as shown in Figure 17A-D. The micrographs in Figure 17A show a representative overview of the particles, which shows that well separated multicore particles with no larger agglomerates are present. In Figure 17B-D representative micrographs of each particle type (PImAA@MCNP, PDha@MCNP, and PDAGA@MCNP) are shown. A slight grey shadow around the inorganic (multi-)core is visible which represents the organic layer. The particle aggregates here exhibit diameters between 150-200 nm and the organic shell is 2 to 5 nm thick. As these images are TEM micrographs from a dry state both shell thickness and aggregation state might differ from their appearance in solution.

The size of the coated nanoparticles was additionally investigated by DLS. The results, shown in Figure 17F show an increase of the hydrodynamic radius from 45 nm (pristine MCNP) to 75 nm upon coating with PDAGA and an in increase to 100 nm upon coating with PImAA or PDha. Since the particle size roughly doubles, it can be assumed that not only a polymer shell is responsible for the increasing radius, but additional aggregation must take place. Additional signals around 200 nm are a further indication for aggregation processes. However, the nano-related properties for iron-oxides are sufficiently preserved through the coating process.

TGA measurements together with DLS results were further used to determine a theoretical thickness of the respective polymer shells. It is possible to estimate a theoretical shell thickness by using the obtained wt.% of polymer together with the hydrodynamic radius from DLS measurements by the following formula:

Equation 1: Formula used for the calculation of shell thickness according to TGA.

$$r_s = \sqrt[3]{r_c^3 + \left(r_c^3 \left(\frac{\rho_c}{\rho_s}\right)\left(\frac{WL}{RM}\right)\right)} - r_c$$

r_s …shell thickness

r_c … core radius (from DLS: MCNP $\langle R_h \rangle_{n,app}$ = 45 nm)

ρ_c … core density (approx. 5.2 g/cm^{-3})

ρ_s … density of shell material (approx. 1.1 g cm^{-3})

WL … weight loss

RM … residual mass

For the three systems the calculations result in shell thicknesses of 5 nm (PDAGA), 6 nm (PDha), and 6 nm (PImAA). The results are fitting well to the measured organic layers from TEM measurements.

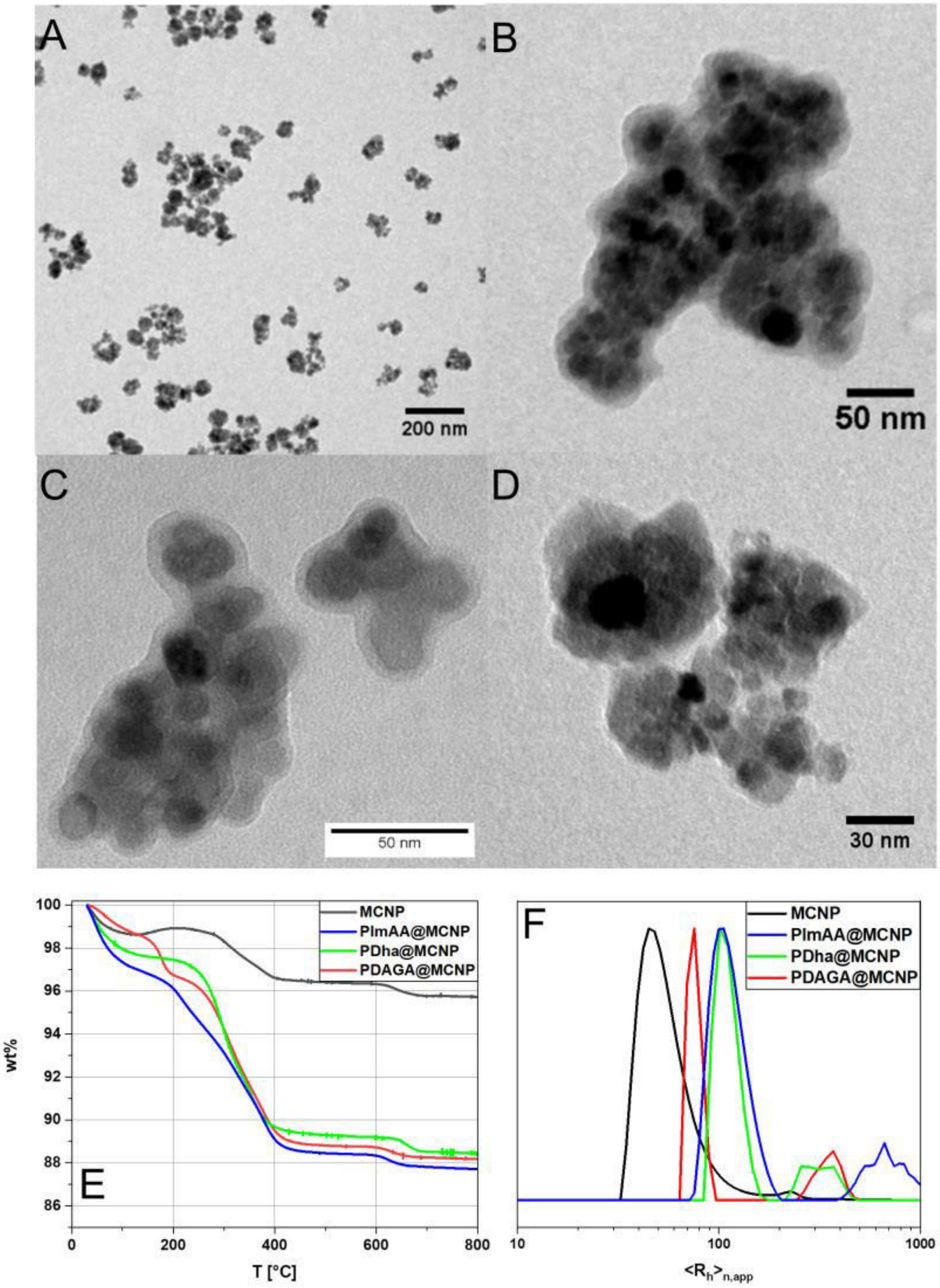

Figure 17: TEM micrographs of A) PDAGA@MCNP (overview) and higher magnifications of B) PDAGA@MCNP; C) PImAA@MCNP; D) PDha@MCNP; E) Thermograms of pristine MCNP (black line, 4% overall weight loss), PImAA@MCNP (blue line, 12.2%), PDha@MCNP (green line, 11.5%), and PDAGA@MCNP (red line, 11.9%); F) Number-weighted DLS CONTIN plots of pristine MCNP (black line, $\langle R_h \rangle_{n,app}$ = 45 nm), PImAA@MCNP (blue line, $\langle R_h \rangle_{n,app}$ = 100 nm), PDAGA@MCNP (red line, $\langle R_h \rangle_{n,app}$ = 75 nm) PDha@MCNP (green line, $\langle R_h \rangle_{n,app}$ = 100 nm). Reprinted from [Langmuir 2020, 36, 6095–6105] with permission of American Chemical Society.

Investigations of the surface charge revealed a strong dependence of zeta potential with the surrounding pH (Figure 18). Thereby all systems showed a switch from positive to negative surface potential when the pH was increased from acidic to basic conditions. The pH value of zero surface charge was strongly depending on the respective polyampholytic coating. While PDAGA@MCNP shows a point of zero charge (pzc) at pH = 3, PDha@MCNP shows a pzc charge at approximately pH = 4.5, and PImAA shows a pzc charge around pH = 6. These values fit very well to the observations of a starting precipitaton of the respective polyampholytes which occurred during their titrations described in chapter 2.2. This shifting of the zero net charge can be explained by the different functional groups of the polymers. Here it can be seen, that the chargeable groups varying from primary amines over imidazole groups to tertiary amines on the one hand and the amount of carboxylic acids on the other hand have tremendous influence on the nanoparticle surface charge. It was further found that a rather good estimation of the pzc can be achieved by comparison of the polyampholytic coating with its corresponding amino acid. Thus glutamic acid (comparable to PDAGA, IEP at pH = 3.08), alanine (comparable to PDha, IEP at pH = 6.11), and histidine (comparable to PImAA, IEP at pH = 7.64) follow a similar trend.

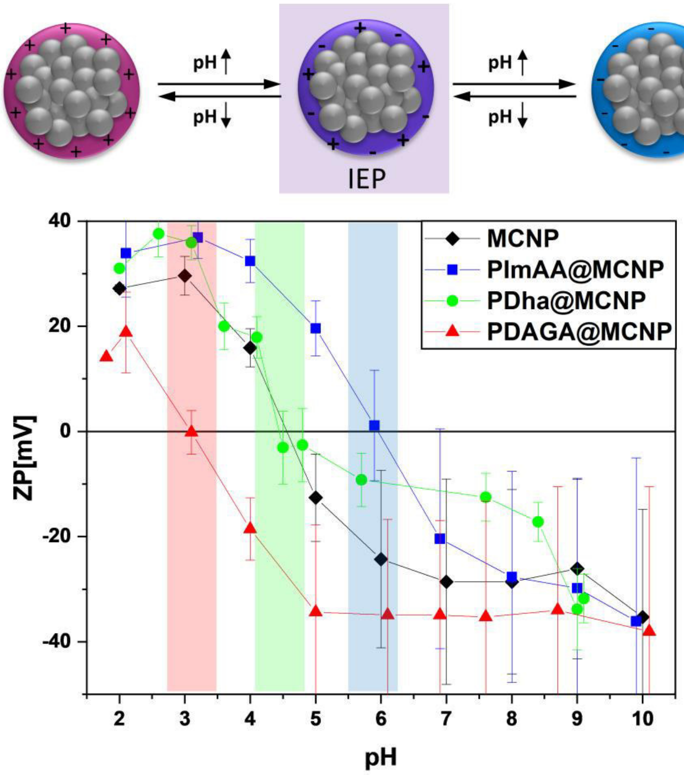

Figure 18: pH-dependent zeta potentials of pristine MCNP (black squares), PImAA@MCNP (blue squares), PDha@MCNP (green squares), and PDAGA@MCNP (red squares). Reprinted from [Langmuir 2020, 36, 6095–6105] with permission of American Chemical Society.

Additionally, all surface-coatings were examined for their pH stability (Figure 19A-C). The particles were exposed to different pH values . The results show that all shells were stable under acidic conditions and towards basic conditions at least to a pH of 9. At a pH of 10, a reduction in the organic content was clearly determined by TGA, which can be attributed to a partial detachment of the polymer shell. This finding fits to the earlier mentioned observation, that the coating process required pH values below 10 for a sufficient attachment of the polyampholytes. We assume that a ligand exchange at the MCNP surface from attached polymer towards hydroxide ions causes the loss of the shell rather than changes in the functional groups of the polymer. It is known from many synthesis protocols that hydroxide ions can be directly used as surface ligands for the respective colloidal nanomaterial.[15] The acidification of the suspension which leads to a protonation of both amine and carboxylic acid did not cause a shell detachment. Furthermore the shell stability over time was examined for one of the three systems by TGA. The results in Figure 19D indicate a good shelf stability of the polymeric shell for at least half a year.

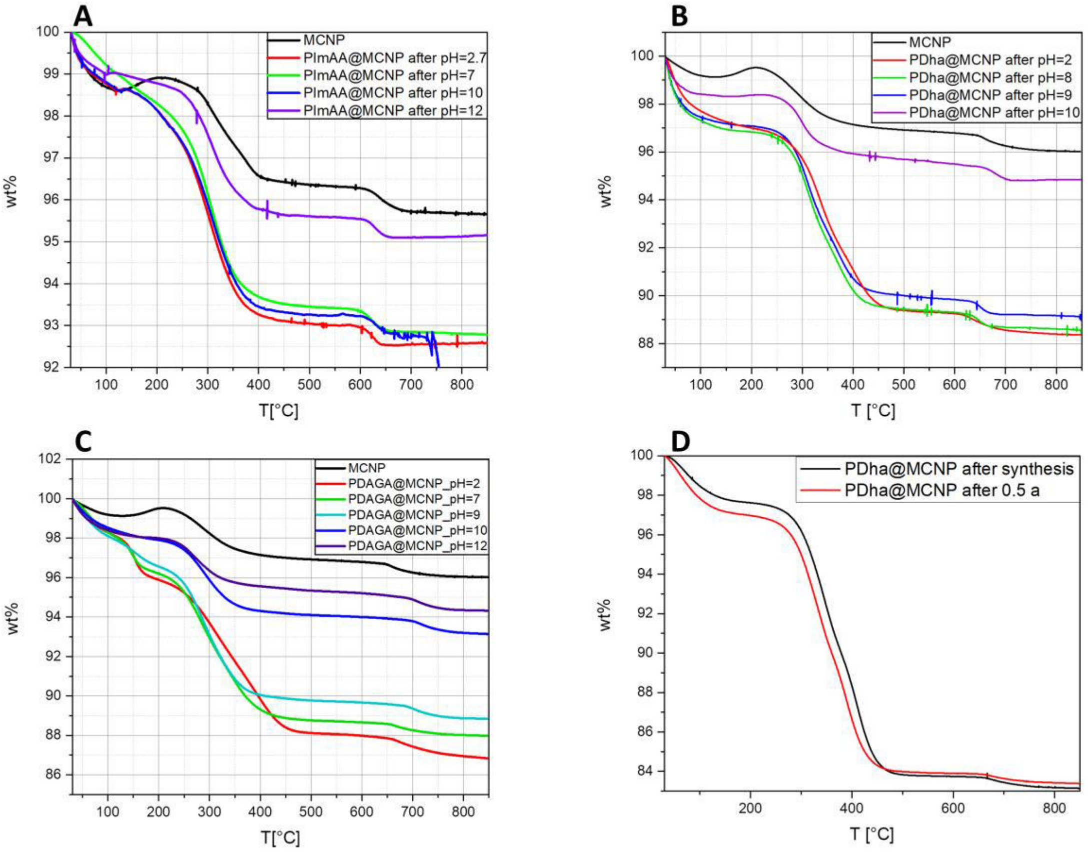

Figure 19: A) Thermograms of MCNP (black line) and PImAA@MCNP after exposure to different pH values: after exposure to pH 2.7 (red line), after exposure to pH 7 (green line), after exposure to pH 10 (blue line), and after exposure to pH 12 (purple line); B) thermograms of MCNP (black line) and PDha@MCNP after exposure to different pH values: after exposure to pH 2 (red line), after exposure to pH 8 (green line), after exposure to pH 9 (blue line), and after exposure to pH 10 (purple line); C) thermograms of MCNP (black line) and PDAGA@MCNP after exposure to different pH values: after exposure to pH 2 (red line), after exposure to pH 7 (green line), after exposure to pH 9 (turquoise line), after exposure to pH 10 (blue line), and after exposure to pH 12 (purple line); D) thermograms of PDha@MCNP directly after synthesis (black, line) and after 0.5 years of storage (red, line). Reprinted from [Langmuir 2020, 36, 6095–6105] with permission of American Chemical Society.

As the zeta potential showed strong a dependence on the surrounding pH we further investigated the hydrodynamic size of PDha@MCNP and PDAGA@MCNP in dependence of the pH (Figure 20A-D). The nanoparticles were exposed to a pH value of about pH = 9 and subsequently titrated. At certain pH values a sample was drawn. The results show that both systems increase in their hydrodynamic size when the pH is lowered. Between pH 4.8 and 9 no drastic change in hydrodynamic size was observed for both systems. However, when the pH was lowered further, especially to pH values of 3 a sudden and strong increase in the hydrodynamic size was observable. While PDha@MCNP increased from $\langle R_h \rangle_{n,app,max}$ = 100 nm to 950 nm PDAGA@MCNP increased from $\langle R_h \rangle_{n,app,max}$ = 100 nm at pH = 9.2 to

$\langle R_h \rangle_{n,app,max}$ = 450 nm at a pH = 3. However, these results are not what we initially expected. Since the pzc is usually accompanied by the lowest electrostatic stability of colloidal systems, an increase in the hydrodynamic diameter is expected in this area. However, here we so far did not find a convincing correlation between the pzc and a change in hydrodynamic size.

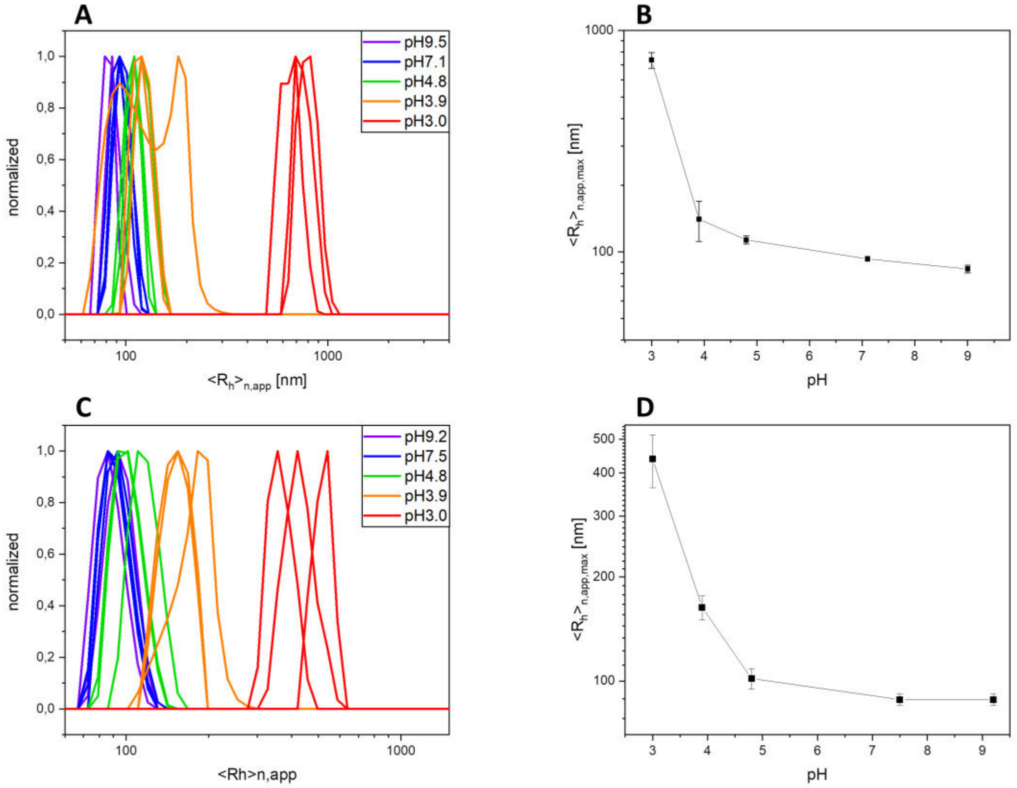

Figure 20: A) Number-weighted DLS CONTIN plots of PDha@MCNP under different pH: pH = 9.5 (purple lines), pH = 7.1 (blue lines), pH = 4.8 (green lines), pH = 3.9 (yellow lines), pH = 3.0 (red lines); B) maxima of $\langle R_h \rangle_{n,app}$ from A) plotted against the respective pH value; C) number-weighted DLS CONTIN plots of PDAGA@MCNP under different pH: pH = 9.2 (purple lines), pH = 7.5 (blue lines), pH = 4.8 (green lines), pH = 3.9 (yellow lines), pH = 3.0 (red lines); D) maxima of $\langle R_h \rangle_{n,app}$ from C) plotted against the respective pH value. Reprinted from [Langmuir 2020, 36, 6095–6105] with permission of American Chemical Society.

3.3.Zwitterionic Copolymers as Coating for MNP

In addition to the above discussed polyampholytes we used copolymers bearing zwitterionic units on the one hand and units acting as surface ligand on the other hand for the surface functionalization of MCNP with the result of enhanced suspension stability.

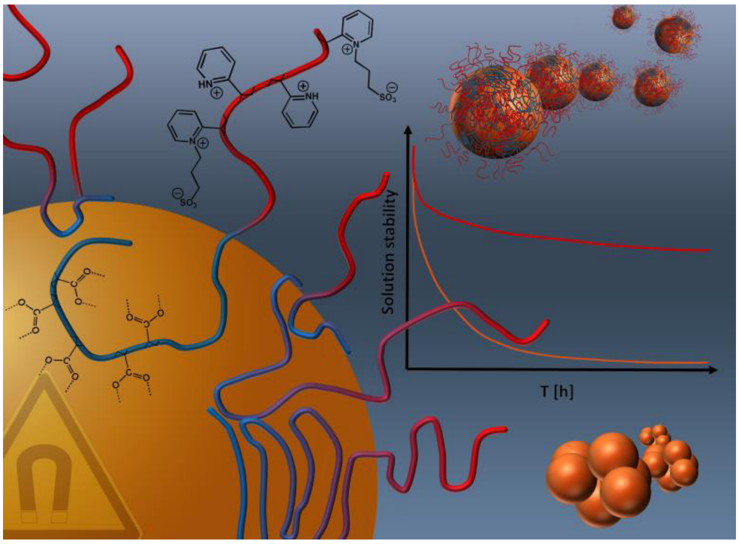

Figure 21: Graphical representation of polyzwitterionic covered MNP for an enhanced suspension stability. Reprinted from [Macromol. Rapid Commun. 2017, 38, 1600637] with permission of John Wiley and Sons.

Zwitterionic polymers are often lacking an inherent binding-group for the successful immobilization at MNP. Different ways of applying selective binding-groups have been examined so far by using initiators bearing binding-groups,[59, 117-118] end-group modification,[89] or the incorporation of a polymer-block bearing multiple binding groups.[119] We were aiming for a copolymer-approach with one polymer-part exhibiting binding capacities while the other one introduces zwitterionic properties. The benefit of a copolymer driven binding in contrast to an end group binding group functionalization lays in the multiple binding-sites created by the polymer, leading to an enhanced stability of the coating. In contrast to polymers which bear the binding-group inherent in their repetitive unit it has to be stressed that the synthesis effort of copolymers is higher but on the other hand allows the introduction of a broader variety of functional groups.

The gradient copolymers which were applied here consisted of poly(2-vinylpyridine)-*grad*-poly(*tert*-butyl acrylate) (P(2VP-*grad*-*t*BA)) which were subsequently deprotected to obtain P(2VP-*grad*-AA). The poly(acrylic acid) served as binding unit while the 2VP units were further transformed into zwitterions(Scheme 4).

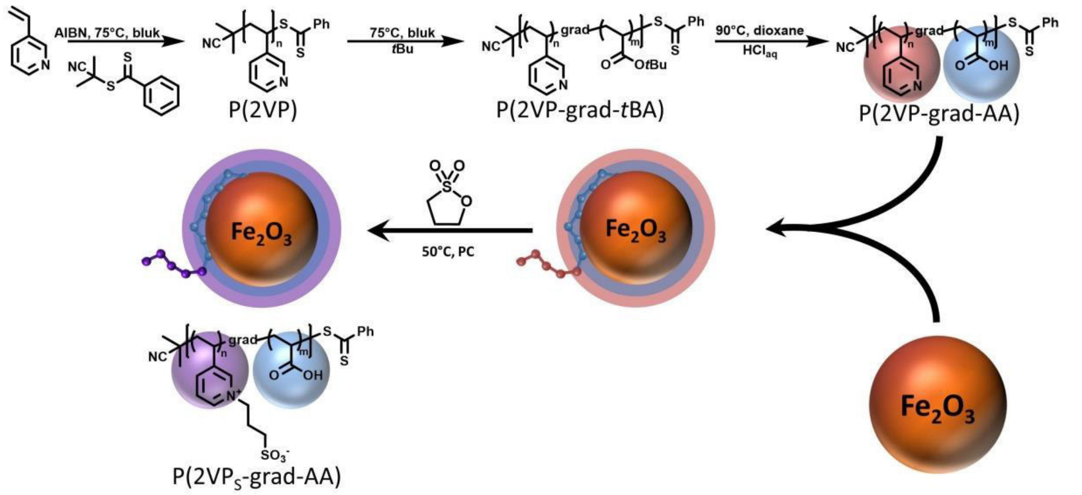

Scheme 4: Graphical representation of P(2VP-*grad*-*t*BA) synthesis using RAFT polymerization and subsequent surface functionalization of MCNP using these bcps.

Two polymers were used for the surface functionalization, which varied in their respective molar mass and ratio of the repetitive units. Thus P(2VP$_{58}$-*grad*-AA$_{30}$) and P(2VP$_{45}$-*grad*-AA$_{37}$) were used for surface functionalization. The electrostatic adsorption of P(2VP-*grad*-AA) was realized by dissolving the polymers in water (pH = 5-6) and subsequently adding a dispersion of MCNP (wt. ratio MCNP:bcp = 1:1).

In order to generate zwitterionic moieties the 2-vinylpyridine units were transformed to a polybetaine structure (poly(3-sulfopropyl)-2-vinylpyridine (P(2VP$_S$-*grad*-AA))) by sultonation using 1,3-propanesultone.

DLS measurements (Figure 22A) revealed a hydrodynamic radius in the range of 35 nm for the pristine MCNP. Upon coating with P(2VP$_S$-*grad*-AA) the hydrodynamic radius increased to values between 37 and 47 nm, depending on the bcp and the pH value (pH = 5.6 and pH = 6.7). The variation of the hydrodynamic radius reveals a slight pH response of the system, which might be explainable by protonation of remaining pyridine groups, which exhibit a pK$_a$ of approximately 5.2 (pK$_a$ (pyridinium ion) = 5.23)[120] and remaining free carboxylic acids (pK$_a$ (PAA) = 4.2).[121] TGA allowed the determination of organic content at the nanoparticle surface (Figure 22B). The coating process using P(2VP-*grad*-AA) resulted in particles with 9 to 12 wt.% polymer. The post modification by 1,3-propanesultone did not lead to significantly different values here. For a further investigation of the pH dependent particle properties zeta potential measurements were performed and revealed that upon coating the pzc was shifted significantly from 6-7 for the pristine MCNP to lower pH values of 4-5. The sultonated 2VP groups lead to a negative surface charge over a broader pH range (Figure 22C).

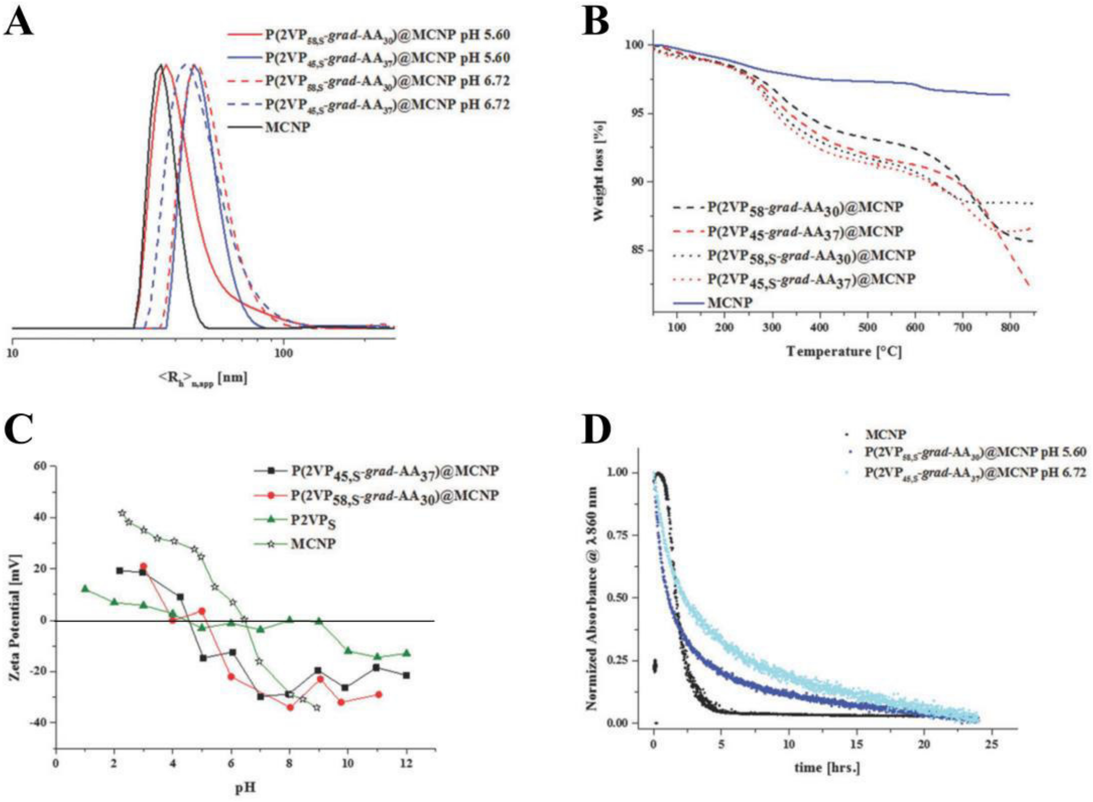

Figure 22: A) Number-weighted DLS CONTIN plots of P(2VP$_{58,S}$-*grad* -AA$_{30}$)@MCNP at pH = 5.6 (red line, ⟨R$_h$⟩$_{n,app}$ = 37 nm), of P(2VP$_{45,S}$-*grad* -AA$_{37}$)@MCNP at pH = 5.6 (blue line, ⟨R$_h$⟩$_{n,app}$ = 47 nm), P(2VP$_{58,S}$-*grad* -AA$_{30}$)@MCNP at pH = 6.7 (red dashed line, ⟨R$_h$⟩$_{n,app}$ = 47 nm), of P(2VP$_{45,S}$-*grad* -AA$_{37}$)@MCNP at pH = 6.7 (blue dashed line, ⟨R$_h$⟩$_{n,app}$ = 42 nm), pristine MCNP (black line, ⟨R$_h$⟩$_{n,app}$ = 35 nm); B) thermograms of P(2VP$_{58}$-*grad*-AA$_{30}$)@MCNP (black dashed line, 11 % overall weight loss), P(2VP$_{45}$-*grad*-AA$_{37}$)@MCNP (red dashed line, 12% overall weight loss), P(2VP$_{58,S}$-*grad*-AA$_{30}$)@MCNP (black dotted line 8 % overall weight loss), P(2VP$_{45,S}$-*grad*-AA$_{37}$)@MCNP (red dotted line, 10 % overall weight loss), pristine MCNP (blue line, 3% overall weight loss); C) pH-dependent zeta-potentials of P(2VP$_{45,S}$-*grad*-AA$_{37}$)@MCNP (black squares), P(2VP$_{58,S}$-*grad*-AA$_{30}$)@MCNP(red dots), P(2VP$_S$) (green triangle), pristine MCNP (white stars); D) sedimentation measurements of MCNP, P(2VP$_{58,S}$-*grad*-AA$_{30}$)@MCNP and P(2VP$_{45,S}$-*grad*-AA$_{37}$)@MCNP at pH 5.60 and 6.72, respectively. Reprinted from [Macromol. Rapid Commun. 2017, 38, 1600637] with permission of John Wiley and Sons.

TEM investigations of the coated nanoparticles showed compared to the pristine MCNP less aggregated particles. The average particle size (diameter) of P(2VP-*grad*-AA)@MCNP was determined to be ≈60–80 nm, which is close to the values from DLS measurements (70–90 nm). The size which was measured after sultonation is comparable to DLS data as well. The coating leads to aggregated particles as the TEM micrographs reveal and in some cases a copolymer coating was visualized (white arrow).

Finally the long-term colloidal stability of the systems was exemplary for P(2VP$_{45,S}$-*grad*-AA$_{37}$)@MCNP investigated in sedimentation measurements with concentrations of 0.1 g L^{-1} at pH values between 5.6 and 6.7 (Figure 22D). The measurements were recorded by measuring the UV-Vis absorbance of the respective suspension at 860 nm over time. The experiments showed that the application of a zwitterionic shell leads to reduced precipitation of the nanoparticles. While pristine MCNP fully precipitate within 5 hours the coated particles show a first rapid clearance of the solution but a prolonged stability of the remaining particles with stabilities up to 20 hours. Hereby a lower pH resulted in slightly reduced precipitation over time. The investigations show that the herein synthesized polymers allow to influence the solution stabilities of MNP.

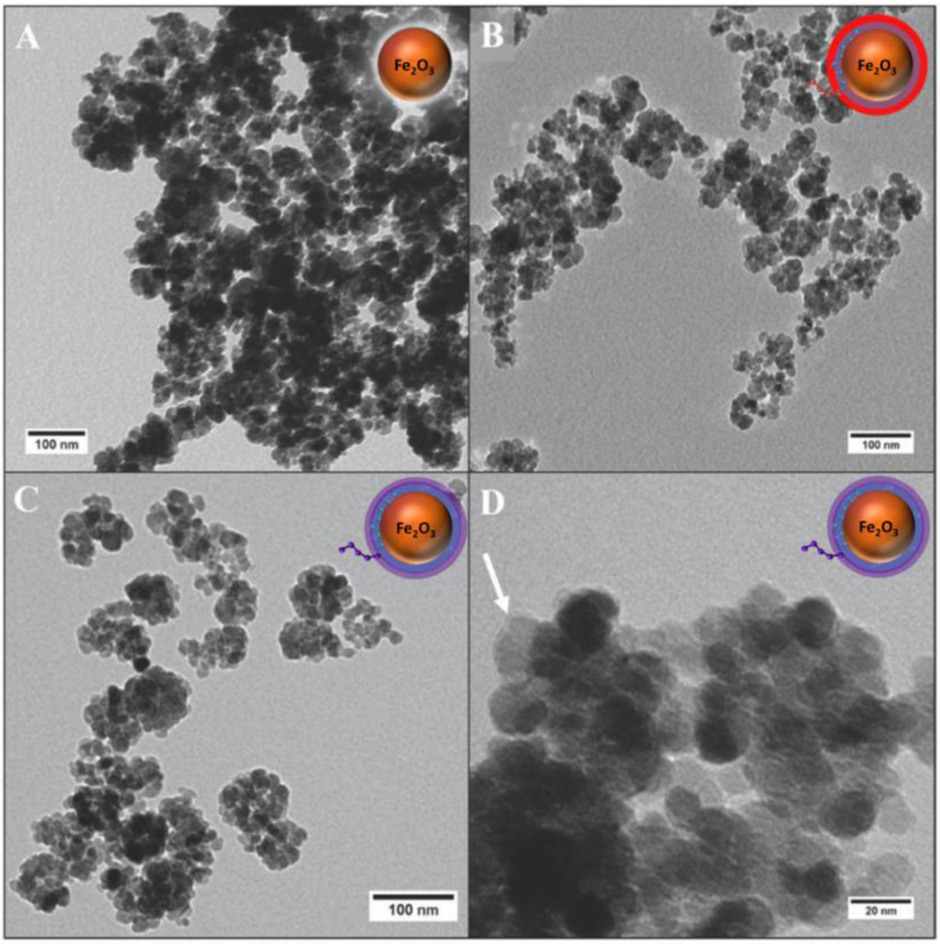

Figure 23: TEM micrographs of A) pristine MCNP, B) 2VP-grad-AA@MCNP; C)-D) 2VP$_S$-*grad*-AA@MCNP. Reprinted from [Macromol. Rapid Commun. 2017, 38, 1600637] with permission of John Wiley and Sons.

3.4. Silane Based Covalent Polymer Coating of MNP

The following chapter describes a versatile and universal approach to access a broad variety of polymeric surfaces at MNP (Figure 24). As the surface modification of MNP is a key element for their introduction into various areas of application a rapid and size maintaining coating procedure is of great value. As described before the manifold fields of application for MNP places special demands on the surface chemistry. To ensure certain physical characteristics like magnetic properties or maintain nanoparticle size in the respective surrounding the desired chemical functionality at the surface has to be adjusted on demand. The environment in which the particles will be potentially applied span from highly saline aqueous media[84], over biological media to organic solvents.[122]

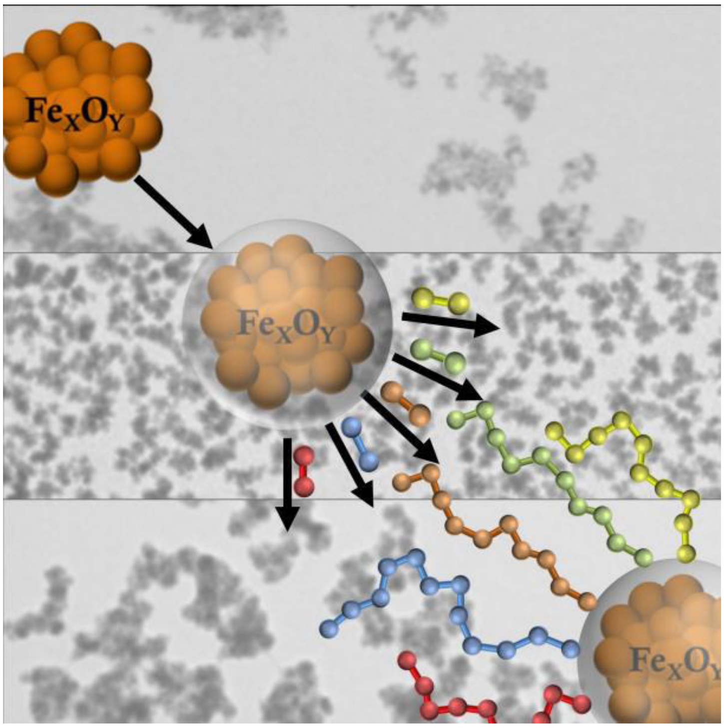

Figure 24: Graphical representation of surface functionalization of MNP Using a thiol-based grafting-through approach. Reprinted from [Surfaces 2020, 3, 116-131].

In order to vary their surface properties in a rapid way we synthesize thiol bearing MNP as a platform for further modification by different polymers. The surface-bound thiol-groups were used as transfer agents in a free radical polymerization process with a broad variety of monomers in order to gain access to different functional groups and thus to a different suspension stability of the nanoparticles.

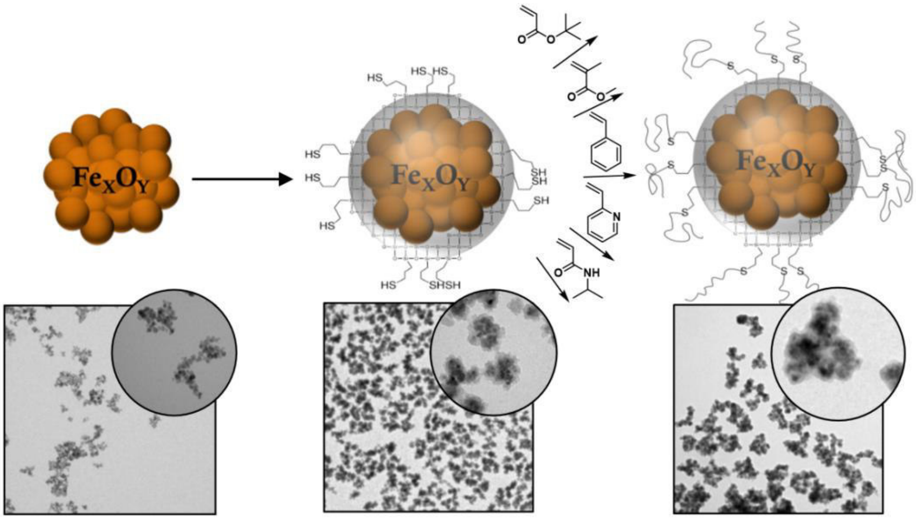

Scheme 5: Graphical representation of surface functionalization of magnetic multicore nanoparticles (MCNP) with (3 mercaptopropyl) trimethoxysilane (MPTS) and subsequent polymerization of different monomers in the presence of MPTS@MCNP. Reprinted from [Surfaces 2020, 3, 116-131].

Due to strong magnetic dipolar-dipolar interactions, single domain MNP tend to build up larger aggregates.[123] Thus the first challenge was the optimization of the silanization in a way that a defined silane coating was obtained while at the same time the nano-particular properties were preserved. Various publications investigate the coating of MNP with silica and present ways for defined nanostructures.[73-76, 78] Yet, it was difficult to simply adapt other protocols if the nanoparticles changed in size, from single to multicore character, or in chemical composition. Therefore it was necessary to optimize the coating procedure for the herein used MCNP. A diluted suspension of MCNP (0.2 mg/ml) at a pH of 11 (adjusted with KOH) was prepared, stirred mechanically and treated with ultra-sonication. To this suspension we added MPTS in dry ethanol at a constant flow rate of 50 µL min^{-1}. Subsequent to the addition of MPTS the mixture was allowed to react for 18 hours. The obtained particles were magnetically separated and washed several times. The silane coating led to a change in the color of the suspension from dark to light brown, a phenomenon that is also described in the literature for similar coating processes.[75]

By variation of the MPTS to MCNP ratio it was possible to gain certain control over both overall size and silane shell thickness. Figure 25A shows DLS data in aqueous conditions for the particles prior and after the coating process. The particles increase in size and size distribution after coating with MPTS. Pristine MCNP exhibited a hydrodynamic radius of 26 nm which increased to hydrodynamic radii of 50 up to 100 nm. Here the hydrodynamic radius increases as the MPTS to MCNP ratio was increased from 1:1 to 4:1. The formed silane shell can further be investigated quantitatively by TGA (Figure 25B). The silane shell consists partially of organic compounds (-$(CH_2)_3$-SH groups) which degrade upon heating under air. The resulting mass loss is proportional to the amount of formed shell. While the pristine nanoparticles show a wt. loss of 2.6 % (attributed to carbonates as discussed in chapter 3.1) the coating leads to an additional wt. loss between 8.2 % (ratio 1:1) and 27.8 % (ratio 4:1). These results indicate the successful development of a silane based shell.

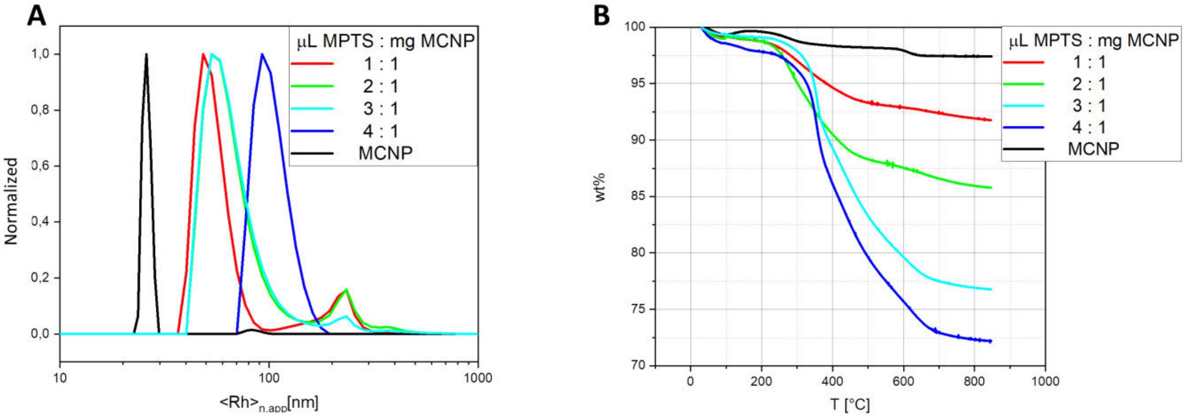

Figure 25: A) Number-weighted DLS CONTIN plots of pristine MCNP (black line, $\langle R_h \rangle_{n,app}$ = 26 nm), and MPTS@MCNP obtained for varying ratios of MPTS to MCNP of 1:1 (red line, $\langle R_h \rangle_{n,app}$ = 48 nm), 2:1 (green line, $\langle R_h \rangle_{n,app}$ = 53 nm), 3:1 (cyan line, $\langle R_h \rangle_{n,app}$ = 52 nm), 4:1 (blue line, $\langle R_h \rangle_{n,app}$ = 93 nm); B) Thermograms of MCNP (black line, 2.6% overall weight loss), MPTS@MCNP obtained from a ratio of MPTS to MCNP of 1:1 (red line, 8,2% overall weight loss), 2:1 (green line, 14,2% overall weight loss), 3:1 (cyan line, 23,2% overall weight loss), 4:1 (blue line, 27,8% overall weight loss). Reprinted from [Surfaces 2020, 3, 116-131].

To further verify the mean size of the MPTS@MCNP nanoparticles and the shell thickness we used TEM measurements (Figure 26). The micrographs show particles in the size range of 100-200 nm in agreement with the DLS results. A light grey shell becomes visible with an increasing ratio of MPTS to MCNP. At ratios of 3:1 and 4:1 the shell is clearly visible. The micrographs furthermore show that the shell diameter can be adjusted from 5 nm for the 3:1 ratio to about 15 nm in case of the 4:1 ratio. The data presented here show that using a 3:1 ratio, MPTS@MCNP feature a fairly thin and a defined shell, which is why these samples were selected for the following modifications.

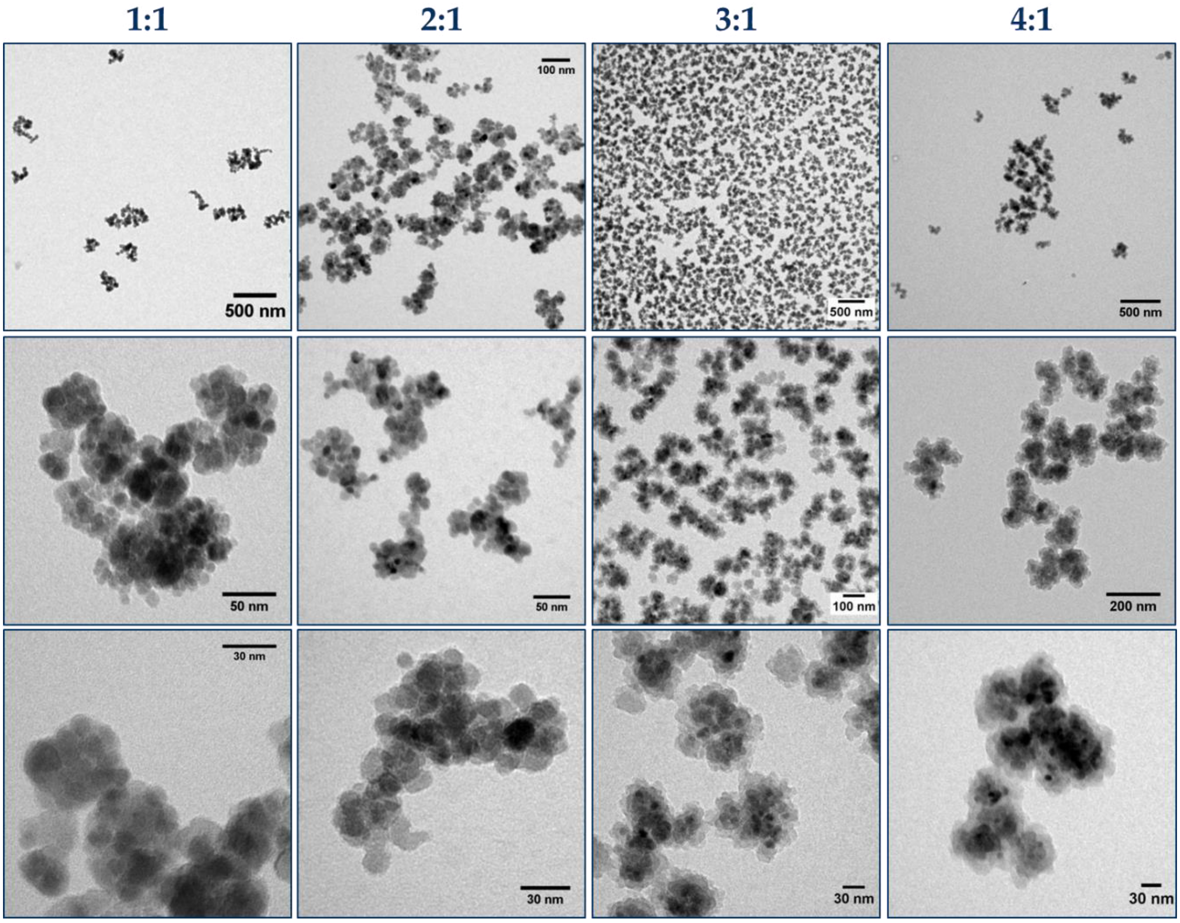

Figure 26: TEM micrographs of MPTS@MCNP obtained from different ratios of MPTS to MCNP at different magnifications. Reprinted from [Surfaces 2020, 3, 116-131].

In the following we used the obtained coated particles for further surface functionalization by a grafting trough approach. The surface bound thiols can act as chain transfer agents during a radical polymerization.[124-126] Thus we added the particles to radical polymerizations of various monomers with the intention that some polymer would be covalently bound to the MPTS@MCNP surface as a side reaction. We polymerized a broad variety of monomers ((*t*BA, MMA, styrene, 2VP, NIPAAm)) using THF as solvent. THF was a suitable solvent for all monomers/polymers while at the same time allowing an excellent dispersion of the nanoparticles. TPO as initiator allowed rather short polymerization times of 20 min. The obtained polymers from the reaction solution were characterized using SEC measurements (Figure 27). Rather broad dispersities around 2 occurred, which is typical for a FRP approach and molar masses between 9 kg mol^{-1} (P2VP) and 141 kg mol^{-1} (PMMA) were reached.

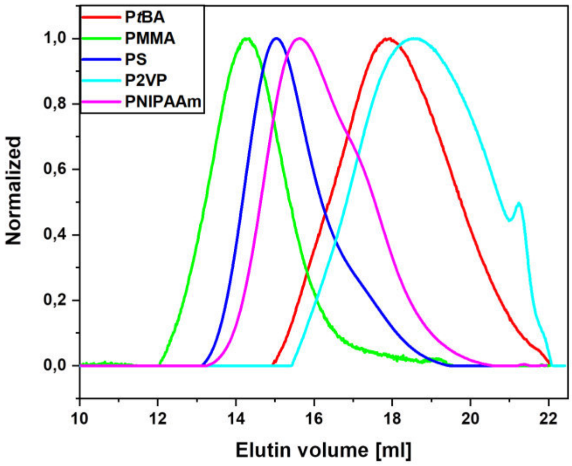

Figure 27: SEC elution traces (DMAc/LiCl) of polymers synthesized by free radical polymerization in the presence of MPTS@MCNP as chain transfer agent: red line: P*t*BA (M_n = 8,900 g mol^{-1}; *Đ* = 2.2); green line: PMMA (M_n = 141,200 g mol^{-1}; *Đ* = *2*.1); blue line: PS (M_n = 58,500 g mol^{-1}; *Đ* = 1.9); cyan line: P2VP (M_n = 5,600 g mol^{-1}; *Đ* = 2.3); pink line: PNIPAAM (M_n = 35,400 g mol^{-1}; *Đ* = 2.0). Reprinted from [Surfaces 2020, 3, 116-131].

An investigation of the particles using DLS revealed an increasing hydrodynamic radius upon polymerization (Figure 28A). MPTS@MCNP exhibited a radius of 51 nm in THF which increased to values between 174 and 224 nm. This size increase cannot simply be explained by the formation of a polymeric shell. We assume a combination of aggregation and shell formation. PMMA@MPTS@MCNP and P2VP@MPTS@MCNP exhibited a shoulder at higher radii, which also indicates the occurrence of secondary aggregation. The thermogravimetric investigation (Figure 28B) of the particles allows a mass quantification of the respective bound polymer. While MPTS@MCNP showed a mass loss of 23.2 % an additional wt. loss was occurring for the polymer grafted particles. The majority of polymer showed a wt. loss between 31 % (PMMA) and 21 % (P*t*BA). Only a grafting using PNiPAAm resulted in 11 wt.% showing an exceptional low polymer content. Additional to the wt. loss it was observed that the onset of the decomposition shifted to lower temperatures, which was an additional indication for the development of a polymeric shell.

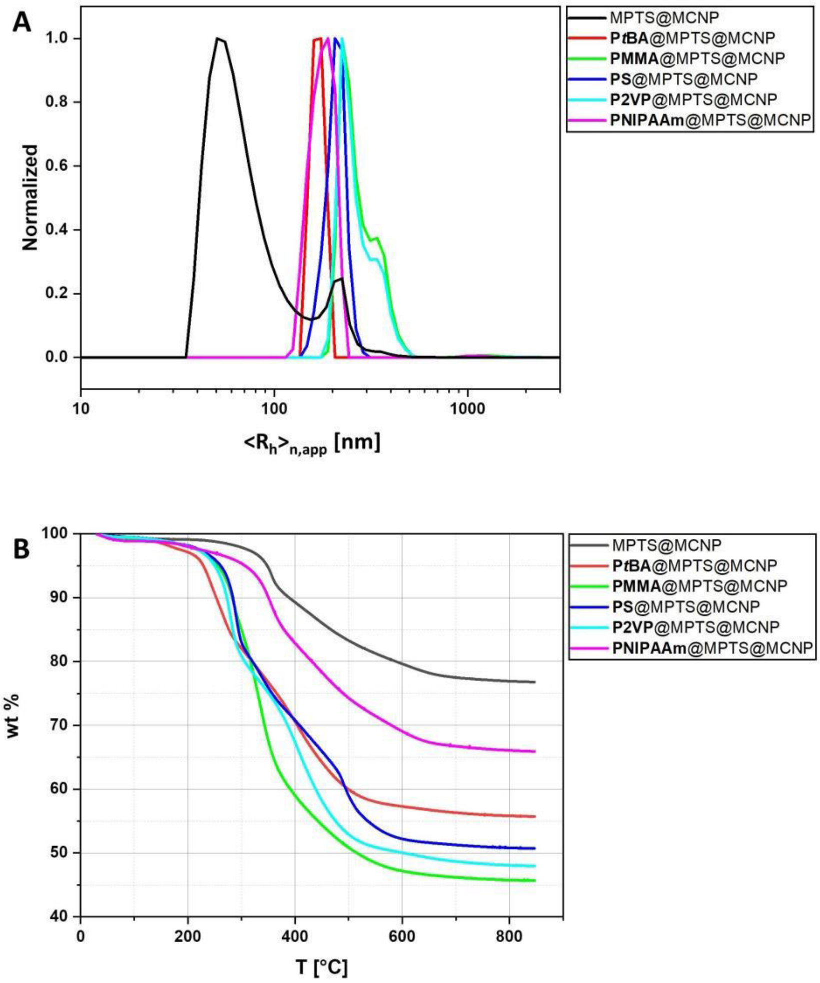

Figure 28: A) Number-weighted DLS CONTIN plots of MPTS@MCNP (black line, $\langle R_h \rangle_{n,app}$ = 51 nm), P*t*BA@MPTS@MCNP (red line, $\langle R_h \rangle_{n,app}$ = 174 nm), PMMA@MPTS@MCNP (green line, $\langle R_h \rangle_{n,app}$ = 224 nm), PS@MPTS@MCNP (blue line, $\langle R_h \rangle_{n,app}$ = 206 nm), P2VP@MPTS@MCNP (cyan line, $\langle R_h \rangle_{n,app}$ = 224 nm); PNIPAAm@MPTS@MCNP (pink line, $\langle R_h \rangle_{n,app}$ = 190 nm); B) Thermograms between 50°C and 850°C under synthetic air of MPTS@MCNP (black line, 23.2% overall weight loss), P*t*BA@MPTS@MCNP (red line, 44.3% overall weight loss), PMMA@MPTS@MCNP (green line, 54,3% overall weight loss), PS@MPTS@MCNP (blue line, 49,3% overall weight loss), P2VP@MPTS@MCNP (cyan line, 52,0% overall weight loss); PNIPAAm@MPTS@MCNP (pink line, 34,1% overall weight loss). Reprinted from [Surfaces 2020, 3, 116-131].

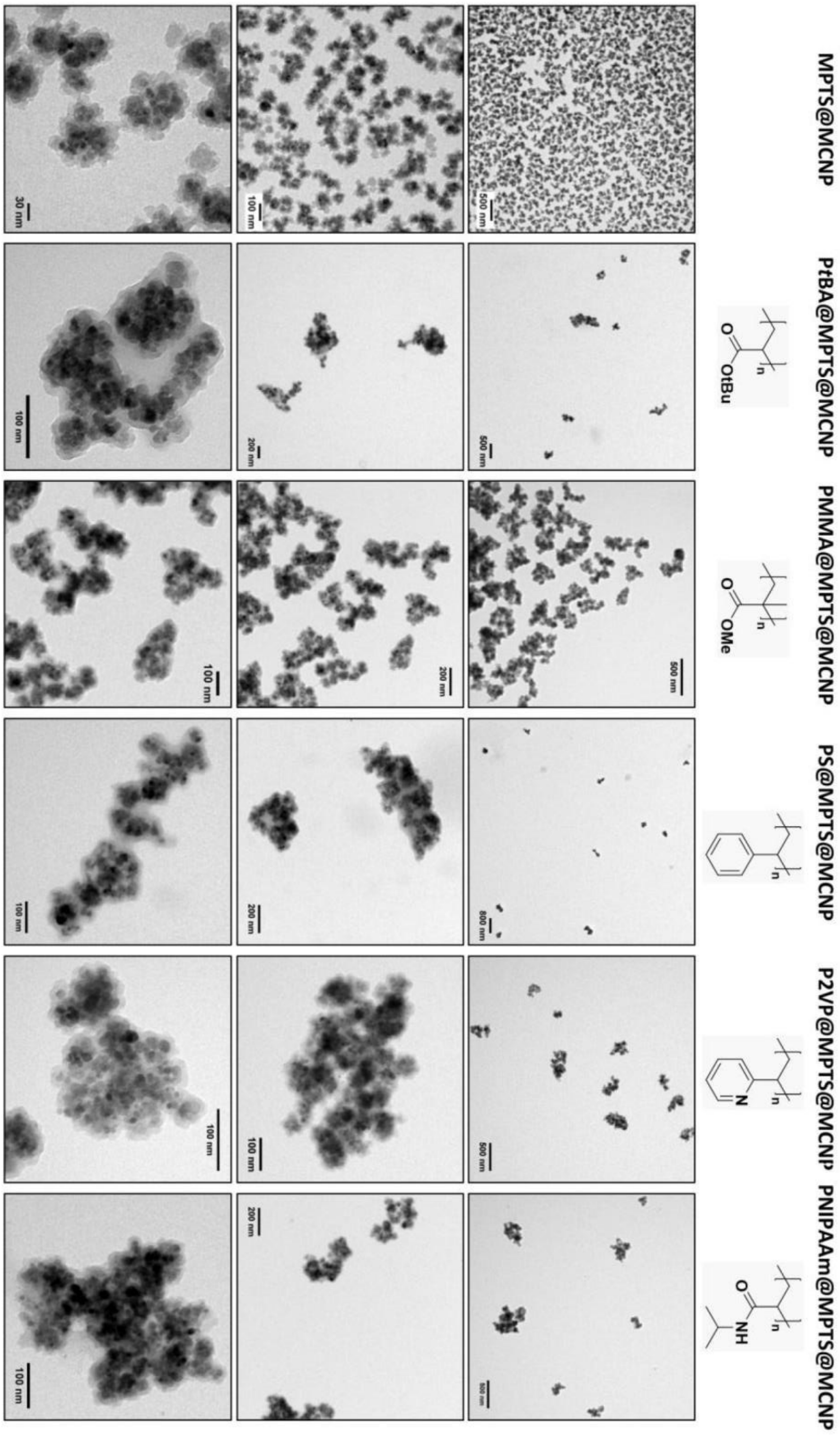

Figure 29: TEM micrographs of different polymer@MPTS@MCNP obtained from polymerizations in the presence of MPTS@MCNP as chain transfer agent at different magnification.

In addition to DLS and TGA analysis we used TEM to investigate the grafted particles. The TEM micrographs in Figure 29 verified the hydrodynamic radii from DLS measurements (between 200 and 400 nm). Further it can be seen that several particles aggregated during the polymerization process as already assumed. However, the polymeric shell is not clearly distinguishable towards the silica shell. Probably due to the high electron contrast of iron oxide compared to the lower electron contrast of silica and organic material.

Moreover, we investigated the functional groups at the nanoparticles using attenuated total reflection Fourier-transform infrared (ATR-FTIR) spectroscopy. The results in Figure 30 show significant signals for all expected functional groups of the respective polymers. Acrylates showed an intense carbonyl band at 1720 cm^{-1}, while the polymers with aromatic ring structures (PS, and P2VP) exhibited ring bands between 1600 - 1570 cm^{-1} and 1500 - 1470 cm^{-1}. PNIPAAm-functionalized particles showed an additional band at 1550 cm^{-1}, which is assigned to an amide functionality. All together the different analytical results confirmed a successful polymer immobilization at the nanoparticle surface.

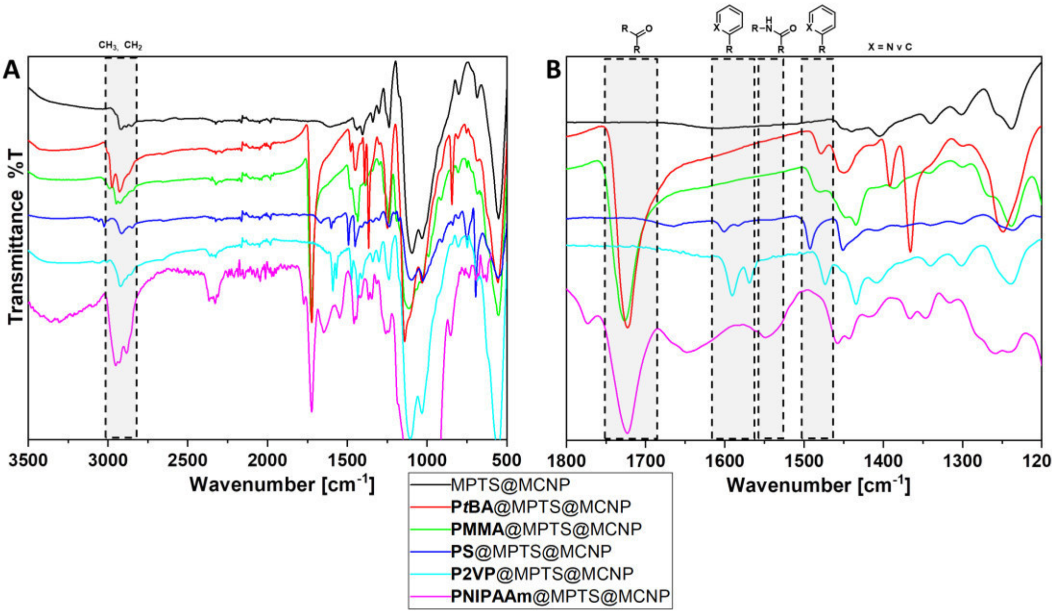

Figure 30: A) ATR-FTIR spectra - black line: MPTS@MCNP; red line: P*t*BA@MPTS@MCNP; green line: PMMA@MPTS@MCNP; blue line: PS@MPTS@MCNP; cyan line: P2VP@MPTS@MCNP; pink line: PNIPAAm@MPTS@MCNP; B) Enlargement of the region within the spectra where functional groups can be assigned. Reprinted from [Surfaces 2020, 3, 116-131].

As the thiols at the particles can reversibly interact with radicals we expected an influence of the nanoparticle concentration on the final properties of the formed polymers. We investigated this in an exemplary set of polymerizations using styrene as monomer. Thus the amount of nanoparticles was varied between 5 and 50 mg while the other components in the polymerization solution remained unchanged. The resulting polymers changed in their molar mass and dispersity (Figure 31). As expected the dispersity decreased constantly with an increasing amount of nanoparticles from 9.6 to 2.8. We ascribe this to the lowered amount of free radicals in the solution as the free radicals at the forming polymers can reversible bind to the thiols at the nanoparticle surface. Simultaneously the M_n of the respective polymers was increasing. However, if the maximum of the weight distribution is considered in the SEC elution traces it was evident that a constant shift was not observable. This leads to the conclusion that the influence of the thiols is more pronounced towards the dispersity and not the resulting molecular mass.

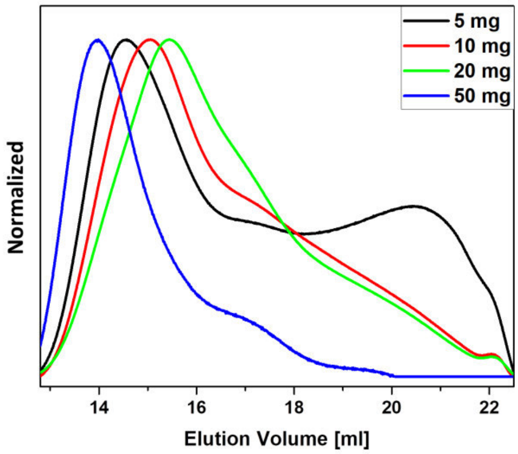

Figure 31: SEC elution traces (DMAc/LiCl) of PS synthesized by free radical polymerization in the presence of different amounts of MPTS@MCNP as chain transfer agent: black line: PS obtained in the presence of 5 mg (M_n = 6,900 g mol^{-1}; $Đ$ = 9.6); red line: PS (10 mg, M_n = 12,800 g mol^{-1}; $Đ$ = 5.2) ; green line: PS (20 mg, M_n = 13,300 g mol^{-1}; $Đ$ = 4.5) ; blue line: PS (50 mg, M_n = 62,600 g mol^{-1}; $Đ$ = 2.8). Reprinted from [Surfaces 2020, 3, 116-131].

Finally we investigated the difference between the surface bound polymers and the polymers obtained from the polymerization solution. Therefore we decomposed the nanoparticles using 1 M HCl / ethyl acetate and 1 M aq. KOH solutions to access the surface bound polymer. Investigations via SEC (Figure 32E) showed that both polymers, the one obtained from the particles and the one from solution, matched well in terms of molar mass. A shoulder at higher elution volume expressed for the polymer in solution is not present for the PS obtained from the particles, which indicates that polymers with lower molar mass are less present on the particle surface.

The results allow the conclusion that a fast and versatile investigation of the polymers at the surface of the nanoparticles can be done by investigating the polymers in the reaction solution in parallel.

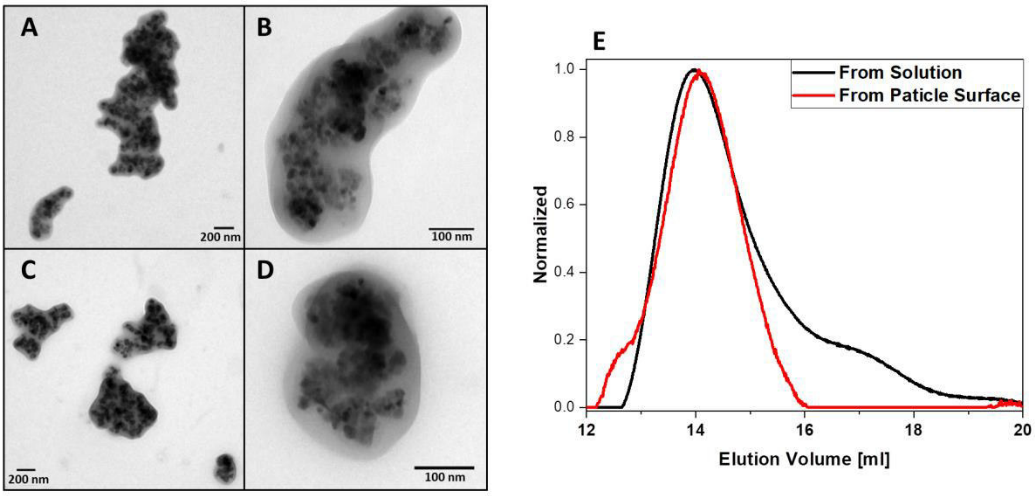

Figure 32: A)-D) TEM micrographs of PS@MPTS@MCNP; E) SEC elution traces (DMAc/LiCl) of PS synthesized by free radical polymerization in the presence of MPTS@MCNP: black line: PS from reaction solution (M_n = 62,600 g mol^{-1}; $Đ$ = 2.78); red line: PS obtained from particle surface (M_n = 165 kg mol^{-1}; $Đ$ = 1.80). Reprinted from [Surfaces 2020, 3, 116-131].

4. Catch and Release Experiments

Parts of this chapter have been published in **P3)** P. Biehl, M. von der Lühe, F. H. Schacher, *Macromolecular Rapid Communications* **2018**, *39*, 1800017; **P6)** P. Biehl, P. Wiemuth, J. G. Lopez, M.-C. Barth, A. Weidner, S. Dutz, K. Peneva, F. H. Schacher, *Langmuir* **2020**, *36,* 6095–6105.

4.1.Catch and Release of Dyes by PDha@MNP

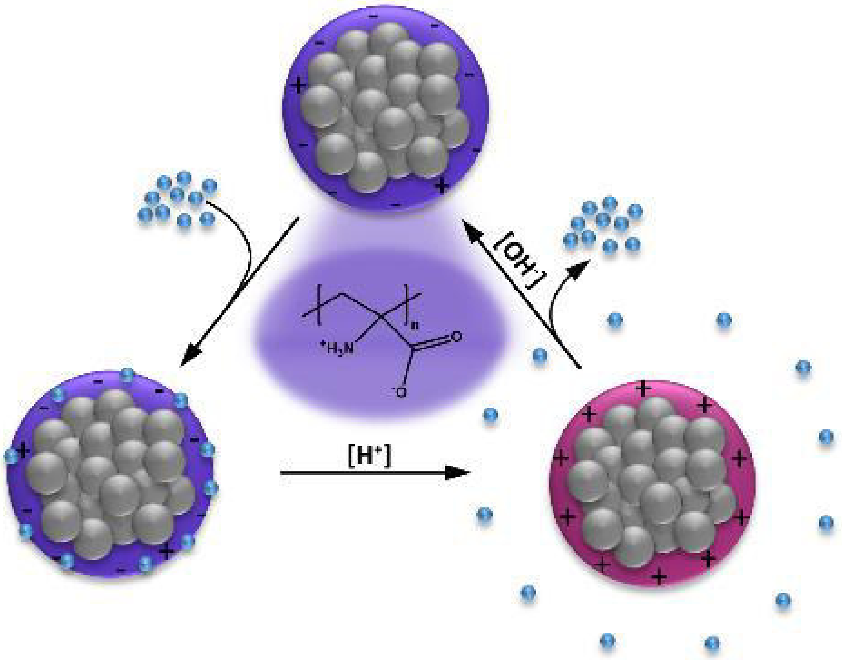

Scheme 6: Graphical representation of adsorption and pH-induced desorption of MB (blue dots) to PDha@MCNP, followed by magnetic separation and recovery of PDha@MCNP. Reprinted from [Macromol. Rapid Commun. 2018, 39, 1800017] with permission of John Wiley and Sons.

We used polydehydroalanine coated magnetic multicore nanoparticles (PDha@MCNP), synthesized as described in chapter 3.2, for adsorption experiments described in the following section. As the polyelectrolyte shell exhibits a pH-dependent surface charge (chapter 3.2) we made use of the electrostatic interactions with its surrounding. In a model experiment we used the cationic dye methylene blue (MB) as exemplary cargo. Considering the zeta potential measurements we expected the surface to be negatively charged under neutral pH conditions which would lead to a rapid adsorption of cationic molecules. Thus we prepared a solution of MB under neutral conditions and exposed PDha@MCNP to this solution (Figure 33A). After magnetic separation the amount of adsorbed MB was determined by UV-Vis spectroscopy. Therefore, an untreated stock solution of MB was compared to the supernatant of the same MB solution after the adsorption to PDha@MCNP had taken place. The results are shown in Figure 33B. As the polyelectrolyte shell switches the surface charge upon pH lowering from negative to positive a subsequent release of the MB could be initiated by exposing the loaded nanoparticles to an acidic environment. At pH = 2 a well visible release takes place (Figure 33A right). However, UV-Vis measurements revealed a non-quantitative release.

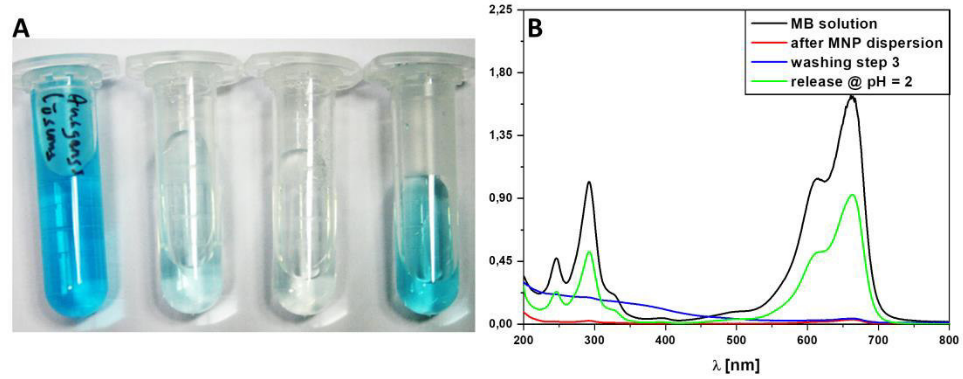

Figure 33: A) Photographs of MB blue solutions (from left to right: prior to PDha@MCNP dispersion, after MCNP dispersion, pH = 7 washing step, pH = 4 desorption), and B) UV-Vis spectra of MB solutions prior to (black line), and after dispersion of 15 mg PDha@MCNP (red line), supernatants of washing steps of the MCNP (blue line), and solution of MB desorbed from PDha@MCNP (green line). Reprinted from [Macromol. Rapid Commun. 2018, 39, 1800017] with permission of John Wiley and Sons.

The adsorption of MB was further investigated in terms of the nanoparticle amount used for adsorption. 2.5 mg, 5 mg, and 15 mg PDha@MCNP were used to adsorb MB (Figure 34). The intensity of the main absorbance band of MB decreased after PDha@MCNP were separated and the remaining absorption intensity was lower the more PDha@MCNP was used. After several washing steps MB was released from the particles at pH = 2. Considering that the particles were loaded with different quantities of MB the subsequent release can be judged by the percentage of released dye. 2.5 mg release 14% of the loaded cargo, while 5 mg PDha@MCNP release 33% of the cargo and 15 mg release 57% of its cargo.

Since a release at pH = 2 represents rather harsh conditions, we investigated higher pH conditions for desorption (Figure 34B). Hence, we used 5 mg of PDha@MCNP for MB adsorption, washed the particles and dispersed them subsequently for 20 s at pH values ranging from pH = 3 to pH = 6. After treating the samples with the respective pH solution, MB is released for pH values 3 and 4 while pH values 5 and 6 did not show any release. The apparent isoelectric point of PDha@MCNP, which is located between pH 4 and 5 (as presented in chapter 3.2), gives a reasonable explanation for the observed release limit between pH = 4 and 5. In addition, the measurements show that the pH not only determines the release qualitatively but also quantitatively, since a pH of 3 releases more MB than a pH of 4. Further desorption steps under the same pH environment show negligible release of MB for all samples.

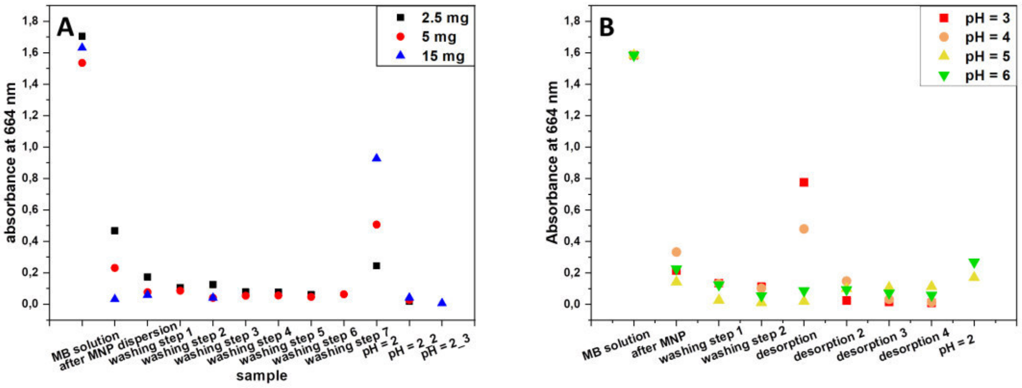

Figure 34: A) Intensities of MB main absorbance band before and after dispersion of different amounts of PDha@MCNP, washing steps, and desorbing solutions and B) intensities of MB main absorbance band before and after dispersion of PDha@MCNP, washing step, and desorbing solutions at different pH values. Reprinted from [Macromol. Rapid Commun. 2018, 39, 1800017] with permission of John Wiley and Sons.

The reversibility of the adsorption/desorption process was investigated by dispersing 15 mg of PDha@MCNP repeatedly in MB solutions (0.008 mg mL^{-1}) and aqueous solutions at pH = 2, followed by a washing step with micro-pure water for nine additional cycles (Figure 35A). While the remaining MB absorption in the starting solution was reduced from 1.6 to 0.03 after the first cycle, the absorption remained at 0.6-0.7 in the three subsequent cycles. In contrast, the absorption of the desorption solutions remains almost constant at 0.9. Between the fourth and fifth cycle the particles were allowed to regenerate in water for 15 hours. As a result, the absorption of the MB solution after treatment with PDha@MCNP was again reduced to 0.28, and the absorption of the desorption solution was increased to 1.0, which indicates a regeneration of the system. The following cycles show a similar adsorption and release behavior as observed for cycles 2-4.

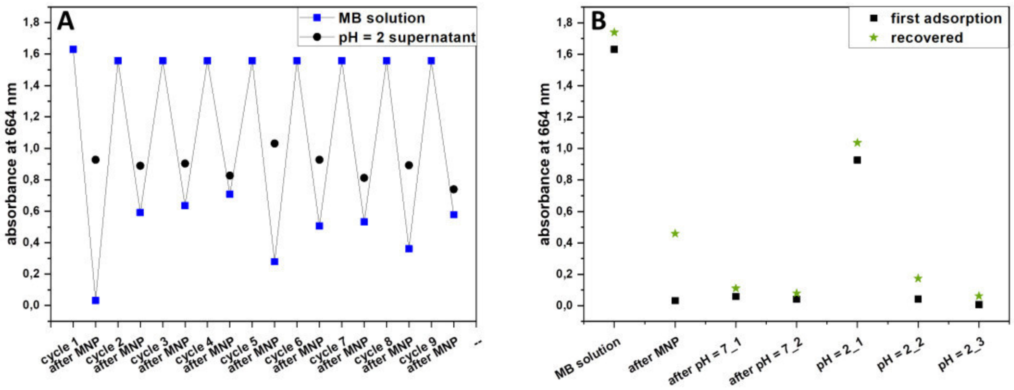

Figure 35: A) 9 consecutive cycles of a MB solution before and after dispersion of PDha@MCNP (black squares), and pH = 2 solutions after desorption of MB (black dots), and B) Initial adsorption/desorption cycle of a 15 mg sample (black squares), and cycle after 24 hours recovery in micro pure water (green stars). Reprinted from [Macromol. Rapid Commun. 2018, 39, 1800017] with permission of John Wiley and Sons.

4.2. Catch and Release of Various Charged Dyes

As the experiments shown in the previous chapter indicated a pH dependent charge related adsorption and desorption of the cationic dye MB to PDha@MCNP, we were further interested in a broader overview about this adsorption and release behavior. Scheme 7 illustrates the pH-dependent surface charge we expect for the nanoparticle system and the resulting interactions with either cationic (red dots) or anionic (blue dots) molecules. In the following we examined a broad variety of anionic and cationic dyes for adsorption and release studies using PDha@MCNP as carrier system.

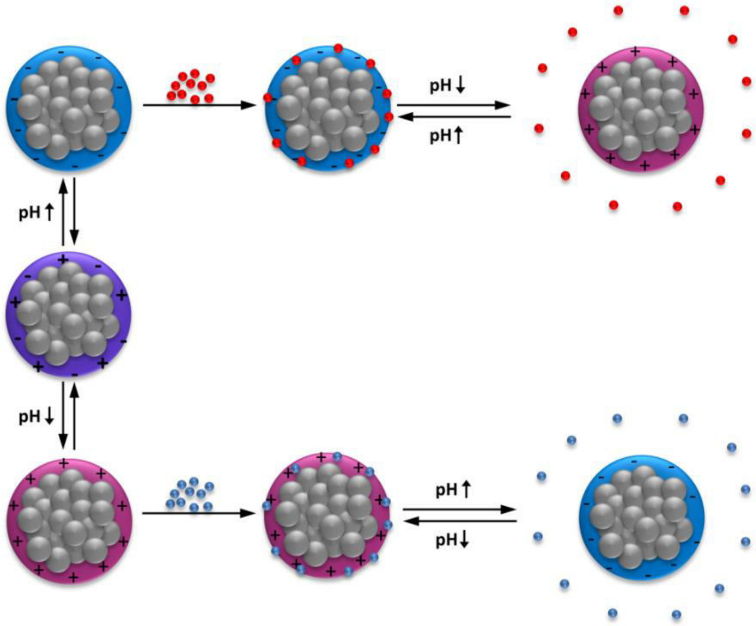

Scheme 7: Graphical representation of the pH-dependent adsorption and release of charged small molecules (model dyes) using PDha@MCNP hybrid nanoparticles. Reprinted from [Langmuir 2020, 36, 6095–6105] with permission of American Chemical Society.

All model dyes we used were water soluble, exhibited either cationic or anionic net charge, and varied in the number of chargeable groups, e.g. the amount of amines (Fuchsine vs. neutral red). The structural formulas of all used dyes are summarized in Scheme 8. The two dyes **PDI-4Pyl** (*N,N´*-Bis(2,6-diisopropylphenyl)-1,6,7,12-tetra-[3-(*N*-methylpyridinium)oxy]perylene-3,4,9,10-tetracarboxylic acid diimide iodide) and **PDI-4S** (*N,N´*-Bis(2,6-diisopropylphenyl)-1,6,7,12-tetra-[(4-sulfuric acid)phenoxy] perylene-3,4,9,10-tetracarboxylic acid diimide)[127-128] are of particular interest as their chemical structures are similar while they exhibit opposite charge. As the PDha@MCNP exhibit a different surface charge with varying pH (as described in chapter 3.2) two different adsorption conditions were investigated (pH = 7, where PDha@MCNP exhibit a negative surface charge and pH = 2 where a positive surface charge was found).

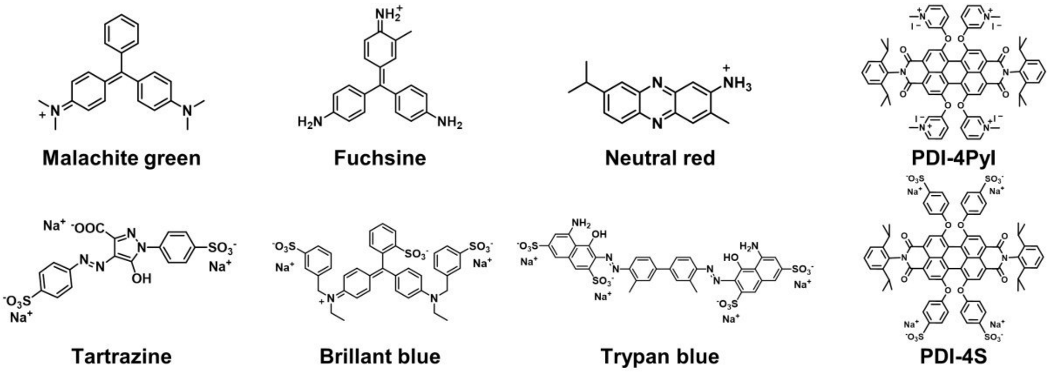

Scheme 8: Structure of charged model dyes investigated in this work: Malachite green, Fuchsine, Neutral red, PDI-4Pyl, Tartrazine, Brillant blue, Trypan blue, and PDI-4S. Reprinted from [Langmuir 2020, 36, 6095–6105] with permission of American Chemical Society.

The adsorption experiments were carried out under similar conditions. A solution of 10 µg ml^{-1} of each dye was added to 2.5 mg PDha@MCNP. The particles were dispersed and subsequently separated. The supernatant and the initial solution of the dye were investigated by UV-Vis as exemplarily shown for three examples in Figure 36A-C. All adsorption processes were completed within a few minutes.

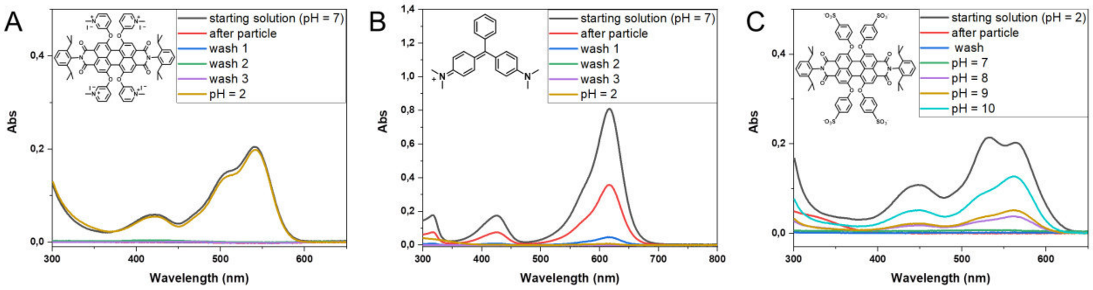

Figure 36: UV-Vis-spectra of adsorption and release experiments of PDha@MCNP with A) PDI-4Pyl (full adsorption and full release); B) Malachite green (partial adsorption and no release), and C) PDI-4S (full adsorption under acidic conditions) using PDha@MCNP. Reprinted from [Langmuir 2020, 36, 6095–6105] with permission of American Chemical Society.

As predicted by the measured surface charge, we observed the general trend that positively charged dyes adsorbed to the particles under neutral conditions and released under acidic conditions, while negatively charged dyes adsorbed under acidic conditions to the particles and got released under neutral or slightly basic conditions. All dyes showed a similar trend and were not adsorbed under opposite conditions, demonstrating the pH-controlled adsorption selectivity of this system.

However, not all dyes adsorbed to the same extent. Table 3 summarizes the adsorption and release behavior of all investigated dyes quantitatively so that (++) describes dye which were removed quantitatively according to UV-Vis measurements, while (+) describes a partial removal of the respective dye, and (0) defines that no adsorption occurred. As an example for a partial removal Figure 36B represents the partial removal as the adsorption band for Malachite green is reduced but still clearly visible. Surprisingly for us the amount of adsorbed dye seems not to depend on its net charge as for example neutral red and PDI-4PyI with a respective charge of +1 and +4 per molecule were removed completely, while Malachite green and Fuchsine just adsorbed in low amounts despite their positive net charge. We assume that structural differences in the dyes are responsible for the different adsorption behavior. The delocalized cationic charge in case of Malachite green and Fuchsine together with an additional steric hindrance by the phenyl groups could be decisivehere. Similar results for the adsorption behavior of dyes based on triarylmethane structures were already described by Meng *et al.*[129] While their adsorption process was mainly described by van der Waals forces, dyes with triarylmethane structure adsorbed well while azobenzene dyes were less effectively adsorbed, which is the direct opposite of what we found for our system based on electrostatic interactions.

Table 3: Adsorption and release of different charged dyes using PDha@MCNP; ++ full adsorption, + partial adsorption, 0 no adsorption, - not carried out. Reprinted from [Langmuir 2020, 36, 6095–6105] with permission of American Chemical Society.

Dye (net charge)	Adsorp.	Desorp.	Adsorp.	Desorption			
	pH = 7	pH = 2	pH = 2	pH = 7	pH = 8	pH = 9	pH = 10
Malachite green (+1)	+	0	0	0	-	-	-
Fuchsine (+1)	+	0	0	0	-	-	-
Neutral red (+1)	++	++	0	0	-	-	-
PDI-4PyI (+4)	++	++	0	0	-	-	-
Tartrazine (-2)	0	0	++	0	+	+	+
Brillant blue (-2)	0	0	++	0	+	+	+
Trypan blue (-4)	0	0	++	0	+	+	+
PDI-4S (-4)	0	0	++	0	+	+	+

4.3. Comparative Adsorption/Release of Charged Dyes to Polyampholytes@MNP

The results for different adsorption and release experiments from the previous chapters using PDha@MCNP suggested that the point of zero charge (pzc) plays an important role for the catch and release behavior of the nanoparticle system towards charged molecules. We found that the crucial pH value at which a release of cationic dyes occurred was located between pH = 4 and 5 which coincided with the pzc for this system. Thus, we wanted to investigate how differently the three systems from chapter 3.2 (PImAA@MCNP, PDha@MCNP, and PDAGA@MCNP) would interact with either cationic or anionic dyes with focus on the underlying polyampholytic shell. For this purpose we used the two perylene based dyes PDI-4PyI and PDI-4S, already described in the previous chapter. As mentioned before the advantage of these two dyes lies in their similar chemical structure which allows a good comparison of the adsorption behavior relaying mainly on the overall net charge of the dye and not on structural differences.

With regard to the comparison of the three polyampholytic shells we also examined the catch and release behavior of pristine MCNP (Figure 37). This revealed the importance of a polyampholytic shell as the control experiments showed neglectable adsorption capability for cationic dyes at neutral pH and just the adsorption of an anionic dyes under acidic conditions and a subsequent release under basic conditions (pH = 8) was observed.

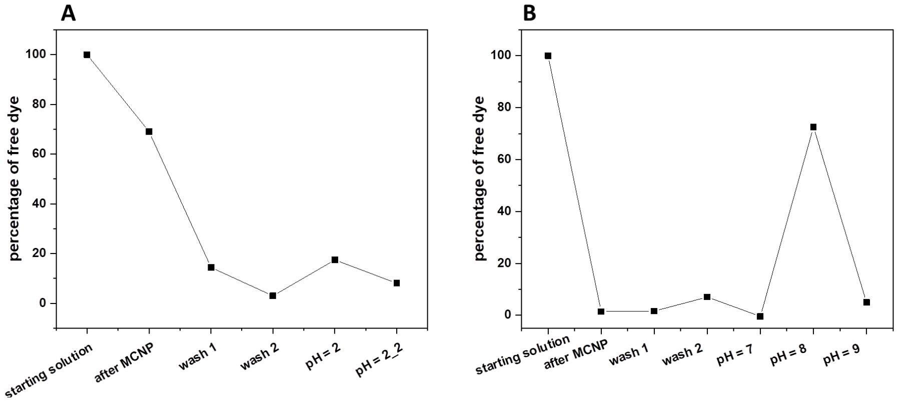

Figure 37: A) Adsorption experiments for PDI-4PyI using pristine MCNP under neutral pH conditions, subsequent washing steps, and pH lowering for potential release; B) Adsorption experiments for PDI-4S using pristine MCNP under pH = 2, subsequent washing steps, and pH increase for potential release. Reprinted from [Langmuir 2020, 36, 6095–6105] with permission of American Chemical Society.

Adsorption and release of PDI-4Pyl

The adsorption and release of the cationic dye PDI-4Pyl was investigated under comparable conditions for all nanoparticle systems. After the dye was adsorbed to the three systems they were subsequently exposed to a gradually lowered pH environment. The pH value was lowered in steps of one pH value and the respective supernatants were investigated using UV-Vis spectroscopy. Finally all values for the released dye were summed up. The percentage of free dye for each step is shown in Figure 38B. We found that the cationic dye was barely adsorbed by the PImAA coated particles, while a complete adsorption was observed for particles coated either with PDha or PDAGA. The poor adsorption properties of the PImAA shell might refer to the pH value of the starting solution which is close to the pzc of PImAA@MCNP. Thus the particles do not exhibit a sufficiently negative surface charge. As a consequence of this no subsequent release study was carried out for PImAA@MCNP. The two systems using PDha or PDAGA as coating both showed a first release when the pH was lowered to 4, even though the PDAGA system was expected to release at lower pH values as the pzc for this system is around pH = 2-3. However, the release PDAGA was highly efficient while the release in case of PDha@MCNP was of 87 %.

Further the maximum loading efficiency of PDha@MCNP and PDAGA@MCNP towards PDI-4Pyl was investigated as shown in Figure 38C and a Langmuir-Isotherm was assumed for the adsorption process. The maximum loading capacity of PDI-4Pyl at PDha@MCNP was found to be 11.4 µg mg^{-1} while PDAGA@MCNP showed a maximum loading capacity of 18.4 µg mg^{-1}. We attribute the higher maximum loading capacity of the PDAGA coated system to the additional carboxylic acid per repeating unit compared to PDha@MCNP, resulting in more potential binding sites. Furthermore it can be seen that the zeta potential of PDha@MCNP at pH = 7 is around -10 mV while PDAGA exhibits -35 mV, which gives an additional explanation for the lower affinity towards cationic dyes.

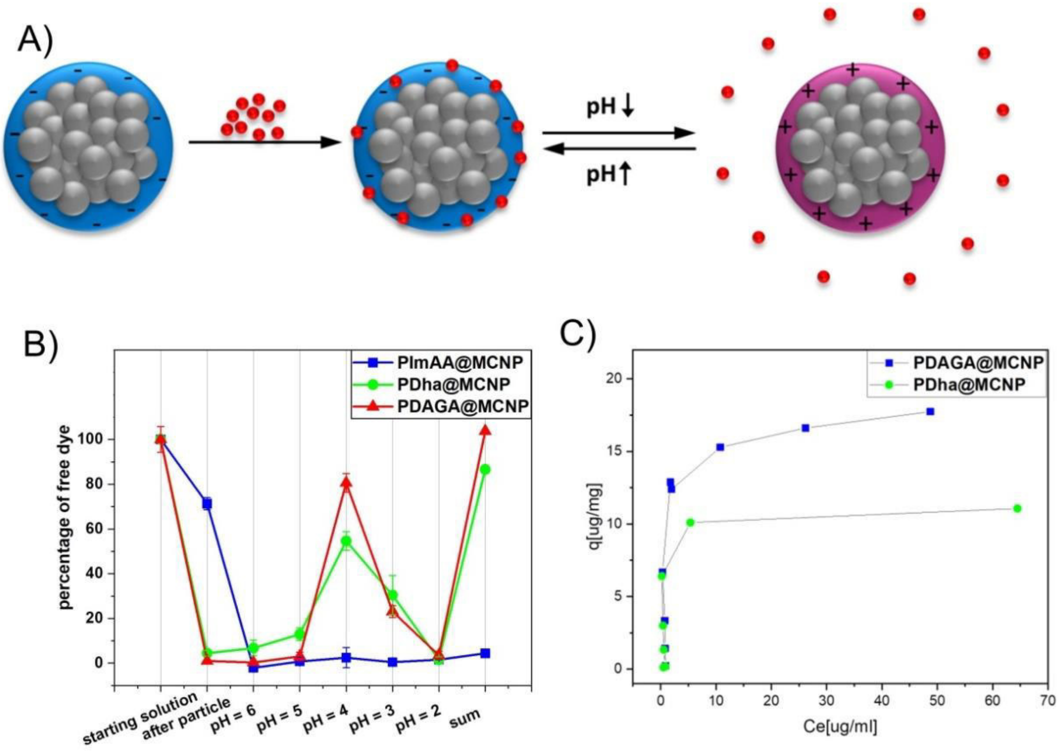

Figure 38: A) Graphical representation of the adsorption / desorption process; B) intensities of the PDI-4Pyl main absorbance band (542 nm) before and after dispersion of coated particles, washing steps, and solutions at different pH values; C) Adsorption isotherm of PDI-4Pyl to PDAGA@MCNP and PDha@MCNP. Conditions: Particles: 2 mg ml^{-1}; PDI-4Pyl: 1–50 µg ml^{-1}; temperature: 25 °C; pH: 7. Reprinted from [Langmuir 2020, 36, 6095–6105] with permission of American Chemical Society.

Adsorption and release of PDI-4S

Further, we examined the adsorption and release behavior of the three systems using the anionically charged dye PDI-4S. In contrast to the previous experiments we started the adsorption process under acidic conditions (pH = 2) and gradually raised the pH value in steps of one pH. The results in Figure 39 show that all nanoparticle systems adsorb the anionic dye completely. The crucial pH value for a release depends strongly on the polyampholytic shell. In case of PDAGA a first release is observed at pH = 5, the PImAA shell leads to a first release at pH = 7, and finally the PDha shell releases the dye at a pH of 8. According to their pzc the sequence in which the systems release is rather surprising, as one would expect that PDha shows a release at lower pH values than PImAA. The systems exhibited different values for the overall release. While PImAA@MCNP and PDha@MCNP both released 83 %, PDAGA released 73 % of the initially applied dye.

The maximum loading capacity of PDI-4S towards the three systems was determined as before for the cationic dye PDI-4Pyl, using a Langmuir adsorption isotherm as fundamental adsorption model at pH = 2. Here the three systems showed quite different capacities. While the capacity for PDAGA@MCNP was 47.3 µg mg^{-1}, PDha@MCNP showed a lower capacity with 15.6 µg mg^{-1}, and 50.5 µg mg^{-1} were found for PImAA@MCNP.

The adsorption experiments of both PDI-dyes show a reproducible adsorption and release behavior of the respective dye with each hybrid system. Depending on the polyampholytic shell different pH values were required for a successful release and individual loading capacities were found, which shows that the respective polyampholyte influences the catch and release behavior both qualitatively and quantitatively.

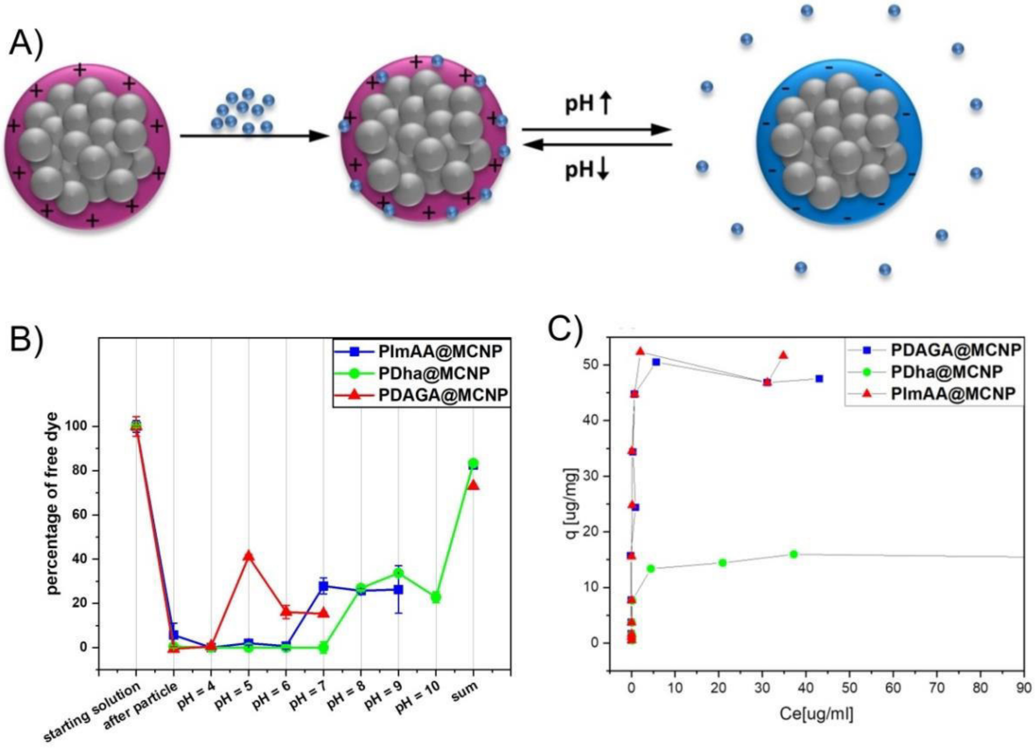

Figure 39: A) Graphical representation of the investigated adsorption/desorption process; B) intensities of the PDI-4S main absorbance band (564 nm) before and after dispersion of coated particles, washing steps, and solutions at different pH values; C) Adsorption isotherm of PDI-4S to PDAGA@MCNP, PDha@MCNP, and PImAA@MCNP. Conditions: Particle concentration 2 mg ml^{-1}; PDI-4S: 1–50 µg ml^{-1}; temperature: 25 °C; pH: 2. Reprinted from [Langmuir 2020, 36, 6095–6105] with permission of American Chemical Society.

4.4. Fluorescent MNP via Dye Adsorption

Using the adsorption process described in the previous chapters it is possible to generate fluorescent MNP. When fluorescent dyes (like PDI-4S or PDI-4Pyl) were adsorbed by the nanoparticles, these were rendered with fluorescence properties, as shown in Figure 40C. The spectra show that PDI-4Pyl maintains its fluorescence at the surface and is not quenched by interfacial processes. The separation of these fluorescent particles by an external magnetic field lowered the fluorescence signal of the investigated solution which gives clear evidence that the fluorescence is coupled to the carrier system. The fluorescence investigations of a PDI-4Pyl solution and the supernatant after adsorption furthermore revealed that the observed adsorption processes are indeed quantitatively also under the accuracy of fluorescence investigations (Figure 40B). The so produced fluorescent nanosensors enable several interesting investigations as the magnetic properties of PDha@MCNP allow a simultaneous investigation on two separated channels (MRI and fluorescence spectroscopy). The distribution of the cargo can thus be followed by fluorescence investigations while at the same time the carrier system can be localized separately, offering highly interesting research potential.

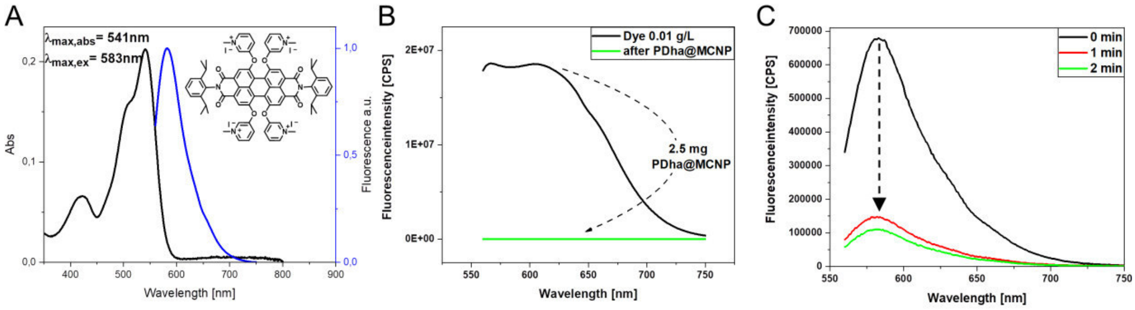

Figure 40: A) Absorption (solid black line) and fluorescence spectra (solid blue line) of PDI-4Pyl in aqueous solution, B) fluorescence intensity of PDI-4Pyl solution before (black line) and after (green line) 2.5 mg PDha@MCNP have been applied to the solution, C) Fluorescence spectra of a 0.1 mg mL^{-1} suspension of PDha@MCNP which has been exposed to PDI-4Pyl as a function of an applied magnetic field. Reprinted from [Langmuir 2020, 36, 6095–6105] with permission of American Chemical Society.

4.5. Catch (and Release) of Nanoparticles

As different charged dyes showed the ability to be adsorbed and subsequently released from the polyelectrolyte coated MNP we wanted to investigate whether a guided transport of charged nanoparticles with our magnetic carrier system would be possible as well. For this purpose we synthesized positively chargeed gold nanoparticles (AuNPs) as shown in Scheme 9, according to the synthesis described by Cao *et al.*[130]

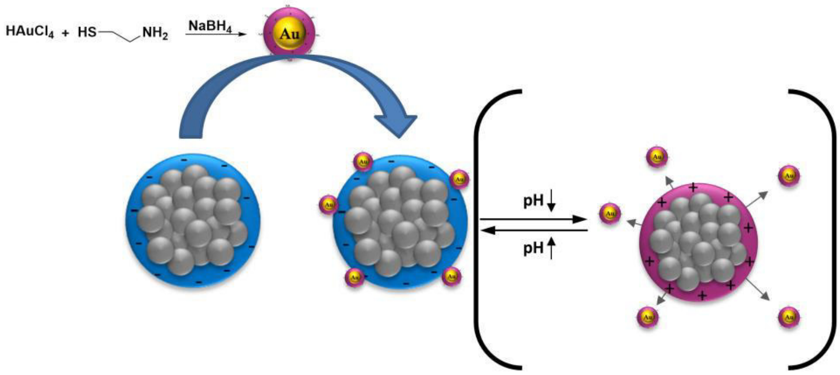

Scheme 9: Graphical representation of adsorption and potential pH induced desorption of cationic goldnanoparticles to polyampholytical coated MCNP.

The synthesized AuNPs were subsequently investigated by DLS, TEM and UV-Vis. DLS investigations revealed a mean hydrodynamic radius of 12 nm which was further confirmed by TEM measurements (Figure 41A, C-D). The TEM micrographs further show spherical nanoparticles with a narrow size distribution. UV-Vis investigations showed an intense absorption band at 528 nm which is based on the characteristic plasmonic resonance of gold nanoparticles.

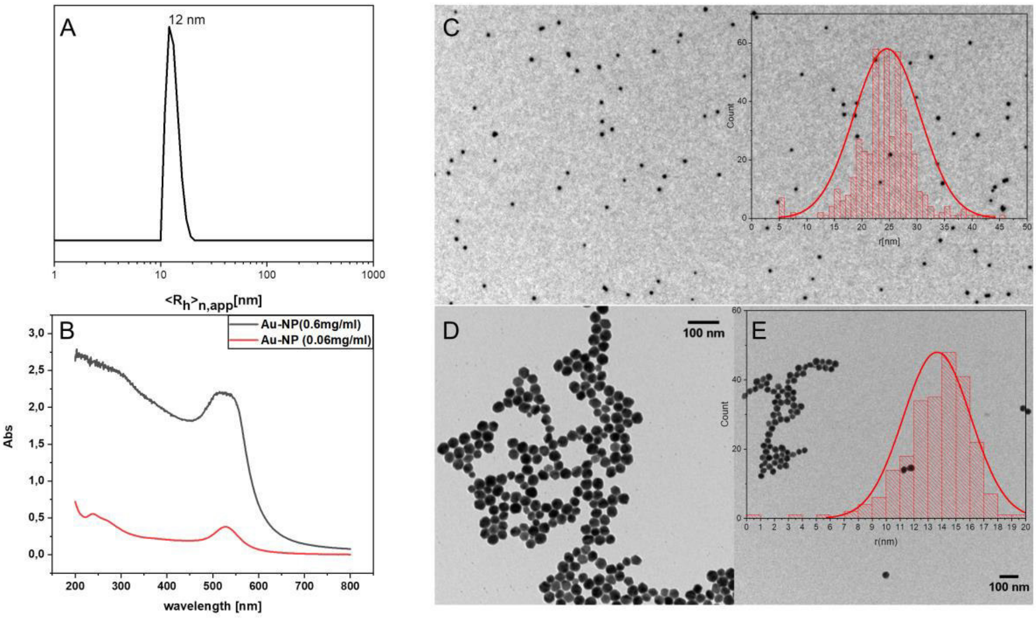

Figure 41: A) Number-weighted DLS CONTIN plot of AuNP; B) UV-Vis spectra of AuNP at a concentration of 0.6 mg ml^{-1} (black line) and at a concentration of 0.06 mg ml^{-1}); C)-E) TEM-micrographs of AuNP at different magnifications; insets: TEM histograms of the underlying micrograph.

The adsorption of cationic charge gold nanoparticles to differently coated MCNP was investigated afterwards. The photograph in Figure 42 demonstrates the adsorption process. While the solution on the left side is intensely colored the addition and subsequent removal of 3 mg PDha@MCNP leads to a transparent clear solution. Investigations of the adsorption capability of the three polyelectrolytic coatings (PDAGA, PImAA and PDha) revealed that a coating of PDha adsorbed most gold nanoparticles while a PDAGA coating adsorbed not quantitatively and a PImAA coating led to no adsorption of gold nanoparticles at all. The lack of an adsorption by PImAA@MCNP towards cationic dyes, described in chapter 4.3, is again reflected in this observation. The different affinity towards these gold nanoparticles indicates again an interesting difference in the properties of the respective coatings.

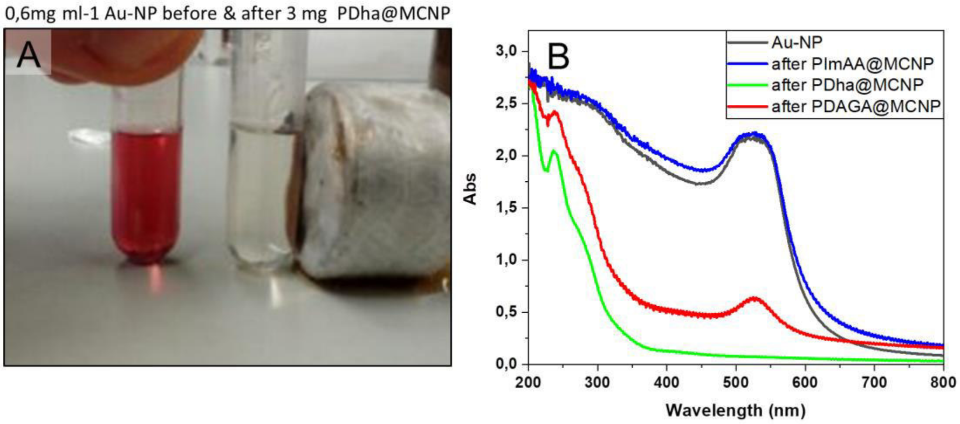

Figure 42: A) Photograph of 0.6 mg ml^{-1} AuNP dispersions (left: prior to addition of PDha@MCNP, right: after 3 mg PDha@MCNP were added and subsequently separated by a magnet); B) UV-Vis spectra of 0.6 mg ml^{-1} AuNP dispersion (black line), 0.6 mg ml^{-1} AuNP dispersion after 3 mg PImAA@MCNP were added and subsequently separated (blue line), 0.6 mg ml^{-1} AuNP dispersion after 3 mg PDha@MCNP were added and subsequently separated (green line), and 0.6 mg ml^{-1} AuNP dispersion after 3 mg PDAGA@MCNP were added and subsequently separated (red line).

The nanoparticle aggregates were further investigated using DLS, zeta potential measurements, UV-Vis, and TEM. The DLS investigations show a strong increase in hydrodynamic size after the gold nanoparticles adsorb to the coated MCNP. All particles exhibit an average size in the range of micrometers. This indicates a strong agglomeration upon exposure to the charged gold nanoparticles. The zeta potential measurements were used to investigate how the surface charge of coated MCNP changes upon adsorption of different amounts of gold nanoparticles. Therefore different ratios of Au-NP were given to PDha@MCNP ranging from a mass ratio Au-NP:PDha@MCNP of 0.6:5 to 0.6:0.1. As expected the pristine gold nanoparticles exhibit a strongly positive surface charge (+ 30 mV). PDha@MCNP on the other hand exhibits negative surface charge at pH = 7. The adsorption of low amounts of gold nanoparticles (ratio AuNP:PDha@MCNP 0.6:5) renders the entire system with a negative surface charge, while higher amounts of gold nanoparticles lead to a positive surface charge (AuNP:PDha@MCNP ratios between 0.6:0.5 and 0.6:0.1). The absorption spectra in Figure 43B show a change in the absorption properties of polyelectrolyte coated MCNP upon adsorption of AuNPs. Without the attachment of AuNP an intense and undefined absorption is starting to rise from 700 nm and reaches a plateau at 400 nm (here exemplary shown for PDha@MCNP). Upon adsorption of the AuNP the absorption intensifies and begins to rise at much higher wavelengths (for Au@PDha@MCNP and Au@PDAGA@MCNP). The more intense absorption at higher wavelength (between 500 and 600 nm) fits well to the adsorption maximum of AuNP at 528 nm. Thus the plasmonic resonance properties of gold nanoparticles seem to be preserved during the adsorption to the MCNP. The TEM micrographs in Figure 43 show Au@PDha@MCNP. Here it is clearly visible that gold nanoparticles as smaller spherical black dots are attached to PDha@MCNP. Also a strong tendency to agglomeration of the resulting particles is visible. Larger aggregates of about 500 nm diameter are visible on these micrographs.

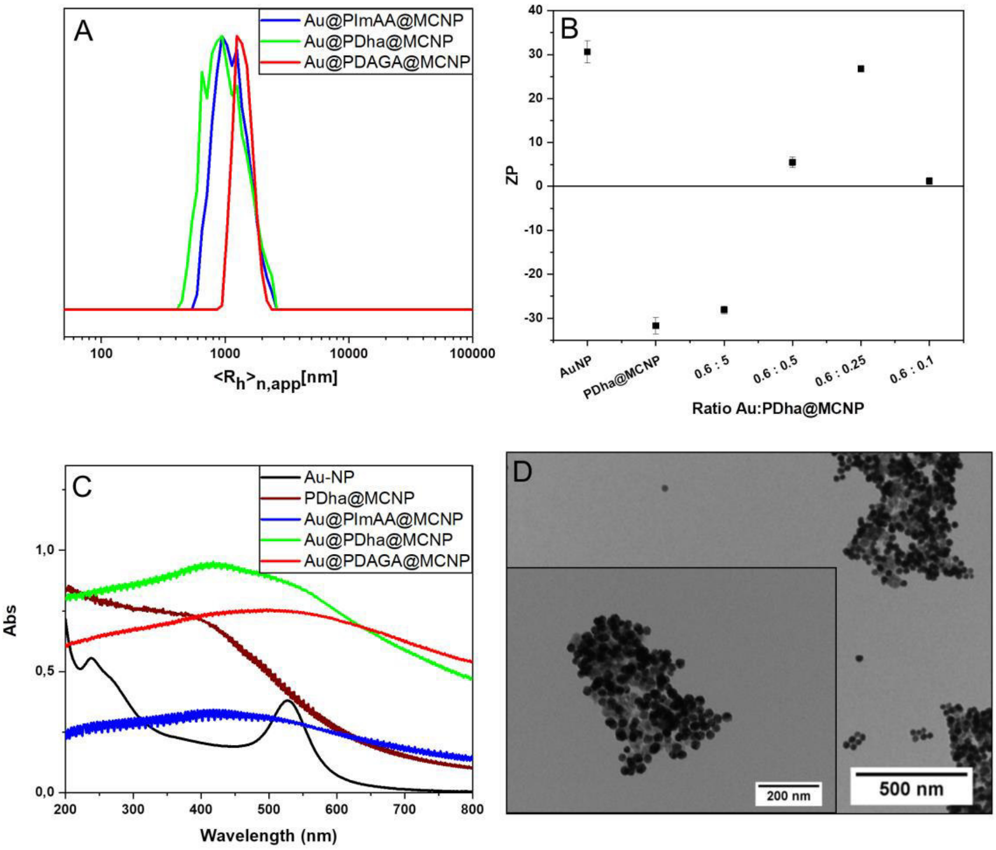

Figure 43: A) Number-weighted DLS CONTIN plots of Au@PImAA@MCNP (blue line, $\langle R_h\rangle_{n,app}$ = nm), and Au@PDha@MCNP (green line, $\langle R_h\rangle_{n,app}$ = nm), and Au@PDAGA@MCNP (red line, $\langle R_h\rangle_{n,app}$ = nm); B) ζ-potentials of AuNP (+31 mV), PDha@MCNP(-32 mV), Au@PDha@MCNP deriving from different AuNP:PDha@MCNP wt. ratios: 0.6:5 (-28 mV), 0.6:0.5 (+5 mV), 0.6:0.25 (+27 MV), and 0.6:0.1 (+1 mV); C) UV-Vis-spectra of AuNP (black line), PDha@MCNP (brown line), Au@PImAA@MCNP (blue line)), Au@PDha@MCNP (green line), and Au@PDAGA@MCNP (red line); D) TEM-micrographs of Au@PDha@MCNP deriving from wt. ratio of AuNP:PDha@MCNP of 0.6:0.1.

Finally we investigated the release behavior of the nanoparticle-nanoparticle carrier system. We found that surprisingly different to the previous observations a lowering of the pH did not lead to a release of AuNP. Even harsh conditions at pH = 2 overnight did not release any gold nanoparticles. We attribute this to the manifold electrostatic binding sites of the gold nanoparticles leading to a stronger entropically based attachment. Further it is possible that the carboxylic acids of the polymer shell act as ligands for the gold nanoparticles and lead to an irreversible binding.

5. Summary

The work presented here aims for the artificial variation of magnetic nanoparticle surfaces using different macromolecular building blocks and grafting methods which incorporated straightforward grafting approaches of various commonly used polymers and furthermore the introduction of novel functional (weak) polyzwitterions as surface ligands. The latter polymers gave access to multi-functional nanocarriers that react both to external magnetic fields and the surrounding pH value. The majority of the polyzwitterions currently investigated consists of functional groups that enable permanent zwitterionic state over a very wide pH range. The novelty of the polymers presented in this work lies in the pH-dependent charge through the use of weak acid and base groups. These weak polyzwitterions expand the latest scope of polymer coatings for magnetic nanoparticles and enable ways of charge-based transport or catch and release at the nanoscale. The synergistic effects by combination of magnetic core and pH responsive shell enable possible applications in various fields, ranging from recyclable wastewater treatment agents to tailored drug delivery nanocarriers, as outlined in this work. The investigation of interfacial electrostatic interactions with charged guests was of great interest according to the application areas. A fundamental understanding of the underlying mechanisms could be obtained by varying both the surrounding pH, guest molecules and polyzwitterion on the surface of the MCNPs. Three different coatings based on polyampholytes enabled hereby changes in the electrostatic interactions and gave insights into the underlying and as yet hardly investigated dependency of functional groups and electrostatic interactions on surfaces. The electrostatic interactions have furthermore been studied intensively to provide a straightforward approach to the synthesis of magnetic nanoparticles with versatile new properties such as fluorescence and plasmonic resonance based on interface adsorption, which allowed the merging of different properties by a noncovalent combination of individual building blocks resulting in new types of nanocomposites.

The work is divided into three sections, which focus on the synthesis of weak poly zwitterions, the surface functionalization of magnetic nanoparticles and the interaction of such particles with charged systems.

The first part of the thesis was focused on the synthesis of the various polyampholytic materials for use as surface coating. The respective materials (PImAA, PDha, and PDAGA) were investigated towards their general characteristics and pH responsive properties. The polyampholytic materials examined here showed a strongly varying charge depending on the pH, which was shown by means of titrations and pH-dependent zeta potential measurements. In consequence it was found that a complete inversion of the polymer charge was possible. The respective functional groups in the polyampholytes determined the isoelectric point of the polymers. Furthermore, the synthesis of polyampholytes (polydehydroalanine) was examined in more detail with regard to a variation of protective groups.

The subsequent functionalization of magnetic nanoparticles by these materials is described in the second part of the work. The chapter focuses on the synthesis and investigation of the resulting hybrid materials. Particular attention was paid to the solution behavior and pH responsiveness of the particles (Figure 44 below). It could be shown that a variation of the polyampholytic coatings, through the change of different (weak) acid and base side groups, the surface properties and the charge of the respective nanomaterial could be strongly influenced. The influence of the pH on the surface charge was examined and it could be shown that the respective nanomaterial varied strongly in their surface properties. More specifically allowed the variation of the coating the shifting of the apparent point of zero charge within a range of up to 3 pH values (between pH 3 and 7) and thus the pH range in which the surface charge of the nanoparticles can be inverted. Further functionalization of magnetic nanoparticles by means of copolymers gave access to zwitterionic nanomaterials, which had improved suspension stability compared to non-functionalized materials.

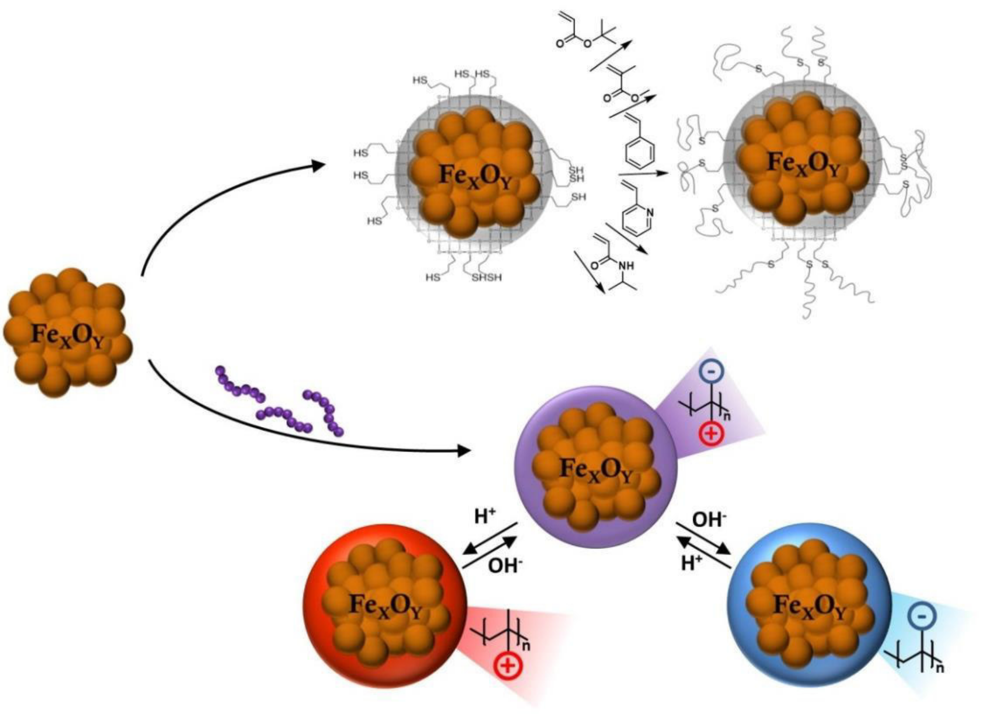

Figure 44: Graphical representation of magnetic nanoparticle surface modifications used within this thesis.

For potential applications of magnetic nanoparticles in various solvents a two-stage coating process was established which allowed a simple and straightforward approach for the covalent immobilization of various polymers at MNPs (Figure 44 above). A first coating was carried out by means of silanization and applied a thin thiol-bearing silane layer to the surface of the magnetic nanoparticles, which was optimized with regard to the coating thickness and overall size of the nanoparticles. In the second step, various monomers (MMA, *t*BA, styrene, 2VP, and NIPAAm) were polymerized and simultaneously grafted to the surface (grafting-through) resulting in various surface coatings. It could be shown that the amount of thiol-functionalized MCNPs directly affected the polymerization process (by means of final polymer dispersity). In addition, the polymers obtained from the polymer solution could be used for the direct analysis of the polymers on the surface of the particles. The process thus enables a straightforward, time- and cost-efficient method for the synthesis of defined tailored nano-structures with adjustable surface properties

Finally, in the third part of the thesis the implementation of polyampholytic coatings with pH response for electrostatically driven interactions towards a number of charged guests is presented. The pH was thereby used to generate either a positive or negative surface charge and thus affected the resulting electrostatic interactions with small dye molecules and other objects (e.g. gold nanoparticles, Figure 45). In a first approach it could be shown that polyampholytes as surface coatings enable the reversible adsorption of small cationic molecules and can be used for several successive cycles using the example of PDha coating. The investigation of the pH dependent release of the cargo molecule hinted towards a significant role of the nanoparticles pzc for the release. Further investigations were supposed to answer whether polyampholytes on nanoparticles can be used as a general nanocarrier platform for adsorption and release on a larger variety of molecules that vary between negative and positive charge and net charge per molecule. It could be observed that neutral conditions enabled a good adsorption of positively charged dyes which were successively released upon acidification, while negatively charged dyes adsorbed under acidic conditions with a subsequent release by an increasing pH.

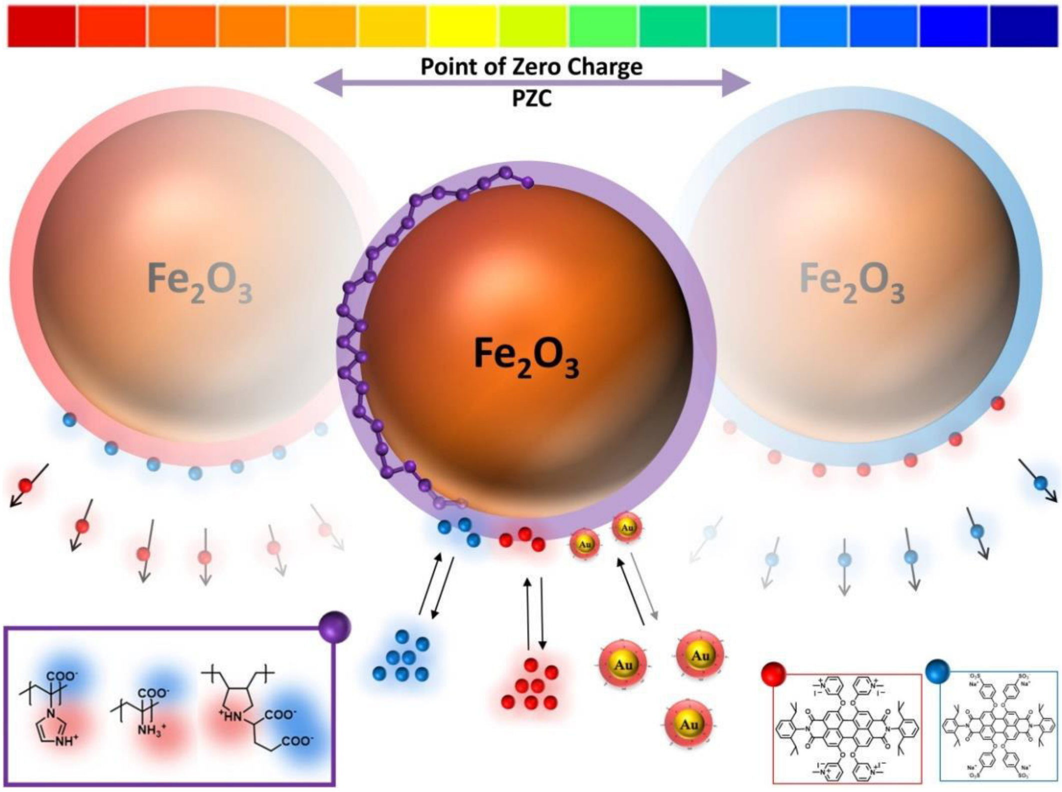

Figure 45: Graphical representation of investigated interactions between polyampholyte coated magnetic nanoparticles and various charged entities.

Furthermore, we observed that successful adsorption was not only determined by the number of charged functional groups in the molecule, but also that the underlying molecular structure played an important role in the adsorption behavior (dyes with triarylmethane structure adsorbed well while azobenzene structures adsorbed less effectively). In addition to the investigation of the cargo we examined and compared the influence of different polyampholytic coatings on their adsorption and release behavior towards a positively and negatively charged dye. Hereby two structurally similar dyes with opposite net charge were investigated as model cargo. We observed that the respective polyampholytic shell had strong influence on the adsorption and release behavior, ranging from a lack of adsorption to varying pH values for a subsequent release. While we initially assumed that the pzc would mainly determine the adsorption and release, we had to recognize that other processes such as the respective functional group are of particular importance for the interactions between molecules and surface.

Besides the investigation of these interfacial processes, we used the adsorption process to generate fluorescent nanoparticles based on weak electrostatic interactions. The resulting particles have the potential to be tracked by two separate visual channels and further offer the opportunity to follow a potential cargo release by fluorescence. In addition, the interplay of positively charged Au nanoparticles with the magnetic nanoparticles enabled a non-covalent fusion of both nanoparticles in one hybrid material, which broadens the scope of electrostatically mediated adsorption processes.

In summary, the thesis describes ways of tailoring magnetic nanoparticle surfaces to generate desired and novel materials for various fields of application. By merging the magnetic properties of the core with the pH dependent charge of polyampholytes, new pH-responsive systems were synthesized which allow a magnetically guided transport of charged guests at the nanoscale, finding potential applications in wastewater treatment, or controlled drug delivery. Moreover, tuning of the respective surface ligand allowed to tailor the adsorption and release of charged molecules and provided information on the fundamental processes in the interplay of electrostatic attraction and repulsion between surface and surrounding.

Nevertheless, many interesting questions towards the variation of surface ligands in the field of nano-science are left unanswered so far. As demonstrated here, the combination of different building blocks can open up new opportunities for the synthesis of fascinating (nano-)materials. By combining other nanomaterials with the interesting features of weak polyzwitterions new fields of application will become accessible and allow charge-controlled processes to shed new light on the synthesis, the properties and application of nanomaterials. The field of biomineralization as one example could profit from the various polymeric materials presented in this work to induce the self-driven synthesis of artificial materials. Merging different nanomaterials in a fast and versatile way, as presented in this work, would enable the interesting combination of different nano-features in one material with the ideal opportunity to use external triggers (like pH) to separate the different building blocks on demand, creating temporary magnetic properties for nanomaterials. This enables to create promising nanomaterials that depend on directional transport in the nanometer range for various applications. In addition, it can be seen that only a few questions about interfacial charge-driven adsorption processes could be answered here. Investigations of the fundamental processes of functional groups on surfaces and interactions with their surroundings (also with biological systems) therefore still bear further potential for research.

6. Zusammenfassung

Die hier vorgestellte Arbeit beschreibt die künstliche Variation magnetischer Nanopartikeloberflächen durch Anwendung verschiedener makromolekularer Bausteine und Pfropfmethoden. Dabei wurden sowohl verschiedene häufig genutzte Polymere als auch neuartige Polymere mit (schwachen) polyzwitterionischen Eigenschaften genutzt.

Die zuletzt genannten Polymere ermöglichten den Zugang zu multifunktionalen Nanoträgersystemen, die sowohl auf externe Magnetfelder als auch auf den umgebenden pH-Wert reagieren. Die Mehrzahl der derzeitig untersuchten Polyzwitterionen trägt funktionelle Gruppen, die einen permanenten zwitterionischen Zustand über einen sehr breiten pH-Bereich ermöglichen. Die Neuheit, der in dieser Arbeit vorgestellten Polymere, liegt in der pH-abhängigen Ladung durch Anwendung von schwachen Säure- und Basengruppen. Diese schwachen Polyzwitterionen erweitern das jüngste Spektrum von Polymerbeschichtungen für magnetische Nanopartikel und ermöglichen neue und interessante Wege, ladungsbasierte Transporte pH-responsiv auf der Nanoebene auszuführen. Die synergistischen Effekte durch die Kombination von Magnetkern und pH-responsiver Hülle ermöglichen potenzielle Anwendungen in verschiedensten Bereichen, die von recycelbaren Abwasserbehandlungsmitteln bis hin zu maßgeschneiderten Nanoträgern für die Arzneimittelabgabe reichen, wie in dieser Arbeit exemplarisch gezeigt werden konnte. Die Untersuchung elektrostatischer Wechselwirkungen von Partikeloberfläche mit geladenen Spezies war, entsprechend der Anwendungsgebiete, von großem Interesse. Ein grundlegendes Verständnis der unterliegenden Mechanismen konnte erlangt werden, indem sowohl umgebender pH-Wert, Gast-Moleküle und Polyzwitterion auf der Oberfläche der MCNPs variiert wurden. Drei unterschiedliche Beschichtungen der Partikel ermöglichten hierbei gezielte Änderungen der elektrostatischen Wechselwirkungen und gaben Einblicke in die zugrunde liegende und noch kaum untersuchten Einflüsse von oberflächlich gebundenen schwachen Polyzwitterionen auf elektrostatische Wechselwirkungen. Die Interaktion der Partikel mit unterschiedlichen Spezies wurden zudem intensiv untersucht, um einen leicht zugänglichen Ansatz für die Synthese magnetischer Nanopartikel mit vielseitigen, neuen Eigenschaften wie Fluoreszenz und plasmonischer Resonanz auf Grundlage von Grenzflächenadsorption zu generieren. Dabei konnten verschiedene Eigenschaften durch nicht-kovalente Kombination einzelner Bausteine zusammengeführt werden und neuartige Nanokomposite generiert werden.

Die gesamte Arbeit teilt sich in drei Abschnitte auf, die sich auf die Synthese schwacher Polyzwitterionen, die Oberflächen-Funktionalisierung magnetischer Nanopartikel und die Wechselwirkung solcher Partikel mit geladenen Systemen fokussieren.

Im ersten Teil der Arbeit wurde die Synthese der verschiedenen polyampholytischen Materialien für eine spätere Anwendung als Oberflächenbeschichtung beschrieben. Anschließend wurden die jeweiligen Materialien (PImAA, PDha und PDAGA) auf ihre allgemeinen Eigenschaften sowie auf ihr pH-responsives Verhalten hin untersucht. Die hier untersuchten polyampholytischen Materialien zeigten eine stark variierende Gesamtladung in Abhängigkeit der pH-Werts, was mittels Titrationen und pH-abhängigen Zeta-Potenzialmessungen gezeigt wurde. Es zeigte sich, dass eine vollständige Inversion der Polymer-Ladung möglich war. Die jeweiligen funktionellen Gruppen in den Polyampholyten bestimmten dabei den isoelektrischen Punkt der Polymere. Ferner wurde die Synthese der Polyampholyte (Poly(dehydroalanin)) im Hinblick auf eine Variation von Schutzgruppen genauer untersucht.

Die anschließende Funktionalisierung magnetischer Nanopartikel, durch diese Materialien, wurde im zweiten Teil der Arbeit beschrieben. Dabei fokussiert das Kapitel sich auf Synthese und Untersuchung der resultierenden Hybridmaterialien. Im Speziellen wurde das Verhalten in Lösung und die pH-Responsivität der Partikel untersucht (Abbildung 46 unten). Durch die gezielte Variation der polyampholytischen Beschichtungen und die damit verbundene Änderung (schwacher) Säure- und Basenseitengruppen war es möglich die Oberflächeneigenschaften und die Ladung des jeweiligen Nanomaterials stark zu beeinflussen. Der umgebende pH-Wert hatte dabei direkten Einfluss auf die Oberflächenladung und es konnte gezeigt werden, dass der apparente

Ladungsnullpunkt (pzc) des jeweiligen Nanomaterials gezielt innerhalb eines Bereichs von bis zu 3 pH-Werten (zwischen pH 3 und 7) verschoben werden konnte. Der pH-Bereich, in dem eine Ladungsinversion der Partikel stattfand wurde damit ebenfalls verschoben. Die weitere Funktionalisierung magnetischer Nanopartikel durch Copolymere ermöglichte den Zugang zu zwitterionischen Nanomaterialien, die eine verbesserte Suspensionsstabilität im Vergleich zu nicht funktionalisierten Materialien aufwiesen.

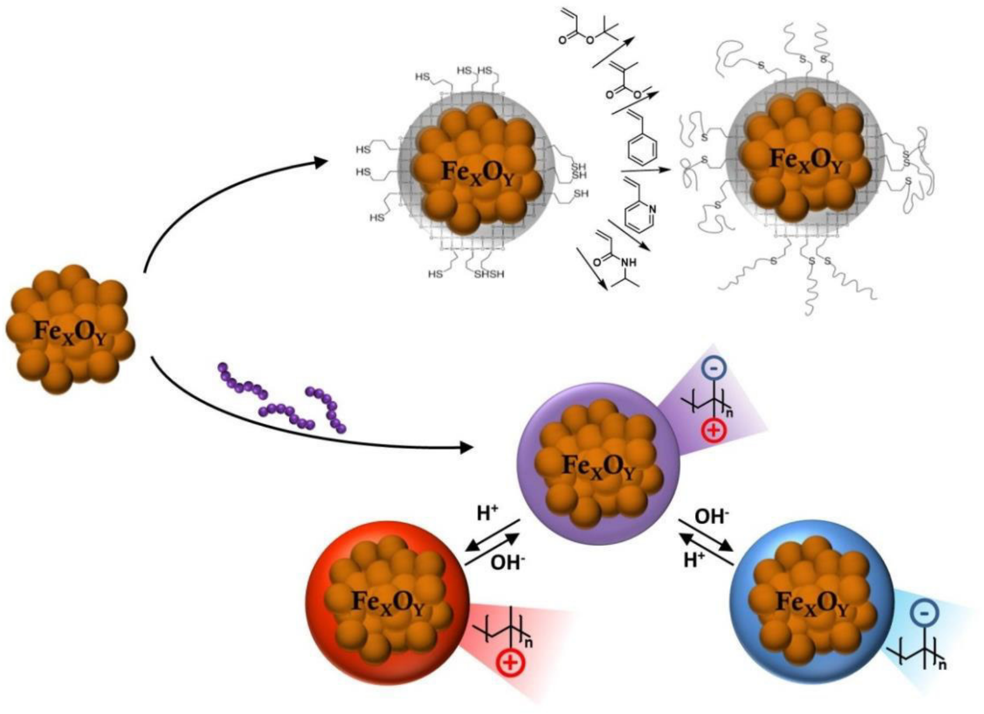

Abbildung 46: Grafische Darstellung der in dieser Arbeit verwendeten Oberflächenmodifikationen magnetischer Nanopartikel.

Mit Hinblick auf verschiedene Einsatzmöglichkeiten magnetischer Nanopartikel in unterschiedlichsten Lösungsmitteln wurde des Weiteren ein zweistufiges Beschichtungsverfahren etabliert, das eine schnelle und simple kovalente Immobilisierung verschiedener Polymere auf MNP ermöglichte (Abbildung 46 oben). Eine erste Beschichtung wurde mittels Silanisierung durchgeführt, wobei eine dünne, Thiol tragende Silanschicht auf die Oberfläche der magnetischen Nanopartikeln aufgebracht wurde, welche hinsichtlich Beschichtungsdicke und Gesamtgröße der Nanopartikel optimiert wurde. Im zweiten Schritt wurden verschiedene Monomere (MMA, tBA, Styrol, 2VP und NIPAAm) polymerisiert und simultan auf diese Oberfläche aufgepfropft, was unterschiedlichste

Oberflächenbeschichtungen ermöglichte. Die Menge an Thiol-funktionalisierten MCNPs hatte dabei direkten Einfluss auf den Polymerisationsprozess (Polymerdispersität). Zudem konnten die aus der Polymerlösung erhaltenen Polymere für die direkte Analyse der Polymere auf der Oberfläche der Partikel genutzt werden. Das Verfahren ermöglicht somit eine einfache, zeit- und kosteneffiziente Methode zur Synthese definierter, maßgeschneiderter Nanostrukturen mit einstellbaren Oberflächeneigenschaften.

Schließlich wurde im dritten Teil der Arbeit die Implementierung polyampholytischer Beschichtungen und die daraus resultierende pH-abhängige Oberflächenladung der Nanomaterialien zu weiteren Untersuchungen elektrostatisch bedingter Wechselwirkungen mit einer Reihe geladener Systeme vorgestellt. Der umgebende pH-Wert bestimmte über positive oder negative Oberflächenladung und somit über die resultierenden elektrostatischen Wechselwirkungen mit kleinen geladenen Farbstoffmolekülen und anderen Objekten (beispielsweise Goldnanopartikeln, Abbildung 47). In einem ersten Ansatz konnte gezeigt werden, dass PDha als Oberflächenbeschichtung die reversible Adsorption kleiner kationischer Moleküle ermöglichte und für mehrere aufeinanderfolgende Adsorptionszyklen verwendet werden konnte. Die Untersuchung der pH-abhängigen Freisetzung der gebundenen Moleküle deutete auf eine signifikante Rolle des pzc der Nanopartikel für die Freisetzung hin. Weitere Untersuchungen sollten beantworten, ob Polyampholyte auf Nanopartikeln als allgemeine Nanoträgerplattform für die Adsorption und Freisetzung an einer größeren Vielfalt von Molekülen verwendet werden können, die zwischen negativer und positiver Ladung und Nettoladung pro Molekül variieren. Es konnte beobachtet werden, dass neutrale Bedingungen eine gute Adsorption von positiv geladenen Farbstoffen ermöglichten, die nacheinander beim Ansäuern freigesetzt wurden, während negativ geladene Farbstoffe unter sauren Bedingungen adsorbierten, mit anschließender Freisetzung durch einen ansteigenden pH-Wert.

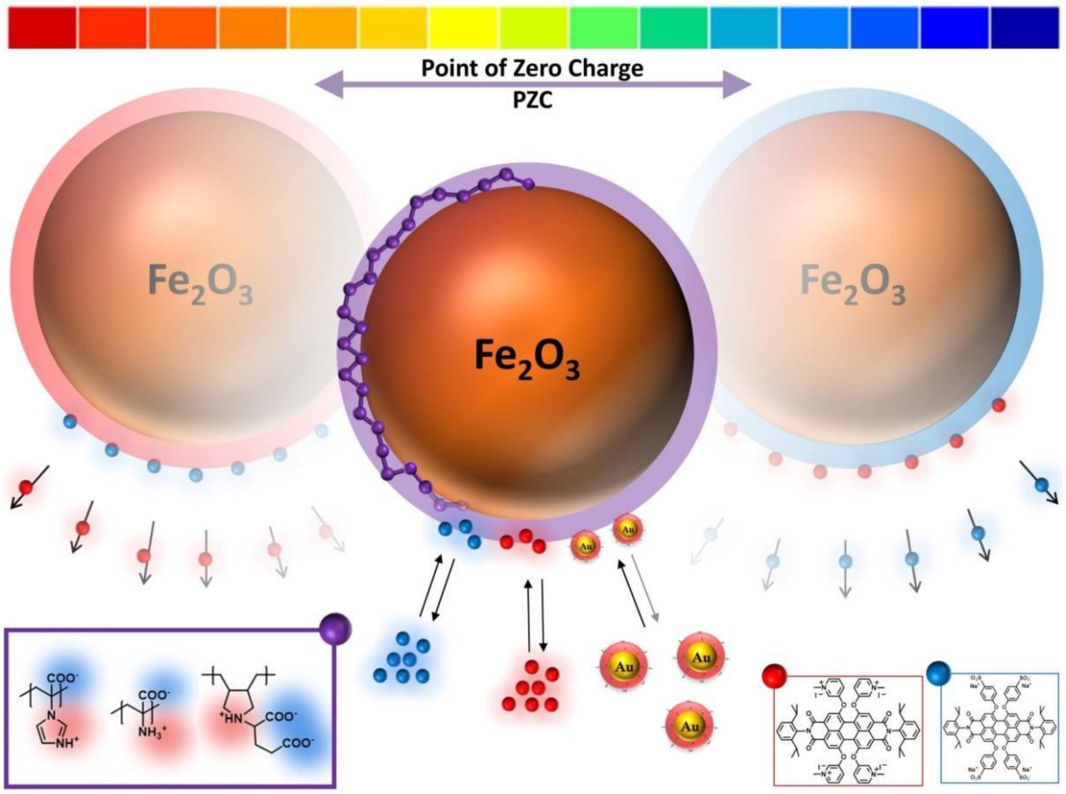

Abbildung 47: Grafische Darstellung der untersuchten Wechselwirkungen zwischen mit Polyampholyten beschichteten magnetischen Nanopartikeln und verschiedenen geladenen Systemen.

Eine erfolgreiche Adsorption wurde hier nicht nur durch die Anzahl der geladenen funktionellen Gruppen im Farbstoffmolekül bestimmt, sondern wesentlich durch die zugrunde liegenden Molekülstrukturen (Farbstoffe mit Triarylmethanstruktur adsorbierten gut, während Azobenzolstrukturen weniger effektiv adsorbierten). Zusätzlich zur Untersuchung der Ladung wurde vergleichend der Einfluss verschiedener polyampholytischer Beschichtungen auf ihr Adsorptions- und Freisetzungsverhalten gegenüber einem positiv und einem negativ geladenen Farbstoff untersucht. Hierbei wurden zwei strukturell ähnliche Farbstoffe mit entgegengesetzter Nettoladung als Modellladung untersucht, die eine permanente Ladung aufwiesen. Es wurde beobachtet, dass die jeweilige polyampholytische Hülle einen starken Einfluss auf das Adsorptions- und Freisetzungsverhalten hatte, das sowohl quantitativer Natur war als auch den pH-Wert für eine anschließende Freisetzung betraf. Während anfänglich davon ausgegangen wurde, dass der pzc der Nanopartikel hauptsächlich die Adsorption und Freisetzung bestimmen würde, zeigte sich, dass andere Prozesse, wie die jeweilige funktionelle Gruppe, für die

Wechselwirkungen von Molekülen und Oberfläche von besonderer Bedeutung waren.

Neben der Untersuchung dieser Grenzflächenprozesse wurde der Adsorptionsprozess verwendet, um fluoreszierende Nanopartikel auf der Basis schwacher elektrostatischer Wechselwirkungen zu erzeugen. Die resultierenden Partikel haben das Potenzial, über zwei separate visuelle Kanäle verfolgt zu werden, und bieten ferner die Möglichkeit, eine potenzielle Freisetzung der Farbstoffmoleküle durch Fluoreszenz zu verfolgen. Darüber hinaus ermöglichte das Zusammenspiel von positiv geladenen Au-Nanopartikel mit den magnetischen Nanopartikeln eine nicht-kovalente Fusion beider Nanopartikel-Systeme in einem Hybridmaterial, was den Anwendungsbereich von elektrostatisch vermittelten Adsorptionsprozessen ergänzend erweiterte.

Zusammenfassend beschreibt diese Arbeit Möglichkeiten, magnetische Nanopartikeloberflächen so anzupassen, dass gewünschte und neuartige Eigenschaften für eine Implementation in verschiedenen Anwendungsbereichen ermöglicht werden. Durch die Verschmelzung der magnetischen Eigenschaften des Kerns mit der pH-abhängigen Ladung von schwachen Polyzwitterionen wurden neue auf den pH-Wert reagierende Systeme hergestellt, die einen magnetisch geführten Transport geladener Einheiten im Nanobereich ermöglichten und potenzielle Anwendungen in der Abwasserbehandlung oder kontrollierte Arzneimittelabgabe finden könnten. Darüber hinaus ermöglichte die Wahl der jeweiligen Oberflächenliganden die Anpassung der Adsorption und Freisetzung von geladenen Molekülen und gab Aufschluss zu den grundlegenden Prozessen im Zusammenspiel von elektrostatischer Anziehung und Abstoßung zwischen Oberflächen und Umgebung.

Im Anschluss an diese Arbeit bleiben weiterhin viele interessante Fragen zur Variation von Oberflächenliganden im Bereich der Nanowissenschaft offen. Wie hier gezeigt, kann die Kombination verschiedener Bausteine neue Möglichkeiten für die Synthese faszinierender (Nano-) Materialien eröffnen. Die Kombination von Nanomaterialien mit den interessanten Eigenschaften schwacher Polyzwitterionen kann neue Anwendungsbereiche erschließen, die es ermöglichen, ladungsgesteuerte Prozesse zu nutzen und so ein neues Licht auf die Synthese, die Eigenschaften und die Anwendung von Nanomaterialien zu werfen. Das Gebiet der Biomineralisierung, als ein Beispiel, könnte von den verschiedenen in dieser Arbeit vorgestellten Polymermaterialien profitieren, um die selbstgesteuerte Synthese künstlicher Materialien zu induzieren. Das schnelle Zusammenführen verschiedener Nanomaterialien, wie in dieser Arbeit vorgestellt, ermöglicht ein Zusammenführen unterschiedlichster (Nano)-Eigenschaften in einem Material. Idealerweise mit der Möglichkeit externe Impulse (pH-Wert) zu nutzen, um die verschiedenen Bausteine bei Bedarf wieder zu trennen. Dadurch ließen sich Materialien schaffen, die nur für einen gewünschten Zeitraum magnetischen Eigenschaften hätten und sich anschließend wieder wie die einzelnen Bausteine verhielten. Die Möglichkeit, so neue vielversprechende Nanomaterialien herzustellen, die in verschiedenen Anwendungsbereichen einen gerichteten Transport im Nanobereich ermöglichen, erlaubt den Umfang der Nanowissenschaften weiter zu verbreitern. Darüber hinaus zeigt sich, dass hier nur einige Fragen zu ladungsbasierten Adsorptionsprozessen an Grenzflächen beantwortet werden konnten. Untersuchungen zu den grundlegenden Prozessen funktioneller Gruppen auf Oberflächen und Wechselwirkungen mit deren Umgebung (auch mit biologischen Systemen) bieten daher weiteres Forschungspotenzial.

7. References

[1] R. Feynman*, Vol. 23*, **2012**.

[2] W. J. Stark, P. R. Stoessel, W. Wohlleben, A. Hafner, *Chem. Soc. Rev.* **2015**, *44*, 5793-5805.

[3] D. J. McClements, H. Xiao, *NPJ Sci. Food* **2017**, *1*, 6.

[4] B. S. Sekhon, *Nanotechnol. Sci. Appl.* **2010**, *3*, 1-15.

[5] S. Neethirajan, D. S. Jayas, *Food Bioproc. Tech.* **2011**, *4*, 39-47.

[6] A. Kausar, I. Rafique, B. Muhammad, *Polym. Plast. Technol. Eng.* **2016**, *55*, 1167-1191.

[7] J. Jeevanandam, A. Barhoum, Y. S. Chan, A. Dufresne, M. K. Danquah, *Beilstein J. Nanotechnol.* **2018**, *9*, 1050-1074.

[8] M. T. Ekvall, M. Lundqvist, E. Kelpsiene, E. Šileikis, S. B. Gunnarsson, T. Cedervall, *Nanoscale Adv.* **2019**, *1*, 1055-1061.

[9] G. Ozin, L. Cademartiri, *Small* **2009**, *5*, 1240-1244.

[10] G. A. Ozin, A. C. Arsenault, L. Cademartiri, *RSC* **2009, 1-54**.

[11] L. Freitas de Freitas, G. H. C. Varca, J. G. Dos Santos Batista, A. Benévolo Lugão, *Nanomaterials* **2018**, *8*, 939.

[12] A.-H. Lu, E. L. Salabas, F. Schüth, *Angew. Chem. Int. Ed.* **2007**, *46*, 1222-1244.

[13] M. Colombo, S. Carregal-Romero, M. F. Casula, L. Gutiérrez, M. P. Morales, I. B. Böhm, J. T. Heverhagen, D. Prosperi, W. J. Parak, C*hem. Soc. Rev.* **2012**, *41*, 4306-4334.

[14] R. A. Sperling, P. Rivera Gil, F. Zhang, M. Zanella, W. J. Parak, *Chem. Soc. Rev.* **2008**, *37*, 1896-1908.

[15] A. Heuer-Jungemann, N. Feliu, I. Bakaimi, M. Hamaly, A. Alkilany, I. Chakraborty, A. Masood, M. F. Casula, A. Kostopoulou, E. Oh, K. Susumu, M. H. Stewart, I. L. Medintz, E. Stratakis, W. J. Parak, A. G. Kanaras, *Chem. Rev.* **2019**, *119*, 4819-4880.

[16] M. Li, H. Schnablegger, S. Mann, *Nature* **1999**, *402*, 393-395.

[17] P. Biehl, M. von der Lühe, S. Dutz, F. H. Schacher, *Polymers* **2018**, *10*, 91.

[18] K. P. García, K. Zarschler, L. Barbaro, J. A. Barreto, W. O'Malley, L. Spiccia, H. Stephan, B. Graham, *Small* **2014**, *10*, 2516-2529.

[19] Y.-S. Chen, Y.-C. Hung, I. Liau, G. S. Huang, *Nanoscale Res. Lett.* **2009**, *4*, 858.

[20] A. Ito, M. Shinkai, H. Honda, T. Kobayashi, *J. Biosci. Bioeng.* **2005**, *100*, 1-11.

[21] D. Maity, G. Kandasamy, A. Sudame, in *Nanotheranostics: Applications and Limitations* (Eds.: M. Rai, B. Jamil), Springer International Publishing, Cham, **2019**, pp. 245-276.

[22] Q. A. Pankhurst, J. Connolly, S. Jones, J. Dobson, *J. Phys. D* **2003**, *36*, R167.

[23] X. Guo, Z. Wu, W. Li, Z. Wang, Q. Li, F. Kong, H. Zhang, X. Zhu, Y. P. Du, Y. Jin, Y. Du, J. You, *ACS Appl. Mater. Interfaces* **2016**, *8*, 3092-3106.

[24] Z. R. Stephen, F. M. Kievit, M. Zhang, *Mater Today (Kidlington)* **2011**, *14*, 330-338.

[25] S. Dutz, *IEEE Trans. Magn.* **2016**, *52*, 1-3.

[26] Y.-w. Jun, Y.-M. Huh, J.-s. Choi, J.-H. Lee, H.-T. Song, KimKim, S. Yoon, K.-S. Kim, J.-S. Shin, J.-S. Suh, J. Cheon, *J. Am. Chem. Soc.* **2005**, *127*, 5732-5733.

[27] J. Motoyama, T. Hakata, R. Kato, N. Yamashita, T. Morino, T. Kobayashi, H. Honda, *Biomagn. Res. Technol.* **2008**, *6*, 4.

[28] C. Martinez-Boubeta, K. Simeonidis, A. Makridis, M. Angelakeris, O. Iglesias, P. Guardia, A. Cabot, L. Yedra, S. Estradé, F. Peiró, Z. Saghi, P. A. Midgley, I. Conde-Leborán, D. Serantes, D. Baldomir, *Sci. Rep.* **2013**, *3*, 1652-1652.

[29] Suriyanto, E. Y. K. Ng, S. D. Kumar, *Biomed. Eng. Online* **2017**, *16*, 36.

[30] S. Tong, C. A. Quinto, L. Zhang, P. Mohindra, G. Bao, *ACS Nano* **2017**, *11*, 6808-6816.

[31] O. Kasyutich, A. Sarua, W. Schwarzacher, *J. Phys. D.* **2008**, *41*, 134022.

[32] S. Majetich, T. Wen, R. Booth, *ACS nano* **2011**, *5*, 6081-6084.

[33] C. Martinezboubeta, K. Simeonidis, A. Makridis, M. Angelakeris, O. Iglesias, P. Guardia, A. Cabot, L. Yedra, S. Estradé, F. Peiró, *Sci. Rep.* **2013**, *3*, 1652.

[34] V. Bhardwaj, A. Kaushik, Z. M. Khatib, M. Nair, A. J. McGoron, *Front. Pharmacol.* **2019**, *10*.

[35] C. L. Ventola, *P T.* **2017**, *42*, 742-755.

[36] L. Shi, E. Buhler, F. Boué, F. Carn, J. *Colloid Interface Sci.* **2017**, *492*, 191-198.

[37] D. Ling, M. J. Hackett, T. Hyeon, *Nano Today* **2014**, *9*, 457-477.

[38] C. D. Walkey, W. C. W. Chan, *Chem. Soc. Rev.* **2012**, *41*, 2780-2799.

[39] I. Lynch, K. A. Dawson, *Nano Today* **2008**, *3*, 40-47.

[40] S. Milani, F. Baldelli Bombelli, A. S. Pitek, K. A. Dawson, J. Rädler, *ACS Nano* **2012**, *6*, 2532-2541.

[41] C. Corbo, R. Molinaro, A. Parodi, N. E. Toledano Furman, F. Salvatore, E. Tasciotti, *Nanomedicine (Lond)* **2016**, *11*, 81-100.

[42] E. Schönemann, J. Koc, N. Aldred, A. S. Clare, A. Laschewsky, A. Rosenhahn, E. Wischerhoff, *Macromol. Rapid Commun.* **2020**, *41*, 1900447.

[43] B. Li, P. Jain, J. Ma, J. K. Smith, Z. Yuan, H.-C. Hung, Y. He, X. Lin, K. Wu, J. Pfaendtner, S. Jiang, *Sci. Adv.* **2019**, *5*, eaaw9562.

[44] F. Wang, J. Yang, J. Zhao, *Polym. Int.* **2015**, *64*, 999-1005.

[45] S. Chen, L. Li, C. Zhao, J. Zheng, *Polymer* **2010**, *51*, 5283-5293.

[46] J. D. Delgado, J. B. Schlenoff, *Macromolecules* **2017**, *50*, 4454-4464.

[47] R. Kumar, G. H. Fredrickson, *J. Chem. Phys.* **2009**, *131*, 104901.

[48] S. Kudaibergenov, W. Jaeger, A. Laschewsky, in *J. Polym. Sci. Pol. Chem.*, Springer Berlin Heidelberg, Berlin, Heidelberg, **2006**, pp. 157-224.

[49] S. Masuda, K. Minagawa, M. Tsuda, M. Tanaka, *Eur. Polym. J.* **2001**, *37*, 705-710.

[50] M. Billing, C. Gräfe, A. Saal, P. Biehl, J. H. Clement, S. Dutz, S. Weidner, F. H. Schacher, *Macromol. Rapid Commun.* **2017**, *38*, 1600637.

[51] Y. Merle, *J. Phys. Chem.* **1987**, *91*, 3092-3098.

[52] C. Lica, M. Segărceanu, M. Pleşca, A. Rikabi, G. Nechifor, *U.P.B. Sci. Bull., Series B* **2014**, *76*, 151-158.

[53] A. V. Dobrynin, R. H. Colby, M. Rubinstein, *J. Polym. Sci. B Polym. Phys.* **2004**, *42*, 3513-3538.

[54] M. Vert, Y. Doi, K.-H. Hellwich, M. Hess, P. Hodge, P. Kubisa, M. Rinaudo, F. Schué, (IUPAC Recommendations 2012), *Pure Appl. Chem.* **2012**, *84*, 377-410.

[55] S. E. Kudaibergenov, N. Nuraje, *Polymers* **2018**, *10*, 1146.

[56] U. Günther, L. V. Sigolaeva, D. V. Pergushov, F. H. Schacher, *Macromol. Chem. Phys.* **2013**, *214*, 2202-2212.

[57] J. Choi, M. F. Rubner, *Macromolecules* **2005**, *38*, 116-124.

[58] E. S. Lee, K. T. Oh, D. Kim, Y. S. Youn, Y. H. Bae, *J. Control. Release* **2007**, *123*, 19-26.

[59] Q. Zhang, G. Nurumbetov, A. Simula, C. Zhu, M. Li, P. Wilson, K. Kempe, B. Yang, l. tao, D. Haddleton, *Polym. Chem.* **2016**.

[60] H. Yabu, R. Koike, d. Y. Hirai, *J. Nanosci. Nanotechnol.* **2017**, *17*, 9251-9256.

[61] P. Li, W. Xiao, P. Chevallier, D. Biswas, X. Ottenwaelder, M.-A. Fortin, J. K. Oh, *ChemistrySelect* **2016**, *1*, 4087-4091.

[62] K. V. Korpany, D. D. Majewski, C. T. Chiu, S. N. Cross, A. S. Blum, *Langmuir* **2017**, *33*, 3000-3013.

[63] C. Monteil, N. Bar, A. Bee, D. Villemin, *Beilstein J. Nanotechnol.* **2016**, *7*, 1447-1453.

[64] E. Amstad, A. U. Gehring, H. Fischer, V. V. Nagaiyanallur, G. Hähner, M. Textor, E. Reimhult, *J. Phys. Chem. C* **2011**, *115*, 683-691.

[65] M. von der Lühe, U. Günther, A. Weidner, C. Gräfe, J. H. Clement, S. Dutz, F. H. Schacher, *RSC Adv.* **2015**, *5*, 31920-31929.

[66] P. Biehl, P. Wiemuth, J. G. Lopez, M.-C. Barth, A. Weidner, S. Dutz, K. Peneva, F. H. Schacher, *Langmuir* **2020**, *36,* 6095–6105.

[67] N. Machida, Y. Inoue, K. Ishihara, *Trans. Mat. Res. Soc. Japan* **2014**, *39*, 427-430.

[68] J. J. Yuan, S. P. Armes, Y. Takabayashi, K. Prassides, C. A. P. Leite, F. Galembeck, A. L. Lewis, *Langmuir* **2006**, *22*, 10989-10993.

[69] X. a. Zhang, W. Lin, S. Chen, H. Xu, H. Gu, *Langmuir* **2011**, *27*, 13669-13674.

[70] L. Zhang, H. Xue, C. Gao, L. Carr, J. Wang, B. Chu, S. Jiang, *Biomaterials* **2010**, *31*, 6582-6588.

[71] Y. Chen, Z. Xiong, L. Zhang, J. Zhao, Q. Zhang, L. Peng, W. Zhang, M. Ye, H. Zou, *Nanoscale* **2015**, *7*, 3100-3108.

[72] M. von der Lühe, A. Weidner, S. Dutz, F. H. Schacher, *ACS Appl. Nano Mater.* **2018**, *1*, 232-244.

[73] D. K. Yi, S. T. Selvan, S. S. Lee, G. C. Papaefthymiou, D. Kundaliya, J. Y. Ying, *J. Am. Chem. Soc.* **2005**, *127*, 4990-4991.

[74] C. Vogt, M. S. Toprak, M. Muhammed, S. Laurent, J.-L. Bridot, R. N. Müller, *J. Nanoparticle Res.* **2010**, *12*, 1137-1147.

[75] W.-Y. Rho, H.-M. Kim, S. Kyeong, Y.-L. Kang, D.-H. Kim, H. Kang, C. Jeong, D.-E. Kim, Y.-S. Lee, B.-H. Jun, *J. Ind. Eng. Chem.* **2014**, *20*, 2646-2649.

[76] S. Kyeong, C. Jeong, H. Y. Kim, D. W. Hwang, H. Kang, J.-K. Yang, D. S. Lee, B.-H. Jun, Y.-S. Lee, *RSC Adv.* **2015**, *5*, 32072-32077.

[77] F. Ye, S. Laurent, A. Fornara, L. Astolfi, J. Qin, A. Roch, A. Martini, M. S. Toprak, R. N. Muller, M. Muhammed, *Contrast Media Mol. Imaging* **2012**, *7*, 460-468.

[78] S. A. McCarthy, G.-L. Davies, Y. K. Gun'ko, *Nat. Protocols* **2012**, *7*, 1677-1693.

[79] W. Stöber, A. Fink, E. Bohn, *J. Colloid Interface Sci.* **1968**, *26*, 62-69.

[80] H. Schmidt, H. Scholze, A. Kaiser, *J. Non. Cryst. Solids* **1984**, *63*, 1-11.

[81] H. Schmidt, *J. Non. Cryst. Solids* **1985**, *73*, 681-691.

[82] R. Kumar, I. Roy, T. Y. Ohulchanskyy, L. N. Goswami, A. C. Bonoiu, E. J. Bergey, K. M. Tramposch, A. Maitra, P. N. Prasad, *ACS Nano* **2008**, *2*, 449-456.

[83] N. Chekina, D. Horak, P. Jendelova, M. Trchova, M. J. Benes, M. Hruby, V. Herynek, K. Turnovcova, E. Sykova, *J. Mater. Chem.* **2011**, *21*, 7630-7639.

[84] E. E. Urena-Benavides, E. L. Lin, E. L. Foster, Z. Xue, M. R. Ortiz, Y. Fei, E. S. Larsen, A. A. Kmetz, II, B. A. Lyon, E. Moaseri, C. W. Bielawski, K. D. Pennell, C. J. Ellison, K. P. Johnston, *Ind. Eng. Chem. Res.* **2016**, *55*, 1522-1532.

[85] Y. Cui, X.-S. Zheng, B. Ren, R. Wang, J. Zhang, N.-S. Xia, Z.-Q. Tian, *Chem. Sci.* **2011**, *2*, 1463-1469.

[86] B. Viltužnik, A. Košak, Y. L. Zub, A. Lobnik, *J. Sol-Gel Sci. Technol.* **2013**, *68*, 365-373.

[87] S. Santra, P. Zhang, K. Wang, R. Tapec, W. Tan, *Anal. Chem.* **2001**, *73*, 4988-4993.

[88] L. G. Bach, M. R. Islam, J. T. Kim, S. Seo, K. T. Lim, *Appl. Surf. Sci.* **2012**, *258*, 2959-2966.

[89] O. Eckardt, C. Pietsch, O. Zumann, M. von der Lühe, D. S. Brauer, F. H. Schacher, *Macromol. Rapid Commun.* **2016**, *37*, 337-342.

[90] P. Biehl, F. H. Schacher, *Surfaces* **2020**, *3*, 116-131.

[91] F. Caruso, *Adv. Mater.* **2001**, *13*, 11-22.

[92] S. T. Milner, *Science* **1991**, *251*, 905-914.

[93] P. Auroy, L. Auvray, L. Leger, *Physica A* **1991**, *172*, 269-284.

[94] F. Zhou, W. Liu, M. Chen, D. C. Sun, *Chem. Comm.* **2001**, 2446-2447.

[95] S. Wang, Y. Zhou, W. Guan, B. Ding, *Appl. Surf. Sci.* **2008**, *254*, 5170-5174.

[96] J.-J. Chen, K. N. Struk, A. B. Brennan, *Langmuir* **2011**, *27*, 13754-13761.

[97] P. Liu, W. M. Liu, Q. J. Xue, *Eur. Polym. J.* **2004**, *40*, 267-271.

[98] S. Liu, F. Zhou, D. Di, S. Jiang, *Colloids Surf. A Physicochem. Eng. Asp.* **2004**, *244*, 87-93.

[99] J. Tian, B. Huang, W. Zhang, *Langmuir* **2019**, *35*, 266-275.

[100] L. E. W. LaConte, N. Nitin, O. Zurkiya, D. Caruntu, C. J. O'Connor, X. Hu, G. Bao, *J. Magn. Reson. Imaging* **2007**, *26*, 1634-1641.

[101] Y. Xie, C. A. S. Hill, Z. Xiao, H. Militz, C. Mai, *Compos. Part A Appl. Sci. Manuf.* **2010**, *41*, 806-819.

[102] J. E. Lofgreen, G. A. Ozin, *Chem. Soc. Rev.* **2014**, *43*, 911-933.

[103] M. M. Waldrop, *Nature* **2016**, *530*, 144-147.

[104] P. D. Stevens, J. Fan, H. M. R. Gardimalla, M. Yen, Y. Gao, *Org. Lett.* **2005**, *7*, 2085-2088.

[105] L. C. Fidale, M. Nikolajski, T. Rudolph, S. Dutz, F. H. Schacher, T. Heinze, *J. Colloid Interface Sci.* **2013**, *390*, 25-33.

[106] S. Dutz, W. Andrä, R. Hergt, R. Müller, C. Oestreich, C. Schmidt, J. Töpfer, M. Zeisberger, M. E. Bellemann, *J. Magn. Magn. Mater.* **2007**, *311*, 51-54.

[107] A. M. Gutierrez, T. D. Dziubla, J. Z. Hilt, *Rev. Environ. Health* **2017**, *32*, 111-117.

[108] G. Bao, S. Mitragotri, S. Tong, *Annu. Rev. Biomed. Eng.* **2013**, *15*, 253-282.

[109] A. Laschewsky, *Polymers* **2014**, *6*, 1544.

[110] J. Koc, T. Simovich, E. Schönemann, A. Chilkoti, H. Gardner, G. W. Swain, K. Hunsucker, A. Laschewsky, A. Rosenhahn, *Biofouling* **2019**, *35*, 454-462.

[111] C. Rössel, M. Billing, H. Görls, G. Festag, M. Grube, P. Bellstedt, I. Nischang, F. H. Schacher, *Polymer* **2017**, *127*, 182-191.

[112] Z. A. Jamiu, H. A. Al-Muallem, S. A. Ali, *Des. Monomers Polym.* **2016**, *19*, 128-137.

[113] M. Billing, F. H. Schacher, *Macromolecules* **2016**, *49*, 3696-3705.

[114] M. Billing, G. Festag, P. Bellstedt, F. H. Schacher, *Polym. Chem.* **2017**, *8*, 936-945.

[115] J. B. Max, D. V. Pergushov, L. V. Sigolaeva, F. H. Schacher, *Polym. Chem.* **2019**.

[116] S. Dutz, J. H. Clement, D. Eberbeck, T. Gelbrich, R. Hergt, R. Müller, J. Wotschadlo, M. Zeisberger, *J. Magn. Magn. Mater.* **2009**, *321*, 1501-1504.

[117] M. Kopeć, J. Spanjers, E. Scavo, D. Ernens, J. Duvigneau, G. Julius Vancso, *Eur. Polym. J.* **2018**, *106*, 291-296.

[118] Y. Song, G. Ye, Y. Lu, J. Chen, J. Wang, K. Matyjaszewski, *ACS Macro Lett.* **2016**, *5*, 382-386.

[119] S. Wan, Y. Zheng, Y. Liu, H. Yan, K. Liu, *J. Mater. Chem.* **2005**, *15*, 3424-3430.

[120] J. G. Kennemur, *Macromolecules* **2019**, *52*, 1354-1370.

[121] A. Michaels, O. Morelos, *Ind. Eng. Chem.* **1955**, *47*, 1801–1809.

[122] J. Cai, Y. Q. Miao, B. Z. Yu, P. Ma, L. Li, H. M. Fan, *Langmuir* **2017**, *33*, 1662-1669.

[123] J. Gao, H. Gu, B. Xu, *Acc. Chem. Res.* **2009**, *42*, 1097-1107.

[124] N. O'Brien, A. McKee, D. C. Sherrington, A. T. Slark, A. Titterton, *Polymer* **2000**, *41*, 6027-6031.

[125] D. J. Forster, J. P. A. Heuts, T. P. Davis, *Polymer* **2000**, *41*, 1385-1390.

[126] O. Eckardt, S. Seupel, G. Festag, M. Gottschaldt, F. H. Schacher, *Polym. Chem.* **2019**, *10*, 593-602.

[127] C. Kohl, T. Weil, J. Qu, K. Müllen, *Chem. Eur. J.* **2004**, *10*, 5297-5310.

[128] T. Weil, T. Vosch, J. Hofkens, K. Peneva, K. Müllen, *Angew. Chem. Int. Ed.* **2010**, *49*, 9068-9093.

[129] L. Meng, X. Zhang, Y. Tang, K. Su, J. Kong, *Sci. Rep.* **2015**, *5*, 7910.

[130] R. Cao, B. Li, *Chem. Commun.* **2011**, *47*, 2865-2867.

List of Abbreviations

δ	chemical shift
λ	wavelength
H_c	coercivity
M_r	remanent magnetization
$\langle R_h \rangle_{n,app}$	number weighted apparent hydrodynamic radius
2VP	2-vinylpyridine
APS	ammonium persulfate
aq.	aqueous
ATR-FTIR	attenuated total reflection-Fourier-transform infrared
Bcp	block-*co*-polymer
BOC	*tert*-butyloxycarbonyl protecting group
BOMA	methyl 2-benzyloxycarbonylaminoacrylate
CBMA	carboxybetaine methacrylate
CTA	chain transfer agent
D	diameter
Đ	dispersity
DDS	drug delivery system
D_h	hydrodynamic diameter
DLS	dynamic light scattering
DMAc	*N,N*-dimethylacetamide
DNA	deoxyribonucleic acid
DP	degree of polymerization
D_s	diameter of single domain
D_{sp}	diameter of superparamagnetism
e.g.	*exempli gratia*/for example
EImA	ethyl 2-(imidazole-1-yl)acrylate
et al.	*et alii*/ and other
EtOH	ethanol
FDA	U.S. food and drug administration
FRP	free radical polymerization
h	hour
IEP	isoelectric point
IR	infrared
K	Kelvin
MB	methylene blue
MCNP	magnetic multicore nanoparticles
MCP	2-(methacryloyloxy) ethyl choline phosphate
MeOH	methanol
min	minute

MMA	methyl methacrylate
M_n	number average molar mass
MNP	magnetic nanoparticle
MPC	phosphorylcholine methacrylate
MPTS	(3-mercaptopropyl)trimethoxysilane
MR	magnetic resonance
MRI	magnetic resonance imaging
M_s	saturation magnetization
NIPAAm	*N*-isopropylacrylamide
NMP	nitroxide mediated polymerizations
NMR	nuclear magnetic resonance
NP	nanoparticle
P	publication
P(2VP)	poly(2-vinylpyridine)
P(2VP-*grad*-AA)	poly(2-vinylpyridine)-*grad*-poly(acrylic acid)
P(2VP-*grad*-*t*BA))	poly(2-vinylpyridine)-*grad*-poly(*tert*-butyl acrylate)
P(CBMA)	poly(carboxybetaine methacrylate)
P(MPC)	poly(phosphorylcholine methacrylate)
P(SPE)	poly(sulfobetaine methacrylate)
P2VP	poly(2-vinylpyridine)
PAA	poly(acrylic acid)
PBOMA	poly(methyl 2-benzyloxycarbonylaminoacrylate)
PDAGA	poly(*N,N*-diallylglutamate)
PDha	polydehydroalanine
PDI-4PyI	(*N,N´*-bis(2,6-diisopropylphenyl)-1,6,7,12-tetra-[3-(*N*-methylpyridinium)oxy]perylene-3,4,9,10-tetracarboxylicacid diimide iodide
PDI-4S	(*N,N´*-bis(2,6-diisopropylphenyl)-1,6,7,12-tetra-[(4-sulfuric acid)phenoxy] perylene-3,4,9,10-tetracarboxylic acid diimide)
PEImA	poly(ethyl 2-(imidazole-1-yl)acrylate)
PImAA	poly((2-imidazol-1-yl)acrylic acid)
pK_a	acid dissociation constant
pK_b	base dissociation constant
PMMA	poly(methyl methacrylate)
PNIPAAm	poly(*N*-isopropylacrylamide)
P*t*BA	poly(*tert*-butyl acrylate)
P*t*BAA	poly(*tert* butoxycarbonyl amino acrylic acid)
P*t*BABA	poly(2-*tert*-butoxycarbonylaminoacrylate)
P*t*BAMA	poly(*tert* butoxycarbonylamino methacrylate)
pzc	point of zero charge
R2	(spin-spin) relaxation rate
R_h	hydrodynamic radius

RT	room temperature
s	second
SEC	size exclusion chromatography
SG1	*N*-*tert*-butyl-*N*-[1-diethylphosphono-(2,2-dimethylpropyl)]nitroxide
SPE	sulfobetaine methacrylate
SPP	sulfobetaine methacrylamide
T	temperature
t	time
T1	longitudinal relaxation time
T2	transverse relaxation time
*t*BA	*tert*-butyl acrylate
*t*BABA	2-*tert*-butoxycarbonylaminoacrylate
*t*BAMA	*tert*-butoxycarbonylamino methacrylate
TEM	transmission electron microscopy
TEOS	tetraethoxysilan
TFA	trifluoroacetic acid
TGA	thermogravimetric analysis
THF	tetrahydrofuran
TMAO	dimethylaminopropylacrylamide-*N*-oxide or trimethylaminoxid
TPO	2,4,6-trimethylbenzoyldiphenylphosphine oxide
UV-Vis	ultraviolet - visible light
wt.	weight

Publication List

[1] M. Billing, C. Gräfe, A. Saal, P. Biehl, J. H. Clement, S. Dutz, S. Weidner, F. H. Schacher, *Macromol. Rapid Commun.* **2017**, *38*, 1600637.

[2] O. Eckardt, B. Wenn, P. Biehl, T. Junkers, F. H. Schacher, *React. Chem. Eng.* **2017***, 2,* 479-486.

[3] P. Biehl, M. von der Lühe, S. Dutz, F. H. Schacher, *Polymers* ***2018,*** *10,* 91.

[4] P. Biehl, M. von der Lühe, F. H. Schacher, *Macromol. Rapid Commun.* **2018**, *39*, 1800017.

[5] B.-D. Lechner, P. Biehl, H. Ebert, S. Werner, A. Meister, G. Hause, K. Bacia, C. Tschierske, A. Blume, *J. Phys. Chem. B* **2018**, *122*, 10861-10871.

[6] J. K. Elter, G. Sentis, P. Bellstedt, P. Biehl, M. Gottschaldt, F. H. Schacher, *Polym. Chem.* **2018**, *9*, 2247-2257.

[7] J. K. Elter, P. Biehl, M. Gottschaldt, F. H. Schacher, *Polym. Chem.* **2019**, *10*, 5425-5439.

[8] K. Kartha, F. Wendler, T. Rudolph, P. Biehl, G. Fernández, F. H. Schacher, *Chemistry* **2019**, *26*, 606-610.

[9] I. Tabujew, M. Heidari, C. Freidel, M. Helm, L. Tebbe, U. Wolfrum, K. Nagel-Wolfrum, K. Koynov, P. Biehl, F. H. Schacher, R. Potestio, K. Peneva, *Biomacromolecules* **2019**, *20,* 4389-4406.

[10] J. H. Kruse, P. Biehl, F. H. Schacher, *Macromol. Rapid Commun.* **2019**, *40*, 1800857.

[11] P. Biehl, F. H. Schacher, *Surfaces* **2020**, *3*, 116-131.

[12] F. Wendler, J. Tom, M. Sittig, P. Biehl, B. Dietzek, F. H. Schacher, *Macromol. Rapid Commun*. **2020**, *41*, 1900607.

[13] R. Wetzel, O. Eckardt, P. Biehl, D. S. Brauer, F. H. Schacher, *Dent. Mater.* **2020**, *36*, 377-386.

[14] P. Biehl, P. Wiemuth, J. G. Lopez, M.-C. Barth, A. Weidner, S. Dutz, K. Peneva, F. H. Schacher, *Langmuir* **2020**, *36,* 6095–6105.

Oral Presentations:

1) P. Biehl, P. Wiemuth, F. H. Schacher*, ‘Polyampholytic hybrid nanoparticles as platform for reversible adsorption Processes’,* ICBZM 2019, 4th International Conference on Bioinspired and Zwitterionic Materials, June 16-19, 2019, Rolduc Abbey, Kerkrade (Netherlands)

Poster Presentations:

1) M. von der Lühe, P. Biehl, F. H. Schacher, ‘*Quantifying the Adsorption of Polydehydroalanine-based Polyelectrolytes onto Iron Oxide Nanoparticles’*, Makromolekulares Kolloquium 2016, 24.02.2016 – 26.02.2016 Universität Freiburg, Freiburg im Breisgau
2) P. Biehl, M. von der Lühe, A. Weidner, S. Dutz, F. H. Schacher, ‘*Surface Modification of Iron Oxide Nanoparticles and their Protein Interactions’,* Biointerfaces International 2016, 23.08.2016 – 25.08.2016, University of Zurich, Zürich
3) P. Biehl, M. von der Lühe, A. Weidner, S. Dutz, F. H. Schacher, *‘Covalent and Non-Covalent Surface Modification of Magnetic Nanoparticles’*, Polymers: from Structure to Function, 11.09.2016 – 13.09.2016, MLU, Halle (Saale)

Acknowledgements/Danksagung

Hier möchte ich mich bei allen bedanken, die mir in den letzten Jahren geholfen haben, diese Arbeit anzufertigen und den Weg dorthin so angenehm gestaltet haben, dass diese Zeit in guter Erinnerung für mich bleibt.

An erster Stelle möchte ich meinem Doktorvater Felix Schacher dafür danken, dass er mich über die Jahre hinweg in meinen Ideen unterstützt und mir viel Freiraum für die Gestaltung meiner Promotion gelassen hat. Dabei hat er nicht nur meine Arbeit unterstützt, sondern hatte zudem immer Verständnis für meine privaten Belange und hat mir die Möglichkeit gegeben, an verschiedenen Projekten mitzuarbeiten und mit anderen Doktoranden und Studenten mein Thema weiter zu entwickeln. All das hat mich nicht nur fachlich weitergebracht, sondern auch vor Herausforderungen gestellt, für die er immer ein offenes Ohr hatte.

Des Weiteren möchte ich mich besonders bei Moritz von der Lühe bedanken, dafür, dass er mich als mein Betreuer in der Masterarbeit in der Arbeitsgruppe aufgenommen und mir geholfen hat in das Thema meiner Dissertation einzusteigen. Die Zusammenarbeit hat mir viel Spaß gemacht und in der Zeit im Labor, Büro und am TEM hatte ich immer einen guten Gesprächspartner.

Kooperationen haben diese Arbeit erst möglich gemacht. Andreas Weidner und Silvio Dutz haben mir stets mit neuen Eisenoxid Nanopartikeln geholfen, eine Grundlage für meine Versuche zu schaffen, wofür ich sehr dankbar war. Javier Garcia Lopez und Marie-Christin Barth möchte ich für die aufwendigen Synthesen der Modellfarbstoffe danken, die für Adsorptionsversuche genutzt wurden. Ich möchte mich natürlich auch bei allen Kooperationspartnern bedanken, die einfach Ideen von mir ausprobiert haben, die mehr oder weniger erfolgversprechend waren und deren Ergebnisse nicht in diese Arbeit direkt eingeflossen sind.

Ich habe etliche analytische Methoden genutzt, um diese Arbeit fertig zu erstellen. Den Leuten, die für mich oder mit mir zusammen gemessen haben und mir Einweisungen in verschiedene Geräte gegeben haben, will ich hier danken. Insbesondere Stephanie Höppener dafür, dass sie immer zur Stelle war, wenn das Elektronenmikroskop mich mal wieder zum Verzweifeln gebracht hat. Grit Festtag für ihren unermüdlichen Kampf gegen verstopfte SEC-Säulen und die Bereitschaft, auch schwer zu vermessende Proben unserer Arbeitsgruppe anzunehmen. Peter Bellstedt und Gabriele Sentis danke ich für die Wartung der NMR Geräte.

Ich bin sehr dankbar dafür, dass ich mich in meiner Zeit hier mit wenig Bürokratie rumschlagen musste. Katja König, Olivia Lindig und Michelle König haben in der Bürokratie der Universität immer einen Überblick behalten, sich um meine Bestellungen gekümmert und mir damit viel Arbeit abgenommen.

Neben fachlicher Kompetenz ist auch die lebendige Zeit im Lab 317 in diese Arbeit eingeflossen. Robert Deubler, Oliver Zumann, Hanna Träger, Kathrin Kowalczuk, Moritz Köhler, Johannes Max und Jasper Hansen haben dafür gesorgt, dass man vielleicht nicht immer die produktivste Zeit im Labor zugebracht hat, aber in jedem Fall eine sehr lebenswerte Zeit hatte. Danke für die guten und schlechten Witze, die grandiosen Unterhaltungen (deep talks) und perfekte Musikauswahl im Labor 317. Mit Felix Wendler hatte ich jemanden, der in einer sehr ähnlichen Lebenssituation wie ich war. Ich möchte ihm hier für die vielen Gespräche über Windeln und Doktorarbeit danken. Die sehr kreativen cryo-TEM Proben von Johanna Elter für mich waren nicht immer die dankbarsten, aber dadurch auch immer wieder eine Herausforderung und immer wieder spannend. Danke für meine Expertise am Elektronenmikroskop. Carsten Rössel möchte ich dafür danken, dass er wie kein anderer die Labore gepflegt und alles in Ordnung gehalten hat. Außerdem für die vielen Gespräche und Tipps, die ich von ihm bekommen habe, wenn ich mich an ihn gewandt habe.

Einen Dank auch an alle Praktikanten und Bacheloranden/Masteranden, die ich betreuen durfte und die mir geholfen haben, nicht nur diese Arbeit zu füllen, sondern mich auch dazu gebracht haben, ihre Projekte im Voraus durchzuplanen, was auch zu einem vorausschauenden Arbeiten erzieht. Neben anderen seien hier namentlich Paul Wiemuth, Jan-Hendrik Kruse, Moritz Köhler und Kathrin Kowalczuk genannt.

Insgesamt möchte ich mich bei der gesamten Arbeitsgruppe Schacher für die Zeit bedanken. Die Arbeitsgruppe hat mich mit durch diese Jahre getragen und in schwierigen Zeiten immer wieder unterstützt.

Zuletzt ein Dank an meine Familie und Freunde dafür, dass ihr meine Zeit in Jena zu einem besonderen Abschnitt in meinem Leben gemacht habt und mich außerhalb des Labors immer unterstützt habt.

Declaration of Authorship / Selbstständigkeitserklärung

Ich erkläre, dass ich die vorliegende Arbeit selbständig und unter Verwendung der angegebenen Hilfsmittel, persönlichen Mitteilungen und Quellen angefertigt habe.

Ort, Datum Unterschrift (Philip Biehl)

Documentation of Authorship

Erklärung zu den Eigenanteilen der Promovendin/des Promovenden sowie der weiteren Doktorandinnen/Doktoranden als Co-Autorinnen/-Autoren an den Publikationen und Zweitpublikationsrechten bei einer kumulativen Dissertation

Für alle in dieser kumulativen Dissertation verwendeten Manuskripte liegen die notwendigen Genehmigungen der Verlage („Reprint permissions“) für die Zweitpublikation vor.

Die Co-Autorinnen/-Autoren der in dieser kumulativen Dissertation verwendeten Manuskripte sind sowohl über die Nutzung, als auch über die oben angegebenen Eigenanteile der weiteren Doktorandin-nen/Doktoranden als Co-Autorinnen/-Autoren an den Publikationen und Zweitpublikationsrechten bei einer kumulativen Dissertation informiert und stimmen dem zu.

Die Anteile der Promovendin/des Promovenden sowie der weiteren Doktorandinnen/Doktoranden als Co-Autorinnen/Co-Autoren an den Publikationen und Zweitpublikationsrechten bei einer kumulativen Dissertation sind in der Anlage aufgeführt.

Ort, Datum Unterschrift (Philip Biehl)

Ich bin mit der Abfassung der Dissertation als publikationsbasierte Dissertation, d.h. kumulativ, einverstanden und bestätige die vorstehenden Angaben.

Ort, Datum Unterschrift (Prof. Dr. Felix H. Schacher)

Declaration on authorship contributions to the included publications/Erklärung zu den Eigenanteilen an den enthaltenen Publikationen

P1 "Zwitterionic Iron Oxide (γ-Fe_2O_3) Nanoparticles Based on P(2VP-*grad*-AA) Copolymers"
M. Billing,[1] C. Gräfe,[2] A. Saal,[3] P. Biehl,[4] J. Clement,[5] S. Dutz,[6] S. Weidner,[7] F. Schacher,[8] *Macromol. Rapid Commun.* **2017**, *38*, 1600637.

Author	**1**	**2**	**3**	**4**	**5**	**6**	**7**	**8**
Conceptual development/contribution	X			X				X
TGA measurements				X				
TEM measurements				X				
Synthesis of magnetic nanoparticles						X		
Synthesis of Polymers and hybrid nanomaterials	X		X					
Preparation and evaluation of toxicity tests		X			X			
MALDI measurements							X	
Preparation of manuscript	X							X
Correction of the manuscript	X	X	X	X	X	X	X	X
Proposed publication equivalent				**0.5**				

" Synthesis, Characterization, and Applications of Magnetic Nanoparticles Featuring Polyzwitterionic Coatings"

P2 P. Biehl,‡1 M. von der Lühe,‡2 S. Dutz,3 F. Schacher,4 *Polymers* **2018**, *10*, 91.

‡Both authors contributed equally to this work

Author	**1**	**2**	**3**	**4**
Conceptual development/contribution	X	X		X
Preparation of manuscript	X	X	X	
Correction of the manuscript	X	X	X	X
Proposed publication equivalent	**0.5**			

"Reversible Adsorption of Methylene Blue as Cationic Model Cargo onto Polyzwitterionic Magnetic Nanoparticles"

P3 P. Biehl,1,‡ M. von der Lühe,2,‡ F. H. Schacher,3 *Macromol. Rapid Commun.* **2018**, *39*, 1800017.

‡Both authors contributed equally to this work

Author	**1**	**2**	**3**
Conceptual development/contribution	X	X	X
Preparation and characterization of polymers and hybrid nanomaterials	X		
adsorption / desorption experiments	X	X	
Preparation of manuscript	X	X	
Correction of the manuscript	X	X	X
Proposed publication equivalent	**1.0**		

P4

"Different Routes to Ampholytic Polydehydroalanine: Orthogonal versus Simultaneous Deprotection"

J. H. Kruse,[1] P. Biehl,[2] F. Schacher[3], *Macromol. Rapid Commun.* **2019**, *40*, 1800857.

Author	1	2	3
Conceptual development/contribution	X	X	X
Synthesis of monomers and subsequent polymerizations	X		
Characterization of polymers	X		
Investigation of protective group cleavage	X		
Preparation of manuscript	X		
Correction of the manuscript	X	X	X
Supervision of JHK		X	
Proposed publication equivalent		**0.5**	

P5

"Surface Functionalization of Magnetic Nanoparticles Using a Thiol-Based Grafting-Through Approach"

P. Biehl,[1] F. H. Schacher,[2] *Surfaces* **2020***, 3,* 116-131.

Author	1	2
Conceptual development/contribution	X	X
Synthesis and experimental implementation	X	
Preparation of manuscript	X	
Correction of the manuscript	X	X
Proposed publication equivalent	**1.0**	

P6

“Weak Polyampholytes at the Interface of Magnetic Nanocarriers: A Facile Catch and Release Platform for Dyes“

P. Biehl,[1] P. Wiemuth,[2] J. G. Lopez,[3] M.-C. Barth,[4] A. Weidner,[5] S. Dutz,[6] K. Peneva,[7] F. H. Schacher,[8] *Langmuir* **2020,** *36,* 6095–6105.

Author	**1**	**2**	**3**	**4**	**5**	**6**	**7**	**8**
Conceptual development/contribution	X							X
Synthesis of magnetic nanoparticles					X			
Preparation and characterization of magnetic nanoparticles with amphiphilic polymer coatings	X	X						
Synthesis of cationic dye PDI-4Pyl			X					
Synthesis of anionic dye PDI-4S				X				
adsorption / desorption experiments for differently charged dyes using PDha@MCNP	X	X						
adsorption / desorption experiments for PImAA@MCNP, PDha@MCNP and PDAGA@MCNP with PDI-4Pyl and PDI-4S	X							
Fluorescence investigations for Dye loaded PDha@MCNP	X							
Preparation of manuscript	X							X
Correction of the manuscript	X	X	X	X	X	X	X	X
Proposed publication equivalent	**1.0**							

Publications P1-P6

Publication P1

“Zwitterionic Iron Oxide (γ-Fe_2O_3) Nanoparticles Based on P(2VP-*grad*-AA) Copolymers”

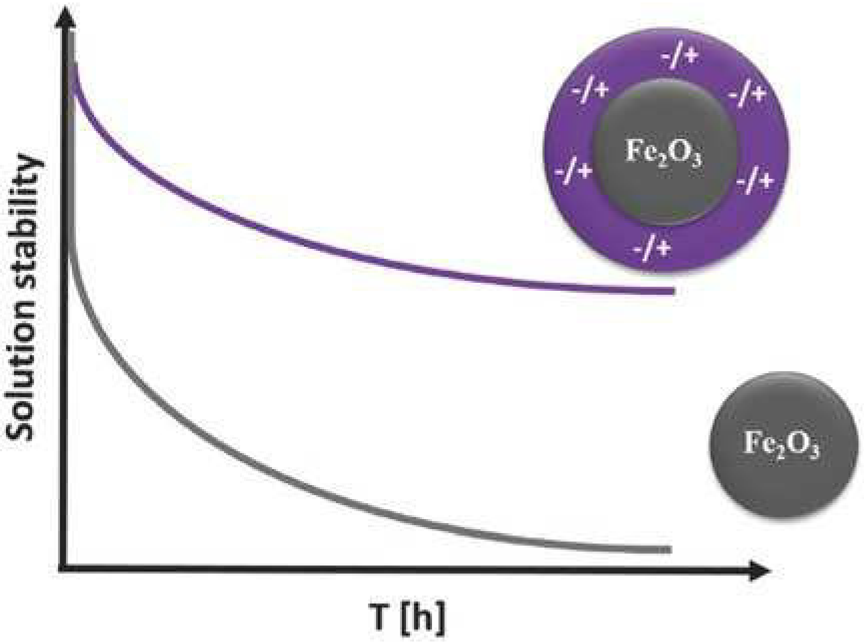

M. Billing, C. Gräfe, A. Saal, P. Biehl, J. Clement, S. Dutz, S. Weidner, F. Schacher

Macromol. Rapid Commun. **2017**, *38*, 1600637.

Volume 38 • Number 4 • February 20, 2017

www.mrc-journal.de

Macromolecular Rapid Communications

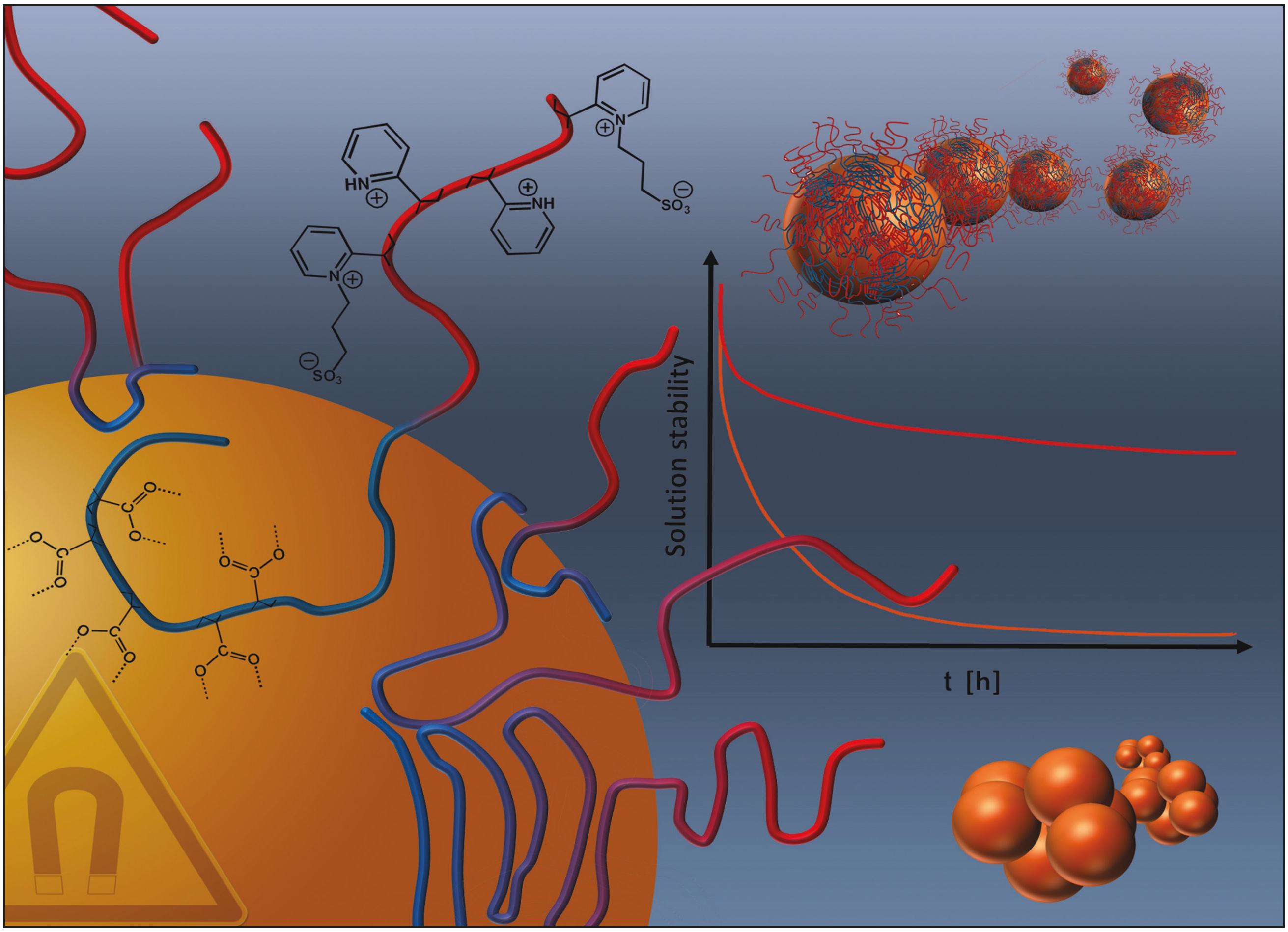

4/2017

WILEY-VCH

Zwitterionic Iron Oxide (γ-Fe_2O_3) Nanoparticles Based on P(2VP-*grad*-AA) Copolymers

Mark Billing, Christine Gräfe, Adrian Saal, Philip Biehl,
Joachim H. Clement, Silvio Dutz, Steffen Weidner, Felix H. Schacher*

This study presents the synthesis and characterization of zwitterionic core–shell hybrid nanoparticles consisting of a core of iron oxide multicore nanoparticles (MCNPs, γ-Fe_2O_3) and a shell of sultonated poly(2-vinylpyridine-*grad*-acrylic acid) copolymers. The gradient copolymers are prepared by reversible addition fragmentation chain transfer polymerization of 2-vinylpyridine (2VP), followed by the addition of *tert*-butyl acrylate and subsequent hydrolysis. Grafting of P(2VP-*grad*-AA) onto MCNP results in P(2VP-*grad*-AA)@MCNP, followed by quaternization using 1,3-propanesultone—leading to P($2VP_S$-*grad*-AA)@MCNP with a zwitterionic shell. The resulting particles are characterized by transmission electron microscopy, dynamic light scattering, and thermogravimetric analysis measurements, showing particle diameters of ≈70–90 nm and an overall content of the copolymer shell of ≈10%. Turbidity measurements indicate increased stability toward secondary aggregation after coating if compared to the pristine MCNP and additional cytotoxicity tests do not reveal any significant influence on cell viability.

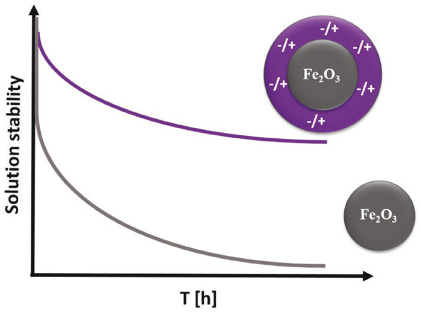

M. Billing, A. Saal, P. Biehl, Prof. F. H. Schacher
Laboratory of Organic and Macromolecular Chemistry
Friedrich-Schiller-University Jena
Humboldtstraße 10, D-07743 Jena, Germany
E-mail: felix.schacher@uni-jena.de
M. Billing, A. Saal, P. Biehl, Dr. J. H. Clement, Prof. F. H. Schacher
Jena Center for Soft Matter (JCSM)
Friedrich-Schiller-University Jena
Philosophenweg 7, D-07743 Jena, Germany
C. Gräfe, Dr. J. H. Clement
Klinik für Innere Medizin II
Abteilung Hämatologie und Internistische Onkologie
Universitätsklinikum Jena
Am Klinikum 1, D.07747 Jena, Germany
Dr. S. Dutz
Institute of Biomedical Engineering and Informatics
Technische Universität Ilmenau
Gustav-Kirchhoff-Str. 2, D.98693 Ilmenau, Germany
Dr. S. Weidner
Bundesanstalt für Materialforschung und -prüfung (BAM)
Richard-Willstätter-Str. 11, D-12489 Berlin, Germany

1. Introduction

The synthesis and surface modification of hybrid inorganic/organic nanomaterials has gained tremendous interest during recent years. One specific example are magnetic nanoparticles (MNPs)[1,2] and, mainly caused by the large surface to volume ratio of such materials, different fields of application have been considered.[3–6] Such materials have been used in drug targeting,[7] therapeutic approaches,[8] as contrast agents in magnetic resonance imaging,[9] and for the separation of proteins and enzymes.[10] In case of Ni and Co, issues related to toxicity often hinder their use in biomedical settings,[11,12] whereas iron oxide nanoparticles in general are being regarded as noncytotoxic and biocompatible.[3] Further, these materials are considered as a cost-effective alternative for waste treatment, due to easy processing and low toxicity.[13] In most applications, the magnetic response of MNPs toward external magnetic fields is exploited and suitable (polymeric)

DOI: 10.1002/marc.201600637

coating materials can be further used to implement sensitivity toward changes in temperature or pH. In addition, such coatings also often improve the solution stability of MNPs,[14] prevent undesired secondary aggregation, and implement additional functionality, such as the use as heterogeneous ligands in controlled radical polymerizations (ATRP).[3,15] Further, surface coating can lead to response to multiple stimuli such as pH/temperature, pH/magnetic field, or temperature/magnetic field.[16] Depending on the functionalities introduced via surface coating, subsequent modifications with antibodies or dyes have been demonstrated,[17,18] thereby further extending possible application fields. In biomedical applications, protein adsorption to the nanoparticle surface depends on a multitude of parameters and can drastically alter solution behavior of MNPs.[19] One often exploited possibility for the formation of a polymeric shell is electrostatic adsorption to the particle surface, as, e.g., shown for poly(acrylic acid), mainly due to the affinity of carboxylates toward (iron) oxide surfaces.[20–22]

Another attractive material for coating of MNPs are polyzwitterions: recent examples include materials based on 2-acrylamido-2-methylpropanesulfonic acid and the corresponding MNPs showed high stability at elevated temperatures and excellent imaging properties.[23] Coatings based on 3-(diethylamino) propylamine exhibited long blood circulation, as well as low cell toxicity and macrophage uptake, and thus represent interesting materials for future contrast agents.[24] Another advantage is that such polymeric shells can lead to increased pH stability and minimized protein adsorption.[25]

In this work, we present the preparation of MNPs with a zwitterionic coating based on sultonated poly(2-vinylpyridine-*grad*-acrylic acid) P($2VP_S$-*grad*-AA) gradient copolymers. The copolymers were synthesized using reversible addition fragmentation chain transfer (RAFT) radical polymerization of 2-vinyl pyridine and *tert*-butyl acrylate (*t*BA), respectively. Subsequent hydrolysis and electrostatic adsorption to MNP rendered P(2VP-*grad*-AA)@MNP hybrid nanoparticles, which could be transformed into zwitterionic materials upon sultonation of the 2VP moieties (P($2VP_S$-*grad*-AA)@MNP).[26] We use two different compositions of the gradient copolymers and the resulting particles were characterized by transmission electron microscopy (TEM), dynamic light scattering (DLS), thermogravimetric analysis (TGA), and zeta potential measurements. Further, cell viability tests reveal no significant cytotoxic effects of the materials for concentrations up to 100 µg cm^{-2}.

2. Experimental Section

Materials and instruments including detailed information for zeta potential, dynamic light scattering (DLS), size exclusion chromatography (SEC), transmission electron microscopy (TEM), matrix-assisted laser desorption/ionization time-of-flight mass spectrometry (MALDI-ToF MS), and cytotoxicity measurement are listed in the Supporting Information.

2.1. Synthesis of P(2VP-*grad*-*t*BA)

AIBN, 2-vinylpyridine, and CTA (2-cyano-2-propyl benzodithioate (CPDB)) were mixed in a Schlenk tube. After three freeze-pump-thaw cycles the reaction was started at 75 °C. After 140 min (170 min in the case of P($2VP_{69}$-*grad*- tBA_{34})) *t*BA was added. After 460 min (410 min) the reaction was finished and the process was aborted by cooling with liquid nitrogen. After two-fold precipitation in hexane the gradient copolymer was dried and characterized. For the determination of the copolymer composition, a sample was taken for SEC before addition of *t*BA.

Feed ratio: P($2VP_{58}$-*grad*-tBA_{30}): CTA/AIBN/VP/*t*BA = 1/0.9/83/210
P($2VP_{45}$-*grad*-tBA_{37}): CTA/AIBN/VP/*t*BA = 1/0.9/50/211

^{1}H-NMR (300 MHz, CD_2Cl_2, δ): 8.51-6.30 (Ar*H*), 2.2-1.1 (overlapping polymer backbone, $-COO(CH_3)_3$) ppm.

2.2. Synthesis of P(2VP-*grad*-AA)

P($2VP_{58}$-*grad*-tBA_{30}) (1 g) or (P($2VP_{45}$-*grad*-tBA_{37}) (1 g) was dissolved in 1,4-dioxane (80 mL) and HCl_{aq} (5 M, 6 eq per repetition unit). The reaction mixture was stirred at 90 °C for 24 h. After cooling down to room temperature (RT) the mixture was neutralized by dilute NaOH and dialyzed against water. Afterward the solvent was removed in vacuo (yield: P($2VP_{45}$-*grad*-AA_{37}) 627 mg; P($2VP_{58}$-*grad*-AA_{30}) 675 mg).

^{1}H-NMR (300 MHz, d-TFA, δ): 8.51-6.30 (Ar*H*), 2.2-1.1 ($-CH_2-CH-$, CH_2-CH-) ppm.

2.3. Synthesis of P(2VP-*grad*-AA)@MCNP

P($2VP_{58}$-*grad*-AA_{30}) or (P($2VP_{45}$-*grad*-AA_{37}) (50.6 mg) was dissolved in water (3 mL, pH 5, adjusted by addition of small amounts of HCl_{aq}) and diluted with water (20 mL, pH 7). The resulting solution was mixed with $MCNP_{aq}$[27] (2 mL, c = 25 mg mL^{-1}). The resulting dispersion was sonicated for 1 h at 50 °C. The particles were separated from the dispersion using an NdFeB magnet (55.0 × 55.0 × 25.0 mm). Afterward, the resulting particles were washed with deionized water five times. After freeze-drying 39 mg of P($2VP_{58}$-*grad*-AA_{30})@MCNP and 41 mg of P($2VP_{45}$-*grad*-AA_{37})@MCNP were obtained.

2.4. Synthesis of P($2VP_S$-*grad*-AA)@MCNP

P($2VP_{58}$-*grad*-AA_{30})@MCNP or (P($2VP_{45}$-*grad*-AA_{37})@MCNP) (the amount of 1,3-propanesultone was calculated based on the assumption that 50 mg copolymers are present in total in the sample) was dispersed in propylene carbonate (3 mL). Afterward 1,3 propanesultone (110 mg, 2.2 eq per repetition unit) was added and the mixture was stirred for 1 h at 50 °C. The particles were separated from the dispersion using an NdFeB magnet (55.0 × 55.0 × 25.0 mm) and washed three times with acetone (to remove residues of 1,3-propanesultone) and two times with deionized water. After freeze-drying 30 mg of P($2VP_{45}$-*grad*-AA_{37})@MCNP and 31 mg of P($2VP_{58}$-*grad*-AA_{30})@MCNP were obtained.

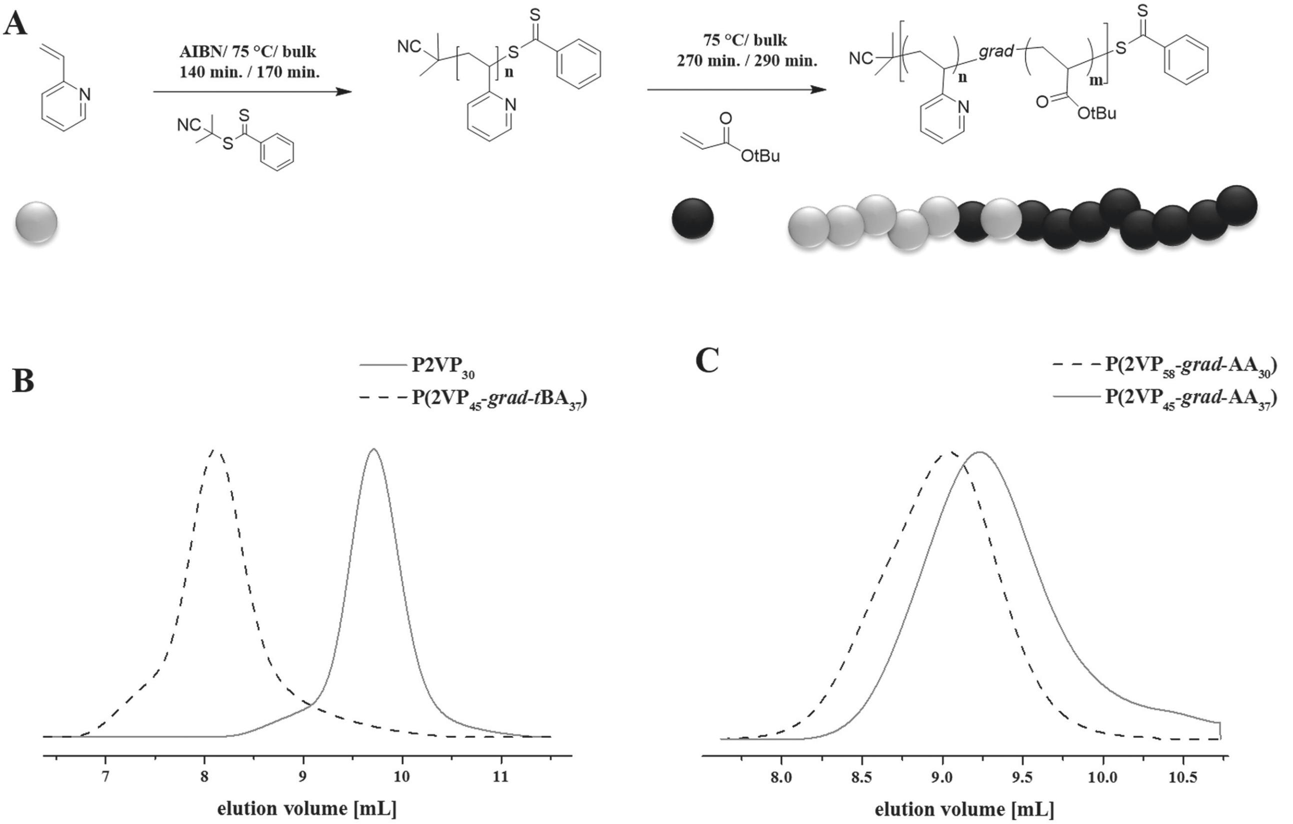

Figure 1. A) Synthesis of P(2VP-*grad*-*t*BA) using RAFT polymerization; B) SEC elution traces of P2VP (solid gray line) and P(2VP$_{45}$-*grad*-*t*BA$_{37}$) (dashed black line, $CHCl_3$/TEA/i-PrOH; 94/4/2); C) SEC elution traces of P(2VP$_{58}$-*grad*-AA$_{30}$) (dashed black line) and P(2VP$_{45}$-*grad*-AA$_{37}$) (gray line, 0.1% TFA + 0.5 M NaCl).

3. Results and Discussion

Herein we report on the preparation and characterization of iron oxide multicore nanoparticles (MCNPs) featuring a zwitterionic gradient copolymer shell. The latter is formed via electrostatic adsorption of poly(2-vinylpyridine)-*grad*-poly(acrylic acid) (P(2VP-*grad*-AA)), followed by quaternization of the P2VP part using 1,3-propanesultone as reported earlier (Figure 1A).[26,28]

The copolymers were synthesized via RAFT polymerization using CPDB as RAFT agent and azobis(isobutyronitrile) AIBN as initiator at an initial feed ratio of CTA/AIBN/VP/*t*BA = 1/0.9/83/210 for P(2VP$_{58}$-*grad*-*t*BA$_{30}$) and CTA/AIBN/VP/*t*BA = 1/0.9/50/211 for P(2VP$_{45}$-*grad*-*t*BA$_{37}$). The polymerization was carried out under bulk conditions at 70 °C and monitored by SEC (Figure 1B). After reaching ≈60% conversion of 2VP (M_n 3.200 g mol^{-1} for P(2VP$_{45}$-*grad*-*t*BA$_{37}$) and M_n 5.300 g mol^{-1} for P(2VP$_{58}$-*grad*-*t*BA$_{30}$); Table 1), *tert*-butyl acrylate was added via syringe and the polymerization was continued for further 270 min (P(2VP$_{45}$-*grad*-*t*BA$_{37}$))/290 min (P(2VP$_{58}$-*grad*-*t*BA$_{30}$) (Figure S1A,B, Supporting Information). The controlled copolymerization behaviour of *t*BA and 2VP under comparable conditions has been shown in previous work.[29] After precipitation into hexane, followed by filtration and drying, characterization via ^{1}H-NMR in CD_2Cl_2 showed the expected signals

Table 1. SEC data of P2VP$_{50}$, P2VP$_{30}$, P(2VP$_{58}$-*grad*-*t*BA$_{30}$), P(2VP$_{55}$-*grad*-*t*BA$_{37}$), P(2VP$_{58}$-*grad*-AA$_{30}$), and P(2VP$_{55}$-*grad*-AA$_{37}$).

	Sample	M_n [g mol^{-1}]	$M_{n,Theo.}$ [g mol^{-1}]	M_w [g mol^{-1}]	PDI
1	P2VP$_{30}$	3200$^{a)}$	3100	3600$^{a)}$	1.13$^{a)}$
2	P2VP$_{50}$	5300$^{a)}$	5200	3200$^{a)}$	1.10$^{a)}$
3	P(2VP$_{58}$-*grad*-*t*BA$_{30}$)$^{c)}$	11 500$^{a)}$	9000	13 400$^{a)}$	1.16$^{a)}$
4	P(2VP$_{45}$-*grad*-*t*BA$_{37}$)$^{c)}$	11 900$^{a)}$	7000	15 000$^{a)}$	1.25$^{a)}$
5	P(2VP$_{58}$-*grad*-AA$_{30}$)	9 300$^{b)}$	7500	11 500$^{b)}$	1.23$^{b)}$
6	P(2VP$_{45}$-*grad*-AA$_{37}$)	5300$^{b)}$	5400	7700$^{b)}$	1.46$^{b)}$

$^{a)}$SEC ($CHCl_3$/TEA/i-PrOH; 94/4/2, PS-calib.); $^{b)}$SEC (0.1% TFA + 0.05 M NaCl, P2VP-calib.); $^{c)}$Composition was determined by a combination of MALDI-ToF MS, ^{1}H-NMR, and SEC.

for P2VP (8.6–6.3 ppm) and P*t*BA (2.2–1.1 ppm) (Figure S2, Supporting Information). The final copolymer composition was determined by comparing the 2VP signal to the backbone signal containing also the signal for the *tert*-butyl group of *t*BA. The exact molar mass of the copolymer was determined by MALDI ToF MS, resulting in 9.717 g mol^{-1} for P($2VP_{58}$-*grad*-AA_{30}) and 9.457 g mol^{-1} for P($2VP_{45}$-*grad*-AA_{37}) (Figure S3, Supporting Information). Together with the molar mass of the P2VP precursor according to SEC, the exact copolymer compositions were determined to P($2VP_{58}$-*grad*-tBA_{30}) and P($2VP_{45}$-*grad*-tBA_{37}).

In order to allow electrostatic attraction of the prepared gradient copolymers to the surface of the herein used multicore iron oxide nanoparticles (MCNP), P*t*BA was converted into poly(acrylic acid).[30] Therefore, the copolymers were dissolved in 1,4-dioxane at 1.25 wt% and HCl_{aq} (5 M) was added in a sixfold excess (to the overall degree of polymerization of the respective gradient copolymer). After stirring for 24 h at 90 °C, the reaction mixture was neutralized using $NaOH_{aq}$ and the copolymers were purified by dialysis against deionized water. After removal of the solvent, the materials were further characterized by ^{1}H-NMR in *d*-TFA. Again, the signals for the 2-vinylpyridine at 8.9–7.7 ppm can be detected, as well as the polymeric backbone at 3.5–1.9 ppm, whereas the signal for the *tert*-butyl group is absent, hinting toward a quantitative removal (Figure S3, Supporting Information). SEC in 0.1% TFA + 0.05 M NaCl afterward ensured the integrity of the gradient copolymers after the deprotection procedure (Figure 1C).

3.1. P(2VP-*grad*-AA)@MCNP

For electrostatic adsorbtion of both P(2VP-*grad*-AA) onto MCNP, the gradient copolymers were dissolved in acidified water (pH 5–6, adjusted by HCl_{aq}) and mixed with a dispersion of MCNP in water (c = 25 mg mL^{-1}, weight ratio 1:1). Afterward the reaction mixture was treated with ultrasound for 1 h at 50 °C (Scheme 1). Subsequently, the particles were separated by a NdFeB magnet from the dispersion and resuspended in water. This procedure was repeated five times and afterward the particles were freeze dried. For investigations in solution, two pH values were chosen to simulate physiologically relevant solution conditions. The pH was adjusted by titration of deionized water with 0.1 M HCl, and all measurements were carried out at a concentration of 0.1 g L^{-1}.

Determination of the hydrodynamic radii of P($2VP_{58}$-*grad*-AA_{30})@MCNP and P($2VP_{45}$-*grad*-AA_{37})@MCNP led to diameter in the range of 72–88 nm, the values were slightly lower if compared to the pristine MCNP (Figure 2C and Table 2).

The nanoparticles were further investigated using TEM (Figure 3). Compared to the pristine MCNP (Figure 3A), P(2VP-*grad*-AA)@MCNP shows less aggregation and more individual nanoparticles are present within the sample micrographs. Evaluation of the average particle diameter of ≈60–80 nm (≈80 particles have been meaured) is in reasonable agreement with values obtained by DLS (D_{DLS} = 70–90 nm).

For determination of the weight loss of the adsorbed organic material on the core-shell nanoparticles, TGA was carried out. The pristine MCNP exhibited a weight loss in three steps of about 3.27% (Table 2). First, from 50 to 140 °C adsorbed water evaporates (0.7%), followed by a mass loss of 1.6% in the temperature range of 200–500 °C, which we attribute to phase transformations of incorporated impurities (hydroxide and hydrated oxides of iron) to hematite. At higher temperatures (500–800 °C) residues of carbonates and salts are vaporized (1.0%).[17] Substracting the weight loss for the pristine MCNP, a weight loss of 10.7% (P($2VP_{58}$-*grad*-AA_{30})@MCNP) and that of 12.0% (P($2VP_{45}$-*grad*-AA_{37})@MCNP) were obtained (Table 2 and Figure 2B). The final mass loss was always calculated at 800 °C.

3.2. P($2VP_S$-*grad*-AA)@MCNP

We now sultonated the P2VP part of the adsorbed P(2VP-*grad*-AA) copolymers to P($2VP_S$-*grad*-AA) and thus prepared zwitterionic P($2VP_S$-*grad*-AA)@MCNP nanoparticles. We have recently shown that by that method degrees of sultonation of roughly 70% are reached and that $P2VP_S$ is soluble over the entire pH range.[26] P(2VP-*grad*-AA)

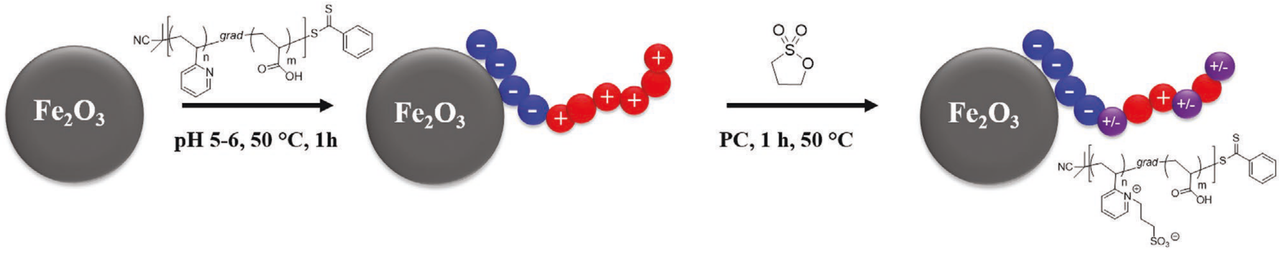

Scheme 1. Grafting of P($2VP_{58}$-*grad*-AA_{30}) and P($2VP_{45}$-*grad*-AA_{37}) onto γ-Fe_2O_3 and sultonation of P($2VP_{58}$-*grad*-AA_{30})@MCNP and P($2VP_{45}$-*grad*-AA_{37})@MCNP.

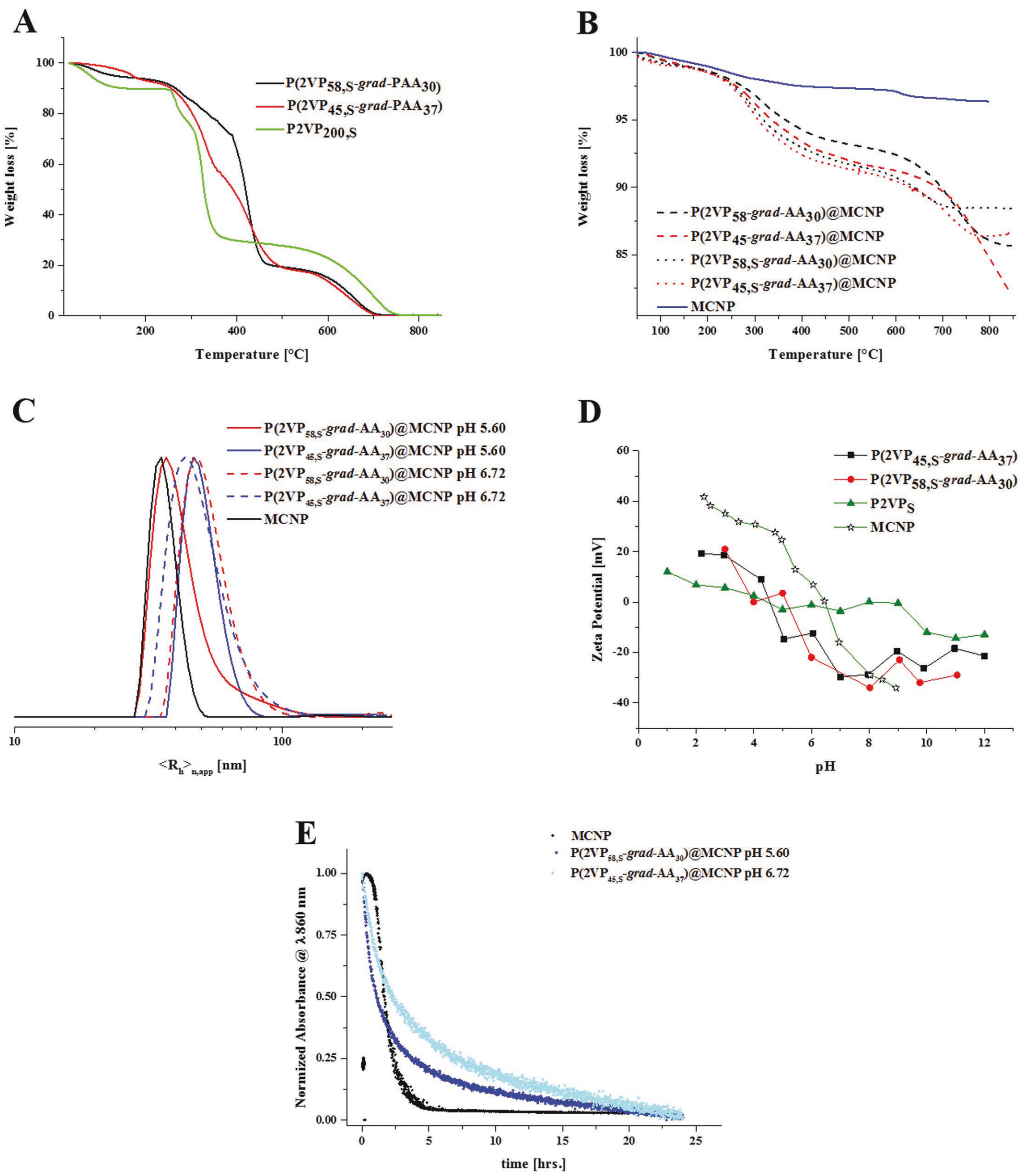

Figure 2. A) TGA measurements of $P2VP_{200,S}$, $P(2VP_{58,S}$-*grad*-$AA_{30})$, and $P(2VP_{45,S}$-*grad*-$AA_{37})$; B) TGA measurements of MCNP, $P(2VP_{58,S}$-*grad*-$AA_{30})$@MCNP, $P(2VP_{45,S}$-*grad*-$AA_{37})$@MCNP, $P(2VP_{58}$-*grad*-$AA_{30})$@MCNP, and $P(2VP_{45}$-*grad*-$AA_{37})$@MCNP; C) DLS measurements of MCNP, $P(2VP_{58,S}$-*grad*-$AA_{30})$@MCNP and $P(2VP_{45,S}$-*grad*-$AA_{37})$@MCNP, $P(2VP_{58}$-*grad*-$AA_{30})$@MCNP at pH 5.60 and 6.72; D) zeta potential measurements of MCNP, $P2VP_{200,S}$, $P(2VP_{58,S}$-*grad*-$AA_{30})$@MCNP, and $P(2VP_{45,S}$-*grad*-$AA_{37})$@MCNP; E) Sedimentation measurements of MCNP, $P(2VP_{58,S}$-*grad*-$AA_{30})$@MCNP and $P(2VP_{45,S}$-*grad*-$AA_{37})$@MCNP at pH 5.60 and 6.72, respectively.

@MCNP were dispersed in propylene carbonate using ultrasound, and 1,3-propanesultone (2.2 eq per P2VP unit) was added. The reaction mixture was stirred at 50 °C for 1 h and afterward the nanoparticles were seperated by a NdFeB magnet and washed three times with acetone and two times with water, followed by freeze drying.

DLS experiments revealed hydrodynamic diameters of 74–94 nm for $P(2VP_{58,S}$-*grad*-$AA_{30})$@MCNP and 84–94 nm for $P(2VP_{45,S}$-*grad*-$AA_{37})$@MCNP, thereby being within in the range of the earlier determined values for $P(2VP_{45}$-*grad*-$AA_{37})$@MCNP and $P(2VP_{58}$-*grad*-$AA_{37})$@MCNP (Table 2 and Figure 2C). TGA measurements of $P(2VP_{58,S}$-*grad*-$AA_{30})$, $P(2VP_{45,S}$-*grad*-$AA_{37})$, and $P(2VP)_{200,S}$ showed main decomposition between 190 and 720 °C (Figure 2A), similar to previously reported P2VP-*b*-PMAA block copolymers.[31] Further, weight losses of 8.3% in the case of $P(2VP_{58,S}$-*grad*-$AA_{30})$@MCNP and 10.3% for $P(2VP_{45,S}$-*grad*-$AA_{37})$@MCNP are found. Diameters

Table 2. $\langle R_h \rangle_{n,app}$ and diameter at pH 5.60 and 6.72 of MCNP, P($2VP_{58}$-*grad*-AA_{30})@MCNP, P($2VP_{58,S}$-*grad*-AA_{30})@MCNP, P($2VP_{45}$-*grad*-AA_{37})@MCNP, P($2VP_{45,S}$-*grad*-AA_{37})@MCNP. Weight loss and r_h of MCNP, P($2VP_{58}$-*grad*-AA_{30})@MCNP, P($2VP_{58,S}$-*grad*-AA_{30})@MCNP, P($2VP_{45}$-*grad*-AA_{37})@MCNP, P($2VP_{45,S}$-*grad*-AA_{37})@MCNP. Diameter investigated by TEM of MCNP, P($2VP_{58,S}$-*grad*-AA_{30})@MCNP, P($2VP_{45,S}$-*grad*-AA_{37})@MCNP.

Entry	Sample	Diameter by DLS [nm]	TEM [nm]
1	MCNP	70	
2	P($2VP_{58,S}$-*grad*-AA_{30})@MCNP pH 5.60	74	76 ± 12
3	P($2VP_{45,S}$-*grad*-AA_{37})@MCNP pH 5.60	94	64 ± 9
4	P($2VP_{58,S}$-*grad*-AA_{30})@MCNP pH 6.72	94	74 ± 12
5	P($2VP_{45,S}$-*grad*-AA_{37})@MCNP pH 6.72	84	81 ± 20
6	P($2VP_{58}$-*grad*-AA_{30})@MCNP pH 5.60	72	74 ± 10
7	P($2VP_{45}$-*grad*-AA_{37})@MCNP pH 5.60	88	70 ± 11
8	P($2VP_{58}$-*grad*-AA_{30})@MCNP pH 6.72	72	69 ± 7
9	P($2VP_{45}$-*grad*-AA_{37})@MCNP pH 6.72	84	82 ± 25
10	P($2VP_{58,S}$-*grad*-AA_{30})@MCNP[a)]	80	–
11	P($2VP_{45,S}$-*grad*-AA_{37})@MCNP[a)]	90	–
	Sample	**Weight loss [%]**	**r_H calc from Equation (1) [nm]**
12	MCNP	3.3	–
13	P($2VP_{58}$-*grad*-AA_{30})@MCNP	10.7	4.8
14	P($2VP_{58,S}$-*grad*-AA_{30})@MCNP	8.3	3.8
15	P($2VP_{45}$-*grad*-AA_{37})@MCNP	12.0	5.4
16	P($2VP_{45,S}$-*grad*-AA_{37})@MCNP	10.3	4.7

[a)] Measured in cell culture medium.

observed in TEM measurements yielded comparable results if compared to DLS data (Table 2 and Figure 2C). Also here, TEM micrographs showed less aggregation of the nanoparticles (Figure 3C) and in some cases the copolymer shell can even be visualized (Figure 3D, white arrow).

The corresponding shell thickness of the sultonated particles was calculated by use of Equation (1) using ρ_K (Fe_3O_4 ≈5.2 g cm^{-3}), WL and RM (weight loss and residual mass measured by TGA) as well as r_K as determined by TEM. Values for ϱ_s were determined by taking the weight fractions of poly(acrylic acid) (PAA) (1.22–1.44 g mL^{-1}) and P2VP (1.1 g mL^{-1}),[32] resulting in a value of $\varrho_s = 1.20$ g mL^{-1}

$$r_H = \sqrt[3]{r_K^3 + \left(r_K^3 \left(\frac{\rho_K}{\rho_H} \right) \left(\frac{WL}{RM} \right) \right)} - r_K \tag{1}$$

By this procedure, copolymer shell thicknesses ranging from 3.8 to 5.4 nm were determined (Table 2). Also zeta potential measurements showed distinct changes after adsorption of the copolymer shell (Figure 2D). Whereas the pristine MCNP exhibits values from −35 mV (pH 9) to +40 mV (pH 2) with only a relatively narrow regime of apparent charge neutrality around pH 6, both P($2VP_{69,S}$-*grad*-AA_{34})@MCNP and P($2VP_{55,S}$-*grad*-AA_{45})@MCNP show negative potentials down to pH 5. At lower pH values, positive values were found (up to +20 mV at pH 1). In comparison, $P2VP_S$ showed negative zeta potentials of −10 mv to −15 mV at high pH, a relatively broad pH range (pH 9–5) of apparent charge neutrality, and a slightly positive zeta potential at low pH (+3 mV to +12 mV).

To evaluate long-term colloidal stability and potential secondary aggregation, we carried out sedimentation measurements at both pH 5.6 and 6.72, at concentrations of 0.1 g L^{-1} (Figure 2E and Figure S4, Supporting Information). Turbidity was determined at 860 nm to exclude absorption by the nanoparticle core or the copolymer coating. The normalized absorbance of the pristine particles in comparison to both P($2VP_{69,S}$-*grad*-AA_{34})@MCNP and P($2VP_{55,S}$-*grad*-AA_{45})@MCNP at two different pH values shows clear differences. Both samples After coating and sultonation, both samples show increased stability at lower pH (5.60), presumably due to increased charge density at the nanoparticle surface, which is caused by protonated 2VP units (Figure 2E). At pH 6.72 slightly faster sedimentation can be observed in both cases, albeit an increased solution stability against secondary aggregation can be observed for all samples after coating with P($2VP_S$-*grad*-AA).

We were also interested to verify biocompatibility of P($2VP_{58,S}$-*grad*-AA_{30})@MCNP and P($2VP_{45,S}$-*grad*-AA_{37})@MCNP. Therefore, human brain microvascular endothelial cells (HBMECs) were used as cell culture model, representing the human blood–brain barrier. HBMECs were incubated with both MCNPs in a concentration range of 5 µg cm^{-2} to 100 µg cm^{-2} for 3 and 24 h and stained with SYTOX Red Dead Cell Stain. As this nucleic acid-intercalating dye cannot cross intact cellular membranes but permeates damaged cell membranes it can be used to brightly label dead cells. The results indicate that both P($2VP_{58,S}$-*grad*-AA_{30})@MCNP and P($2VP_{45,S}$-*grad*-AA_{37})@MCNP do not show cytotoxic effects (Figure S5, Supporting Information) under these conditions. The slight increase of SYTOX-positive cell populations from 3.4 ± 0.7% in control

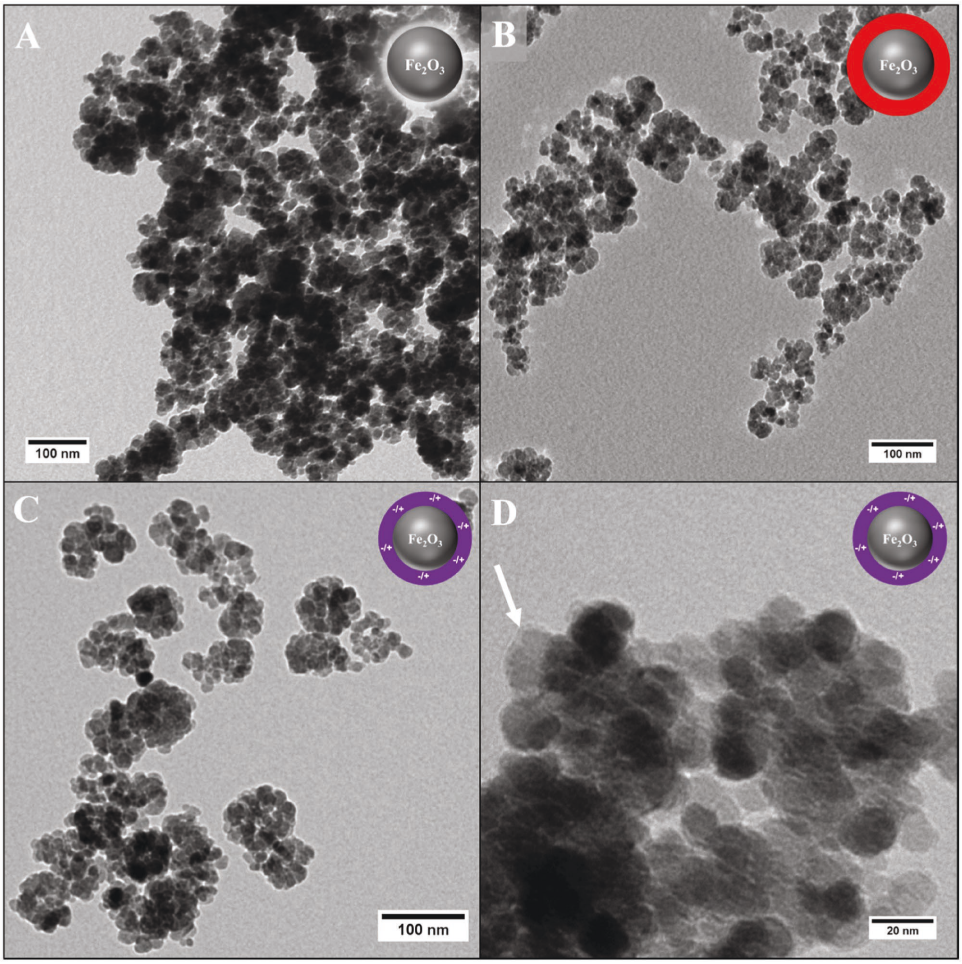

Figure 3. A) TEM micrographs of pristine MCNP, B) P(2VP$_{58}$-*grad*-AA$_{30}$)@MCNP at pH 6.72, and C) P(2VP$_{58,S}$-*grad*-AA$_{30}$)@MCNP at pH 6.72; D) A higher magnification where the polymeric shell can also be distinguished, highlighted by the white arrow.

cells to 5.7 ± 3.2% or 6.5 ± 3.7% for HBMEC treated with 100 µg cm^{-2} P(2VP$_{58,S}$-*grad*-AA$_{30}$)@MCNP or P(2VP$_{45,S}$-*grad*-AA$_{37}$)@MCNP, respectively, is not statistically significant and even absent upon 24 h incubation.

4. Conclusion

Gradient P(2VP-*grad*-AA) copolymers of different composition were synthesized using RAFT polymerization techniques and electrostatically adsorbed onto magnetic iron oxide nanoparticles. Subsequent sultonation to P(2VP$_S$-*grad*-AA)@MCNP yielded zwitterionic hybrid core–shell nanoparticles and the successful coating was proven using TGA, zeta potential measurements, DLS, and TEM investigations. In all cases, ≈ 10 wt. % copolymer coating was achieved and the particles showed distinct differences concerning pH-dependant surface charge or sedimentation stability at different pH values, compared to the pristine particles. Further, SYTOX stain tests as well as flow cytometry showed no significant toxicity so far. Such materials might be of interest as future contrast agents where circulation time is important or to control (possibly prevent) undesired adsorption of proteins to the nanoparticle surface.

Supporting Information

Supporting Information is available from the Wiley Online Library or from the author.

Acknowledgements: The authors thank Grit Festag (FSU Jena) for help with SEC measurements and Andreas Weidner for help with the preparation of MCNP. The authors would further like to acknowledge the NMR-platform at the Friedrich-Schiller-University Jena for support in NMR spectroscopy.

Received: October 13, 2016; Revised: November 9, 2016; Published online: December 22, 2016; DOI: 10.1002/marc.201600637

Keywords: block copolymer; controlled radical polymerization; hybrid nanoparticles; iron oxide nanoparticles; sulfobetaines

[1] Z. Karimi, L. Karimi, H. Shokrollahi, *Mater. Sci. Eng.: C* **2013**, *33*, 2465.
[2] A. Kowalczuk, R. Trzcinska, B. Trzebicka, A. H. E. Müller, A. Dworak, C. B. Tsvetanov, *Prog. Polym. Sci.* **2014**, *39*, 43.
[3] L. C. Fidale, M. Nikolajski, T. Rudolph, S. Dutz, F. H. Schacher, T. Heinze, *J. Colloid Interface. Sci.* **2013**, *390*, 25.
[4] L. Dykman, N. Khlebtsov, *Chem. Soc. Rev.* **2012**, *41*, 2256.
[5] N. A. Frey, S. Peng, K. Cheng, S. Sun, *Chem. Soc. Rev.* **2009**, *38*, 2532.
[6] D. Scheid, D. Stock, T. Winter, T. Gutmann, C. Dietz, M. Gallei, *J. Mater. Chem. C* **2016**, *4*, 2187.
[7] W.-H. Chiang, V. T. Ho, H.-H. Chen, W.-C. Huang, Y.-F. Huang, S.-C. Lin, C.-S. Chern, H.-C. Chiu, *Langmuir* **2013**, *29*, 6434.
[8] S. Dutz, R. Hergt, *Nanotechnology* **2014**, *25*, 452001.
[9] S. A. Anderson, R. K. Rader, W. F. Westlin, C. Null, D. Jackson, G. M. Lanza, S. A. Wickline, J. J. Kotyk, *Magn. Res. Med.* **2000**, *44*, 433.
[10] H.-H. Yang, S.-Q. Zhang, X.-L. Chen, Z.-X. Zhuang, J.-G. Xu, X.-R. Wang, *Anal. Chem.* **2004**, *76*, 1316.
[11] P. Padwal, R. Bandyopadhyaya, S. Mehra, *Langmuir* **2014**, *30*, 15266.
[12] K. Mijnendonckx, N. Leys, J. Mahillon, S. Silver, R. Van Houdt, *BioMetals* **2013**, *26*, 609.
[13] X. Li, Z. Wang, H. Lu, C. Zhao, H. Na, C. Zhao, *J. Membr. Sci.* **2005**, *254*, 147.
[14] R. Matsuno, K. Yamamoto, H. Otsuka, A. Takahara, *Macromolecules* **2004**, *37*, 2203.
[15] H. Arami, A. Khandhar, D. Liggitt, K. M. Krishnan, *Chem. Soc. Rev.* **2015**, *44*, 8576.
[16] R. Cheng, F. Meng, C. Deng, H.-A. Klok, Z. Zhong, *Biomaterials* **2013**, *34*, 3647.
[17] M. von der Lühe, U. Günther, A. Weidner, C. Gräfe, J. H. Clement, S. Dutz, F. H. Schacher, *RSC Adv.* **2015**, *5*, 31920.
[18] J. Gao, H. Gu, B. Xu, *Acc. Chem. Res.* **2009**, *42*, 1097.
[19] R. A. Sperling, W. J. Parak, *Phil. Trans. R. Soc. A: Math. Phys. Eng. Sci.* **2010**, *368*, 1333.
[20] J. Fresnais, M. Yan, J. Courtois, T. Bostelmann, A. Bée, J. F. Berret, *J. Colloid Interface Sci.* **2013**, *395*, 24.
[21] R. Sondjaja, T. Alan Hatton, M. K. C. Tam, *J. Magn. Magn. Mater.* **2009**, *321*, 2393.
[22] M. Szekeres, I. Tóth, E. Illés, A. Hajdú, I. Zupkó, K. Farkas, G. Oszlánczi, L. Tiszlavicz, E. Tombácz, *Int. J. Mol. Sci.* **2013**, *14*, 14550.
[23] E. L. Foster, Z. Xue, C. M. Roach, E. S. Larsen, C. W. Bielawski, K. P. Johnston, *ACS Macro Lett.* **2014**, *3*, 867.
[24] W. Xiao, J. Lin, M. Li, Y. Ma, Y. Chen, C. Zhang, D. Li, H. Gu, *Contrast Media Mol. Imaging* **2012**, *7*, 320.
[25] H. Wei, N. Insin, J. Lee, H.-S. Han, J. M. Cordero, W. Liu, M. G. Bawendi, *Nano Lett.* **2012**, *12*, 22.
[26] M. Billing, J. K. Elter, F. H. Schacher, *Polymer* **2016**, *104*, 40.
[27] S. Dutz, J. H. Clement, D. Eberbeck, T. Gelbrich, R. Hergt, R. Müller, J. Wotschadlo, M. Zeisberger, *J. Magn. Magn. Mater.* **2009**, *321*, 1501.
[28] J. Bohrisch, U. Wendler, W. Jaeger, *Macromol. Rapid Commun.* **1997**, *18*, 975.
[29] E. Čadová, J. Konečný, J. Kříž, R. Svitáková, P. Holler, J. Genzer, P. Vlček, *J. Polym. Sci. Part A: Polym. Chem.* **2010**, *48*, 735.
[30] M. Nemati, S. M. Hosseini, *Ionics* **2016**, *22*, 899.
[31] M. Kamachi, M. Kurihara, J. K. Stille, *Macromolecules* **1972**, *5*, 161.
[32] J. Brandrup, E. H. Immergut, *Polymer Handbook*, New York, Wiley **1989**.

Supporting Information

for *Macromol. Rapid Commun.,* DOI: 10.1002/marc.201600637

Zwitterionic Iron Oxide (γ-Fe_2O_3) Nanoparticles Based on P(2VP-*grad*-AA) Copolymers

Mark Billing, Christine Gräfe, Adrian Saal, Philip Biehl, Joachim H. Clement, Silvio Dutz, Steffen Weidner, Felix H. Schacher*

Supporting information

Zwitterionic Iron Oxide (Fe_2O_3) Nanoparticles Based on P(2VP-*grad*-AA) Copolymers

*Mark Billing,[1,2] Christine Gräfe,[3] Adrian Saal,[1,2] Philip Biehl,[1,2] Joachim H. Clement,[2,3] Silvio Dutz,[4] Steffen Weidner,[5] Felix H. Schacher[1,2]**

[1] Laboratory of Organic and Macromolecular Chemistry, Friedrich-Schiller-University Jena,
Humboldtstraße 10, D-07743 Jena, Germany

felix.schacher@uni-jena.de

[2] Jena Center for Soft Matter (JCSM), Friedrich-Schiller-University Jena, Philosophenweg 7,
D-07743 Jena, Germany

[3] Klinik für Innere Medizin II, Abteilung Hämatologie und Internistische Onkologie,
Universitätsklinikum Jena, Jena Germany

[4] Institute of Biomedical Engineering and Informatics, Technische Universität Ilmenau,
Ilmenau Germany

[5] Bundesanstalt für Materialforschung und -prüfung (BAM), Berlin, Germany

Experimental Section:

2-Vinylpyridine (Sigma Aldrich, 97%) was distilled prior to use and stored under argon at -20 °C. 4-Cyano-4-(phenylcarbonothioylthio)pentanoic acid (STREM CHEMICALS, INC., min. 97 %) was used as received. 1,3-Propanesultone (Sigma Aldrich, 98%) was used without further purification**.** Azobisisobutyronitrile (Sigma Aldrich, 98%) was prior to use recrystallized from methanol. *Tert*-butyl acrylate (Alfa Aesar + 98%) contained 4-methoxyphenol as inhibitor which was removed by column chromatography over neutral aluminum oxide and subsequent distillation before use. Tetrahydrofuran (THF) and dichloromethane (DCM) were purified using a PureSolv-EN^{TM} Solvent purification System (Innovative Technology). Any glassware was cleaned in a KOH/*iso*-propanol bath and dried at 110 °C. All deuterated solvents were obtained from Deutero. For dialysis, a Spectra/Por$^{®}$ dialysis membrane with a nominal MWCO of 1000 g mol^{-1} was used.

Synthesis of Magnetic Multicore Nanoparticles (MCNP): The magnetic multicore nanoparticles were prepared as described before.[1] Briefly: a 1 M $NaHCO_3$ solution was slowly added to a $FeCl_2$/$FeCl_3$ solution (total Fe-concentration: 1.25 M; Fe^{2+}/Fe^{3+} ratio = 1/1.3) with a rate of 0.75 ml/min under permanent stirring up to pH = 8, leading to the formation of a brownish precipitate. Afterwards, the solution was boiled for 5 minutes to form an almost black precipitate under the release of CO_2. The magnetic nanoparticles were then washed with water to remove remaining NaCl.

Nuclear Magnetic Resonance Spectroscopy (NMR): ^{1}H-NMR and ^{13}C-NMR spectra were recorded in $CDCl_3$ (or CD_2Cl_2) on a Bruker AC 300-MHz spectrometer at 298 K. Chemical shifts are given in parts per million (ppm, δ scale) relative to the residual signal of the deuterated solvent.

Size-Exclusion Chromatography (SEC): SEC was performed on a Shimadzu system equipped with a SCL-10A system controller, a LC-10AD pump, and a RID-10A refractive index detector using a solvent mixture containing chloroform ($CHCl_3$), triethylamine (TEA), and *iso*-propanol (*i*-PrOH) (94:4:2) at a flow rate of 1 mL min^{-1} on a PSS SDV linear S 5-µm column at 40 °C. The system was calibrated with PMMA (410-88 000 g mol^{-1}), PEO (440 – 44 700) and PS (310-128 000 g mol^{-1}) standards.

Water based SEC: SEC was performed on a Jasco system equipped with a DG-980-50 degasser, a PU-980 pump, a RI-930 Plus refractive index detector and a UV-975 UV-vis-detector. The measurements were carried out in water as solvent with 0.1% TFA and 0.05M

NaCl at a flow rate of 1 mL min^{-1} on a PSS SUPREMA-MAX guard/300 Å column at 30°C. The system was calibrated with poly(2-vinyl pyridine) (1 300 - 81 900 g mol^{-1}) standards.

Dynamic Light Scattering (DLS): DLS measurements were performed using an ALV laser CGS3 Goniometer equipped with a 633 nm HeNe Laser at 25 °C and at a detection angle of 90 °. The CONTIN analysis of the obtained correlation functions was performed using the ALV 7002 FAST Correlator Software. Samples were measured at a typical concentration of 0.1 g L^{-1}.

Zeta-Potential Measurements: The samples for the zeta-potential measurements were prepared by titration of a 1 g L^{-1} solution of the investigates material in 0.1N HCl with 0.1N NaOH. For the titration and pH detection, a Metrohm 765 Dosimat titrator with a Greisinger electronic GMH3539 digital pH-/mV-electrode with thermometer was used. 1 mL samples for the measurements were taken at the desired pH-values. The ζ-potentials were measured using a Zetasizer Nano ZS from Malvern *via* M3-PALS technique with a He-Ne laser operating at 633 nm. The detection angle was 13°. The electrophoretic mobilities (u) were converted into ζ-potentials *via* the Smoluchowski equation:

$$\zeta = \frac{u\eta}{\varepsilon}$$

where η denotes the viscosity and ε the permittivity of the solution.

UV-Vis Spectroscopy: UV/Vis absorption spectra were recorded with an Agilent Technologies Cary 60 UV-Vis in Suprasil quartz glass cuvettes 104-QS (Hellma Analytics) with a thickness of 10 mm. The temperature during the measurements was controlled by a Agilent Technology SINGLE CELL PELTIER ACCESSORY CARY thermostat. The UV-Vis samples were prepared from a stock solution (4 mg mL^{-1}) of the desired polymer in water and stock solutions of the salts (0.3 mol L^{-1}). For the measurements under basic conditions, NaOH was added weighed as solid or as 0.25 M solution. The pH value was detected by using a Hanna Instruments HI98103 Checker® pH Tester. UV-Vis sedimentation experiments were conducted at 860 nm at a concentration of 0.1 g L^{-1}.

TGA: TGA measurements were carried out under air on a PerkinElmer Thermogravimetric Analyzer TGA 800 equipped with a PerkinElmer FT-IR / NIR Spectrometer Frontier and a PerkinElmer TG-IR-GCMS Interface. Typical samples were measured in a temperature range of 300- 850 °C, 10 K/min.

TEM: For TEM from aqueous dispersions, copper grids were rendered hydrophilic by Ar plasma cleaning for 30 s (Diener electronics). 15 µL of the respective sample dispersion were applied to the grid and excess sample was blotted with a filter paper. TEM images were acquired with a200 kVFEI Tecnai G^2 20 equipped with a 4k x 4k Eagle HS CCD and a 1k x 1k Olympus MegaView camera for overview images. Typical sample concentrations were 0.1 g L^{-1}

Magnets: NdFeB magnets were purchased from Magnets4you GmbH.

Ultra-sonication:

Ultra-sonication was performed using an ElmaSonic S30H ultrasonic unit.

MALDI-ToF-MS: MALDI-TOF mass spectra were recorded using a Autoflex III mass spectrometer (Bruker Daltonik GmbH, Bremen, Germany) in the linear mode using an acceleration voltage of 20 kV. Sample spots were prepared by dropping premixed sample/matrix solutions (10/50 v/v) containing analyte (2 mg mL-1) and trans-2-[3-(4-tert-Butylphenyl)-2-methyl-2-propenylidene]malononitrile (DCTB) 10 mg mL-1) as matrix on a stainless steel traget. For one spectrum 2000 Laser shots were accumulated at four different sample spot positions.

In vitro Cell Viability Assay

For viability assays nanoparticles were dissolved in *aqua bidest.* (4mg/ml), treated with ultrasound for 60 min and stored at 4 °C.

Cytotoxic effects were investigated with a cell culture-based viability assay using SYTOX® Red Dead Cell Stain and subsequent analysis by flow cytometry. Human brain microvascular endothelial cells (HBMEC) were cultured in RPMI 1640 (Life Technologies) supplemented with 10% fetal bovine serum (FBS, Biochrom-Seromed) at 37°C and 5% CO_2 in a humidified atmosphere. Initially, $1x10^7$ cells were stained in 7ml serum-free RPMI 1640 supplied with 10µM CellTracker™ Green BODIPY® Dye (Thermo Fisher Scientific) for 30 min at 37°C. Stained cells were pelleted by centrifugation (5 min, 300 rcf) and resuspended in fresh RPMI 1640 supplemented with 10% FBS, 100 U/ml penicillin/0.1 mg/ml streptomycin (Life Technologies). 60,000 cells/cm^2 were seeded into 12-well plates in duplicate and cultured overnight. Nanoparticles were added in a concentration range of 5 µg/cm^2 to 100 µg/cm^2 corresponding to 18.9 ng/µl and 377.9 ng/µl respectively and incubated for 3 h or 24 h. Negative controls were treated with *aqua bidest.*. When incubation time was complete, incubation medium was collected, cells were harvested using HyQtase (GE Healthcare Life Sciences) and centrifuged for 5 min at 300 rcf, 4°C. After two washing steps with ice-cold PBS/2mM EDTA (PE), cell pellets were stained in 300 µl 2.5 nM SYTOX® Read Dead Cell Stain (Thermo Fisher Scientific) for 20 min at 4°C. Samples were immediately analyzed with the FACSCalibur cytometer (BD Biosciences) with 10,000 events per sample. Nanoparticle-derived events were excluded from data acquisition and analysis based on gating of cellular CellTracker™ green positive stain. Data analysis was performed with the FlowJo software (FlowJo LLC).

Statistics

Data of independent experiments with multiple determinations are presented as mean ± standard deviation. In order to test statistical significance a one-way analysis of variance (ANOVA) followed by Dunnett’s multiple comparison test comparing the means of distinct incubation conditions was used (Prism 6, GraphPad Software). Differences are considered to be statistically significant for $p < 0.05$.

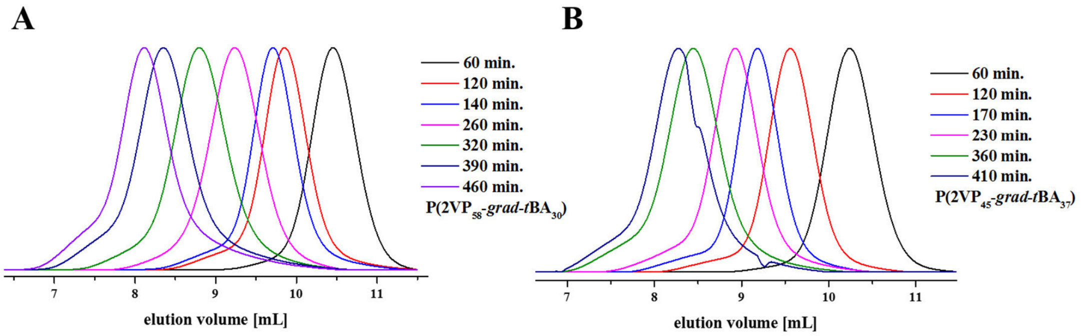

Figure S1: SEC-traces of polymerization procedure of (A) P(2VP$_{58}$-*grad*-*t*BA$_{30}$) and (B) P(2VP$_{45}$-*grad*-*t*BA$_{37}$). CHCl$_3$/TEA/i-PrOH; 94/4/2.

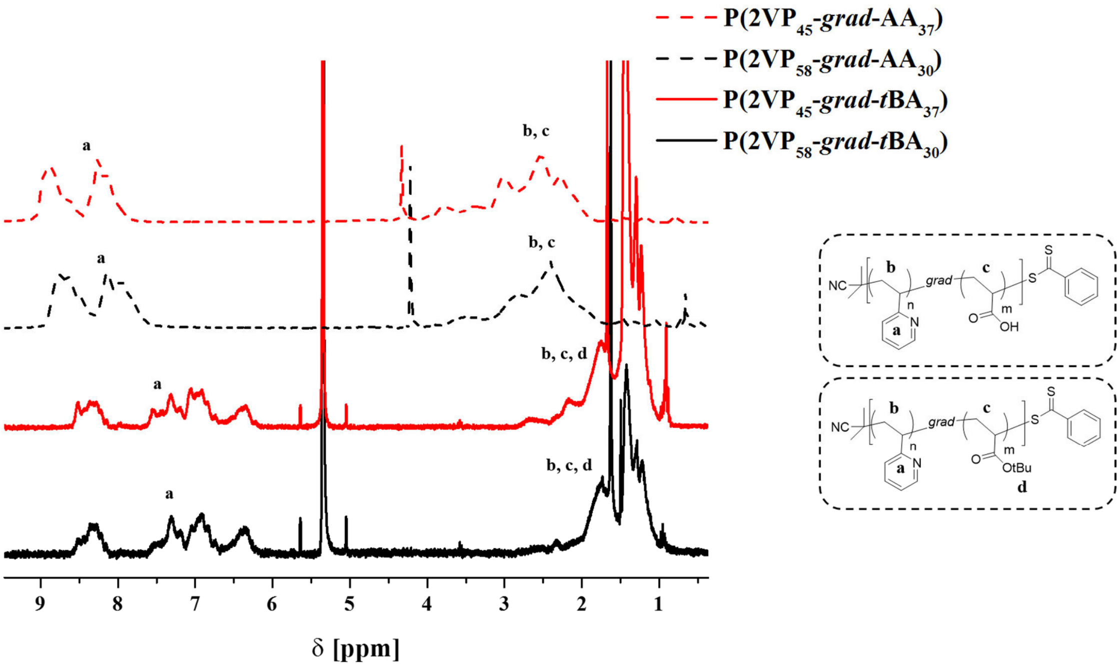

Figure S2: ^{1}H-NMR of P(2VP$_{58}$-*grad*-*t*BA$_{30}$) (black line CD$_2$Cl$_2$), P(2VP$_{45}$-*grad*-*t*BA$_{37}$) (red line CD$_2$Cl$_2$), P(2VP$_{58}$-*grad*-AA$_{30}$) (black dashed *d*-TFA), P(2VP$_{45}$-*grad*-AA$_{37}$) (red dashed *d*-TFA).

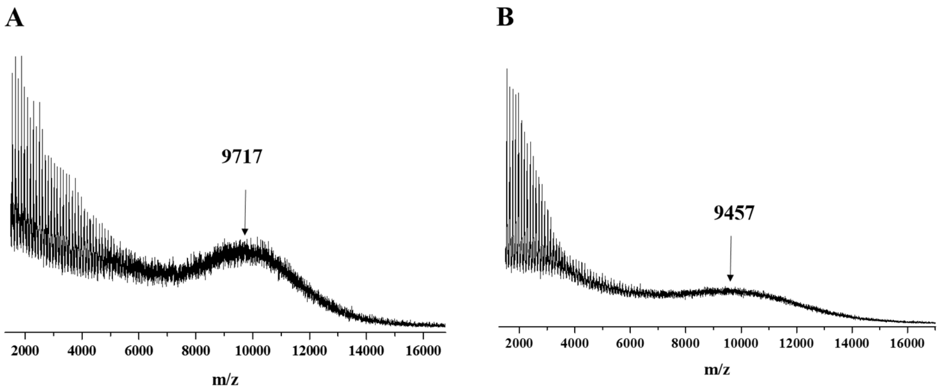

Figure S3: MALDI-ToF-MS in DCTB of A) P(2VP$_{58}$-*grad*-*t*BA$_{30}$) and (B) P(2VP$_{45}$-*grad*-*t*BA$_{37}$).

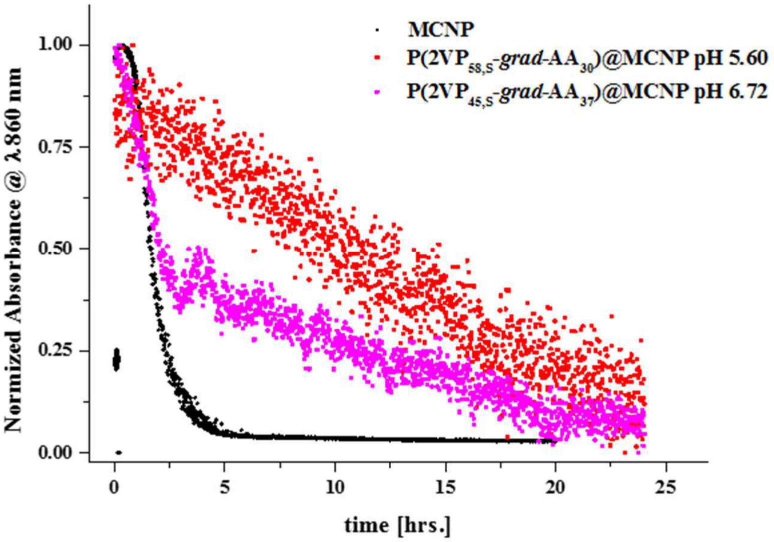

Figure S4: Sedimentation measurements of MCNP, P(2VP$_{58,S}$-grad-AA$_{30}$)@MCNP and P(2VP$_{45,S}$-grad-AA$_{37}$)@MCNP at pH 6.72 and 5.60, respectively.

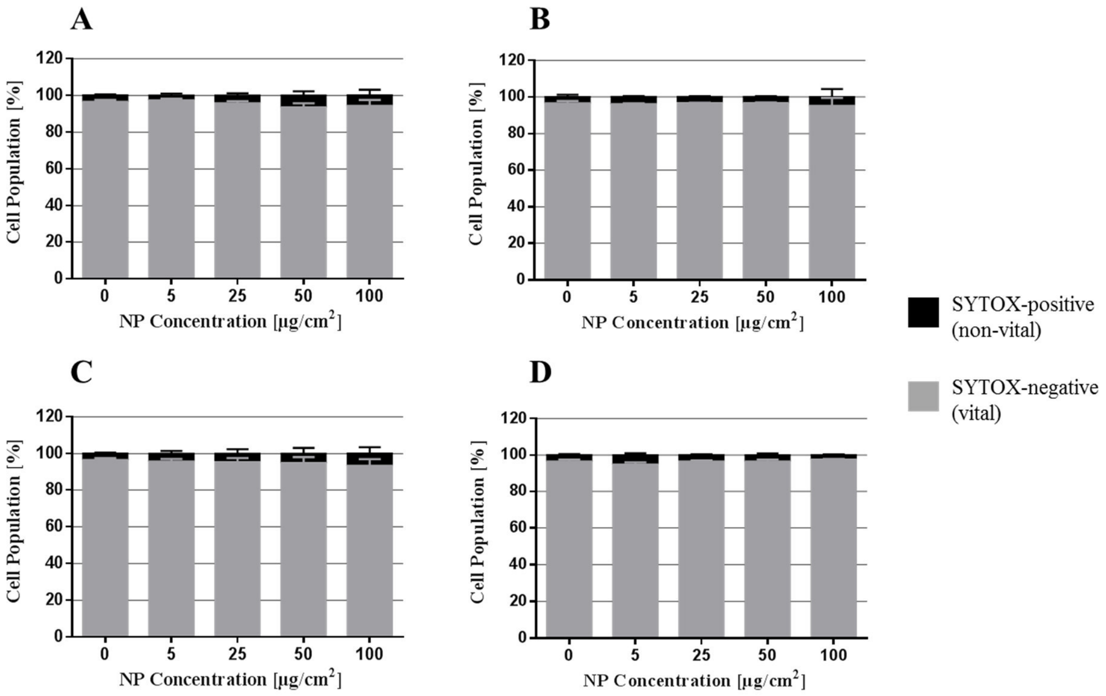

Figure S5: SYTOX® Red Dead Cell viability assay of HBMEC incubated with P(2VP$_{58,S}$-*grad*-AA$_{30}$)@MCNP and P(2VP$_{45,S}$-*grad*-AA$_{37}$)@MCNP for 3 and 24h. HBMEC were stained with CellTracker™ green BODIPY® (10µM) prior to seeding of 60,000 cells/cm^2 into 12 well plates. Cells were incubated with P(2VP$_{58,S}$-*grad*-AA$_{30}$)@MCNP for 3h (A) and 24h (B) or P(2VP$_{45,S}$-*grad*-AA$_{37}$)@MCNP for 3 (C) and 24h (D). Negative controls were incubated with *aqua bidest.*. Collected incubation medium and harvested cells were stained with SYTOX® Red Dead Cell Stain (2.5nM) and analyzed by flow cytometry. Presented data are means+standard deviation of three independent experiments.

References:

[1] S. Dutz, J. H. Clement, D. Eberbeck, T. Gelbrich, R. Hergt, R. Müller, J. Wotschadlo, M. Zeisberger, *"Ferrofluids of Magnetic Multicore Nanoparticles for Biomedical Applications"*, *J. Magn. Magn. Mater.* **2009**, *321*, 1501-1504.

Publication P2

"Synthesis, Characterization, and Applications of Magnetic Nanoparticles Featuring Polyzwitterionic Coatings"

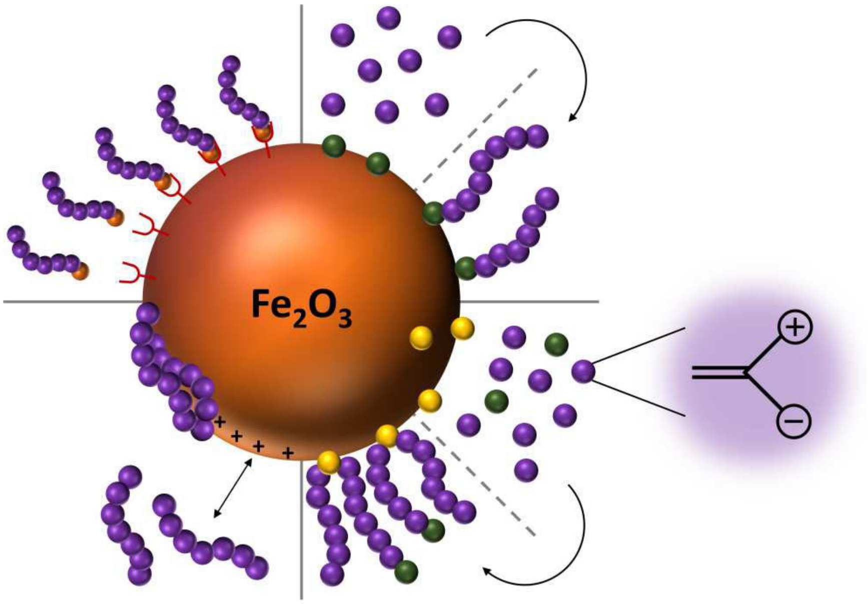

P. Biehl,[‡] M. von der Lühe,[‡] S. Dutz, F. Schacher

[‡]Both authors contributed equally to this work.

Polymers **2018**, *10*, 91.

polymers

Review

Synthesis, Characterization, and Applications of Magnetic Nanoparticles Featuring Polyzwitterionic Coatings

Philip Biehl [1,2], Moritz von der Lühe [1,2], Silvio Dutz [3,*] and Felix H. Schacher [1,2,*]

[1] Institute of Organic and Macromolecular Chemistry (IOMC), Friedrich Schiller University Jena, Humboldtstraße 10, 07743 Jena, Germany; philip.biehl@uni-jena.de (P.B.); moritz.von-der-luehe@uni-jena.de (M.v.d.L.)
[2] Jena Center for Soft Matter (JCSM), Friedrich Schiller University Jena, Philosophenweg 7, 07743 Jena, Germany
[3] Institute of Biomedical Engineering and Informatics, Technische Universität Ilmenau, 98693 Ilmenau, Germany
* Correspondence: silvio.dutz@tu-ilmenau.de (S.D.); felix.schacher@uni-jena.de (F.H.S.)

Received: 30 November 2017; Accepted: 12 January 2018; Published: 18 January 2018

Abstract: Throughout the last decades, magnetic nanoparticles (MNP) have gained tremendous interest in different fields of applications like biomedicine (e.g., magnetic resonance imaging (MRI), drug delivery, hyperthermia), but also more technical applications (e.g., catalysis, waste water treatment) have been pursued. Different surfactants and polymers are extensively used for surface coating of MNP to passivate the surface and avoid or decrease agglomeration, decrease or modulate biomolecule absorption, and in most cases increase dispersion stability. For this purpose, electrostatic or steric repulsion can be exploited and, in that regard, surface charge is the most important (hybrid) particle property. Therefore, polyelectrolytes are of great interest for nanoparticle coating, as they are able to stabilize the particles in dispersion by electrostatic repulsion due to their high charge densities. In this review article, we focus on polyzwitterions as a subclass of polyelectrolytes and their use as coating materials for MNP. In the context of biomedical applications, polyzwitterions are widely used as they exhibit antifouling properties and thus can lead to minimized protein adsorption and also long circulation times.

Keywords: hybrid materials; magnetic nanoparticles; polyzwitterions; polyampholytes

---

1. Introduction and Scope

For decades, magnetic nanoparticles (MNP) have been in focus within a range of scientific disciplines as they show high potential in a variety of different application fields, ranging from chemistry, biology, medicine to physics. One unifying aspect herein are surface properties of such nanomaterials. To date, there have been several reviews focusing on surface modifications of nanomaterials with polyelectrolytes, and most of them have focused on biomedical applications of these materials [1–7]. However, to our knowledge the only example specifically focusing on zwitterionic coating materials for nanomaterials was written by García et al. and here the central aspect is the behavior under in vivo conditions [4]. Within this review article, we therefore focus on the preparation and characterization of MNP featuring zwitterionic coating materials as they open up an interesting area of bio-repellent, pH responsive, and dispersion-stable hybrid materials. The magnetic core enables the selective separation of these particles for analytical issues and external magnetic fields can be used for biomedical applications like hyperthermia and drug targeting. This review aims to serve as a guide for various synthetic strategies for immobilizing polyzwitterions at the surface of magnetic nanoparticles which have been explored during the last decade and is structured as follows: we begin with a section on different magnetic core materials, followed by the synthesis of polyzwitterions, suitable methods for nanoparticle coating, and finally we discuss important characterization methods for such hybrid materials. Throughout the different chapters, we also showcase potential application fields.

2. The Core: Materials for Magnetic Nanoparticles

All chemical elements or compounds of our planet show under certain conditions different magnetic effects. Since we focus herein on magnetic nanoparticles for medical and technical applications, we concentrate on materials with ferro- or ferrimagnetic, superparamagnetic, and superferrimagnetic behavior at room temperature. In that regard, three classes of materials exist.

Metals—The only metallic elements showing ferromagnetism at room temperature are iron, cobalt, and nickel. The preparation of nanoparticles hereof is possible and such materials show promising magnetic behavior for medical applications [8–13]. Since such nanoparticles show a strong oxidation tendency to non-magnetic oxides (e.g., antiferromagnetic FeO, CoO, NiO), an oxidation-protective layer is necessary. Due to this fact, and also the toxicity of Ni and Co, metallic nanoparticles play only a minor role regarding their applications in medicine [14].

Alloys—The second group of ferromagnetic materials are the ferromagnetic alloys, e.g., CoPt, FePt, FeNi, or FeCo. The preparation of magnetic nanoparticles consisting of ferromagnetic alloys is described in the literature by several groups [15–17]. Up to now, none of those nanostructures has found access in medical applications mainly due to two facts: First, some of the ferromagnetic alloys (e.g., AlNiCo, CoPt, FeCoCr) show a hard-magnetic behavior (a remnant magnetization and coercivity), leading to potential agglomeration of the particles due to the remanence, and exposing the patient to the risk of vessel embolism. Second, most of the alloys with promising magnetic behavior contain toxic components (e.g., Ni or Co) which inhibit the application of such materials in the human body.

Oxides—The group of magnetic oxide materials can be divided into mixed oxides with different crystal structures (e.g., the magnetic garnets and the ferrites) as well as the pure metallic oxides. Since the saturation magnetization of all garnets is very low, these materials are not suitable for application in medicine. Depending on their composition, the ferrites show soft- or hard-magnetic behavior. Despite some groups having found promising magnetic properties of soft-magnetic ferrites for certain medical applications only very few studies can be found in the literature [18–21]. Representative hard-magnetic ferrites with promising magnetic behavior for medical application are barium-, strontium- or cobalt-ferrite. Since cobalt-ferrite ($CoFe_2O_4$) shows less toxic effects than Ba-or Sr-ferrite, nanoparticles of this material find increasing application for medical purposes, e.g., for magnetic hyperthermia as minimal invasive tumor treatment and for lab-on-a-chip applications in diagnostics [22–24]. The promising magnetic properties of cobalt-ferrite can be tuned by variation of the Co/Fe-ratio and thus this material will play a major role in the future in our opinion. As Ni and Co form no oxides showing ferromagnetism at room temperature, only iron has to be considered in this case. Here, mainly four different oxides have to be mentioned: iron(III) oxide (Fe_2O_3) and iron(II,III) oxide (Fe_3O_4), as well as the rather unstable iron(II) oxide (FeO) and iron(I) oxide (Fe_2O). From Fe_2O_3 several phases exist, e.g., α-, β-, γ-, or ε-Fe_2O_3, which all show different magnetic behavior. Of the iron oxides only maghemite (γ-Fe_2O_3) and magnetite (Fe_3O_4) show ferromagnetic behavior or, more precisely, ferrimagnetism due to the spinell structure (a subtype of the cubic lattice). A comprehensive work on the nature of iron oxides and their properties is given by Schwertmann [25].

The preparation of iron oxide magnetic nanoparticles was described by Khallafalla [26] and Massart [27] in 1980 for the first time. After that, a lot of different preparation routes were developed and such MNP show promising magnetic properties for different biomedical applications [28,29].

2.1. Magnetic Properties of Magnetic Nanoparticles

Beside other parameters like magnetic anisotropy or shape, the magnetic behavior of magnetic particles is determined by the particle size. For macroscopic particles in the size range of µm and above, several areas of homogeneous magnetization are formed. These so-called magnetic domains are separated by Bloch walls [30,31]. Due to this domain formation, the magnetic stray field of the particle is minimized and the domain formation in the absence of an external magnetic field is energetically favorable [32] compared to a homogeneously magnetized particle. The magnetization directions of all domains in the particle are statistically oriented, which leads to a compensation of all magnetic moments within the particle, resulting in no external magnetization of the particle without an external magnetic field.

With decreasing dimensions of the magnetic particle, the relative proportion of wall energy to that of the entire particle energy increases. Due to energetic reasons, no magnetic domains are formed below a critical particle size and the whole particle shows a spontaneous magnetization in one direction. The direction of the magnetization of these so-called single domain particles is determined by the crystal lattice of the particle and is named "the easy axis". The critical size for the formation of single domain particles is given by the material specific magnetic anisotropy K and the form factor (ratio of particle length in different directions related to the magnetic field) of the particle [33]. For cubic and spherical particles made of magnetite, the theoretical upper limit for the formation single domain particles is about 80 nm [34,35], which was confirmed experimentally by Dutz et al. [36].

A further decrease of the particle size leads to a decrease of the magnetic anisotropy energy of the particles. In this case a certain probability exists, that for finite temperatures the thermal energy exceeds the anisotropy energy due to thermic variations and the particle spontaneously changes the orientation of magnetization [37]. This leads to a thermally induced temporal attenuation (relaxation) of the remnant magnetization M_R following Equation (1):

$$M_R(t) = M_R(t = 0) \times e^{-t/\tau N} \tag{1}$$

The so-called Neel relaxation time τ_N, after which M_R reaches a value close to zero, can be estimated from the ratio of the anisotropy energy ($K \times V$) to the thermal energy ($k \times T$) with the Boltzmann constant k and the temperature T following Equation (2) where τ_0 is the minimum natural relaxation time of 10^{-9} s:

$$\tau_N = \tau_0 \times e^{(K \times V)/(k \times T)} \tag{2}$$

Hence, the magnetic behavior of very small particles depends strongly on the relation of measurement time t_M and Neel relaxation time τ_N. If $t_M << \tau_N$, there is not enough time for relaxation processes and the particles show a stable hysteretic behavior. If $t_M > \tau_N$, the Neel relaxation occurs, leading to attenuation of M_R and thus no coercivity can be observed. This phenomenon is called superparamagnetism. Superparamagnetic particles show no coercivity and remnant magnetization in quasi-static measurements (e.g., vibrating sample magnetometry) but a pronounced hysteresis when exposed to a high frequency alternating magnetic field. In other words, for predetermined magnetic field parameters (frequency and field strength), it depends on the particle size whether the particles show any hysteresis or not.

A special case of magnetism can occur if small superparamagnetic particles form a larger cluster. In the absence of an external magnetic field these clusters show superparamagnetic behavior with no remnant magnetization or coercivity. If the particles are exposed to an external field, depending on the strength of the particle interactions, a collective magnetism may result and the clusters show ferrimagnetic behavior with an observable hysteresis. This so-called superferrimagnetism is typical for magnetic multicore particles [38–40] and such particles show very promising properties for medical applications [38,41–43].

From the considerations above it becomes obvious, that the particle size plays a crucial role for the magnetic behavior of magnetic nanoparticles. Besides the size, also the size distribution is an important factor for the resulting magnetic properties, which will not be treated in detail in this review. Detailed discussions on the theory of size distribution influence can be found by Hergt et al. [44] whereas Müller et al. showed the influence in experiments [45].

2.2. Preparation of Magnetic Nanoparticles

The following section briefly covers the main preparation routes for magnetic nanoparticles. Detailed information can be found in excellent reviews on this topic [46–49]. Magnetic nanoparticles are obtained by three different preparation routes.

(i) biomineralization
(ii) physical methods
(iii) chemical methods

(i) By means of *biomineralization* some living organisms prepare magnetic particles for use for their sense of direction [50]. For example, magnetotactic bacteria are capable of preparing magnetosomes (protein coated nanosized crystals of magnetic iron oxide). The bacteria use the particles as a compass to find their preferred habitat in anaerobic areas at the bottom of the sea [51]. Under anaerobic synthesis conditions in the lab, which are similar to the conditions of their habitat, uniform particles of 20 to 45 nm core diameter may be produced [52–54]. Despite the fact that magnetosomes show excellent magnetic properties for medical application (especially hyperthermia) [55,56], they have found no application in medicine until now due to their bacterial protein coating. Current recent research on magnetosomes focuses on elucidation and optimization of the biomineralization process [57,58] with the aim to develop wet chemical preparation routines which emulate the biologic process, thus providing MNP with similar magnetic behavior.
(ii) The *physical methods* can be divided into "top down" and "bottom up" procedures. Top down methods are based on the size reduction of macroscopic magnetic materials to the nanometer range, e.g., by means of milling. A major drawback of these methods is the difficulty of adjusting the desired particle size and shape [59]. Furthermore, the milling procedure leads to lattice defects that cause deviations in the magnetic properties compared to regular particles of the same size [60]. Bottom up methods use the condensation of nanoparticles from either a liquid or gaseous phase. A promising bottom up method for the synthesis of MNP powders is laser evaporation. Starting materials are coarse metal oxide powders of a few µm sized particles, which are evaporated by means of a laser. As a result of the steep temperature gradient outside of the evaporation zone, a very fast condensation and nucleation takes place from the gas phase and nanoparticles are formed [61,62].The resulting mean particle sizes (20 to 50 nm) and magnetic phase are tuned by laser power and composition of the atmosphere in the evaporation chamber [63].
(iii) The *chemical methods* provide a multitude of different bottom up synthesis routes for the preparation of MNP, from which the most prominent will be described shortly.

The *co-precipitation* synthesis procedure is a very simple method for the preparation of MNP. Most scientific work uses aqueous media for precipitation. Very often, the magnetic iron oxides are prepared by means of a co-precipitation from aqueous Fe^{2+} and Fe^{3+} salt solutions, to which a base is added. Magnetic phase and particle size can be tuned by variation of iron salts, Fe^{2+}/Fe^{3+} ratio, temperature, pH, and the type of base used. Pioneering work on this preparation route was performed by Khallafalla and Reimers [26] and Massart [27]. For this method, particles are in the superparamagnetic size range from 5 to 15 nm and the obtained size distribution is relatively broad. By varying the reaction conditions, the size can be increased to up to 40 nm. In this size range, the particles show single domain ferrimagnetic behavior. Different modifications of this method were reported over recent years. Upon applying high pressure homogenization during precipitation [64] or using slower reaction conditions [39], superferrimagnetic clusters of single crystals of 10 to 15 nm are formed, which show very promising magnetic properties for medical applications [42,65]. Furthermore, size control of the resulting magnetite nanoparticles could also be shown by reactions carried out at high temperatures [66]. Co-precipitation is also used for the preparation of ferrites, e.g., cobalt ferrite by replacing a part of the Fe^{2+} by Co^{2+} in the starting solutions [67].

The *thermal decomposition* of organometallic compounds (non-magnetic precursors) in boiling organic solvents is another promising way for MNP preparation and the resulting particles show a very narrow size distribution. Usually iron carbonyls or iron acetylacetonates are used as non-magnetic precursors and oleic acid or fatty acids serve as surfactants. By variation of the proportion of precursors to the starting agents (surfactants and solvents), the size and morphology of the resulting particles can be controlled. Thermal decomposition of non-magnetic precursors leads to pure iron (metal). Afterwards, in a further step these metal particles are oxidized to iron oxide by mild heating under oxidative conditions. A simple one-step route to prepare magnetite particles is given by the thermal decomposition of precursors with cationic iron centers (e.g., $Fe(acac)_3$). Pioneering work in the preparation of iron oxide by thermal decomposition was performed by Hyeon et al. [68] and Park et al. [69] who prepared nearly monodisperse particles of about 13 nm. The well-known method of Hyeon and Park was modified by several groups and MNP in size of up to 30 nm with nearly monodisperse size distribution were obtained.

Micro-emulsion synthesis is a two-phase method for the production of nearly monodisperse MNP. For this purpose, a water-in-oil microemulsion is prepared by dispersion of nanosized water droplets (10–50 nm) in an oil phase, stabilized by surfactant molecules at the water/oil interface [70]. Since these droplets are used as micro-reaction vessels, the distance for diffusion and thus the nucleation and growth of particles is limited, which results in very uniform particles [71]. Due to their narrow size distribution, MNP from the microemulsion synthesis show magnetic properties promising for medical applications [72].

Hydrothermal synthesis performed in aqueous media at temperatures above 200 °C is realized in autoclaves at pressures above 2000 psi. This route exploits the ability of water to hydrolyze and dehydrate metal salts at high temperatures. Due to the low solubility of the obtained metal oxide particles in water at such temperatures [73,74], a precipitation takes place and by variation of concentration, temperature, and autoclaving time, particle size and morphology can be controlled [75,76]. Longer autoclaving time leads to increasing particle size, but also broader size distributions. Sizes typically are in the range from 10 to 50 nm and for short autoclaving times, monodisperse particles can be obtained [76].

The *polyol synthesis* bases on the oxidative alkaline hydrolysis of Fe^{2+} and Fe^{3+} salts in a polyol mixture (e.g., poly(ethylene glycol) (PEG)/diethylene glycol or *N*-methyldiethanolamine). Size and structure of the resulting MNP can be tuned by either reaction conditions or the employed solvents [77]. Despite the fact that the particles are not monodisperse in size, they show interesting magnetic behavior for application in hyperthermia due to their special morphology. So called "flower-shaped MNP" can be synthesized by this procedure under certain reaction conditions [77] which show excellent heating performance for hyperthermia [43]. Similar to co-precipitated clusters, these particles exhibit a multicore structure and consist of single cores of about 8 to 10 nm. These cores form clusters of about 30 nm and show very promising properties for hyperthermia as shown before [42].

Other preparation routes for magnetic nanoparticles, which are not demonstrated here in this article because the resulting particles are not of high interest for medical applications, are Glass Crystallization [78], Spray and Laser Pyrolysis [79], Sonolysis [48,79], Microwave Irradiation Synthesis [79], and Sol-gel Reactions [80].

2.3. Recent Developments in the Synthesis of Magnetic Nanoparticles

Over the past 10 years, the major aim of magnetic nanoparticle preparation was to develop strategies for a versatile and robust protocol for the synthesis of tailor-made samples. Due to the high diversity of the required magnetic properties of the particles for the different applications outlined above and below, several structural parameters (e.g., size and size distribution) have to be tuned. For example, medical applications benefit in three ways from magnetic particles. First, magnetic particles can be manipulated mechanically by an external magnetic field (gradient), resulting in a rotation or attraction of the MNP which can find application in magnetic drug targeting [81,82]. Second, due to their magnetic moment, MNP are a source of a magnetic stray field, which can be detected by appropriate sensors and might find application in medical imaging [83]. Finally, if MNP are exposed to an alternating magnetic field, the particles are heated up due to reversal magnetization losses and the generated heat can be used for therapeutical applications, e.g., hyperthermia as an example for minimal invasive cancer therapy [28,84].

To obtain MNP which show promising magnetic behavior for mechanical manipulation, MNP with a high magnetic moment are needed and quite often this is translated into a large particle volume. Several groups obtained different strategies for the preparation of so called large single domain particles (LSDP) [85–90]. Despite the fact that the steric stabilization of such large particles is challenging (due to the strong tendency to form agglomerates) sedimentation stable dispersions of large single domain particles exist [86,91]. A possible solution for the challenging stabilization of LSDP is the use of Co-ferrites. They show magnetic properties similar to that of LSDP but much smaller diameters of about 10 to 15 nm [92], which enable sufficient steric stabilization.

The ideal MNP for application in medical imaging need a magnetic behavior, which is described by a high initial susceptibility. The preparation of such particles is challenging since the size of the particles has to be exactly adjusted and the particles need a very narrow size distribution. Usually the thermal decomposition method is the most promising way for the preparation of such particles. Krishnan et al. prepared particles of 25 nm size which exhibited a very narrow size distribution, and so far showed the best performance for magnetic particle imaging [93]. Similar preparation routes to obtain MNP of well-defined size and narrow size distribution are described by other groups in the literature.

For magnetic heating applications (medical or technical) the MNP have to be optimized in a way that reversal magnetization losses are as high as possible for given magnetic field parameters. To reach this aim several strategies exist. For the application of relatively low magnetic fields (<10 kA/m), small MNP with a size of about 10 nm and resulting superparamagnetic behavior are the most promising candidates, which mostly consist of iron oxide. If higher magnetic fields (10 to 30 kA/m) are acceptable, larger ferrimagnetic particles show much better heating performance than superparamagnetic examples. This is due to different mechanisms of internal reversal of magnetization in ferrimagnetic and superparamagnetic samples by means of hysteresis or Neel relaxation, respectively. Such magnetic behavior can be obtained from single-domain iron oxide particles with larger diameter as described above as LSDP for drug targeting or by Co-ferrites which combine a small particle diameter with a defined hysteretic behavior [22]. Also for heating applications, the particle size distribution plays a crucial role in obtaining the ideal heating performance. Usually a narrow size distribution is preferred but for some combinations of particle size, magnetic field frequency, and strength a higher heating performance also for MNP featuring a broader size distribution has been reported [45,94].

Over the past years two different particle types were developed which show a magnetic behavior that cannot be achieved by the classical single-core particles. One example is again the so called superferrimagnetic multicore-particles. This particle type consist of primary cores in the range of 10 nm with superparamagnetic behavior which form clusters of about 50 nm or larger [39,41,43,95]. Due to the statistical orientation of the easy axis of the single cores within the clusters, the resulting magnetization without any external field is relatively low in comparison to single core particles of comparable size. Due to this fact these large particles show a relatively weak remnant magnetization and also only a very low agglomeration tendency. Therefore, such particles are relatively stable against sedimentation, which is a general requirement for medical applications. If these particles are exposed to an external magnetic field, the clusters show a coercivity higher than that observed for the size of the constituting primary particles but lower than reported for single-domain particles in the size regime of the clusters. Up to now there is no existing theory capable of completely describing the magnetic behavior of these particles, but experimental investigations revealed promising results in different application areas [38,41,43]. Exchange-coupled magnetic nanoparticles are the second novel particle type [96,97]. These particles benefit from the exchange coupling between a magnetically hard core (e.g., Co-ferrite) and a magnetically soft shell (e.g., Mn-ferrite). This interaction enables tuning of the magnetic properties of the nanoparticle and the maximization of the reversal magnetization losses, which renders these particles very interesting for heating applications [96,98,99]. Typically, at first the hard magnetic core is prepared and then the soft magnetic shell is deposited on the core surface. By changing the material combinations and ratio of core and shell size the resulting magnetic properties can be tuned.

3. The Shell: Polyzwitterions

In the field of polyelectrolytes, polyzwitterions have gained significant interest over recent years due to their tunability concerning charge density, net charge, and as anti-fouling coatings of different surfaces. Polyzwitterions are defined by IUPAC as polyelectrolytes that, unlike polyampholytes, carry both cationic and anionic groups in every repeating unit [100]. Nevertheless, in the literature the term polyzwitterion is sometimes mixed up with that of polyampholytes (Figure 1). In this review, we focus on polyzwitterionic materials as coatings on magnetic nanoparticles.

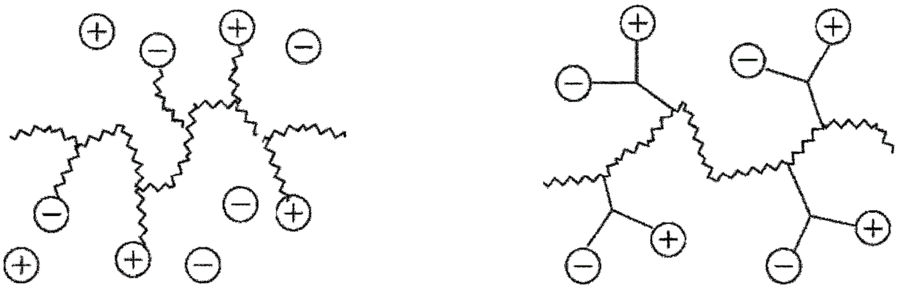

Figure 1. Polyampholyte (**left**) bearing both negative and positive charges statistically distributed along the polymer backbone, and (**right**) polyzwitterion, bearing both charges in every repeating unit. Reprinted from [101].

As mentioned above, polyzwitterions are of great interest as coating materials especially for biomedical applications, as they are reported to inhibit non-specific protein adsorption [102,103]. For example, betaines like poly(carboxybetaine acrylamide) (pCBAA) [104], poly(sulfobetaine methacrylate) (pSBMA) [105], or poly(carboxybetaine methacrylate) (pCBMA) [106] show ultralow biofouling, which was attributed to their strong hydration capacity caused by electrostatic interactions between the zwitterionic moieties and water [107]. Furthermore, the attachment of polyzwitterions onto MNPs is not accompanied by a huge increase in their hydrodynamic radii, which is of great interest as a specific size between 30 and 200 nm is targeted for MNPs to achieve longer circulation times [108], and ideal properties for passive accumulation within tumor tissue [109]. At the moment, poly(ethylene glycol) (PEG) is still the most commonly used polymeric coating if the minimization of unspecific protein adsorption is targeted [110,111], with the major drawback that these systems tend to undergo oxidative degradation. Additionally, these polyether compounds exhibit the so-called "stealth" effect preventing a response of the immune system [112]. In contrast to this, zwitterionic moieties are often found in biological systems as is the case for different phospholipids, which build up the main component of biomembranes [113], featuring zwitterionic, hydrophilic head groups (phosphatidyl-cholin, -Ethanolamin, -Serin) and enzymes which consist of polypeptides. Compared to other polyions, polyzwitterions exhibit long circulation times [114–116], whereas polycations usually show unspecific and fast binding to cell membranes and might cause cytotoxic side effects [117].

Nevertheless, binding to cell membranes is in general possible also possible for polyzwitterions without the challenge of overcoming repulsive forces from the (in general) negatively charged cell surface.

The given definition of polyzwitterions as polyelectrolytes, which carry both anionic and cationic functionalities in every repeating unit still allows several possibilities for the implementation of the respective functional groups in the polymer structure (Figure 2). Different synthetic routes to obtain polyzwitterions are discussed in the following chapter. A detailed discussion on the various possibilities and synthetic routes can be found in an excellent recent review [101].

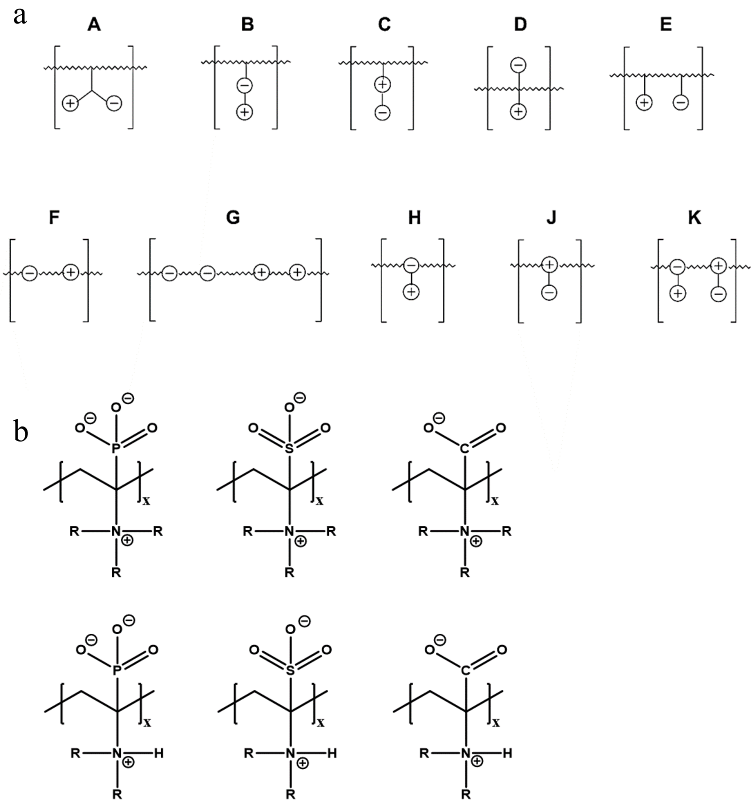

Figure 2. (**a**) Different arrangements of the functional groups in polyzwitterionic chains, reprinted from [101], and (**b**) commonly employed zwitterionic repeating units in polymeric materials.

It has been discussed that the implementation of zwitterionic moieties in the side chains (A–D) is often easier than directly within the polymer backbone (E–K). Along the same lines, the functionalization of cationic groups such as ammonium moieties is usually more straightforward if compared to the anionic counterparts, concluding that structure C is the most common polyzwitterion structure found in the literature today. The high amount of ionic groups per monomer unit results in rather high charge densities, whereas the net charge of polyzwitterions remains low over a wide pH range (depending on the nature of the ionic groups) due to the stoichiometric presence of oppositely charged groups. Besides the arrangement of the charged functionalities, their chemical design has a major influence on the properties of the resulting material. For cationic groups, most examples reported rely on amines or their quaternized ammonium analogues. Whilst the charge density of the primary amine depends on the pH value of the surrounding medium, upon quaternization these groups are permanently charged. For negative charges, the employed variety of functional groups is broader. Most common are carboxylates, sulfonates, and phosphates [118–121], less common examples are phosphonates [122–124], phosphinates [123], boronates [125] or sulfonamides [126]. Since sulfuric acids commonly show pKa values <1, the charge density of sulfonates does not depend on the pH (in the range of 1–14), whereas phosphates (pKa = around 2) and carboxylates (pKa between 1 and 5) show pH-dependent charge characteristics (degrees of neutralization). Different combinations of the above mentioned weak and strong functional groups lead to four possible categories of polyzwitterions with the combinations of cation/anion: weak/weak (e.g., primary amine/carboxylic acid), weak/strong (e.g., primary amine/sulfonic acid), strong/weak (e.g., quaternized amine/carboxylic acid), and strong/strong (e.g., quaternized amine/sulfonic acid).

4. Coating of Magnetic Nanoparticles

In general, coating procedures for magnetic iron oxide nanoparticles can be divided into adsorptive and covalent techniques. Covalent approaches can be further subdivided into grafting-to, grafting-from, and grafting-through approaches (Figure 3).

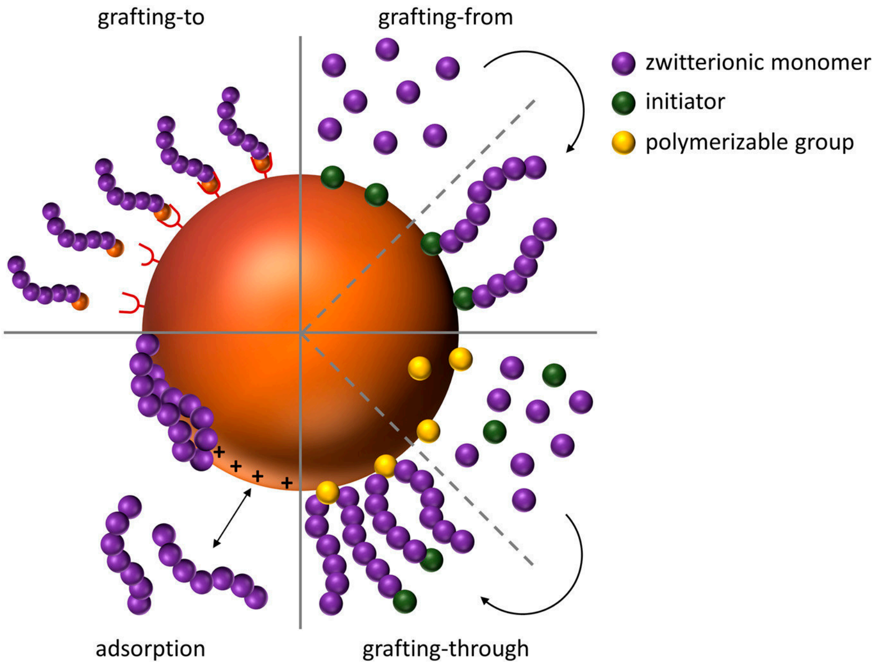

Figure 3. Schematic representation of different grafting methods of polymers to nanoparticle surfaces.

For covalent attachment of a polymeric shell, prior functionalization of the nanoparticle surface is necessary. The most prominent example is the synthesis of a thin SiO_2 shell on the surface which can be prepared using the Stoeber process [127]. If functional silane precursors are used, the resulting SiO_2 surface exhibits additional functional groups such as amines [128] or thiols [129], which can later on be used for grafting procedures of polyelectrolytes [128]. For grafting-to, the respective polyelectrolyte is functionalized with an appropriate endgroup capable of reacting with the modified nanoparticle surface, whereas in grafting-from approaches, the nanoparticle surface is functionalized with an initiator, followed by subsequent surface-initiated polymerization. Covalent grafting-to can be achieved with polyelectrolytes endcapped with triethoxysilanes, which can be bound to the modified nanoparticle surface (e.g., silica precoating). Grafting-from can be realized by functionalization of the nanoparticle surface with initiators for polymerization, e.g., *N*-(2-aminoethyl)-2-bromo-2-methylpropanamide, which has been used for the Atom Transfer Radical Polymerization (ATRP) of carboxybetaine methacrylate from iron oxide nanoparticles [130]. For grafting-through, polymerizable groups can be introduced—for example by condensation of γ-methacryloxy-propyl-trimethoxysilane (MPS) [131].

The most common way to attach polyelectrolytes to nanoparticle surfaces is chemisorption or physisorption by either complexation of iron ions at the surface, electrostatic interactions between polymer and nanoparticle or by exploiting hydrophobic interactions (van-der-Waals forces,

Figure 4). Specific examples are the chemisorption of polymers featuring carboxylic acid moieties, as for example shown by von der Lühe et al., who immobilized polydehydroalanine on pristine MNPs [132] or Poimbo Garcia et al. who used MNPs which were stabilized by oleic acid and immobilized amphiphilic zwitterionic polymers by hydrophobic interactions at the hydrophobic surface of the nanoparticles [133]. Other strategies which have been reported are to conduct emulsion polymerizations or the synthesis of MNP in the presence of polyzwitterions as shown by Mincheva et al. who simply added polyelectrolytes during the respective MNPs synthesis [134].

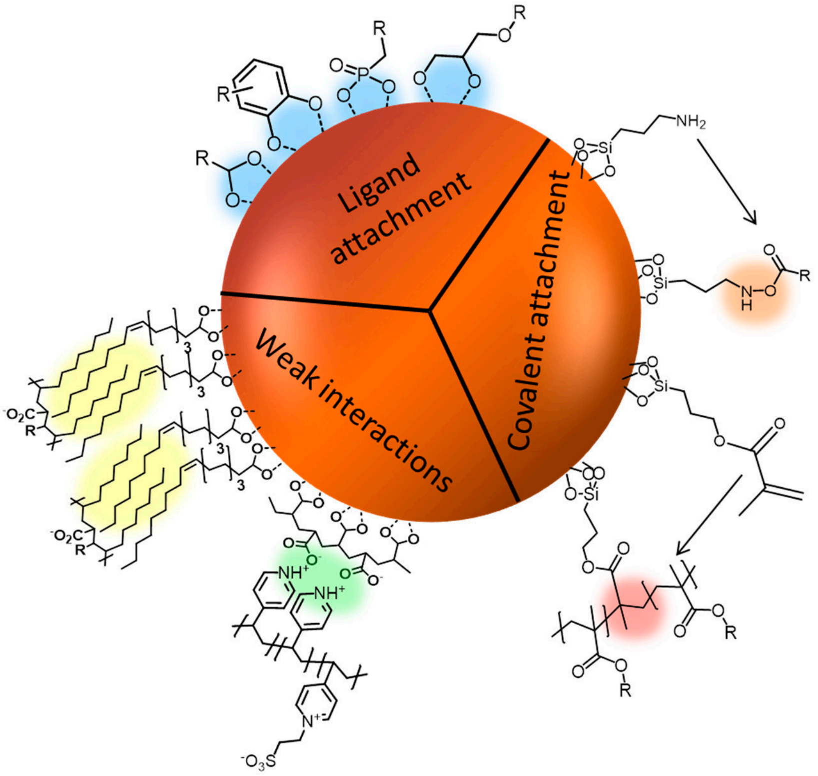

Figure 4. Schematic representation of applied immobilization techniques for polyzwitterions at the surface of magnetic nanoparticles (MNPs).

There are two possible strategies for adsorptive surface modifications, either the adsorption of end-functionalized polyelectrolytes in analogy to the covalent grafting-to, or adsorption of the polyelectrolyte chain. The latter can be realized utilizing either the anionic groups of the polyelectrolyte itself, or special anchor groups which can be introduced by the formation of copolymers or block copolymers. Suitable anchor groups besides the functional groups present in the polyelectrolyte are for example catechol derivatives like dopamine [135], arsenic acid or phosphonates [136]. Among the groups which are used for immobilization one of the most prominent examples is the carboxyl group. Here, direct complexation of the iron oxide surface is possible in different ways (Figure 5). Usually, multiple carboxylic groups per polymer chain are used for the immobilization to deliberately avoid the detachment of the polymeric shell at low concentrations. The binding mode for each carboxylate can be bidentate chelate (A), bidentate bridging (B), or monodentate (C), and depends on the surrounding solution conditions (e.g., pH) as well as on the substituent (R) of the carboxylic acid [137].

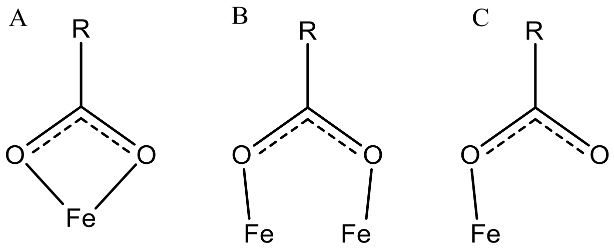

Figure 5. Carboxylate binding models: (**A**) bidentate chelate; (**B**) bidentate bridging; and (**C**) monodentate coordination. Reprinted from [137] with permission from ACS Publications.

Further prominent anchoring groups are catechols as this mimics the anchoring mechanism of marine mussels in nature, which use dopamin groups in their adhesive mussel foot proteins. A few examples use vinyl-catechols as one segment in block copolymers to facilitate anchoring at the surface of magnetic nanoparticles [138,139]. However, to our knowledge there are no examples so far for block copolymers consisting of a vinyl-catechol segment and a block of polyzwitterionic species. Instead there is an example where the catechol anchoring group appears only as an end group of polyzwitterions, as shown by Zhang et al. [135]. As catechols exhibit an extremely strong binding affinity to surfaces (especially to iron oxide) one catechol group per polymer allows in this case satisfying anchoring at the nanomaterial surface. Derivatives of catechol groups can also strongly influence the binding affinity to iron oxide surfaces. In general, catechol derivatives featuring electron withdrawing substituents lead to an enhanced binding affinity and thus to an enhanced stability of the resulting hybrid materials. Amstad et al. investigated different catechol-derived anchoring groups and were able to show that a stronger binding affinity does not necessarily result in an improved dispersion stability, but an optimal binding affinity of the anchors was identified (Figure 6). If the binding affinity is too strong, as in the example of applying mimosine as ligand system, the complexation can even lead to the removal of Fe^{3+}-ions which gradually dissolves the nanoparticles [140].

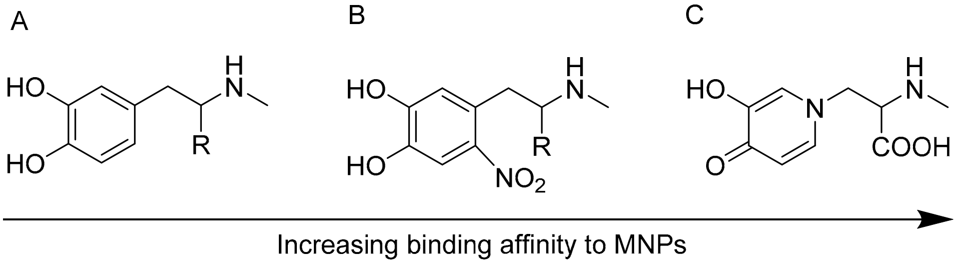

Figure 6. Catechol derivatives with increasing binding affinity to MNPs. (**A**) Catechol; (**B**) Nitrocatechol; (**C**) Mimosine. Reprinted from [140] with permission of ACS Publications.

Less frequently used anchoring groups for the immobilization of polymers at MNPs are phosphate anchoring groups. Miles et al. report in this context on the synthesis of MNPs which are modified by poly(ethylene glycol) (PEG) with different anchoring groups like monophosphonate and triphosphate and compared these to carboxylic acid moieties. The magnetite surface coverage was observed to be most satisfying in density and stability under physiological conditions with the triphosphate anchoring group. The observed grafting density is attributed to the three binding possibilities, resulting in an increased stabilization. Furthermore, phosphate groups show lower interactions with phosphate salts present under physiological conditions [141]. Similar observations concerning the anchoring stability of PEG-trisphosphate modified MNPs were made by Goff et al. [142]. Additional investigations of Maliakal et al. showed, that phosphonate groups form more stable bonds to metal oxide nanoparticles compared to carbonates [143].

The grafting method itself has a large impact on the properties of the resulting coating. Adsorption leads to the formation of thin monolayers, since further adsorption is inhibited due to the high surface concentration if compared to the surrounding solution, resulting in a rather high diffusion barrier [144,145]. Compared to that, polyelectrolytes which are bound to the NP surface with end-functionalities form thicker but typically less dense coatings. Nevertheless, typically the highest grafting densities can be achieved with grafting-from approaches [145].

5. Characterization Methods

Several established methods exist for the investigation of nanoparticles or the corresponding hybrid materials. Herein we want to focus on characterization methods which mainly target shell thickness and shell characteristics as well as the altered properties of the core-shell construct after successful coating (Figures 7 and 8).

As already mentioned in Section 2, both the core size and the size distribution have tremendous influence on the characteristics of any nanomaterial and, hence, reliable methods to determine these parameters are crucial. In that regard, dynamic light scattering (DLS) can be a useful tool. DLS uses Brownian motion to provide information about the hydrodynamic radius (R_h), size distribution (polydispersity, PDI), and the colloidal stability of nanoparticles in solution [146]. Quite often, PDI values from 0.1 to 0.25 are used to confirm a narrow size distribution, whereas a PDI value higher than 0.5 is often referred to as a broad distribution [147]. The size distributions resulting from DLS are of high value concerning the aggregation behavior prior to and after surface modification as well as the apparent changes in nanoparticle size. However, this method merely provides an average value whereas transmission electron microscopy (TEM) provides supplementary information about size, shape, and shell thickness of individual nanoparticles or clusters thereof. Especially regarding the latter case, TEM investigations can be easily used to get an impression about the effect of the polymeric shell on the MNP aggregation behavior. However, the results have to be interpreted with care as aggregation of the nanoparticles and damaging of organic nanostructures can occur during drying processes. For this reason, TEM and DLS are often used in combination [148]. Additionally, cryo TEM has to be applied for samples which are sensitive to drying processes. Cryo TEM reveals structural information without drying the artifacts as the samples are measured in a vitrified aqueous surrounding. The aqueous sample is therefore vitrified by plunging into liquid ethane. This technique is of special interest when it comes to the visualization of clustering processes [149], samples which include liposome-like structures [150,151], or the visualization of biological interaction processes with the respective nanoparticles (Figure 7) [152].

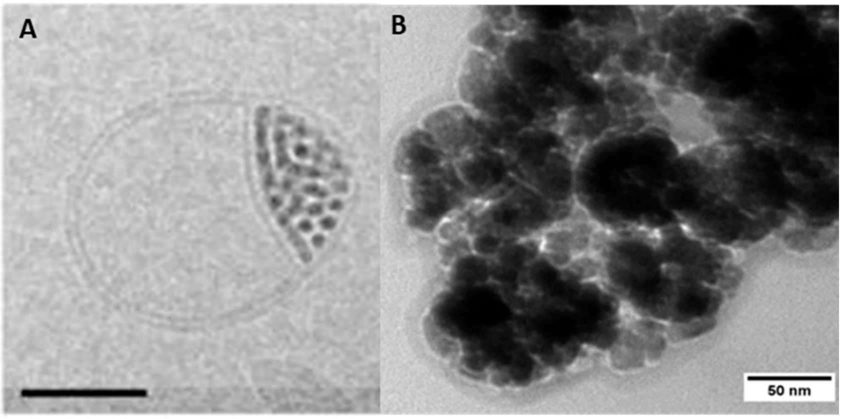

Figure 7. Cryo-TEM (transmission electron microscopy) micrographs of (**A**) lipid bilayer splitting around incorporated MNPs (scale bar = 50 nm). Reprinted from [151] with permission of ACS Publications. (**B**) Protein corona of bovine serum albumin formed at the surface of MNPs (unpublished own data).

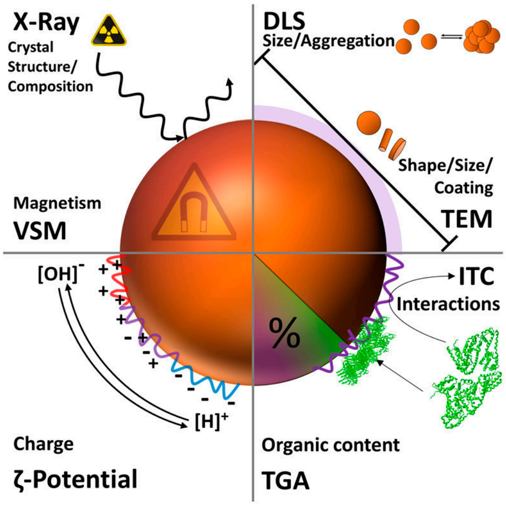

Figure 8. Schematic representation of different analysis techniques for magnetic nanoparticles and the corresponding surface modifications.

The zeta potential of nanoparticles has tremendous influence on their suspension stability, eventual secondary aggregation, or any interaction with other materials. The zeta potential is measured by laser doppler velocimetry as the electrophoretic mobility of the respective colloidal suspension and represents the potential at the slipping plane of a particle in solution during movement [153]. In general, high values result in an improved stabilization, while a value close to zero typically leads to fast aggregation and eventual precipitation in aqueous media. Due to the adsorption of protein upon contact with biological media, the biological identity of nanoparticles can strongly differ from their synthetic identity concerning aggregation and surface charge [154]. Therefore, it is important to note that high zeta potential values are not necessarily an indication for dispersion stability in biological media. According to several reports, zwitterionic coatings seem to be beneficial with regard to dispersion stability over extended broad pH ranges and at different salt concentrations [4].

Powder X-ray investigations are most often used to obtain information about the crystal structure and phase of the magnetic core. This method provides information regarding the crystallinity of nanoparticles, as well as the average nanoparticle diameter. In addition, information on eventual crystalline organic shells can also be obtained but data analysis in these cases can be rather challenging [155]. The magnetic properties of magnetic nanoparticles are determined by vibrating sample magnetometry (VSM). The magnetic properties can be used to estimate the amount of diamagnetic material in the sample, for example the organic material representing the shell. Comparison of the weight of a sample with the corresponding magnetic properties allows calculation of the amount of diamagnetic organic material. Furthermore, this method validates whether the investigated nanoparticles are (still) superparamagnetic. Thermogravimetric analysis (TGA) can be used to determine the overall amount of organic material located at the surface of inorganic nanoparticles. Thereby, one clear benefit is that small samples amounts can be used to verify the presence of organic surface coatings. This tool is of utmost interest when it comes to a quantitative evaluation of coating processes and/or the determination of biological adsorption processes [156]. Isothermal titration calorimetry (ITC), usually a method used for the quantification of binding processes, is an attractive method to investigate interactions of MNPs with other molecules. This technique is often used for the quantification of interactions between small molecules and enzymes or DNA and has therefore the potential to quantify the adsorption of proteins or macromolecules onto the surface of nanoparticles. There are few examples in the literature of the investigation of magnetic nanoparticles using ITC but it can be used to determine the binding affinity K_a (binding strength), the binding enthalpy ΔH, as well as the binding stoichiometry n. This allows, for example, for quantification of the protein repellence of a given nanomaterial [157–160].

6. Synthesis of Polyzwitterionic Shell Materials

The first polyampholytes were described in the 1950s by Alfrey, Fuoss, Morawetz, and Pinner as copolymers of methacrylic acid and either 2/4-vinyl pyridine or *N*,*N*-diethylamino methacrylate [161,162]. The first synthetic polyzwitterion matching the previously mentioned IUPAC definition was described by Harry Ladenheim and Herbert Morawetz, who synthesized poly(4-vinyl pyridine betaine) by quaternization of poly(4-vinyl pyridine) with ethylbromoacetate and subsequent hydrolysis of the resulting ester in 1957 [163]. After these first approaches, a lot of progress was made in the synthesis of polyzwitterions by various techniques. Most noticeable in our opinion is the utilization of controlled polymerization techniques and the large variety of monomers which has been made accessible. Controlled polymerization techniques not only allow control over molar mass, dispersity, and polymer architecture but also provide access to block copolymers featuring polyzwitterionic or polyampholytic blocks [164–167]. For a detailed overview on synthetic access and properties of polyzwitterions we refer the reader to an excellent recent review article [101]. However, many approaches today using polyzwitterions as coating materials for MNPs still report on polymer-analogous reactions like for example the quaternization of poly(4-vinyl pyridine) to generate zwitterionic polymers [132,134,136,164,168,169]. Quite often the dispersity of the polymers used for surface functionalization is of secondary importance. This can be of advantage if polymerization is impeded by certain groups which have to be protected prior to polymerization or when polymers are of interest but naturally not of polyzwitterionic character. Commonly used techniques in that respect are different protection/deprotection strategies for different functional groups, quaternization of amines (often coupled with the introduction of anionic moieties, resulting in the formation of betaines), or esterification as an intermediate step. Some polyzwitterions can also be obtained by direct polymerization of the corresponding monomer without any subsequent modification being necessary [135,166]. In most cases, nanoparticle synthesis and surface functionalization are two separate steps which have the advantage that the properties and characteristics of the respective building blocks can be adjusted (and investigated) separately prior to the formation of core-shell hybrid materials. On the other hand, direct one-pot approaches can reduce the overall synthetic efforts and are attractive concerning scalability. In the following, polyzwitterions and, in one case, a polyampholyte which were used for coating of magnetic nanoparticles are discussed. They are listed and arranged according to the techniques used for immobilization on the MNP surface.

6.1. Covalent Surface Functionalization

In the first section, covalently grafted polyzwitterions are discussed. The examples are summarized in Table 1.

Urena-Benavides et al. formed iron oxide nanoclusters with silica shells, which were then functionalized with amino groups on the surface using 3-aminopropyl triethoxysilane (**1**). The amino groups were used to covalently graft a poly(2-acrylamido-3-methylpropanesulfonate-*co*-acrylic acid) copolymer to the nanoparticle surface. The resulting hybrid particles showed reduced adsorption to porous materials (Figure 9C) [128]. Zhang et al. prepared an ATRP initiator bearing an amine functionality at the chain end, which was used for surface immobilization of the initiator onto superparamagnetic nanospheres. The initiator was then used for the surface initiated polymerization of carboxybetaine methacrylate (CBMA **2**). Furthermore, both pristine and PCBMA functionalized MNP were further functionalized with antibodies of the β subunit of human chorionic gonadotropin (anti-β-hCG). The particles showed reduced non-specific protein adsorption, and have high potential for biosensing applications (Figure 9A) [130]. An example of grafting-through surface functionalization was presented by Chen et al. (**3**). They published the synthesis of polyzwitterion coated magnetic nanoparticles via a grafting-through approach. At first, the magnetite nanoparticles were coated with a thin silica shell using the Stöber-process, followed by grafting with 3-(trimethoxysilyl)propyl methacrylate (γ-MPS), creating reactive double-bonds on the nanoparticle surface. The zwitterionic shell was then synthesized by copolymerization of methacrylic acid (MAA), *N*,*N*′-methylenebisacrylamide (MBA) as crosslinker, and 2-(methacryloyloxy)ethyl-dimethyl-(3-sulfopropyl) ammonium hydroxide (MSA) as zwitterionic co-monomer [131].

Table 1. Structures, binding method, potential application (if provided) and type of polyelectrolyte combination for polyzwitterions which were used for covalent surface functionalization of magnetic nanoparticles (MNP).

Nr.	Polyzwitterionic Unit Structure/Name	Binding Method	Application	Type of Polyelectrolyte +/−
1	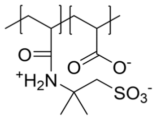 P(AMPS-*co*-AA) [128]	covalent attachment via grafting-to to amino-silylated particles		weak/strong
2	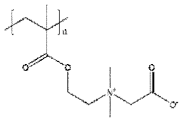 PCBMA [130]	grafting-from	Sensing	Strong/weak
3	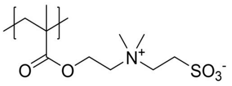 PMSA [131]	grafting-through using γ-MPS (silylation)	Isolation of glycoptides from biological samples (bioseparation)	strong/strong

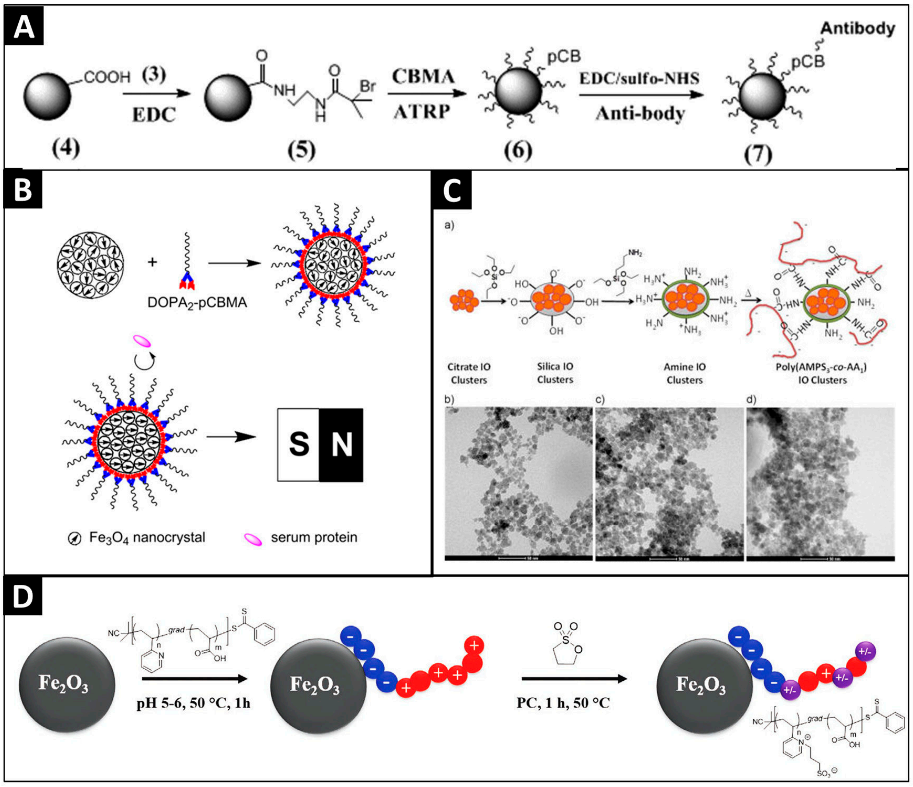

Figure 9. (**A**) Grafting-from approach for the polymerization of CBMA (carboxybetaine methacrylate). Reprinted from [130] with permission of ACS Publications; (**B**) Preparation of pCBMA-DOPA-2-MNPs and their magnetization in the presence of a permanent magnet. Reprinted from [135] with permission of Elsevier; (**C**) Scheme of the synthesis of poly(AMPS-*co*-AA) MNPs. Reprinted from [128] with permissions of ACS Publications; (**D**) Scheme of grafting-to of P(2VP-*grad*-AA) onto MNP and subsequent sultonation of P(2VP-*grad*-AA)@MNP, reprinted from [164] with permission of John Wiley and Sons.

6.2. Electrostatic Adsorption

In the following section, polyzwitterions, which were adsorbed onto MNP will be discussed, and the shown examples are summarized in Table 2.

Table 2. Structures, binding method, potential application (if provided) and type of polyelectrolyte combination for polyzwitterions which were used for adsorptive surface functionalization of MNP.

Nr.	Polyzwitterionic Unit Structure/Name	Binding Method	Application	Type of Polyelectrolyte +/−
4	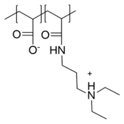 P(AA-*stat*-PDEAPA) [170]	carboxyl group anchoring, grafting-to		weak/weak
5	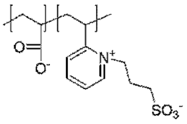 P(2VP-*grad*-AA) [164]	carboxyl group anchoring, grafting-to	antifouling	weak/weak
6	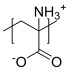 PDha[132]	carboxyl group anchoring, grafting-to	antifouling	weak/weak
7	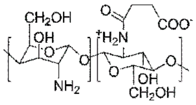 NSOCMS [168]	carboxyl group anchoring, grafting-to		weak/weak
8	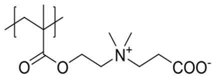 PCBMA[135]	Catechol anchoring, grafting-to		strong/weak
9	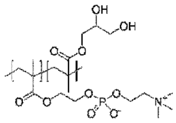 PMPC-*b*-PGMA [166]	adsorption via bishydroxides of the PGMA block, grafting-to		strong/weak

Although we mainly focus on polyzwitterionic coating materials, here we also included one example of a polyampholyte to show that the resulting hybrid materials can show similar properties to the examples discussed before. Xiao et al. coated in a first step iron oxide nanoparticles with poly(acrylic acid) (PAA) and modified them in a second step by esterification with 3-(diethylamino)propylamine, resulting in a polyampholytic shell material. The resulting nanoparticles exhibited low macrophage cell uptake and low cell toxicity (**4**) [170]. Billing et al. showed one of the few examples where controlled polymerization techniques were applied to generate polyzwitterions as coating materials for MNPs. Using reversible addition–fragmentation chain transfer (RAFT)-polymerization, gradient copolymers consisting of 2-vinyl pyridine and *tert*-butyl acrylate (poly(2-vinylpyridine-grad-*tert*-butylacrylate)) were prepared (**5**). Subsequently, the *tert*-butylgroups were hydrolyzed to acrylic acid and the 2-vinylpyridine moieties were sultonated to generate a zwitterionic unit (Figure 9D). As a result of the functionalization, an increased stability towards secondary aggregation was observed and cytotoxicity tests did not show a significant influence on cell viability [164]. Von der Lühe et al. showed the synthesis of zwitterionic polydehydroalanine (**6**). This polymer exhibits a high charge to volume ratio as it consists of a polymeric backbone with directly attached amine and carboxylic acid functionalities. As these functional groups would impede direct polymerization, both functionalities had to be protected prior to polymerization. The protective groups were cleaved off afterwards to generate a polyzwitterion and the carboxyl groups were used for immobilization at the surface of sub 10 nm MNPs [132] and multicore nanoparticles with 80 nm in diameter. The PDha@MC particles were further used for the adsorption and selective desorption of both polyanions and polycations [171]. Zhu et al. used O-carboxymethylchitosan as a naturally occurring polysaccharide and modified the material by functionalization with carboxylic acid groups, followed by immobilization at the surface of MNPs. The resulting nanoparticles were well dispersed in aqueous media and showed good cytocompatibility (**7**) [168]. Besides carboxylic acids, other functionalities like catechols, phosphonates, or oligoglycols can be used for the immobilization of polyzwitterions on nanoparticle surfaces. Dopamine was used by Zhang et al. who synthesized a double-dopamine functionalized ATRP initiator, where all catecholic moieties were protected with *tert*-butyldimethylsilyl ethers (TBDMS, Figure 9B) (**8**). The initiator was then used for the polymerization of carboxybetainemethacrylate (CBMA). After deprotection of the catecholic hydroxyl groups, the polyzwitterion was used to coat iron oxide MNPs. The resulting hybrids showed increased dispersion stability in solutions of varying ionic strength and blood serum compared to pristine and citrate stabilized MNPs. Furthermore, macrophage uptake was drastically decreased [135]. Yuan et al. synthesized poly[2-(methacryloyloxy)ethyl phosphorylcholine]-*block*-(glycerol monomethacrylate) (PMPC-*b*-PGMA) block copolymers by ATRP (**9**). The double-hydrophilic block copolymer was added to a co-precipitation of $FeCl_2$ and $FeCl_3$.The bis-hydroxides of the PGMA block ensured efficient immobilization of the polymer on the surface of the resulting nanoparticles, and the zwitterionic block increased long term-stability [166].

6.3. Other Methods

In this last section, less frequently employed functionalization methods, like pre-functionalization approaches with polyelectrolytes, utilizing hydrophilic/hydrophobic interactions, or the addition of polyzwitterions during MNP preparation are discussed. The discussed examples are summarized in Table 3.

The use of non-covalent interactions (electrostatic or hydrophobic-hydrophilic interactions) to immobilize polyelectrolytes at the surface of MNPs leads to systems which allow the detachment of the respective polymeric shell under specific conditions, which can be either a benefit or a drawback. In order to generate a high surface charge at the surface of MNPs, Yeh et al. used poly(acrylic acid) as a first layer. By applying poly(4-vinylpyridinium *N*-ethylsulfonate), attractive electrostatic interactions led to the formation of a second layer (**10**). It is noteworthy that the direct attachment of the polyzwitterion is also possible without the underlying PAA layer but the resulting surface coating was by far less stable afterwards [172]. V. G. Demillo et al. took advantage of hydrophilic hydrophobic interactions. They produced multifunctional magnetofluorescent NPs by encapsulating quantum dots and MNPs within a polymeric shell. Poly(maleic anhydride-*alt*-1-octadecene) (PMAO) was used as precursor and modified by opening the anhydrous rings in the polymer in a first step with 3-(dimethyl-amino)-1-propylamine (**11**). In a second step the generated tertiary amines were reacted with β-propiolactone and 1,3-propanesultone resulting in betaine structures. As the polymer backbone has an amphiphilic character these polymers were immobilized at the nanoparticles by using hydrophilic hydrophobic interactions between the polyampholytes and the hydrophobic nanoparticles [169]. A similar approach was performed by Wang et al. who prepared microspheres of chitosan and poly(aspartic acid) with encapsulated magnetic nanoparticles and CdTe quantum dots (**12**). The 110–320 nm large microspheres are of interest in the context of biolabeling and imaging [173]. Pombo-Garcia et al. utilized hydrophobic interactions for the functionalization of ultra small superparamagnetic iron oxide nanoparticles with poly(maleic anhydride-*alt*-1-decene), which was previously substituted with 3-(dimethylamino)propylamine to give a zwitterionic polymer (PMAL) (**13**). The surface coating was realized by intercalation of decene with previously attached oleic acid [133]. The resulting hybrids were characterized concerning protein adsorption and biocompatibility. R. Mincheva et al. showed the in-situ formation of polyzwitterion-coated magnetic nanoparticles by adding the polymeric shell material during the synthesis of MNPs. The two biocompatible polyelectrolytes (*N*-carboxyethylchitosan (CECh) (**14**) and poly(2-acrylamido-2-methylpropanesulfonic acid) (PAMPS) (**15**) are capable of stabilizing MNPs in aqueous solution. CECh was synthesized by a polymer-analogous reaction with acrylic acid, while PAMPS was synthesized directly by free radical polymerization of 2-acrylamido-2-methylpropanesulfonic acid. Here, both suspension stability and particle size as well as the resulting magnetic properties were investigated and the obtained nanocomposites were further used for electrospinning [134].

Table 3. Structures, binding method, potential application (if provided), and type of polyelectrolyte combination for polyzwitterions which were used for surface functionalization of MNP via the formation of polyelectrolyte complexes, hydrophilic/hydrophobic interactions, or by addition as surfactant during co precipitation.

Nr.	Polyzwitterionic Unit Structure/Name	Binding Method	Application	Type of Polyelectrolyte +/−
10	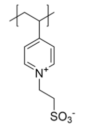 P4VP-SB [172]	electrostatic interactions PAA@MNP	isolation of glycopeptides from biological samples (bio-separation)	strong/strong
11	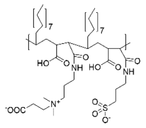 PMAO-CB-SB [169]	hydrophilic hydrophobic interactions	cancer diagnosis	strong/weak
12	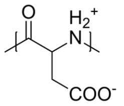 PAsp [173]	polyelectrolyte complexes between chitosan (CS) and poly(aspartic acid) (PAsp) with encapsulated MNP		weak/weak
13	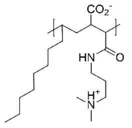 PMAL [133]	hydrophilic hydrophobic interactions	anti-fouling	weak/weak
14	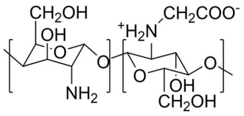 CeCh [134]	adsorption via carboxylates	electro spinning	weak/weak
15	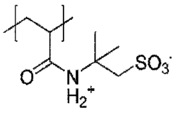 PAMPS [134]	sulfonate anchoring	electro spinning	weak/strong

7. A Short Note on Application Fields

Different applications of specific core-shell combinations have been already showcased throughout the last chapters. Nevertheless, by far the highest application potential for polyzwitterion-coated magnetic nanoparticles in our opinion is within the field of biomedical applications. As demonstrated in Section 2, magnetic cores are of high interest for applications like MRI imaging, drug delivery, and hyperthermia [170]. This potential might even be increased with polyzwitterionic coatings, since the circulation times can be prolonged and secondary (unspecific) aggregation is prevented.

Further, these materials (especially the multicore iron oxide NPs) are promising with regard to bioseparation approaches as the magnetic nanoparticles enable a facile and fast way of binding and separating biomolecules (e.g., glycopeptides) from complex biological systems by external magnetic fields. As this allows an enrichment of the respective molecules, rather high detection sensitivities can be achieved. Further analysis of any separated molecules or macromolecules can afterwards be realized by techniques such as mass spectrometry or various spectroscopy methods [131,172,174].

Besides biomedical applications, the polyzwitterionic magnetic hybrid materials are also constantly discussed with regard to technical applications such as extraction processes (e.g., wastewater treatment or organic pollutant extraction) [136], as the zwitterionic surface enables adsorption of cationic metal ions, which could possibly be released by changes in pH. The benefit of the magnetic cores in this case is again the possibility of mechanical manipulation, in particular the separation from dispersions by an external magnetic field. This property also renders these materials interesting for catalytic processes, as such heterogeneous catalysts can be easily separated, purified if necessary, and reused in further cycles [175]. Finally, magnetic imaging is also of interest in other fields like subsurface imaging. Here, the low tendency for interaction with surrounding materials of different polarity enables the use of polyzwitterionic surface coatings on MNPs in imaging for oil recovery as shown by Ureña-Benavides et al. [128].

8. Conclusions and Outlook

The synthesis and exploitation of magnetic hybrid materials–in our case consisting of a magnetic core and an organic shell—has already arrived in a broad variety of research areas. However, still only a certain number of research groups have reported on the use of polyzwitterions as coating materials, which we mainly attribute to the fact that the synthesis of polyzwitterions can be challenging and that PEG still is the most prominent biocompatible shell material in many applications. Nevertheless, magnetic hybrid materials which are functionalized by polyzwitterions show several benefits compared to the gold standard PEG, like close similarities to biological tissue, multiple ways of immobilization, and, in some cases, pH responsive behavior rendering those examples interesting candidates for drug delivery systems in the near future. The adjustment of charge at the particle surface allows a potential change in solubility of the particles as well as a change in adsorptive behavior towards any suitable guest molecules (or cargo).

Further advance in the context of biomedical applications clearly requires progress concerning the understanding of interactions with proteins and biological macromolecules. Along the same line, a closer look at the influence of the actual combination of strong and weak polyelectrolyte building blocks on the resulting interactions with biological tissues has to be taken as well. The qualitative as well as the quantitative binding of different proteins to the surface of the respective materials might give further information on processes which are important in understanding the governing factors in protein corona formation. Furthermore, basic investigations on the suspension stability depending on ionic strength, and the response to the presence of different counter ions or biological fluids are further important aspects. The examples outlined above also suggest that combinations of PEG and polyzwitterions within polymeric shells are definitely an aspect of interest.

Acknowledgments: The authors are grateful for financial support from the DFG in the framework of the priority program SPP1681 (Moritz von der Lühe and Felix H. Schacher: SCHA1640/7-1 and Silvio Dutz: DU1293/4-1). Philip Biehl is grateful for a fellowship (Landesgraduiertenstipendium of the Friedrich Schiller University Jena).

Conflicts of Interest: The authors declare no conflict of interest.

References

1. Veiseh, O.; Gunn, J.W.; Zhang, M. Design and fabrication of magnetic nanoparticles for targeted drug delivery and imaging. *Adv. Drug Deliv. Rev.* **2010**, *62*, 284–304. [CrossRef] [PubMed]
2. Cao, B.; Tang, Q.; Cheng, G. Recent advances of zwitterionic carboxybetaine materials and their derivatives. *J. Biomater. Sci.* **2014**, *25*, 1502–1513. [CrossRef] [PubMed]
3. Wu, W.; Wu, Z.; Yu, T.; Jiang, C.; Kim, W.-S. Recent progress on magnetic iron oxide nanoparticles: Synthesis, surface functional strategies and biomedical applications. *Sci. Technol. Adv. Mater.* **2015**, *16*. [CrossRef] [PubMed]

4. García, K.P.; Zarschler, K.; Barbaro, L.; Barreto, J.A.; O'Malley, W.; Spiccia, L.; Stephan, H.; Graham, B. Zwitterionic-Coated "Stealth" Nanoparticles for Biomedical Applications: Recent Advances in Countering Biomolecular Corona Formation and Uptake by the Mononuclear Phagocyte System. *Small* **2014**, *10*, 2516–2529. [CrossRef] [PubMed]
5. Liu, T.-Y.; Hu, S.-H.; Liu, D.-M.; Chen, S.-Y.; Chen, I.W. Biomedical nanoparticle carriers with combined thermal and magnetic responses. *Nano Today* **2009**, *4*, 52–65. [CrossRef]
6. Ai, H. Layer-by-layer capsules for magnetic resonance imaging and drug delivery. *Adv. Drug Deliv. Rev.* **2011**, *63*, 772–788. [CrossRef] [PubMed]
7. Xing, R.; Liu, G.; Zhu, J.; Hou, Y.; Chen, X. Functional Magnetic Nanoparticles for Non-Viral Gene Delivery and MR Imaging. *Pharm. Res.* **2014**, *31*, 1377–1389. [CrossRef] [PubMed]
8. Bodker, F.; Morup, S.; Linderoth, S. Surface effects in metallic iron nanoparticles. *Phys. Rev. Lett.* **1994**, *72*, 282–285. [CrossRef] [PubMed]
9. Hacliipanayis, C.G.; Bonder, M.J.; Balakrishanan, S.; Wang, X.; Mao, H.; Hadjipanayis, G.C. Metallic Iron Nanoparticles for MRI Contrast Enhancement and Local Hyperthermia. *Small* **2008**, *4*, 1925–1929.
10. Li, Y.F.; Hu, Y.J.; Huang, G.J.; Li, C.Z. Metallic iron nanoparticles: Flame synthesis, characterization and magnetic properties. *Particuology* **2013**, *11*, 460–467. [CrossRef]
11. Yamamuro, S.; Ando, T.; Sumiyama, K.; Uchida, T.; Kojima, I. Monodisperse Metallic Iron Nanoparticles Synthesized from Noncarbonyl Complex. *Jpn. J. Appl. Phys. Part 1* **2004**, *43*, 4458–4459. [CrossRef]
12. Seong, G.; Takami, S.; Arita, T.; Minami, K.; Hojo, D.; Yavari, A.R.; Adschiri, T. Supercritical hydrothermal synthesis of metallic cobalt nanoparticles and its thermodynamic analysis. *J. Supercrit. Fluids* **2011**, *60*, 113–120. [CrossRef]
13. Zeisberger, M.; Dutz, S.; Müller, R.; Hergt, R.; Matoussevitch, N.; Bönnemann, H. Metallic cobalt nanoparticles for heating applications. *J. Magn Magn. Mater.* **2007**, *311*, 224–227. [CrossRef]
14. Tran, N.; Webster, T.J. Magnetic nanoparticles: Biomedical applications and challenges. *J. Mater. Chem.* **2010**, *20*, 8760–8767. [CrossRef]
15. Lee, J.G.; Li, P.; Dong, X.L.; Choi, C.J. Fabrication of Ferromagnetic Mn-Al Alloy Nanoparticles Using a Plasma Arc-discharge Process. *Korean J. Met. Mater.* **2010**, *48*, 357–362. [CrossRef]
16. Wang, C.H.; Meyer, J.; Teichert, N.; Auge, A.; Rausch, E.; Balke, B.; Hutten, A.; Fecher, G.H.; Felser, C. Heusler Nanoparticles for Spintronics and Ferromagnetic Shape Memory Alloys. *J. Vac. Sci. Technol. B* **2014**, *32*. [CrossRef]
17. White, C.W.; Withrow, S.P.; Sorge, K.D.; Meldrum, A.; Budai, J.D.; Thompson, J.R.; Boatner, L.A. Oriented Ferromagnetic Fe-Pt Alloy Nanoparticles Produced in Al_2O_3 by Ion-Beam Synthesis. *J. Appl. Phys.* **2003**, *93*, 5656–5669. [CrossRef]
18. Lasheras, X.; Insausti, M.; de Muro, I.G.; Garaio, E.; Plazaola, F.; Moros, M.; De Matteis, L.; de la Fuente, J.M.; Lezama, L. Chemical Synthesis and Magnetic Properties of Monodisperse Nickel Ferrite Nanoparticles for Biomedical Applications. *J. Phys. Chem. C* **2016**, *120*, 3492–3500. [CrossRef]
19. Rodrigues, A.R.O.; Gomes, I.T.; Almeida, B.G.; Araujo, J.P.; Castanheira, E.M.S.; Coutinho, P.J.G. Magnetic liposomes based on nickel ferrite nanoparticles for biomedical applications. *Phys. Chem. Chem. Phys.* **2015**, *17*, 18011–18021. [CrossRef] [PubMed]
20. Ruthradevi, T.; Akbar, J.; Kumar, G.S.; Thamizhavel, A.; Kumar, G.A.; Vatsa, R.K.; Dannangoda, G.C.; Martirosyan, K.S.; Girija, E.K. Investigations on nickel ferrite embedded calcium phosphate nanoparticles for biomedical applications. *J. Alloy. Compd.* **2017**, *695*, 3211–3219. [CrossRef]
21. Tomitaka, A.; Jeun, M.; Bae, S.; Takemura, Y. Evaluation of Magnetic and Thermal Properties of Ferrite Nanoparticles for Biomedical Applications. *J. Magn.* **2011**, *16*, 164–168. [CrossRef]
22. Peeples, B.; Goornavar, V.; Peeples, C.; Spence, D.; Parker, V.; Bell, C.; Biswal, D.; Ramesh, G.T.; Pradhan, A.K. Structural, Stability, Magnetic, and Toxicity Studies of Nanocrystalline Iron Oxide and Cobalt Ferrites for Biomedical Applications. *J. Nanopart. Res.* **2014**, *16*, 2290. [CrossRef]
23. Salunkhe, A.B.; Khot, V.M.; Thorat, N.D.; Phadatare, M.R.; Sathish, C.I.; Dhawale, D.S.; Pawar, S.H. Polyvinyl alcohol functionalized cobalt ferrite nanoparticles for biomedical applications. *Appl. Surf. Sci.* **2013**, *264*, 598–604. [CrossRef]
24. Sanpo, N.; Berndt, C.C.; Wen, C.; Wang, J. Transition metal-substituted cobalt ferrite nanoparticles for biomedical applications. *Acta Biomater.* **2013**, *9*, 5830–5837. [CrossRef] [PubMed]

25. Cornell, R.M.; Schwertmann, U. *The Iron Oxides: Structure, Properties, Reactions, Occurences and Uses*; Wiley-VCH: Weinheim, Germany, 2003.
26. Khalafalla, S.E.; Reimers, G.W. Preparation of Dilution-Stable Aqueous Magnetic Fluids. *IEEE Trans. Magn.* **1980**, *16*, 178–183. [CrossRef]
27. Massart, R. Preparation of aqueous ferrofluids without using surfactant—Behavior as a function of the pH and the counterions. *C. R. Seances Acad. Sci. Ser. C* **1980**, *291*, 1–3.
28. Krishnan, K.M. Biomedical Nanomagnetics: A Spin through Possibilities in Imaging, Diagnostics, and Therapy. *IEEE Trans. Magn.* **2010**, *46*, 2523–2558. [CrossRef] [PubMed]
29. Pankhurst, Q.A.; Thanh, N.T.K.; Jones, S.K.; Dobson, J. Progress in Applications of Magnetic Nanoparticles in Biomedicine. *J. Phys. D* **2009**, *42*. [CrossRef]
30. Bloch, F. Zur Theorie des Austauschproblems und der Remanenzerscheinung der Ferromagnetika. *Z. Phys.* **1932**, *74*, 295–335. [CrossRef]
31. Weiss, P. L'hypothese du Champ Moleculaire et la Propriete Ferromagnetique. *J. Phys. Radium* **1907**, *6*, 661–690. [CrossRef]
32. Landau, L.D.; Lifshitz, E.M. On the Theory of the Dispersion of Magnetic Permeability in Ferromagnetic Bodies. *Phys. Z. Sowjetunion* **1935**, *8*, 153–167.
33. Kittel, C. Theory of the Structure of Ferromagnetic Domains in Films and Small Particles. *Phys. Rev.* **1946**, *70*, 965–971. [CrossRef]
34. Butler, R.F.; Banerjee, S.K. Theoretical Single-Domain Grain Size Range in Magnetite and Titanomagnetite. *J. Geophys. Res.* **1975**, *80*, 4049–4058. [CrossRef]
35. Fabian, K.; Kirchner, A.; Williams, W.; Heider, F.; Leibl, T.; Hubert, A. Three-dimensional micromagnetic calculations for magnetite using FFT. *Geophys. J. Int.* **1996**, *124*, 89–104. [CrossRef]
36. Dutz, S. *Nanopartikel in der Medizin*; Verlag Dr. Kovac: Hamburg, Germany, 2008.
37. Néel, L. Influence des fluctuations thermiques a l'aimantation des particules ferromagnetiques. *C. R. Acad. Sci.* **1949**, *228*, 664–668.
38. Dutz, S. Are Magnetic Multicore Nanoparticles Promising Candidates for Biomedical Applications? *IEEE Trans. Magn.* **2016**, *52*. [CrossRef]
39. Dutz, S.; Andrä, W.; Hergt, R.; Müller, R.; Oestreich, C.; Schmidt, C.; Töpfer, J.; Zeisberger, M.; Bellemann, M.E. Influence of Dextran Coating on the Magnetic Behaviour of Iron Oxide Nanoparticles. *J. Magn. Magn. Mater.* **2007**, *311*, 51–54. [CrossRef]
40. Suzdalev, I.P.; Maksimov, Y.V.; Buravtsev, V.N.; Imshennik, V.K.; Kazakevich, A.G.; Novichikhin, S.V. The formation and properties of a system of iron oxide nanoclusters. *Colloid J.* **2000**, *62*, 224–233.
41. Blanco-Andujar, C.; Ortega, D.; Southern, P.; Pankhurst, Q.A.; Thanh, N.T.K. High Performance Multi-core Iron Oxide Nanoparticles for Magnetic Hyperthermia: Microwave Synthesis, and the Role of Core-to-Core Interactions. *Nanoscale* **2015**, *7*, 1768–1775. [CrossRef] [PubMed]
42. Dutz, S.; Kettering, M.; Hilger, I.; Müller, R.; Zeisberger, M. Magnetic multicore nanoparticles for hyperthermia-influence of particle immobilization in tumour tissue on magnetic properties. *Nanotechnology* **2011**, *22*. [CrossRef] [PubMed]
43. Lartigue, L.; Hugounenq, P.; Alloyeau, D.; Clarke, S.P.; Levy, M.; Bacri, J.-C.; Bazzi, R.; Brougham, D.F.; Wilhelm, C.; Gazeau, F. Cooperative Organization in Iron Oxide Multi-Core Nanoparticles Potentiates Their Efficiency as Heating Mediators and MRI Contrast Agents. *ACS Nano* **2012**, *6*, 10935–10949. [CrossRef] [PubMed]
44. Hergt, R.; Dutz, S.; Roder, M. Effects of size distribution on hysteresis losses of magnetic nanoparticles for hyperthermia. *J. Phys. Condens. Matter* **2008**, *20*. [CrossRef] [PubMed]
45. Müller, R.; Dutz, S.; Neeb, A.; Cato, A.C.B.; Zeisberger, M. Magnetic heating effect of nanoparticles with different sizes and size distributions. *J. Magn. Magn. Mater.* **2013**, *328*, 80–85. [CrossRef]
46. Barry, S.E. Challenges in the Development of Magnetic Particles for Therapeutic Applications. *Int. J. Hyperth.* **2008**, *24*, 451–466. [CrossRef] [PubMed]
47. Laurent, S.; Forge, D.; Port, M.; Roch, A.; Robic, C.; Elst, L.V.; Müller, R.N. Magnetic Iron Oxide Nanoparticles: Synthesis, Stabilization, Vectorization, Physicochemical Characterizations, and Biological Applications. *Chem. Rev.* **2008**, *108*, 2064–2110. [CrossRef] [PubMed]
48. Lu, A.H.; Salabas, E.L.; Schüth, F. Magnetic Nanoparticles: Synthesis, Protection, Functionalization, and Application. *Angew. Chem. Int. Ed.* **2007**, *46*, 1222–1244. [CrossRef] [PubMed]

49. Reddy, L.H.; Arias, J.L.; Nicolas, J.; Couvreur, P. Magnetic Nanoparticles: Design and Characterization, Toxicity and Biocompatibility, Pharmaceutical and Biomedical Applications. *Chem. Rev.* **2012**, *112*, 5818–5878. [CrossRef] [PubMed]
50. Krishnan, K.M. *Fundamentals and Applications of Magnetic Materials*; Oxford University Press: Oxford, UK, 2016.
51. Bazylinski, D.A.; Garrattreed, A.J.; Frankel, R.B. Electron microscopic studies of magnetosomes in magnetotactic bacteria. *Microsc. Res. Tech.* **1994**, *27*, 389–401. [CrossRef] [PubMed]
52. Faivre, D.; Schuler, D. Magnetotactic Bacteria and Magnetosomes. *Chem. Rev.* **2008**, *108*, 4875–4898. [CrossRef] [PubMed]
53. Schüler, D.; Frankel, R.B. Bacterial magnetosomes: Microbiology, biomineralization and biotechnological applications. *Appl. Microbiol. Biotechnol.* **1999**, *52*, 464–473. [CrossRef] [PubMed]
54. Timko, M.; Molcan, M.; Hashim, A.; Skumiel, A.; Müller, M.; Gojzewski, H.; Jozefczak, A.; Kovac, J.; Rajnak, M.; Makowski, M.; et al. Hyperthermic Effect in Suspension of Magnetosomes Prepared by Various Methods. *IEEE Trans. Magn.* **2013**, *49*, 250–254. [CrossRef]
55. Hergt, R.; Hiergeist, R.; Zeisberger, M.; Schuler, D.; Heyen, U.; Hilger, I.; Kaiser, W.A. Magnetic Properties of Bacterial Magnetosomes as Potential Diagnostic and Therapeutic Tools. *J. Magn. Magn. Mater.* **2005**, *293*, 80–86. [CrossRef]
56. Molcan, M.; Gojzewski, H.; Skumiel, A.; Dutz, S.; Kovac, J.; Kubovcikova, M.; Kopcansky, P.; Vekas, L.; Timko, M. Energy Losses in Mechanically Modified Bacterial Magnetosomes. *J. Phys. D* **2016**, *49*. [CrossRef]
57. Baumgartner, J.; Carillo, M.A.; Eckes, K.M.; Werner, P.; Faivre, D. Biomimetic Magnetite Formation: From Biocombinatorial Approaches to Mineralization Effects. *Langmuir* **2014**, *30*, 2129–2136. [CrossRef] [PubMed]
58. Scheffel, A.; Gruska, M.; Faivre, D.; Linaroudis, A.; Plitzko, J.M.; Schüler, D. An acidic protein aligns magnetosomes along a filamentous structure in magnetotactic bacteria. *Nature* **2006**, *440*, 110–114. [CrossRef] [PubMed]
59. DeCastro, C.L.; Mitchell, B.S. Nanoparticles from Mechanical Attrition. In *Synthesis, Functionalization, and Surface Treatment of Nanoparticles*; Baraton, M.-I., Ed.; American Scientific Publishers: Valencia, CA, USA, 2002.
60. Dutz, S.; Hergt, R.; Mürbe, J.; Müller, R.; Zeisberger, M.; Andrä, W.; Töpfer, J.; Bellemann, M.E. Hysteresis Losses of Magnetic Nanoparticle Powders in the Single Domain Size Range. *J. Magn. Magn. Mater.* **2007**, *308*, 305–312. [CrossRef]
61. Kurland, H.-D.; Grabow, J.; Staupendahl, G.; Andrä, W.; Dutz, S.; Bellemann, M.E. Magnetic Iron Oxide Nanopowders Produced by CO_2 Laser Evaporation. *J. Magn. Magn. Mater.* **2007**, *311*, 73–77. [CrossRef]
62. Kurland, H.-D.; Grabow, J.; Staupendahl, G.; Müller, F.A.; Müller, E.; Dutz, S.; Bellemann, M.E. Magnetic iron oxide nanopowders produced by CO_2 laser evaporation—'In situ' coating and particle embedding in a ceramic matrix. *J. Magn. Magn. Mater.* **2009**, *321*, 1381–1385. [CrossRef]
63. Stötzel, C.; Kurland, H.-D.; Grabow, J.; Dutz, S.; Müller, E.; Sierka, M.; Müller, F.A. Control of the Crystal Phase Composition of Fe_xO_y Nanopowders Prepared by CO_2 Laser Vaporization. *Cryst. Growth Des.* **2013**, *13*, 4868–4876. [CrossRef]
64. Grüttner, C.; Müller, K.; Teller, J.; Westphal, F.; Foreman, A.; Ivkov, R. Synthesis and Antibody Conjugation of Magnetic Nanoparticles with Improved Specific Power Absorption Rates for Alternating Magnetic Field Cancer Therapy. *J. Magn. Magn. Mater.* **2007**, *311*, 181–186. [CrossRef]
65. Dutz, S.; Clement, J.H.; Eberbeck, D.; Gelbrich, T.; Hergt, R.; Müller, R.; Wotschadlo, J.; Zeisberger, M. Ferrofluids of magnetic multicore nanoparticles for biomedical applications. *J. Magn. Magn. Mater.* **2009**, *321*, 1501–1504. [CrossRef]
66. Sun, S.; Zeng, H. Size-Controlled Synthesis of Magnetite Nanoparticles. *J. Am. Chem. Soc.* **2002**, *124*, 8204–8205. [CrossRef] [PubMed]
67. Kuckelhaus, S.; Garcia, V.A.P.; Lacava, L.M.; Azevedo, R.B.; Lacava, Z.G.M.; Lima, E.C.D.; Figueiredo, F.; Tedesco, A.C.; Morais, P.C. Biological investigation of a citrate-coated cobalt-ferrite-based magnetic fluid. *J. Appl. Phys.* **2003**, *93*, 6707–6708. [CrossRef]
68. Hyeon, T.; Lee, S.S.; Park, J.; Chung, Y.; Bin Na, H. Synthesis of highly crystalline and monodisperse maghemite nanocrystallites without a size-selection process. *J. Am. Chem. Soc.* **2001**, *123*, 12798–12801. [CrossRef] [PubMed]

69. Park, J.; Lee, E.; Hwang, N.M.; Kang, M.S.; Kim, S.C.; Hwang, Y.; Park, J.G.; Noh, H.J.; Kini, J.Y.; Park, J.H.; et al. One-nanometer-scale size-controlled synthesis of monodisperse magnetic iron oxide nanoparticles. *Angew. Chem. Int. Ed.* **2005**, *44*, 2872–2877. [CrossRef] [PubMed]
70. Zhou, Z.H.; Wang, J.; Liu, X.; Chan, H.S.O. Synthesis of Fe_3O_4 nanoparticles from emulsions. *J. Mater. Chem.* **2001**, *11*, 1704–1709. [CrossRef]
71. Okoli, C.; Sanchez-Dominguez, M.; Boutonnet, M.; Jaras, S.; Civera, C.; Solans, C.; Kuttuva, G.R. Comparison and Functionalization Study of Microemulsion-Prepared Magnetic Iron Oxide Nanoparticles. *Langmuir* **2012**, *28*, 8479–8485. [CrossRef] [PubMed]
72. Zeng, Q.; Baker, I.; Loudis, J.A.; Liao, Y.; Hoopes, P.J.; Weaver, J.B. Fe/Fe oxide nanocomposite particles with large specific absorption rate for hyperthermia. *Appl. Phys. Lett.* **2007**, *90*. [CrossRef]
73. Hao, Y.L.; Teja, A.S. Continuous hydrothermal crystallization of α-Fe_2O_3 and Co_3O_4 nanoparticles. *J. Mater. Res.* **2003**, *18*, 415–422. [CrossRef]
74. Lv, Y.D.; Wang, H.; Wang, X.F.; Bai, J.B. Synthesis, characterization and growing mechanism of monodisperse Fe_3O_4 microspheres. *J. Cryst. Growth* **2009**, *311*, 3445–3450. [CrossRef]
75. Chen, D.; Xu, R. Hydrothermal synthesis and characterization of nanocrystalline Fe_3O_4 powders. *Mater. Res. Bull.* **1998**, *33*, 1015–1021. [CrossRef]
76. Xu, C.; Teja, A.S. Continuous hydrothermal synthesis of iron oxide and PVA-protected iron oxide nanoparticles. *J. Supercrit. Fluids* **2008**, *44*, 85–91. [CrossRef]
77. Hugounenq, P.; Levy, M.; Alloyeau, D.; Lartigue, L.; Dubois, E.; Cabuil, V.; Ricolleau, C.; Roux, S.; Wilhelm, C.; Gazeau, F.; et al. Iron Oxide Monocrystalline Nanoflowers for Highly Efficient Magnetic Hyperthermia. *J. Phys. Chem. C* **2012**, *116*, 15702–15712. [CrossRef]
78. Müller, R.; Hergt, R.; Dutz, S.; Zeisberger, M.; Gawalek, W. Nanocrystalline Iron Oxide and Ba Ferrite Particles in the Superparamagnetism-Ferromagnetism Transition Range with Ferrofluid Applications. *J. Phys. Condens. Matter* **2006**, *18*, S2527–S2542. [CrossRef]
79. Faraji, M.; Yamini, Y.; Rezaee, M. Magnetic Nanoparticles: Synthesis, Stabilization, Functionalization, Characterization, and Applications. *J. Iran. Chem. Soc.* **2010**, *7*, 1–37. [CrossRef]
80. Xu, J.; Yang, H.B.; Fu, W.Y.; Du, K.; Sui, Y.M.; Chen, J.J.; Zeng, Y.; Li, M.H.; Zou, G. Preparation and Magnetic Properties of Magnetite Nanoparticles by Sol-Gel Method. *J. Magn. Magn. Mater.* **2007**, *309*, 307–311. [CrossRef]
81. Alexiou, C.; Arnold, W.; Klein, R.J.; Parak, F.G.; Hulin, P.; Bergemann, C.; Erhardt, W.; Wagenpfeil, S.; Lubbe, A.S. Locoregional Cancer Treatment with Magnetic Drug Targeting. *Cancer Res.* **2000**, *60*, 6641–6648. [PubMed]
82. Lubbe, A.S.; Bergemann, C.; Riess, H.; Schriever, F.; Reichardt, P.; Possinger, K.; Matthias, M.; Dorken, B.; Herrmann, F.; Gurtler, R.; et al. Clinical Experiences with Magnetic Drag Targeting: A Phase I Study With 4′-Epidoxorubicin in 14 Patients with Advanced Solid Tumors. *Cancer Res.* **1996**, *56*, 4686–4693. [PubMed]
83. Gleich, B.; Weizenecker, R. Tomographic Imaging Using the Nonlinear Response of Magnetic Particles. *Nature* **2005**, *435*, 1214–1217. [CrossRef] [PubMed]
84. Dutz, S.; Hergt, R. Magnetic Particle Hyperthermia—A Promising Tumour Therapy? *Nanotechnology* **2014**, *25*. [CrossRef] [PubMed]
85. Dutz, S.; Hergt, R.; Mürbe, J.; Töpfer, J.; Muller, R.; Zeisberger, M.; Andrä, W.; Bellemann, M.E. Magnetic Nanoparticles for Biomedical Heating Applications. *Z. Phys. Chem.* **2006**, *220*, 145–151. [CrossRef]
86. Bordelon, D.E.; Cornejo, C.; Gruttner, C.; Westphal, F.; DeWeese, T.L.; Ivkov, R. Magnetic Nanoparticle Heating Efficiency Reveals Magneto-Structural Differences when Characterized with Wide Ranging and High Amplitude Alternating Magnetic Fields. *J. Appl. Phys.* **2011**, *109*. [CrossRef]
87. Meng, L.; Gan, N.; Li, T.; Cao, Y.; Hu, F.; Zheng, L. A Three-Dimensional, Magnetic and Electroactive Nanoprobe for Amperometric Determination of Tumor Biomarkers. *Int. J. Mol. Sci.* **2011**, *12*, 362–375. [CrossRef] [PubMed]
88. Gonzalez-Fernandez, M.A.; Torres, T.E.; Andres-Verges, M.; Costo, R.; de la Presa, P.; Serna, C.J.; Morales, M.R.; Marquina, C.; Ibarra, M.R.; Goya, G.F. Magnetic nanoparticles for power absorption: Optimizing size, shape and magnetic properties. *J. Solid State Chem.* **2009**, *182*, 2779–2784. [CrossRef]
89. Bae, K.H.; Park, M.; Do, M.J.; Lee, N.; Ryu, J.H.; Kim, G.W.; Kim, C.; Park, T.G.; Hyeon, T. Chitosan Oligosaccharide-Stabilized Ferrimagnetic Iron Oxide Nanocubes for Magnetically Modulated Cancer Hyperthermia. *Acs Nano* **2012**, *6*, 5266–5273. [CrossRef] [PubMed]

90. Nishio, K.; Ikeda, M.; Gokon, N.; Tsubouchi, S.; Narimatsu, H.; Mochizuki, Y.; Sakamoto, S.; Sandhu, A.; Abe, M.; Handa, H. Preparation of size-controlled (30–100 nm) magnetite nanoparticles for biomedical applications. *J. Magn. Magn. Mater.* **2007**, *310*, 2408–2410. [CrossRef]
91. Verges, M.A.; Costo, R.; Roca, A.G.; Marco, J.F.; Goya, G.F.; Serna, C.J.; Morales, M.P. Uniform and Water Stable Magnetite Nanoparticles with Diameters Around the Monodomain-Multidomain Limit. *J. Phys. D* **2008**, *41*. [CrossRef]
92. Ristic, M.; Krehula, S.; Reissner, M.; Jean, M.; Hannoyer, B.; Music, S. Synthesis and properties of precipitated cobalt ferrite nanoparticles. *J. Mol. Struct.* **2017**, *1140*, 32–38. [CrossRef]
93. Khandhar, A.P.; Keselman, P.; Kemp, S.J.; Ferguson, R.M.; Goodwill, P.W.; Conolly, S.M.; Krishnan, K.M. Evaluation of PEG-coated iron oxide nanoparticles as blood pool tracers for preclinical magnetic particle imaging. *Nanoscale* **2017**, *9*, 1299–1306. [CrossRef] [PubMed]
94. Ludwig, R.; Stapf, M.; Dutz, S.; Müller, R.; Teichgräber, U.; Hilger, I. Structural Properties of Magnetic Nanoparticles Determine Their Heating Behavior—An Estimation of the In Vivo Heating Potential. *Nanoscale Res. Lett.* **2014**, *9*, 602. [CrossRef] [PubMed]
95. Hergt, R.; Dutz, S.; Müller, R.; Zeisberger, M. Magnetic Particle Hyperthermia: Nanoparticle Magnetism and Materials Development for Cancer Therapy. *J. Phys. Condens. Matter* **2006**, *18*, S2919–S2934. [CrossRef]
96. Lee, J.-H.; Jang, J.-T.; Choi, J.-S.; Moon, S.H.; Noh, S.-H.; Kim, J.-W.; Kim, J.-G.; Kim, I.-S.; Park, K.I.; Cheon, J. Exchange-Coupled Magnetic Nanoparticles for Efficient Heat Induction. *Nat. Nanotechnol.* **2011**, *6*, 418–422. [CrossRef] [PubMed]
97. Lottini, E.; Lopez-Ortega, A.; Bertoni, G.; Turner, S.; Meledina, M.; Van Tendeloo, G.; Fernandez, C.D.J.; Sangregorio, C. Strongly Exchange Coupled CorelShell Nanoparticles with High Magnetic Anisotropy: A Strategy toward Rare-Earth-Free Permanent Magnets. *Chem. Mater.* **2016**, *28*, 4214–4222. [CrossRef]
98. Phadatare, M.R.; Meshram, J.V.; Gurav, K.V.; Kim, J.H.; Pawar, S.H. Enhancement of Specific Absorption Rate by Exchange Coupling of the Core-Shell Structure of Magnetic Nanoparticles for Magnetic Hyperthermia. *J. Phys. D* **2016**, *49*. [CrossRef]
99. Zhang, Q.; Castellanos-Rubio, I.; Munshi, R.; Orue, I.; Pelaz, B.; Gries, K.I.; Parak, W.J.; del Pino, P.; Pralle, A. Model Driven Optimization of Magnetic Anisotropy of Exchange-Coupled Core-Shell Ferrite Nanoparticles for Maximal Hysteretic Loss. *Chem. Mater.* **2015**, *27*, 7380–7387. [CrossRef]
100. Barón, M.; Hellwich, K.H.; Hess, M.; Horie, K.; Jenkins, A.D.; Jones, R.G.; Kahovec, J.; Kratochvíl, P.; Metanomski, W.V.; Mormann, W.; et al. Glossary of Class Names of Polymers Based on Chemical Structure and Molecular Architecture (Iupac Recommendations 2009). *Pure Appl. Chem.* **2009**, *81*, 1131–1186. [CrossRef]
101. Laschewsky, A. Structures and Synthesis of Zwitterionic Polymers. *Polymers* **2014**, *6*, 1544–1601. [CrossRef]
102. Branch, D.W.; Wheeler, B.C.; Brewer, G.J.; Leckband, D.E. Long-term stability of grafted polyethylene glycol surfaces for use with microstamped substrates in neuronal cell culture. *Biomaterials* **2001**, *22*, 1035–1047. [CrossRef]
103. Sharma, S.; Johnson, R.W.; Desai, T.A. Evaluation of the Stability of Nonfouling Ultrathin Poly(ethylene glycol) Films for Silicon-Based Microdevices. *Langmuir* **2004**, *20*, 348–356. [CrossRef] [PubMed]
104. Yang, W.; Xue, H.; Li, W.; Zhang, J.; Jiang, S. Pursuing "Zero" Protein Adsorption of Poly(carboxybetaine) from Undiluted Blood Serum and Plasma. *Langmuir* **2009**, *25*, 11911–11916. [CrossRef] [PubMed]
105. Lalani, R.; Liu, L. Electrospun Zwitterionic Poly(Sulfobetaine Methacrylate) for Nonadherent, Superabsorbent, and Antimicrobial Wound Dressing Applications. *Biomacromolecules* **2012**, *13*, 1853–1863. [CrossRef] [PubMed]
106. Zhang, Z.; Chen, S.; Jiang, S. Dual-Functional Biomimetic Materials: Nonfouling Poly(carboxybetaine) with Active Functional Groups for Protein Immobilization. *Biomacromolecules* **2006**, *7*, 3311–3315. [CrossRef] [PubMed]
107. Jiang, S.; Cao, Z. Ultralow-Fouling, Functionalizable, and Hydrolyzable Zwitterionic Materials and Their Derivatives for Biological Applications. *Adv. Mater.* **2010**, *22*, 920–932. [CrossRef] [PubMed]
108. Alexis, F.; Pridgen, E.; Molnar, L.K.; Farokhzad, O.C. Factors Affecting the Clearance and Biodistribution of Polymeric Nanoparticles. *Mol. Pharm.* **2008**, *5*, 505–515. [CrossRef] [PubMed]
109. Jang, S.H.; Wientjes, M.G.; Lu, D.; Au, J.L.-S. Drug Delivery and Transport to Solid Tumors. *Pharm. Res.* **2003**, *20*, 1337–1350. [CrossRef] [PubMed]

110. Ma, H.; Hyun, J.; Stiller, P.; Chilkoti, A. "Non-Fouling" Oligo(ethylene glycol)-Functionalized Polymer Brushes Synthesized by Surface-Initiated Atom Transfer Radical Polymerization. *Adv. Mater.* **2004**, *16*, 338–341. [CrossRef]
111. Li, L.; Chen, S.; Zheng, J.; Ratner, B.D.; Jiang, S. Protein Adsorption on Oligo(ethylene glycol)-Terminated Alkanethiolate Self-Assembled Monolayers: The Molecular Basis for Nonfouling Behavior. *J. Phys. Chem. B* **2005**, *109*, 2934–2941. [CrossRef] [PubMed]
112. Knop, K.; Hoogenboom, R.; Fischer, D.; Schubert, U.S. Poly(ethylene glycol) in Drug Delivery: Pros and Cons as Well as Potential Alternatives. *Angew. Chem. Int. Ed.* **2010**, *49*, 6288–6308. [CrossRef] [PubMed]
113. Singer, S.J.; Nicolson, G.L. The Fluid Mosaic Model of the Structure of Cell Membranes. *Science* **1972**, *175*, 720–731. [CrossRef] [PubMed]
114. Zhou, Z.; Wang, L.; Chi, X.; Bao, J.; Yang, L.; Zhao, W.; Chen, Z.; Wang, X.; Chen, X.; Gao, J. Engineered Iron-Oxide-Based Nanoparticles as Enhanced T_1 Contrast Agents for Efficient Tumor Imaging. *ACS Nano* **2013**, *7*, 3287–3296. [CrossRef] [PubMed]
115. Wang, J.; Yuan, S.; Zhang, Y.; Wu, W.; Hu, Y.; Jiang, X. The effects of poly(zwitterions)s *versus* poly(ethylene glycol) surface coatings on the biodistribution of protein nanoparticles. *Biomater. Sci.* **2016**, *4*, 1351–1360. [CrossRef] [PubMed]
116. Muro, E.; Fragola, A.; Pons, T.; Lequeux, N.; Ioannou, A.; Skourides, P.; Dubertret, B. Comparing Intracellular Stability and Targeting of Sulfobetaine Quantum Dots with Other Surface Chemistries in Live Cells. *Small* **2012**, *8*, 1029–1037. [CrossRef] [PubMed]
117. Mayhew, E.; Harlos, J.P.; Juliano, R.L. The effect of polycations on cell membrane stability and transport processes. *J. Membr. Biol.* **1973**, *14*, 213–228. [CrossRef] [PubMed]
118. Lowe, A.B.; McCormick, C.L. Synthesis and Solution Properties of Zwitterionic Polymers. *Chem. Rev.* **2002**, *102*, 4177–4190. [CrossRef] [PubMed]
119. Kudaibergenov, S.; Jäger, W.; Laschewsky, A. Polymeric Betaines: Synthesis, Characterization, and Application. *Adv. Polym. Sci.* **2006**, *201*, 157–224.
120. Singh, P.K.; Singh, V.K.; Singh, M. Zwitterionic Polyelectrolytes: A Review. *e-Polymers* **2007**, *7*, 335–368. [CrossRef]
121. Tarannum, N.; Singh, M. Advances in synthesis of Sulfo and Carbo Analogues of Polybetaines: A Review. *Rev. Adv. Sci. Eng.* **2013**, *2*, 90–111. [CrossRef]
122. Ostermayer, B.; Albrecht, O.; Vogt, W. Polymerizable Lipid Analogs of Diacetylenic Phosphonic-Acids—Synthesis, Spreading Behavior and Polymerization at the Gas-Water Interface. *Chem. Phys. Lipids* **1986**, *41*, 265–291. [CrossRef]
123. Hamaide, T.; Germanaud, L.; Leperchec, P. New Polymeric Phosphonatobetaine, Phosphinatobetaine and Carboxybetaine. 1. Syntheses and Characterization by Ir Spectroscopy. *Makromol. Chem.* **1986**, *187*, 1097–1107. [CrossRef]
124. Al-Hamouz, O.C.S.; Ali, S.A. pH-responsive polyphosphonates using butler's cyclopolymerization. *J. Polym. Sci. Polym. Chem.* **2012**, *50*, 3580–3591. [CrossRef]
125. Xue, C.H.; Cai, F.F.; Liu, H.Y. Ultrasensitive fluorescent responses of water-soluble, zwitterionic, boronic acid-bearing, regioregular head-to-tail polythiophene to biological species. *Chem. Eur. J.* **2008**, *14*, 1648–1653. [CrossRef] [PubMed]
126. Yoshizawa, M.; Hirao, M.; Ito-Akita, K.; Ohno, H. Ion conduction in zwitterionic-type molten salts and their polymers. *J. Mater. Chem.* **2001**, *11*, 1057–1062. [CrossRef]
127. Stöber, W.; Fink, A.; Bohn, E. Controlled growth of monodisperse silica spheres in the micron size range. *J. Colloid Interface Sci.* **1968**, *26*, 62–69. [CrossRef]
128. Urena-Benavides, E.E.; Lin, E.L.; Foster, E.L.; Xue, Z.; Ortiz, M.R.; Fei, Y.; Larsen, E.S.; Kmetz, A.A., II; Lyon, B.A.; Moaseri, E.; et al. Low Adsorption of Magnetite Nanoparticles with Uniform Polyelectrolyte Coatings in Concentrated Brine on Model Silica and Sandstone. *Ind. Eng. Chem. Res.* **2016**, *55*, 1522–1532. [CrossRef]
129. Bach, L.G.; Islam, M.R.; Kim, J.T.; Seo, S.; Lim, K.T. Encapsulation of Fe_3O_4 magnetic nanoparticles with poly(methyl methacrylate) *via* surface functionalized thiol-lactam initiated radical polymerization. *Appl. Surf. Sci.* **2012**, *258*, 2959–2966. [CrossRef]

130. Zhang, X.A.; Lin, W.; Chen, S.; Xu, H.; Gu, H. Development of a Stable Dual Functional Coating with Low Non-specific Protein Adsorption and High Sensitivity for New Superparamagnetic Nanospheres. *Langmuir* **2011**, *27*, 13669–13674. [CrossRef] [PubMed]
131. Chen, Y.; Xiong, Z.; Zhang, L.; Zhao, J.; Zhang, Q.; Peng, L.; Zhang, W.; Ye, M.; Zou, H. Facile synthesis of zwitterionic polymer-coated core-shell magnetic nanoparticles for highly specific capture of N-linked glycopeptides. *Nanoscale* **2015**, *7*, 3100–3108. [CrossRef] [PubMed]
132. Von der Lühe, M.; Günther, U.; Weidner, A.; Grafe, C.; Clement, J.H.; Dutz, S.; Schacher, F.H. SPION@polydehydroalanine hybrid particles. *RSC Adv.* **2015**, *5*, 31920–31929. [CrossRef]
133. Pombo-Garcia, K.; Weiss, S.; Zarschler, K.; Ang, C.-S.; Hübler, R.; Pufe, J.; Meister, S.; Seidel, J.; Pietzsch, J.; Spiccia, L.; et al. Zwitterionic Polymer-Coated Ultrasmall SuperparamagneticIron Oxide Nanoparticles with low Protein Interaction and High Biocompatibility. *ChemNanoMat* **2016**, *2*, 959–971. [CrossRef]
134. Mincheva, R.; Stoilova, O.; Penchev, H.; Ruskov, T.; Spirov, I.; Manolova, N.; Rashkov, I. Synthesis of Polymer-Stabilized Magnetic Nanoparticles and Fabrication of Nanocomposite Fibers Thereof Using Electrospinning. *Eur. Polym. J.* **2008**, *44*, 615–627. [CrossRef]
135. Zhang, L.; Xue, H.; Gao, C.; Carr, L.; Wang, J.; Chu, B.; Jiang, S. Imaging and Cell Targeting Characteristics of Magnetic Nanoparticles Modified by a Functionalizable Zwitterionic Polymer with Adhesive 3,4-Dihydroxyphenyl-L-Alanine Linkages. *Biomaterials* **2010**, *31*, 6582–6588. [CrossRef] [PubMed]
136. Monteil, C.; Bar, N.; Bee, A.; Villemin, D. An Efficient Recyclable Magnetic Material for the Selective Removal of Organic Pollutants. *Beilstein J. Nanotechnol.* **2016**, *7*, 1447–1453. [CrossRef] [PubMed]
137. Korpany, K.V.; Majewski, D.D.; Chiu, C.T.; Cross, S.N.; Blum, A.S. Iron Oxide Surface Chemistry: Effect of Chemical Structure on Binding in Benzoic Acid and Catechol Derivatives. *Langmuir* **2017**, *33*, 3000–3013. [CrossRef] [PubMed]
138. Yabu, H.; Koike, R.; Hirai, D.Y. Preparation of Poly(Vinyl Catechol-*block*-Styrene) (PVCa-*b*-PSt) Stabilized Iron Oxide Nanoparticles by Ligand Exchange and Janus Particle Formation. *J. Nanosci. Nanotechnol.* **2017**, *17*, 9251–9256. [CrossRef]
139. Li, P.; Xiao, W.; Chevallier, P.; Biswas, D.; Ottenwaelder, X.; Fortin, M.-A.; Oh, J.K. Extremely Small Iron Oxide Nanoparticles Stabilized with Catechol-Functionalized Multidentate Block Copolymer for Enhanced MRI. *ChemistrySelect* **2016**, *1*, 4087–4091. [CrossRef]
140. Amstad, E.; Gehring, A.U.; Fischer, H.; Nagaiyanallur, V.V.; Hähner, G.; Textor, M.; Reimhult, E. Influence of Electronegative Substituents on the Binding Affinity of Catechol-Derived Anchors to Fe_3O_4 Nanoparticles. *J. Phys. Chem. C* **2011**, *115*, 683–691. [CrossRef]
141. Miles, W.C.; Huffstetler, P.P.; Goff, J.D.; Chen, A.Y.; Riffle, J.S.; Davis, R.M. Design of stable polyether-magnetite complexes in aqueous media: Effects of the anchor group, molecular weight, and chain density. *Langmuir* **2011**, *27*, 5456–5463. [CrossRef] [PubMed]
142. Goff, J.D.; Huffstetler, P.P.; Miles, W.C.; Pothayee, N.; Reinholz, C.M.; Ball, S.; Davis, R.M.; Riffle, J.S. Novel Phosphonate-Functional Poly(ethylene oxide)-Magnetite Nanoparticles Form Stable Colloidal Dispersions in Phosphate-Buffered Saline. *Chem. Mater.* **2009**, *21*, 4784–4795. [CrossRef]
143. Maliakal, A.; Katz, H.; Cotts, P.M.; Subramoney, S.; Mirau, P. Inorganic Oxide Core, Polymer Shell Nanocomposite as a High *K* Gate Dielectric for Flexible Electronics Applications. *J. Am. Chem. Soc.* **2005**, *127*, 14655–14662. [CrossRef] [PubMed]
144. Caruso, F. Nanoengineering of Particle Surfaces. *Adv. Mater.* **2001**, *13*, 11–22. [CrossRef]
145. Babu, K.; Dhamodharan, R. Synthesis of Polymer Grafted Magnetite Nanoparticle with the Highest Grafting Density via Controlled Radical Polymerization. *Nanoscale Res. Lett.* **2009**, *4*, 1090–1102. [CrossRef] [PubMed]
146. Hassan, P.A.; Rana, S.; Verma, G. Making Sense of Brownian Motion: Colloid Characterization by Dynamic Light Scattering. *Langmuir* **2015**, *31*, 3–12. [CrossRef] [PubMed]
147. Lu, X.-Y.; Wu, D.-C.; Li, Z.-J.; Chen, G.-Q. Polymer Nanoparticles. *Prog. Mol. Biol. Transl. Sci.* **2011**, *104*, 299–323. [PubMed]
148. Lim, J.; Yeap, S.P.; Che, H.X.; Low, S.C. Characterization of magnetic nanoparticle by dynamic light scattering. *Nanoscale Res. Lett.* **2013**, *8*, 381. [CrossRef] [PubMed]
149. Mestrom, L.; Lenders, J.J.M.; de Groot, R.; Hooghoudt, T.; Sommerdijk, N.A.J.M.; Artigas, M.V. Stable ferrofluids of magnetite nanoparticles in hydrophobic ionic liquids. *Nanotechnology* **2015**, *26*, 1–9. [CrossRef] [PubMed]

150. Wang, F.; Zhang, X.; Liu, Y.; Lin, Z.Y.; Liu, B.; Liu, J. Profiling Metal Oxides with Lipids: Magnetic Liposomal Nanoparticles Displaying DNA and Proteins. *Angew. Chem. Int. Ed.* **2016**, *55*, 12063–12067. [CrossRef] [PubMed]
151. Bonnaud, C.; Monnier, C.A.; Demurtas, D.; Jud, C.; Vanhecke, D.; Montet, X.; Hovius, R.; Lattuada, M.; Rothen-Rutishauser, B.; Petri-Fink, A. Insertion of Nanoparticle Clusters into Vesicle Bilayers. *ACS Nano* **2014**, *8*, 3451–3460. [CrossRef] [PubMed]
152. Hofmann, D.; Tenzer, S.; Bannwarth, M.B.; Messerschmidt, C.; Glaser, S.-F.; Schild, H.; Landfester, K.; Mailaender, V. Mass Spectrometry and Imaging Analysis of Nanoparticle-Containing Vesicles Provide a Mechanistic Insight into Cellular Trafficking. *ACS Nano* **2014**, *8*, 10077–10088. [CrossRef] [PubMed]
153. Clogston, J.D.; Patri, A.K. Zeta Potential Measurement. In *Characterization of Nanoparticles Intended for Drug Delivery*; McNeil, S.E., Ed.; Humana Press: Totowa, NJ, USA, 2011; pp. 63–70.
154. Monopoli, M.P.; Aberg, C.; Salvati, A.; Dawson, K.A. Biomolecular Coronas Provide the Biological Identity of Nanosized Materials. *Nat. Nanotechnol.* **2012**, *7*, 779–786. [CrossRef] [PubMed]
155. López, J.; González, F.; Bonilla, F.; Zambrano, G.; Gomez, M. Synthesis and characterization of Fe_3O_4 magnetic nanofluid. *Rev. LatinAm. Metal. Mat.* **2010**, *30*, 60–66.
156. Mansfield, E.; Tyner, K.M.; Poling, C.M.; Blacklock, J.L. Determination of Nanoparticle Surface Coatings and Nanoparticle Purity Using Microscale Thermogravimetric Analysis. *Anal. Chem.* **2014**, *86*, 1478–1484. [CrossRef] [PubMed]
157. Liu, S.; Han, Y.; Qiao, R.; Zeng, J.; Jia, Q.; Wang, Y.; Gao, M. Investigations on the Interactions between Plasma Proteins and Magnetic Iron Oxide Nanoparticles with Different Surface Modifications. *J. Phys. Chem. C* **2010**, *114*, 21270–21276. [CrossRef]
158. Qin, L.; Xu, Y.; Han, H.; Liu, M.; Chen, K.; Wang, S.; Wang, J.; Xu, J.; Li, L.; Guo, X. β-Lactoglobulin (BLG) binding to highly charged cationic polymer-grafted magnetic nanoparticles: Effect of ionic strength. *J. Colloid Interface Sci.* **2015**, *460*, 221–229. [CrossRef] [PubMed]
159. Zhao, T.; Chen, K.; Gu, H. Investigations on the Interactions of Proteins with Polyampholyte-Coated Magnetite Nanoparticles. *J. Phys. Chem. B* **2013**, *117*, 14129–14135. [CrossRef] [PubMed]
160. Joseph, D.; Sachar, S.; Kishore, N.; Chandra, S. Mechanistic insights into the interactions of magnetic nanoparticles with bovine serum albumin in presence of surfactants. *Colloids Surf. B Biointerfaces* **2015**, *135*, 596–603. [CrossRef] [PubMed]
161. Alfrey, T.; Fuoss, R.M.; Morawetz, H.; Pinner, H. Amphoteric Polyelectrolytes. II. Copolymers of Methacrylic Acid and Diethylaminoethyl Methacrylate[1]. *J. Am. Chem. Soc.* **1952**, *74*, 438–441. [CrossRef]
162. Alfrey, T.; Morawetz, H.; Fitzgerald, E.B.; Fuoss, R.M. Synthetic electrical analog of Proteins[1]. *J. Am. Chem. Soc.* **1950**, *72*, 1864. [CrossRef]
163. Ladenheim, H.; Morawetz, H. A new type of polyampholyte: Poly(4-vinyl pyridine betaine). *J. Polym. Sci.* **1957**, *26*, 251–254. [CrossRef]
164. Billing, M.; Gräfe, C.; Saal, A.; Biehl, P.; Clement, J.H.; Dutz, S.; Weidner, S.; Schacher, F.H. Zwitterionic Iron Oxide (γ-Fe_2O_3) Nanoparticles Based on P(2VP-*grad*-AA) Copolymers. *Macromol. Rapid Commun.* **2017**, *38*. [CrossRef] [PubMed]
165. Billing, M.; Schacher, F.H. ATRP of *tert*-Butoxycarbonylaminomethyl acrylate (*t*BAMA): Well-Defined Precursors for Polyelectrolytes of Tunable Charge. *Macromolecules* **2016**, *49*, 3696–3705. [CrossRef]
166. Yuan, J.J.; Armes, S.P.; Takabayashi, Y.; Prassides, K.; Leite, C.A.P.; Galembeck, F.; Lewis, A.L. Synthesis of Biocompatible Poly[2-(methacryloyloxy)ethyl phosphorylcholine]-Coated Magnetite Nanoparticles. *Langmuir* **2006**, *22*, 10989–10993. [CrossRef] [PubMed]
167. Hildebrand, V.; Heydenreich, M.; Laschewsky, A.; Möller, H.M.; Müller-Buschbaum, P.; Papadakis, C.M.; Schanzenbach, D.; Wischerhoff, E. "Schizophrenic" self-assembly of dual thermoresponsive block copolymers bearing a zwitterionic and a non-ionic hydrophilic block. *Polymer* **2017**, *122*, 347–357. [CrossRef]
168. Zhu, A.; Yuan, L.; Dai, S. Preparation of Well-Dispersed Superparamagnetic Iron Oxide Nanoparticles in Aqueous Solution with Biocompatible *N*-Succinyl-*O*-carboxymethylchitosan. *J. Phys. Chem. C* **2008**, *112*, 5432–5438. [CrossRef]
169. Demillo, V.G.; Zhu, X. Zwitterionic Amphiphile Coated Magnetofluorescent Nanoparticles—Synthesis, Characterization and Tumor Cell Targeting. *J. Mater. Chem. B* **2015**, *3*, 8328–8336. [CrossRef] [PubMed]

170. Xiao, W.; Lin, J.; Li, M.; Ma, Y.; Chen, Y.; Zhang, C.; Li, D.; Gu, H. Prolonged *in vivo* circulation time by zwitterionic modification of magnetite nanoparticles for blood pool contrast agents. *Contrast Media Mol. Imaging* **2012**, *7*, 320–327. [CrossRef] [PubMed]
171. Von der Lühe, M.; Weidner, A.; Dutz, S.; Schacher, F.H. Reversible Electrostatic Adsorption of Polyelectrolytes and Bovine Serum Albumin onto Polyzwitterion-Coated Magnetic Multicore Nanoparticles: Implications for Sensing and Drug Delivery. *Appl. Nano Mater.* **2017**. in Revision. [CrossRef]
172. Yeh, C.-H.; Chen, S.-H.; Li, D.-T.; Lin, H.-P.; Huang, H.-J.; Chang, C.-I.; Shih, W.-L.; Chern, C.-L.; Shi, F.-K.; Hsu, J.-L. Magnetic Bead-Based Hydrophilic Interaction Liquid Chromatography for Glycopeptide Enrichments. *J. Chromatogr. A* **2012**, *1224*, 70–78. [CrossRef] [PubMed]
173. Wang, C.; Wang, L.; Yang, W. Preparation and Characterization of Functional Inorganic/Organic Composite Microspheres via Electrostatic Interaction. *J. Colloid Interface Sci.* **2009**, *333*, 749–756. [CrossRef] [PubMed]
174. Zhao, Y.; Chen, Y.; Xiong, Z.; Sun, X.; Zhang, Q.; Gan, Y.; Zhang, L.; Zhang, W. Synthesis of Magnetic Zwitterionic-Hydrophilic Material for the Selective Enrichment of N-Linked Glycopeptides. *J. Chromatogr. A* **2017**, *1482*, 23–31. [CrossRef] [PubMed]
175. Fidale, L.C.; Nikolajski, M.; Rudolph, T.; Dutz, S.; Schacher, F.H.; Heinze, T. Hybrid Fe_3O_4@amino Cellulose Nanoparticles in Organic Media—Heterogeneous Ligands for Atom Transfer Radical Polymerizations. *J. Colloid Interface Sci.* **2013**, *390*, 25–33. [CrossRef] [PubMed]

Publication P3

“Reversible Adsorption of Methylene Blue as Cationic Model Cargo onto Polyzwitterionic Magnetic Nanoparticles”

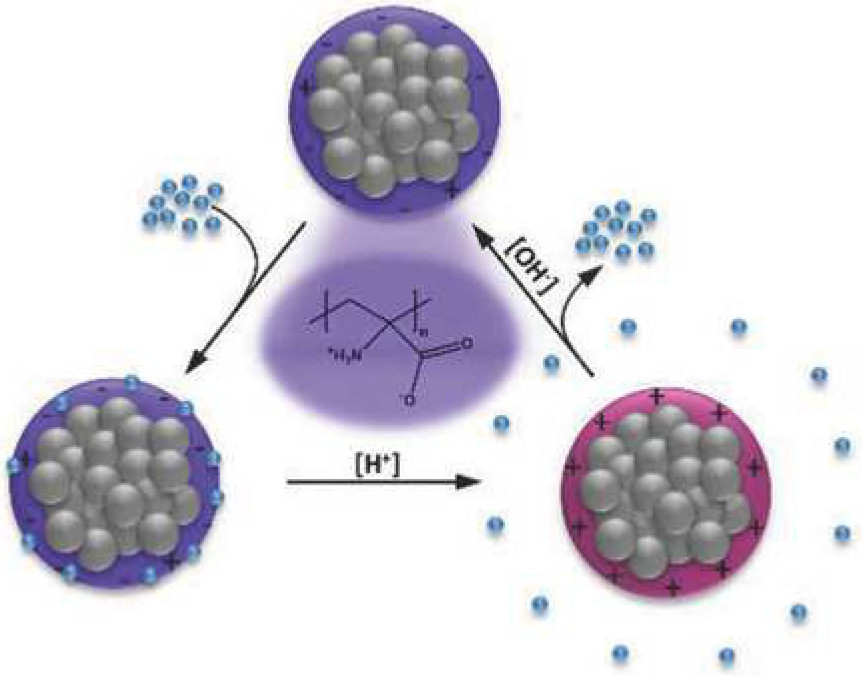

P. Biehl,‡ M. von der Lühe,‡ F. H. Schacher
‡Both authors contributed equally to this work

Macromol. Rapid Commun. **2018**, *39*, 1800017

COMMUNICATION

Hybrid Materials

Macromolecular
Rapid Communications
www.mrc-journal.de

Reversible Adsorption of Methylene Blue as Cationic Model Cargo onto Polyzwitterionic Magnetic Nanoparticles

*Philip Biehl, Moritz von der Lühe, and Felix H. Schacher**

The reversible electrostatic adsorption of the cationic dye methylene blue (MB) as a model compound to polydehydroalanine (PDha)-coated magnetic multicore nanoparticles (MCNP) is presented. The pH responsiveness of the zwitterionic coating material enables reversible switching of the net surface charge of the PDha@MCNP hybrid particles by changes in pH and thus allows reversible adsorption of MB at neutral pH and desorption at low pH values. The resulting hybrid materials can be very interesting systems in the context of water purification, and the reversible adsorption is studied using UV–vis spectroscopy under varying surrounding conditions. The particles are characterized using dynamic light scattering, zeta potential measurements, transmission electron microscopy, and thermogravimetric analysis.

1. Introduction

Due to their unique properties, i.e., the possibility of magnetic separation and magnetic targeting by external magnetic fields, magnetic nanoparticles (MNP) have gained tremendous interest for numerous fields of applications in recent years.[1–3] Besides technical applications (e.g., waste water treatment[4] and catalysis[5]) such materials are extensively investigated with regard to biomedical applications (e.g., magnetic resonance imaging,[6,7] drug delivery,[8–10] and hyperthermia[11–13]). Polymeric surfactants are widely used to functionalize the surface of MNP in order to improve dispersion stability and introduce additional functional groups or even targeting moieties.[5,14,15] In this context, polyzwitterions as a subclass of polyelectrolytes are of interest as coating materials since they are capable to increase dispersion stability while at the same time reduce unspecific protein adsorption, or exhibit pH-dependent surface charge.[16,17] In many application fields, the ability to host small guest molecules is desirable, e.g., in heavy metal removal from aqueous media,[18] drug delivery, or catalysis. In particular, wastewater treatment aims at the removal of heavy metal ions, whereas reversible drug binding and release is desired in the context of drug delivery. Regarding separation applications, several examples describe the use of magnetic nanoparticles with polyzwitterionic surfaces for the use of biomolecule adsorption (e.g., glycopeptides) from complex matrices for analytical investigations.[19–21] However, potential recovery of the respective nanomaterials and use in several consecutive adsorption/desorption processes has not been described to our knowledge. Even though iron oxide-based nanomaterials already received great attention as a potential adsorbent in wastewater treatment, the synthesis of the respective materials still poses a challenge regarding production costs. Thus, a system which is capable of reversible adsorption due to electrostatic interactions and which ideally can be used multiple times in adsorption/desorption processes is highly desirable.

We recently reported on the successful coating of multicore magnetic iron oxide nanoparticles (MCNP) using polydehydroalanine (PDha), a polyzwitterionic material.[17] Further, it could be demonstrated that the observed charge reversibility of the resulting PDha@MCNP can be exploited for reversible electrostatic adsorption of both polyanions and polycations. However, questions regarding the general use of this system and also the possibility to perform such adsorption/desorption cycles multiple times are still unanswered. Herein, we extend this approach to a cationic model dye, methylene blue (MB), to investigate whether such hybrid core–shell nanoparticles are of interest with regard to water purification strategies. MB can easily be adsorbed to the negatively charged PDha@MCNP particles at neutral pH due to attractive electrostatic interactions, and, in addition, can easily be detected and quantified using UV–vis spectroscopy. MB in this study serves as model system and we demonstrate multiple reversible adsorption/desorption cycles under different conditions (pH) and in dependence of the amount of PDha@MCNP hybrid nanoparticles added to the solution (**Scheme 1**).

2. Experimental Section

All chemicals and solvents were purchased from Sigma-Aldrich, Merck, or ABCR in analytical grade and used as received. *N*-(*tert*-butoxycarbonyl)-D-serine methyl ester was purchased from Carbolution chemicals. All deuterated solvents were purchased from Eurisotop or Deutero.

P. Biehl, M. von der Lühe, Prof. F. H. Schacher
Institute of Organic Chemistry and Macromolecular Chemistry (IOMC), Friedrich Schiller University Jena
Humboldtstraße 10, 07743 Jena, Germany
E-mail: felix.schacher@uni-jena.de

P. Biehl, M. von der Lühe, Prof. F. H. Schacher
Jena Center for Soft Matter (JCSM)
Friedrich Schiller University Jena
Philosophenweg 7, 07743 Jena, Germany

The ORCID identification number(s) for the author(s) of this article can be found under https://doi.org/10.1002/marc.201800017.

DOI: 10.1002/marc.201800017

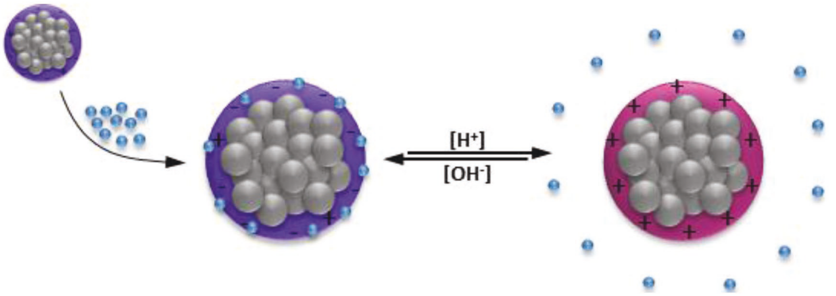

Scheme 1. Adsorption and pH induced desorption of MB to PDha@MCNP, followed by magnetic separation and recovery of PDha@MCNP.

2.1. Synthesis of MCNP

Multicore iron oxide nanoparticles were synthesized by slowly adding a 1 M $NaHCO_3$ solution to an $FeCl_2/FeCl_3$ solution (total Fe-concentration 1.25 M; Fe^{2+}/Fe^{3+} ratio = 1:1.3) at a rate of 0.75 mL min^{-1} under permanent stirring up to pH = 8, leading to the formation of a brownish precipitate. Afterward, the solution was boiled for 5 min to form an almost black precipitate. The magnetic nanoparticles were then washed twice with distilled water.[22] Dynamic light scattering: $\langle R_h \rangle_{n,app} = 51$ nm.

Thermogravimetric analysis (TGA, 30–800 °C, atmosphere: synthetic air): 5% wt. loss (Figure S1, Supporting Information).

2.2. Synthesis of *tert*-butoxycarbonylaminomethylacrylate (*t*BAMA)

10 g (45.6 mmol) of *N*-(*tert*-butoxycarbonyl)-D-serine methyl ester was dissolved in 200 mL dichloromethane. To this solution, 6 mL (77.5 mmol, 1.7 equiv.) of methanesulfonyl chloride was added. The reaction mixture was cooled with an ice water bath to 0 °C and 23 mL (165.9 mmol, 3.6 equiv.) of triethylamine was added dropwise (within 30 min), meanwhile a change of the color of the solution from clear to slightly orange could be observed. After the complete addition, the solution was stirred at 0 °C for 1 h, brought to room temperature and stirred again for another 2 h. The reaction mixture was then washed with a 1% solution of potassium bisulfate in water until the organic phase was neutral. The organic phase was dried over Na_2SO_4 and the solvent was removed under reduced pressure. The crude product was purified via column chromatography with silica gel and a mixture of 20% ethyl acetate and 80% *n*-hexane as mobile phase.[23] Yield: 80%

^{1}H NMR (300 MHz, $CDCl_3$, δ): 7.2 (s, 1H, NH), 6.1 (s, 1H, CH_2), 5.7 (d, 1H, CH_2), 3.8 (s, 3H, OCH_3), 1.5 (s, 9H, *t*-butyl)

2.3. Synthesis of Polydehydroalanine (PDha)

In a typical reaction, 8 g of *t*BAMA was dissolved in a 8 mL of a solution of Lucirin-diphenyl(2,4,6-trimethylbenzoyl)phosphine oxide (TPO) in 1,4-dioxane. The mixture was irradiated using a 100 W UV-cube for 5 min. The resulting P*t*BAMA was precipitated in a mixture of hexane and methyl acetate (4:1), filtered off, and dried under vacuum. Several batches of this reaction were combined afterward. Yield: 52%

Size exclusion chromatography (SEC) ($CHCl_3$, poly(methyl methacrylate) (PMMA) calibration): $M_n = 22\,800$ g mol^{-1}; $Đ = 2.94$

^{1}H-NMR of P*t*BAMA: (300 MHz, D_2O/NaOD, pH = 8; δ): 7.6 (s, NH_2), 3.3 ppm (s, 3H, O-CH_3), 2.4 (m, 2H, CH_2), 1.4 ppm(s, 9H, *t*Butyl).

10 g P*t*BAMA was dissolved in 160 mL trifluoroacetic acid (TFA) and 40 mL H_2O. The mixture was stirred at 50 °C for 1 h and afterward precipitated in MeOH. The dried polyelectrolyte was then dissolved in 80 mL 1,4-dioxane and a solution of 10.24 g LiOH in 80 mL H_2O was added. The mixture was stirred under reflux (100 °C) for 3 h and neutralized with diluted HCl_{aq}. During the neutralization, PDha precipitated.[24] The signals for the methyl ester as well as for the *tert*-butyl group are missing in the ^{1}H-NMR spectrum after successful deprotection of P*t*BAMA. Yield: 97%

^{1}H-NMR of PDha: (300 MHz, D_2O/NaOD, pH = 8; δ): 1.8–2.8 (m, 2H, CH_2)

2.4. PDha@MCNP

3.2 g PDha was dissolved in 200 mL micropure water/NaOH at pH = 12. The solution was titrated to pH = 5 with 0.1 M HCl. 40 mL of a dispersion of MCNP (10 g L^{-1}) was added and dispersed in the PDha solution. The mixture was ultrasonicated at 50 °C for 1 h. The resulting PDha@MCNP particles were magnetically separated afterward, the supernatant was removed and the particles were redispersed in MilliQ water using ultrasonication. This procedure was repeated five times.[24] Dynamic light scattering: $\langle R_h \rangle_{n,app} = 51$ nm

TGA (30–800 °C, atmosphere: synthetic air): 12% wt. loss (Figure S1, Supporting Information), leading to a PDha content for PDha@MCNP of 7%.

3. Results and Discussion

The synthesis and characterization of PDha@MCNP has been described earlier: briefly, PDha was dissolved at pH = 12, titrated to pH = 5 and, subsequently, MCNP were dispersed in the solution. After 1 h of ultrasonication at 50 °C, the resulting PDha@MCNP particles were magnetically separated and washed five times with micropure water. The magnetic multicore nanoparticles consist of primary cores of about 10 nm (X-ray diffraction), which form clusters of about 50 nm and mainly consist of maghemite (γ-Fe_2O_3). Subsequent TGA revealed a PDha content of 7% in accordance with earlier studies, corresponding to a shell thickness of ≈4 nm. Transmission electron microscopy images clearly reveal the appearance of an organic shell around the particles after the coating process (Figure S3, Supporting Information). We have already described the pH-dependent stability of the PDha shell as well as the pH dependent zeta potential of PDha@MCNP.[17] Briefly, the particles exhibit a

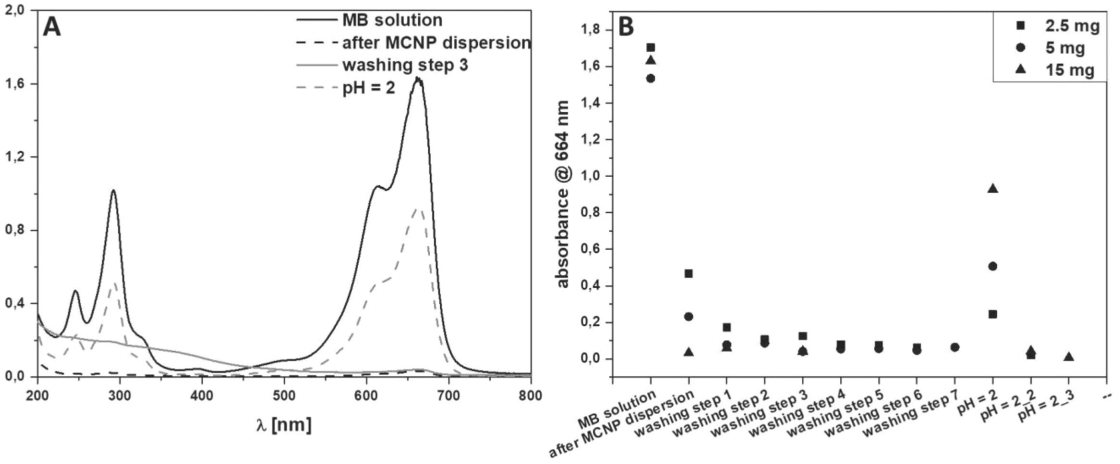

Figure 1. A) UV–vis spectra of methylene blue solution prior to (solid black line) and after dispersion of 15 mg PDha@MCNP (dashed black line), supernatants of washing steps of the MCNP (solid gray line), and solution of MB desorbed from PDha@MCNP (dashed gray line). B) Intensities of MB main absorbance band before and after dispersion of different amounts of PDha@MCNP, washing steps, and desorbing solutions.

zeta potential of +14.9 mV at pH = 2, +13.6 mV at pH = 4, and –22.2 mV at pH = 7.

3.1. Adsorption of MB to Different Amounts of PDha@MCNP

For the adsorption experiments, each 0.25, 0.5, and 1.5 mL of a PDha@MCNP dispersion in micropure water ($c = 10$ g L^{-1}) were magnetically separated and dispersed in 1 mL of a 0.008 g L^{-1} MB solution, so that MB solutions with 2.5, 5, and 15 mg PDha@MCNP content were obtained. The samples were vortexed for 20 s, magnetically separated, and washed several times with 1 mL micropure water until the main absorbance band of MB at 664 nm did not further decrease. Subsequently, the particles were dispersed in each 1 mL of micropure water/HCl at pH = 2, and again magnetically separated after 20 s of vortexing. **Figure 1**A exemplarily shows UV–vis spectra of the MB solution before and after dispersion of PDha@MCNP, the supernatant of the last washing step, and the solution with the desorbed MB. For all three samples, the intensity of the main absorbance band of MB drastically decreased after magnetic separation of the particles and the remaining MB absorption decreases with increasing PDha@MCNP concentration (Figure 1B). The corresponding molar ratios of MB:Dha units in the polymeric shell for the different samples were calculated to 1:76 (2.5 mg PDha@MCNP), and this led to a loading of 1:98, corresponding to 78% adsorption efficiency. In case of 5 mg PDha@MCNP the initial ratio is 1:161 and after adsorption a value of 1:186 was found, corresponding to an efficiency of 87%. Finally, for 15 mg PDha@MCNP the initial ratio is given by 1:434 prior and 1:455 after adsorption, leading to 95% of the maximum loading. However, these ratios have to be considered as rather rough approximations as parts of the polymer are attached to the nanoparticle surface and are thus not available for MB binding. After washing of the particles the supernatant showed only minor absorbance and subsequent dispersion in solutions at pH = 2 resulted in a visible blue coloration after PDha@MCNP were magnetically separated for all samples investigated (**Figure 2**A).

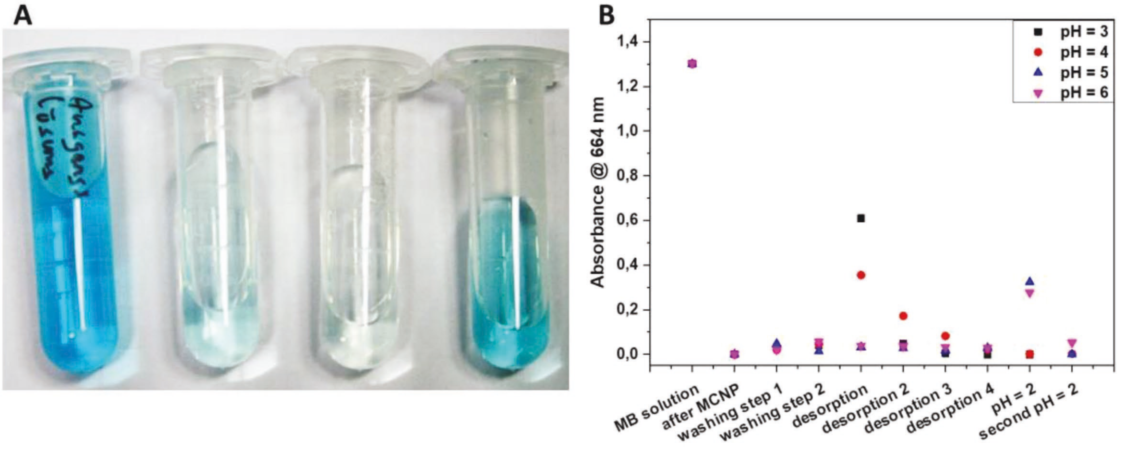

Figure 2. A) Photograph of MB solutions (from left to right: prior to PDha@MCNP dispersion, after MCNP dispersion, pH = 7 washing step, pH = 4 desorption) and B) intensities of MB main absorbance band before and after dispersion of PDha@MCNP, washing step, and desorbing solutions at different pH values.

Here again the intensity of the MB main absorption band increases with increasing amount of PDha@MCNP. After an additional second treatment of the PDha@MCNP dispersion with pH = 2 solutions, no remaining MB absorbance in UV–vis was found. This indicates that a rapid MB desorption within one washing step at pH = 2 can be achieved.

As the maximum loading of PDha@MCNP with MB was of interest, solutions with different concentrations of MB (0.55, 0.31, 0.053, 0.031, and 0.008 mg mL^{-1}) were prepared and 2.5 mg of PDha@MCNP was exposed to 1 mL of the respective solution. As the solutions were too concentrated for a sufficient determination of the amount of adsorbed MB using UV–vis, the samples were diluted prior to UV–vis measurements and the respective mass of MB which could be detected was adjusted accordingly. The results show an increased loading with increasing MB concentration and for the system used here the threshold for the loading of MB onto PDha@MCNP was determined to be ≈1:15 (MB:Dha, Table S4, Supporting Information).

Table 1. Calculated MB amounts and deviations.

pH	Initial amount of MB[a)] [mg]	Sum of remaining and desorbed MB[a)] [mg]	Deviation [%]
2	0.008	0.005	39
3	0.007	0.004	51
4	0.007	0.004	58
5	0.007	0.002	74
6	0.007	0.002	75

[a)] Calculated from the UV–vis absorbance of the respective solution.

3.2. pH-Dependent Desorption

Since pH = 2 represents rather harsh conditions, we also investigated milder desorption conditions. Therefore, each 5 mg of PDha@MCNP was used for MB adsorption as described before, washed with 1 mL micropure water two times, and dispersed for 20 s at different pH values for the desorption (four times respectively—pH values of 3, 4, 5, and 6 were investigated). The absorption intensities at 664 nm are shown in Figure 2B. The initial MB solution showed an intensity maximum at 664 nm of I = 1.3 in UV–vis-absorption, which vanished after MCNP treatment for all samples. Furthermore, all washing solutions show only negligible absorption. After treatment with the respective desorption solutions, the UV–vis absorption is increased for pH 3–4 with a clear dependency on the pH being observable. For the sample at pH = 5 and 6, the UV–vis-absorbance remains in the range of micropure water after washing of the particles, indicating that nearly no desorption took place. Higher pH values lead to a deprotonation of the −COOH moiety, resulting in a polyanion while at neutral pH values PDha is a polyzwitterion due to partial protonation of the amine. At low pH values, protonation of both the carboxylic acid and the amine leads to the formation of a polycation. We have shown this using pH-dependent zeta potential measurements of PDha@MCNP, revealing a surface charge of 12 mV at pH 6 and + 10 mV at pH 4. Therefore, the apparent isoelectric point of the hybrid particles is located between pH 4 and 6 and provides a reasonable explanation for successful detachment beginning at pH = 5 or lower. A second desorption step shows minor MB amounts for all samples. In the third desorption step no MB can be detected, except for the sample at pH = 4. After four desorption steps, the samples were dispersed in water at pH = 2 to desorb the remaining MB from the particles. An increase in MB UV–vis absorption can be observed for the pH 5 and 6 samples. However, the overall amount of released MB is lower compared to samples where release has initially been carried out at pH 3 and pH 4. In summary, in direct comparison to desorption at pH = 2, multiple desorption steps are necessary to completely desorb the MB at increasing pH. Strikingly, the sum of remaining MB in the initial solution and MB after desorption from the MCNP is distinctly smaller than the initial amount of MB present in solution (**Table 1**, for detailed calculations see the Supporting Information). For pH 2–4, the deviations are in the range of 39–58%. We assume that parts

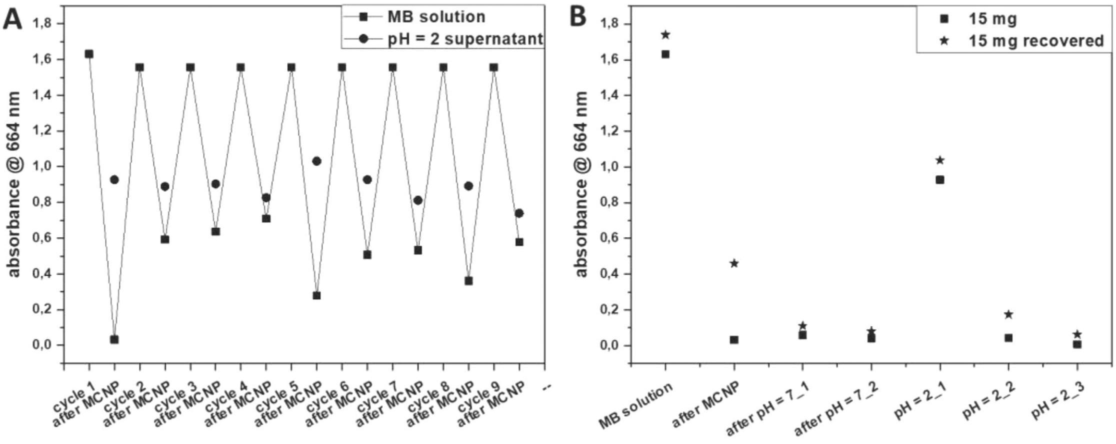

Figure 3. A) Nine consecutive cycles of a MB solution before and after dispersion of PDha@MCNP (black squares) and pH = 2 solutions after desorption of MB (black dots). B) Initial adsorption/desorption cycle of a 15 mg sample (black squares) and cycle after 24 h recovery in micropure water (black stars).

of MB are irreversibly bound to the PDha shell or the MCNP surface. After dissolution of the iron oxide cores in *conc*. HCl, a small amount of MB can be detected in UV–vis, but not quantified due to the high absorbance of $FeCl_3$ (Figure S5, Supporting Information).

3.3. Reversibility

To investigate the reversibility of the adsorption/desorption process, the initial 15 mg sample was repeatedly dispersed in MB (0.008 mg mL^{-1}) solutions and aqueous solutions at pH = 2, with one washing step with micropure water in between for nine additional cycles. Whereas the remaining MB absorbance in the initial solution was decreased to 0.03 after the first cycle, the remaining absorbance is increased to 0.6–0.7 after the following three cycles (**Figure 3**). In contrast to that, the absorbance of different solutions created during desorption remains nearly constant at 0.9. After the fourth cycle, the sample was allowed to stand in micropure water for 15 h, and in the following cycle the remaining absorbance of the MB solution after MCNP treatment was again decreased to 0.28, and the absorbance of the desorption solution was increased to 1.0. This indicates a partial regeneration of the system with time. During the following cycles, both values change back to the range of the initial cycles (2–4).

Again, the deviation between the initial solution and the sum of remaining and desorbed MB was calculated and found to be 44% during the first cycle, but only 3–22% in the following cycles. Together with the decreasing adsorption efficacy, this supports our previous assumption of a certain amount of irreversibly bound MB.

The dispersion stability of PDha@MCNP was altered during the adsorption of MB. Whereas magnetic separation of the particles before MB adsorption took 20 min, the particles can be separated within a few minutes after the adsorption of MB. After desorption of MB, the initial dispersion stability is retained. The zeta potential of the particles prior to, after adsorption of MB, and after desorption of MB at pH = 2 and redispersion in micropure water was also investigated. Prior to adsorption, the measurements revealed a zeta potential of -41.8 ± 20.2 mV, which was slightly decreased to -38.3 ± 9.5 mV upon adsorption of MB. After the desorption at pH = 2, and subsequent redispersion of the particles at neutral pH, the zeta potential was slightly decreased to -34.9 ± 4.8 mV, which we dedicate to slight remaining protonation of the shell due to the desorption at pH = 2. Considering the rather large error for all zeta potential measurements it can be said that the overall zeta potential of the particles (and with that the colloidal stability) is not significantly affected during adsorption and desorption processes shown here, which we regard as important considering multiple cycles of use. Further dynamic light scattering investigations indicate that the hydrodynamic radius of the particles is not affected by the adsorption of MB (Figure S2, Supporting Information). Although the shell stability under the given pH values was demonstrated previously, a sample of PDha@MCNP was characterized via TGA after the adsorption/desorption procedure and showed a decrease of the PDha amount of 0.5% which is within or at least close to the error of the measurement technique.

4. Conclusions

In summary, we synthesized zwitterionic PDha@MCNP hybrid core–shell nanoparticles and demonstrated that this system is capable of reversible adsorption of small cationic molecules—hereby using methylene blue as model compound. Upon changing the pH of the surrounding medium, MB can be readily desorbed. While at pH = 2 the cargo is desorbed within seconds due to protonation of the zwitterionic shell material (PDha), at higher pH values complete desorption could only be realized in multiple steps and pH values above pH = 4 show no efficient cargo release. Whereas the desorption at pH = 2 is interesting for potential technical applications such as water purification, partial desorption at higher pH values might be interesting in the context of biomedical applications, e.g., to release cargo over a defined time period. Furthermore, we demonstrated the reversibility of the adsorption/desorption process by performing nine consecutive cycles and also provided first hints toward time dependent regeneration of the system. After the first cycle, a major decrease in adsorption efficacy can be observed, but in the following cycles the efficiency remains nearly constant. Although desorption already takes place at increased pH if compared to previous experiments with polyelectrolytes, the required conditions are still not in the region of biomedical applications. In upcoming experiments, we want to investigate additional pH dependent polyzwitterions which will shift the pH regime for adsorption/desorption cycles to different values.

Supporting Information

Supporting Information is available from the Wiley Online Library or from the author.

Acknowledgements

P.B. and M.v.d.L. contributed equally to this work. The authors thank Silvio Dutz and Andreas Weidner (both Technische Universität Ilmenau) for the synthesis of the MCNP. M.v.d.L. and F.H.S. are grateful for financial support from the Deutsche Forschungsgesellschaft in the framework of the priority program SPP1681 (SCHA1640/7-1). P.B. is grateful for a fellowship (Landesgraduiertenstipendium of the Friedrich Schiller University Jena).

Conflict of Interest

The authors declare no conflict of interest.

Keywords

hybrid materials, magnetic nanoparticles, polyzwitterions, reversible adsorption

Received: January 8, 2018
Revised: February 10, 2018

---

[1] M. K. Lima-Tenório, E. A. Gómez Pineda, N. M. Ahmad, H. Fessi, A. Elaissari, *Int. J. Pharm.* **2015**, *493*, 313.

[2] G. Giakisikli, A. N. Anthemidis, *Anal. Chim. Acta* **2013**, *789*, 1.
[3] Q. M. Kainz, O. Reiser, *Acc. Chem. Res.* **2014**, *47*, 667.
[4] K. Dutta, S. De, *J. Mater. Chem. A* **2017**, *5*, 22095.
[5] L. C. Fidale, M. Nikolajski, T. Rudolph, S. Dutz, F. H. Schacher, T. Heinze, *J. Colloid Interface Sci.* **2013**, *390*, 25.
[6] Y. Gong, M. Fan, F. Gao, J. Hong, S. Liu, S. Luo, J. Yu, J. Huang, *Colloids Surf., B* **2009**, *71*, 243.
[7] S. Hong-Ying, W. Chang-Qiang, L. Dan-Yang, A. Hua, *Chin. Phys. B* **2015**, *24*, 127506.
[8] L. Alupei, C. A. Peptu, A. M. Lungan, J. Desbrieres, O. Chiscan, S. Radji, M. Popa, *Int. J. Biol. Macromol.* **2016**, *92*, 561.
[9] S. J. Mattingly, M. G. O'Toole, K. T. James, G. J. Clark, M. H. Nantz, *Langmuir* **2015**, *31*, 3326.
[10] P. Padwal, R. Bandyopadhyaya, S. Mehra, *Langmuir* **2014**, *30*, 15266.
[11] P. Wust, B. Hildebrandt, G. Sreenivasa, B. Rau, J. Gellermann, H. Riess, R. Felix, P. M. Schlag, *Lancet Oncol.* **2002**, *3*, 487.
[12] K. Maier-Hauff, F. Ulrich, D. Nestler, H. Niehoff, P. Wust, B. Thiesen, H. Orawa, V. Budach, A. Jordan, *J. Neuro-Oncol.* **2011**, *103*, 317.
[13] S. Dutz, R. Hergt, *Nanotechnology* **2014**, *25*, 452001.
[14] B. Pelaz, P. del Pino, P. Maffre, R. Hartmann, M. Gallego, S. Rivera-Fernández, J. M. de la Fuente, G. U. Nienhaus, W. J. Parak, *ACS Nano* **2015**, *9*, 6996.
[15] S. Bolisetty, J. J. Vallooran, J. Adamcik, R. Mezzenga, *ACS Nano* **2013**, *7*, 6146.
[16] M. von der Lühe, U. Günther, A. Weidner, C. Gräfe, J. H. Clement, S. Dutz, F. H. Schacher, *RSC Adv.* **2015**, *5*, 31920.
[17] M. von der Lühe, A. Weidner, S. Dutz, F. H. Schacher, *ACS Appl. Nano Mater.* **2018**, *1*, 232.
[18] O. Ozay, S. Ekici, Y. Baran, S. Kubilay, N. Aktas, N. Sahiner, *Desalination* **2010**, *260*, 57.
[19] C.-H. Yeh, S.-H. Chen, D.-T. Li, H.-P. Lin, H.-J. Huang, C.-I. Chang, W.-L. Shih, C.-L. Chern, F.-K. Shi, J.-L. Hsu, *J. Chromatogr. A* **2012**, *1224*, 70.
[20] Y. Chen, Z. Xiong, L. Zhang, J. Zhao, Q. Zhang, L. Peng, W. Zhang, M. Ye, H. Zou, *Nanoscale* **2015**, *7*, 3100.
[21] Y. Zhao, Y. Chen, Z. Xiong, X. Sun, Q. Zhang, Y. Gan, L. Zhang, W. Zhang, *J. Chromatogr. A* **2017**, *1482*, 23.
[22] S. Dutz, M. Kettering, I. Hilger, R. Müller, M. Zeisberger, *Nanotechnology* **2011**, *22*, 265102.
[23] U. Günther, L. V. Sigolaeva, D. V. Pergushov, F. H. Schacher, *Macromol. Chem. Phys.* **2013**, *214*, 2202.
[24] M. von der Lühe, U. Günther, A. Weidner, C. Gräfe, J. H. Clement, S. Dutz, F. H. Schacher, *RSC Adv.* **2015**, *5*, 31920.

Supporting Information

for *Macromol. Rapid Commun.,* DOI: 10.1002/marc.201800017

Reversible Adsorption of Methylene Blue as Cationic Model Cargo onto Polyzwitterionic Magnetic Nanoparticles

Philip Biehl, Moritz von der Lühe, and Felix H. Schacher*

Supporting Information

Reversible Adsorption of Methylene Blue as Cationic Model Cargo onto Polyzwitterionic Magnetic Nanoparticles

Philip Biehl,† Moritz von der Lühe,† Felix H. Schacher*

P. Biehl, M. von der Lühe, Prof. Dr. F. H. Schacher
Institute of Organic Chemistry and Macromolecular Chemistry (IOMC), Friedrich Schiller University Jena, Humboldtstraße 10, 07743 Jena, Germany
Jena Center for Soft Matter (JCSM), Friedrich Schiller University Jena, Philosophenweg 7, 07743 Jena, Germany
† Both Authors contributed equally to this work.

Materials and Methods

Instrumentation

Size exclusion chromatography in $CHCl_3$: SEC measurements were performed on a Shimadzu system equipped with a Size exclusion chromatography (SEC) SCL-10A system controller, a LC-10AD pump, and a RID-10A refractive index detector using a solvent mixture containing chloroform, triethylamine, and *iso*propanol (94:4:2) at a flow rate of 1 mL min^{-1} on a PSS-SDV-linear M 5 μm column at 40°C. The system was calibrated with PMMA (410-88 000 Da) standards.

Zeta potential measurements: the zeta potentials were measured on a ZetaSizer Nano ZS from Malvern *via* M3-PALS technique with a laser beam at 633 nm. The detection angle was 13°.

Dynamic light scattering: Dynamic light scattering (DLS) measurements were performed using an ALV Laser CGS 3 Goniometer equipped with a 633 nm HeNe Laser. DLS measurements were performed at 25 °C and at a detection angle of 90°. The CONTIN algorithm was used to evaluate the obtained data.

Thermogravimetric Analysis: The samples (prepared and washed as described in the nanoparticle coating section) were magnetically separated and freeze dried for 72 hours. TGA measurements were carried out from 30 °C up to 800 °C under air with a heating range of 10 K/min in a Perkin Elmer TGA8000 device.

UV/Vis measurements were performed on an Agilent Cary 60 in a Hellma quarz glass cuvette with a path length of 10 mm at room temperature in solvent. The absorbance was measured in a range from 200 nm to 800 nm in 5 nm steps.

PDha@MCNP Characterization

All TGA values used for calculations have been rounded to 0.5 % to match the error of the TGA experiments. Overall weight loss (850 °C) and water content (150 °C) were derived from the respective thermograms (**Figure S1**). The pristine MCNP show an overall weight loss of 4.0 %, 2.0 % thereof are water, and the remaining 2.0 % presumably result from carbonates remaining from the MCNP synthesis. For the calculation of PDha contents, the respective water content, and 2.0 % weight loss of pristine MCNP were deducted from the overall weight loss (**Table S1**).

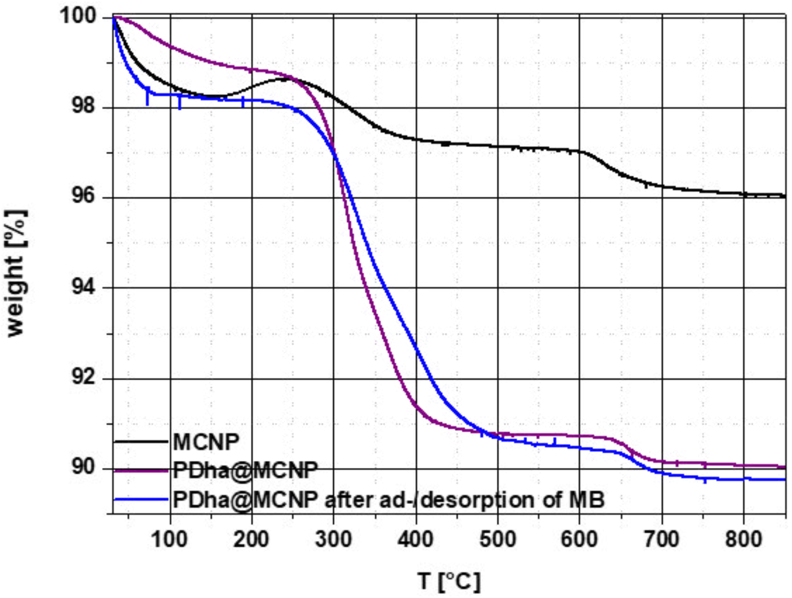

Figure S1. Thermograms of pristine MCNP (black line, overall weight loss 4.0 %), PDha@MCNP (purple line, 12.0 %), and PDha@MCNP after adsorption desorption of methylene blue (blue line, 10.0 %).

Table S1. TGA results and calculation of PDha content.

sample	overall weight loss[a] [%]	water content[a] [%]	carbonate content[b] [%]	PDha content[b] [%]
MC1707	4.0	2.0	2.0	-
PDha@MC1707	10.0	1.0	2.0	7.0
PDha@MC1707 after MB ad-/desorption	10.5	2.0	2.0	6.5

a) determined from TGA, b) calculated from TGA results

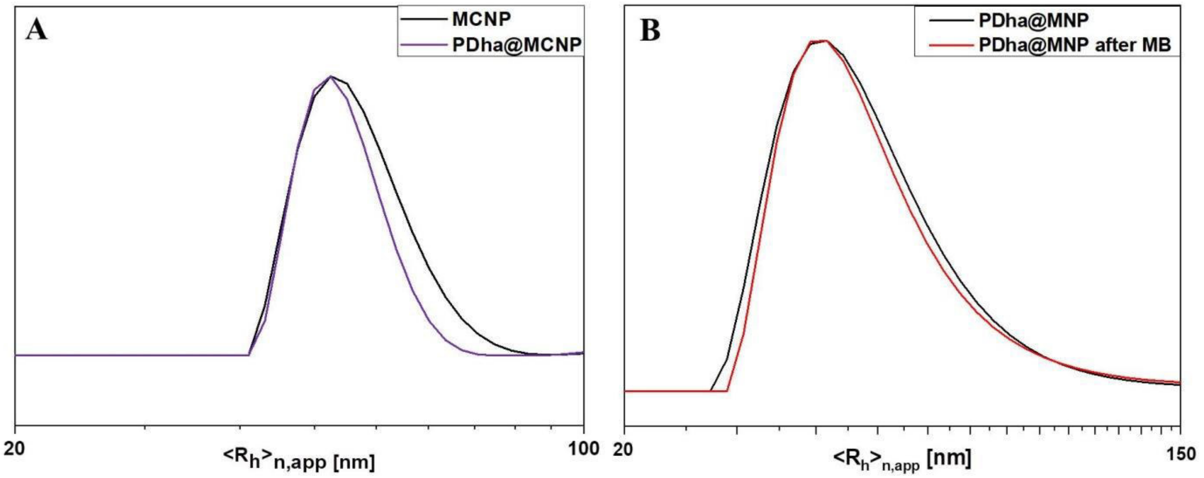

Figure S2. A) Number-weighted DLS CONTIN plots of pristine MCNP (black line, $\langle R_h \rangle_{n,app}$ = 51 nm; diameter of 102 nm), and PDha@MCNP (purple line, $\langle R_h \rangle_{n,app}$ = 51 nm; diameter of 102 nm). B) Number-weighted DLS CONTIN plots of PDha@MCNP (black line), and PDha@MCNP after MB adsorption (red line).

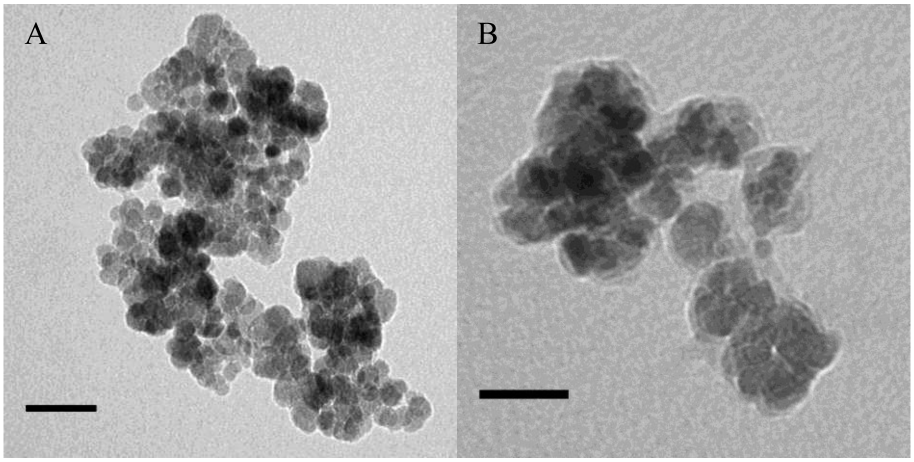

Figure S3. (A) TEM micrograph of MCNP scale bar 50 nm, (B) TEM micrograph of PDha@MCNP scale bar 50 nm.

Calculations of MB Content

UV/Vis measurements of a series of MB solutions at varying concentration were performed at pH = 7. The resulting calibration curve is shown in Figure S4.

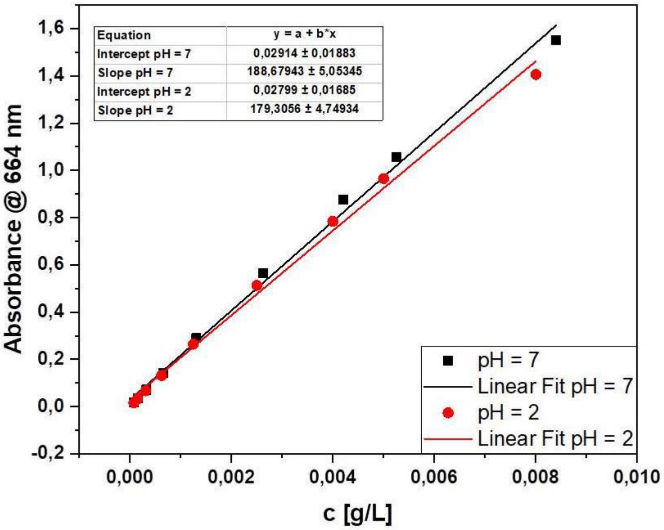

Figure S4. Calibration curves for concentration calculation of MB.

Equation 1. pH = 7: $$c\,[g/L] = \frac{A - 0.02914}{188.679}$$ pH = 2: $$c[g/L] = \frac{A - 0.02799}{179.306}$$

Table S2. Amounts of MB calculated from the UV/Vis adsorptions of initial solutions, supernatants after washing and desorption steps (all solutions had a volume of 1ml), and deviations between initial content, and the actual amount desorbed from the particles.

Sample		**Intensity (664 nm)**	**m (MB) [µg]**	**Overall amount of MB [µg]**	**Deviation [µg (%)]**
2.5 mg	MB solution	1.705	8.88	5.86	3.03 (34.1)
	after MCNP	0.467	2.32		
	washing step 1	0.173	0.76		
	washing step 2	0.106	0.41		
	washing step 3	0.125	0.51		
	washing step 4	0.079	0.26		
	washing step 5	0.077	0.25		
	washing step 6	0.062	0.17		
	washing step 7	0.000	0.00		
	pH = 2_1	0.245	1.21		
	pH = 2_2	0.000	0.00		
5 mg	MB solution	1.535	7.98	4.90	3.08 (38.6)
	after MCNP	0.231	1.07		
	washing step 1	0.077	0.25		
	washing step 2	0.086	0.30		
	washing step 3	0.040	0.06		
	washing step 4	0.054	0.13		
	washing step 5	0.056	0.14		
	washing step 6	0.047	0.09		
	washing step 7	0.063	0.18		
	pH = 2_1	0.507	2.67		
	pH = 2_2	0.027	0.00		

Table S3. Amounts of MB calculated from the UV/Vis adsorptions of initial solutions, supernatants after washing and desorption steps (all solutions had a volume of 1ml), and deviations between initial content, and the actual amount desorbed from the particles.

Sample		**Intensity (664 nm)**	**m (MB) [µg]**	**Overall amount of MB [µg]**	**Deviation [µg (%)]**
15 mg	MB solution	1.631	8.49	5.02	3.27 (38.6)
	after MCNP	0.032	0.02		
	washing step 1	0.059	0.16		
	washing step 3	0.041	0.06		
	pH = 2_1	0.928	5.02		
	pH = 2_2	0.042	0.08		
	pH = 2_3	0.000	0		

Table S4. Amounts of MB calculated from the UV/Vis adsorptions of initial solutions, supernatants after adsorption to 2.5 mg PDha@MCNP (all solutions had a volume of 1ml), and calculated ratios of Dha:MB.

Sample		**Intensity (664 nm)**	**m_1 (MB) [mg]**	**m_2 (MB) [mg]**	**Adsorbed MB [mg]**	**Ratio Dha:MB**
MB 0.55 mg/ml	MB solution	1,07171[a]	0,00553[a]	0,55256[c]	0,04433	14
	after MCNP	0,98806[a]	0,00508[a]	0,50823[c]		
MB 0.31 mg/ml	MB solution	0,60856[a]	0,00307[a]	0,30709[c]	0,04082	16
	after MCNP	0,53154[a]	0,00266[a]	0,26627[c]		
MB 0,05 mg/ml	MB solution	1,03249[b]	0,00532[b]	0,05318[d]	0,01718	37
	after MCNP	0,70836[b]	0,00360[b]	0,03600[d]		
MB 0,03 mg/ml	MB solution	0,60263[b]	0,00304[b]	0,03040[d]	0,01544	42
	after MCNP	0,31123[b]	0,00150[b]	0,01495[d]		
MB 0,008 mg/ml	MB solution	1,705	0,00888	0,00888	0,00656	98
	after MCNP	0,467	0,00232	0,00232		

[a] obtained from a solution diluted by 100 [b] obtained from a solution diluted by 10 [c] m_1 multiplied by 100 [d] m_1 multiplied by 10

Table S5. Amounts of MB calculated from the UV/Vis adsorptions of initial solutions, supernatants after washing and desorption steps (all solutions had a volume of 1ml), and deviations between initial content, and the actual amount desorbed from the particles.

Sample		**Intensity (664 nm)**	**m (MB) [µg]**	**Overall amount of MB [µg]**	**Deviation [µg (%)]**
pH = 3	MB solution	1.301	6.74	3.24	3.50 (51.9)
	after MCNP	0.000	0.00		
	washing step 1	0.031	0.01		
	washing step 2	0.041	0.06		
	pH = 3_1	0.609	3.08		
	pH = 3_2	0.047	0.10		
	pH = 3_3	0.005	N/D		
	pH = 3_4	0.000	0.00		
	pH = 2	0.000	0.00		

Table S6. Amounts of MB calculated from the UV/Vis adsorptions of initial solutions, supernatants after washing and desorption steps at pH = 4 (all solutions had a volume of 1ml), and deviations between initial content and the actual amount desorbed from the particles.

Sample		**Intensity (664 nm)**	**m (MB) [µg]**	**Overall amount of MB [µg]**	**Deviation [µg (%)]**
pH = 4	MB solution	1.301	6.74	2.80	3.94 (58.4)
	after MCNP	0.000	0.00		
	washing step 1	0.020	N/D		
	washing step 2	0.045	0.08		
	pH = 4_1	0.355	1.73		
	pH = 4_2	0.172	0.76		
	pH = 4_3	0.082	0.28		
	pH = 4_4	0.029	N/D		
	pH = 2	0.000	6.74		

Table S7. Amounts of MB calculated from the UV/Vis adsorptions of initial solutions, supernatants after washing and desorption steps at pH = 5 (all solutions had a volume of 1ml), and deviations between initial content and the actual amount desorbed from the particles.

Sample		**Intensity (664 nm)**	**m (MB) [µg]**	**Overall amount of MB [µg]**	**Deviation [µg (%)]**
pH = 5	MB solution	1.301	6.74	1.77	5.0 (73.8)
	after MCNP	0.000	0.00		
	washing step 1	0.048	0.10		
	washing step 2	0.013	N/D		
	pH = 5_1	0.032	0.02		
	pH = 5_2	0,027	N/D		
	pH = 5_3	0,018	N/D		
	pH = 5_4	0,029	N/D		
	pH = 2	0.323	1.65		

Table S8. Amounts of MB calculated from the UV/Vis adsorptions of initial solutions, supernatants after washing and desorption steps at pH = 6 (all solutions had a volume of 1ml), and deviations between initial content and the actual amount desorbed from the particles.

Sample		**Intensity (664 nm)**	**m (MB) [µg]**	**Overall amount of MB [µg]**	**Deviation [µg (%)]**
pH = 6	MB solution	1.304	6.76	1.66	5.10 (75.4)
	after MCNP	0.000	0.00		
	washing step 1	0.022	N/D		
	washing step 2	0.058	0.15		
	pH = 4_1	0.038	0.05		
	pH = 4_2	0.037	0.04		
	pH = 4_3	0.033	0.02		
	pH = 4_4	0.030	0.01		
	pH = 2	0.278	1.39		

Table S9. Amounts of MB calculated from the UV/Vis adsorptions of initial solutions, supernatants after washing and desorption steps in 9 consecutive cycles (all solutions had a volume of 1ml), and deviations between initial content and the actual amount desorbed from the particles.

Cycle	**Initial MB solution**		**After MCNP**		**Desorption supernatant**		**Sum (after + desorbed)**	**Deviation**
	Intensity	**m [µg]**	**Intensity**	**m [µg]**	**Intensity**	**m [µg]**	**[µg]**	**[µg (%)]**
1	1.631	8.490	0.03236	0.017	0.928	5.017	5.034	3.456 (41)
2	1.557	8.098	0.59189	2.983	0.889	4.803	7.786	0.312 (4)
3	1.557	8.098	0.63627	3.218	0.903	4.882	8.100	0.000 (0)
4	1.557	8.098	0.70878	3.602	0.827	4.456	8.058	0.040 (0.5)
5	1.557	8.098	0.27935	1.326	1.031	5.594	6.920	1.178 (15)
6	1.557	8.098	0.50696	2.532	0.928	5.017	7.549	0.549 (7)
7	1.557	8.098	0.53223	2.666	0.812	4.374	7.041	1.057 (13)
8	1.557	8.098	0.36105	1.759	0.893	4.821	6.581	1.517 (19)
9	1.557	8.098	0.57766	2.907	0.739	3.968	6.875	1.223 (15)

Zeta Potential

Table S10. Zeta potentials of MCNP nad PDha@MCNP prior to and after adsorption of MB.

sample	zeta potential[a] [mV]
MCNP	+45.5 ± 10.4
PDha@MCNP	-41.8 ± 20.2
MB@PDha@MCNP	-38.3 ± 9.5
PDha@MCNP after MB desorption	-34.9 ± 4.8

a) determined using a Malvern Zetasizer Nano ZS

Irreversible Binding of MB

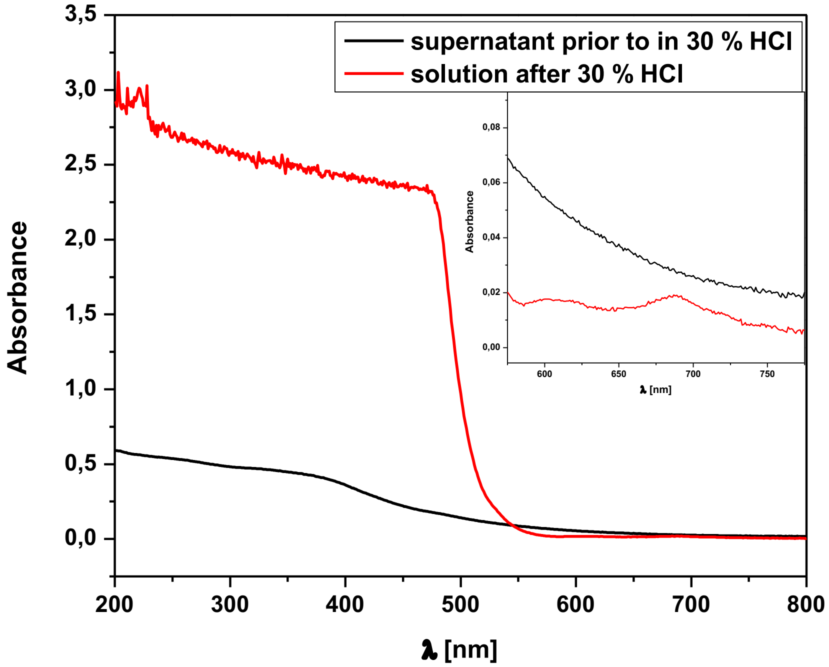

Figure S5. UV/Vis spectra of the supernatant of PDha@MCNP after desorption of MB (black line), and a solution of the same sample after dissolution of the MCNP cores in *conc.* HCl (red line), showing the presence of MB (inset).

Publication P4

"Different Routes to Ampholytic Polydehydroalanine: Orthogonal versus Simultaneous Deprotection"

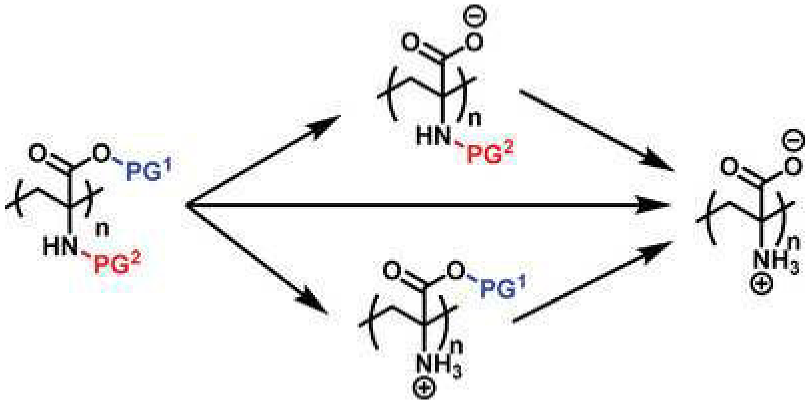

J. H. Kruse, P. Biehl, F. Schacher

Macromol. Rapid Commun. **2019**, *40*, 1800857.

Macromolecular
Rapid Communications
www.mrc-journal.de

Different Routes to Ampholytic Polydehydroalanine: Orthogonal versus Simultaneous Deprotection

*Jan-Hendrik Kruse, Philip Biehl, and Felix Helmut Schacher**

Polydehydroalanine (PDha) is a polyampholyte featuring both a –NH_2 and a –COOH in every repeat unit and with that presents a rather high charge density. The synthesis and polymerization of two monomers, benzyl 2-*tert*-butoxycarbonylaminoacrylate and methyl 2-benzyloxycarbonylaminoacrylate is herein reported, which feature different protective groups and, after polymerization, the resulting P*t*BABA and PBOMA can be transformed into PDha using polymer-analogous modification reactions. More important, the current choice of protective groups allows either simultaneous deprotection in one step in both cases, but also the orthogonal deprotection of either –NH_2 or –COOH moiety for P*t*BABA, given that appropriate conditions are chosen. The polymers are prepared using free radical polymerization and all (intermediate) polymeric materials are investigated using a combination of NMR spectroscopy and size exclusion chromatography.

Polyelectrolytes are an interesting class of polymers featuring solution behavior differing from uncharged materials.[1] Especially with regard to any interaction with charged surfaces, polyelectrolytes, or particles of opposite charge, a wide range of possible applications are discussed or already performed, such as their use as flocculation agents, for oil drilling, mineral processing, or drug delivery approaches.[2–6] If the ionic moieties of the respective polyelectrolyte are weak acids or bases, the degree of charge strongly depends on the pH-value (weak polyelectrolytes), whereas in case of strong polyelectrolytes the charge is independent of the pH-value of the surrounding medium.[7]

Subclasses of polyelectrolytes are polyampholytes and polyzwitterions. These contain oppositely charged moieties along the polymeric backbone, and in the latter case both are situated within every repeat unit, which again has a strong influence on the resulting properties. In that regard, the behavior of synthetic polyzwitterions is often considered as similar to that of many naturally occurring polyzwitterions, which leads to a good biocompatibility of such materials in general.[1,8,9] Therefore, polyzwitterions are often applied in drug delivery, surface coatings for various biomaterials, and in general where resistance to unwanted biofouling is desirable.[10–13]

Polyzwitterions with tunable charge feature at least one of the ionizable components as weak acid or base and can thus in principle exist as polyanion, polycation, or polyzwitterion at different pH-values. One example for such materials with a very high charge density additionally is polydehydroalanine (PDha).[14–16] At high pH, PDha is a polyanion, whereas it behaves like a polyzwitterion with varying charge density in the pH range of 10–4 and as polycation at low pH, although solubility in water is limited below the isoelectric point. So far, studies on PDha-based homopolymers as coating materials for magnetic nanoparticles demonstrate good biocompatibility.[9] Therefore, PDha coated magnetic nanoparticles are in the future interesting candidates for diagnostic applications.[17–20] Furthermore it is an interesting material for other applications such as surface coating, or as building block for interpolyelectrolyte complexes, for which the invertible charge could offer a straightforward way to introduce charge disbalance or affect complex stability.[19,21] Besides, polyzwitterions like PDha can be used as selective layers in membranes for chemical separation.[12,22]

For the (controlled) polymerization of PDha a protection of the amine and carboxyl functionality is required, which renders a subsequent deprotection necessary to turn the respective polymer into a polyampholyte.[14,16] So far, *tert*-butoxycarbonylaminomethylacrylate (*t*BAMA) was utilized, where the carboxyl group is protected with a methyl ester and the amino group with a *tert*-butyloxycarbonyl (Boc) group. However, during deprotection of either functional group it was observed that contrary to expectations also the other protective group is partially removed, even under varying conditions.[16,21] We herein report on two alternative monomers, benzyl 2-*tert*-butoxycarbonylaminoacrylate (*t*BABA) and methyl 2-benzyloxycarbonylaminoacrylate (BOMA), where deprotection can be either carried out in an orthogonal manner or even simultaneously in one step. We therefore demonstrate monomer synthesis, polymerization via free radical polymerization, and the subsequent deprotection of the resulting materials. The polymers were characterized by NMR spectroscopy and size exclusion chromatography (SEC) before and after the deprotection steps.

We designed two monomers as precursors to PDha-based polymeric materials featuring different combinations of

---

J.-H. Kruse, P. Biehl, Prof. F. H. Schacher
Institute of Organic Chemistry and Macromolecular Chemistry
Friedrich-Schiller-University Jena
Humboldtstraße 10, D-07743 Jena, Germany
E-mail: felix.schacher@uni-jena.de

J.-H. Kruse, P. Biehl, Prof. F. H. Schacher
Jena Center for Soft Matter
Friedrich-Schiller-Universität Jena
Philosophenweg 7, 07743 Jena, Germany

The ORCID identification number(s) for the author(s) of this article can be found under https://doi.org/10.1002/marc.201800857.

DOI: 10.1002/marc.201800857

protective groups for –NH$_2$ and –COOH. In the first case, according to our own experience the acid-labile methyl ester of *t*BAMA (or, at least upon deprotection of the –NH$_2$ moiety) is substituted with a benzyl ester, which is reported to be more stable under acidic conditions and can be easily introduced.[23] This combination of protecting groups ideally allows the orthogonal deprotection of both functional groups after the polymerization. In the second case, the amine is protected with a carboxybenzyl (Cbz) group and the carboxyl group is again protected with a methyl ester. These two protecting groups are both base-labile and can therefore be completely removed simultaneously, which significantly reduces the synthetic effort for the synthesis of PDha.[23]

These two monomers were each synthesized in two-step procedures (**Figure 1**A). *t*BABA was synthesized starting from the Boc protected amino acid serine. In the first step, the benzyl ester was introduced with a yield of 83%. In the second step, the hydroxyl group was eliminated with a yield of 93% after column chromatography and recrystallization.[24] In NMR measurements, the large signal of the Boc group at 1.5 ppm can clearly be seen, as well as the aromatic signals of the benzyl ester in the characteristic region at about 7.4 ppm. BOMA was synthesized starting from the methyl ester protected serine (Figure 1B). The Cbz group was introduced with a yield of 89%. Subsequently, the hydroxyl group was again eliminated to form a polymerizable double bond.[25] The respective signals can be seen in the same region as for *t*BABA as two singlets at about 5.75 and 6.25 ppm. The methyl ester signal and the aromatic signals of the Cbz group are found in the characteristic regions at about 3.8 and 7.4 ppm.

Subsequently, both monomers were polymerized using free radical polymerization with the photoinitiator diphenyl(2,4,6-trimethylbenzoyl)phosphine oxide (TPO) at room temperature (Figure S1, Supporting Information). We chose this approach as our main focus in this work is put on orthogonal or simultaneous deprotection of the resulting materials. Monomer to initiator ratios ranging from 100:1 to 400:1 were applied and dioxane was added as solvent in a weight ratio of 1:1 in relation to the monomer (**Table 1**). The highest yields of such polymerizations were 62% for *t*BABA and 53% for BOMA with dispersities ranging from 1.5 to 2. Several polymerization attempts under the same conditions for P*t*BABA resulted in molar masses between 13 000 and 18 000 g mol^{-1} with a monomer to initiator ratio of 100:1. This demonstrates acceptable reproducibility for this polymerization. For PBOMA molar masses between 15 000 and 50 000 g mol^{-1} were reached with varying ratios of monomer to initiator. In the latter case, we attribute the rather poor reproducibility of the results for a monomer to initiator ratio of 400:1 to presumably rather high viscosity during the polymerization.

After successful polymerization, both P*t*BABA and PBOMA were deprotected using different strategies (**Figure 2**). Initially, we tried to remove the Boc group of P*t*BABA under reflux conditions in a mixture of trifluoroacetic acid (TFA) and dichloromethane.

However, this surprisingly led to an almost complete deprotection of both protecting groups and to the formation of

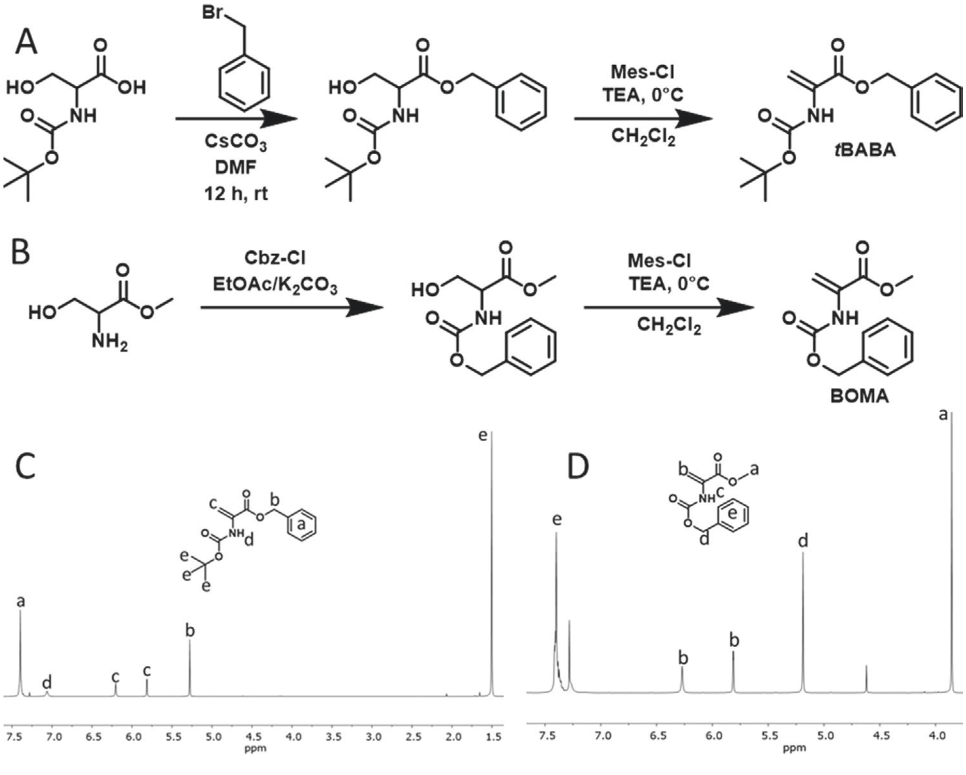

Figure 1. A) Synthesis of *t*BABA, B) synthesis of BOMA, C) ^{1}H-NMR of *t*BABA (300 MHz, CDCl$_3$), D)^{1}H-NMR of BOMA (300 MHz, CDCl$_3$).

Table 1. Overview of applied conditions and resulting polymers before and after deprotection.

Sample	M_{n}[a)]	M_{w}[a)]	Đ[a)]	Ratio M:I[b)]	M_{n}[c)]	M_{w}[c)]	Đ[c)]
					After deprotection		
P*t*BABA	18 000	36 400	2.02	100	–	–	–
P*t*BABA	13 900	21 300	1.53	100	–	–	–
P*t*BABA	13 400	25 000	1.86	100	6000 (PABA)	17 700 (PABA)	2.91 (P*t*BAA)
P*t*BABA	16 600	32 200	1.95	100	5200 (PDha)	16 300 (PDha)	3.15 (PDha)
PBOMA	15 400	24 000	1.56	400	–	–	–
PBOMA	46 200	82 200	1.78	400	–	–	–
PBOMA	32 600	60 300	1.85	250	–	–	–
PBOMA	45 400	71 200	1.57	350	13 700 (PDha)	24 000 (PDha)	1.76 (PDha)

[a)] Via THF SEC (PMMA calibration); [b)] Ratio monomer/solvent: 1/1; [c)] Via DMSO SEC (PMMA calibration)

PDha, leaving only a small residual signal of the benzyl ester according to NMR measurements and indicating that this protective group is also acid labile to a certain extent (**Figure** 3B). Therefore, a milder method for an orthogonal cleavage of the Boc group was applied, where phenol in combination with $SiCl_4$ was used.[26] Here, we could achieve selective deprotection of the $-NH_2$ group leading to the formation of PABA. The signals of the Boc group at about 1.5 ppm disappear completely, whereas the aromatic signals of the benzyl ester remain. However, it is rather difficult to fully remove phenol from the resulting material and, hence, traces are visible in the NMR spectrum (Figure 3B). Regarding the orthogonal deprotection of the carboxyl group, we first tried to apply Pd-catalyzed hydrogenation. However, this was not successful under usual conditions and we therefore switched to an alkaline deprotection methodology in analogy to the procedure reported for the methyl ester of P*t*BAMA.[14] Although the benzyl ester is supposed to be slightly more stable under alkaline conditions, the aromatic signals in the NMR disappear completely after the deprotection, while the signal of the Boc group stays unchanged and P*t*BAA is formed selectively (Figure 3B).

The direct and simultaneous deprotection of PBOMA to PDha was carried out under alkaline conditions. The Cbz group turned out to be even more base-labile than the methyl ester and hence the deprotection in one step could be conducted successfully by dissolving PBOMA in dioxane and refluxing it with an aqueous solution of LiOH (**Figure** 4A). The ^{1}H-NMR after deprotection shows a complete deprotection of both protecting groups and only the signal of the polymer backbone between 2 and 3 ppm can be seen, the small signal at 3.7 ppm derives from residual dioxane (Figure 4B).

SEC data with DMSO as eluent confirmed the polymeric character of PDha and PABA after the respective deprotection steps (**Figure 5**). Due to its limited solubility even in polar solvents like DMSO or dimethylacetamide, P*t*BAA could so far not be analyzed using SEC experiments. Since the protecting groups account for a large share of the overall mass, the molar masses are significantly lower after the deprotection (Table 1). Besides, the dispersity of the resulting polymers seems to increase, which we tentatively attribute to interactions with the column material as well as the different SEC setup that is used (Figure S1C, Supporting Information).

As described, the deprotected polymers are only soluble in polar solvents. While PABA and PDha are soluble in DMSO and basic water, P*t*BAA is only soluble in basic water. Therefore, these deprotection methods are most interesting for (block) copolymers, in which the solubility can be adapted by combination with other monomers.

In an attempt to broaden our platform of monomers which can be used for the preparation of PDha, we demonstrated the synthesis of *t*BABA and BOMA, followed by the free radical polymerization to P*t*BABA and PBOMA. Whereas in earlier studies rather harsh conditions were applied to deprotect –COOH or $-NH_2$ moiety of PDha precursor polymers, here we could show that in case of P*t*BABA both protecting groups can be removed orthogonally. On the other hand, in case of PBOMA both protecting groups can be removed simultaneously, which can be of interest if only the final PDha is desirable. In our opinion, these results increase the versatility with which PDha-based structures can be incorporated into copolymers, block copolymers, or any other polymer-based materials, especially if other functional groups are present which might not sustain harsh conditions necessary for deprotection steps.

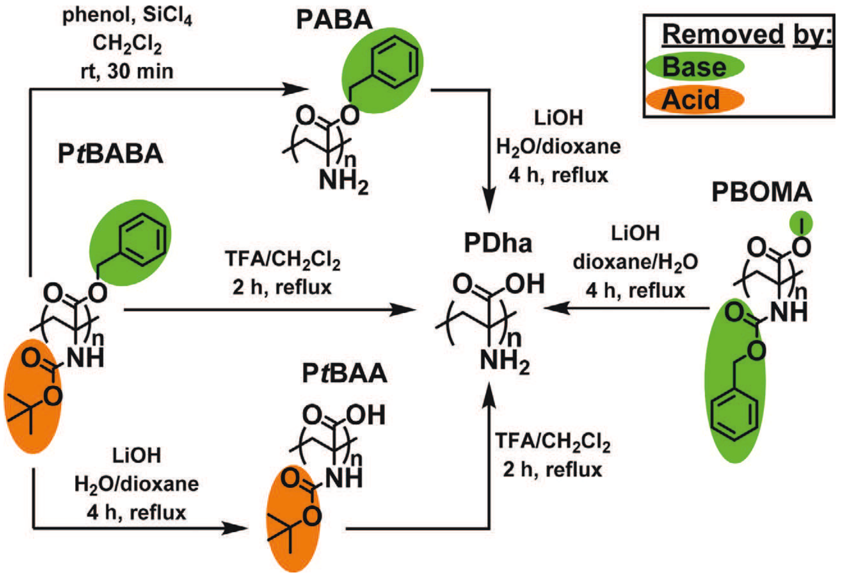

Figure 2. Overview of the deprotection steps of P*t*BABA and PBOMA and their deprotection products poly(benzyl aminoacrylate) (PABA), poly(*tert*-butoxycarbonylaminoacrylate) (P*t*BAA) and polydehydroalanine (PDha).

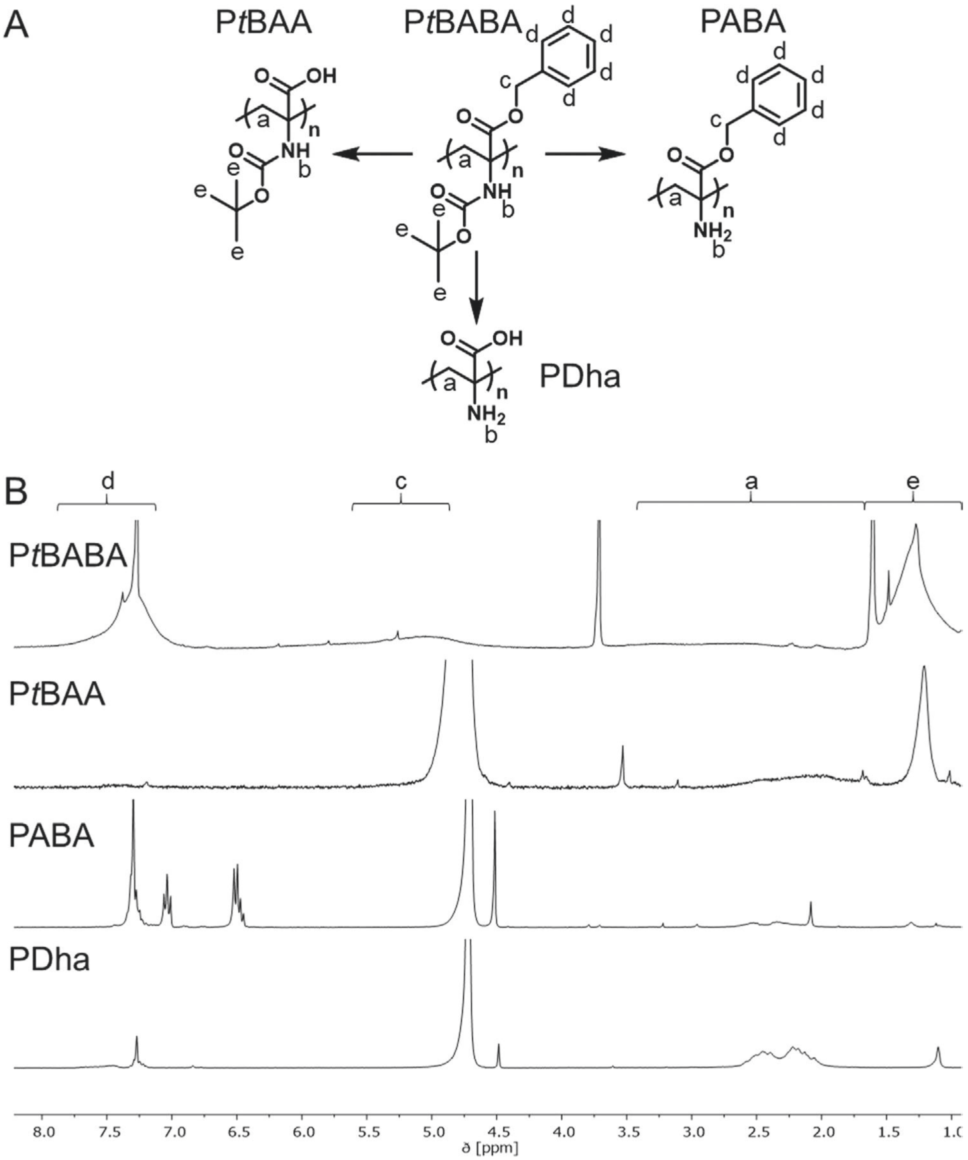

Figure 3. A) Overview of deprotection steps of P*t*BABA, B) ^{1}H-NMR of P*t*BABA ($CDCl_3$), P*t*BAA (D_2O), PABA (D_2O) and PDha (D_2O).

Experimental Section

Materials and Instruments: *Chemicals*: Cesium carbonate (99%), benzyl bromide (98%), benzyl chloroformate (98%), silicon tetrachloride (99%), and methanesulfonyl chloride (≥99.7%) were purchased from Sigma-Aldrich. TFA (≥99.9%) was purchased from Roth, triethylamine (≥99.0%) from CHEMSOLUTE and *N*-(*tert*-butoxycarbonyl)-L-serine (98%) from Carbolution Chemicals. The UV photoinitiator, Lucirin-TPO ((diphenylphosphoryl)(mesityl)methanone), was kindly provided by BASF. All Chemicals were used as received.

Nuclear Magnetic Resonance Spectroscopy: ^{1}H-NMR spectra were measured on a 300 MHz Bruker AVANCE spectrometer using $CDCl_3$, DMSO-d_6 or D_2O with NaOD as deuterated solvents at a temperature of 298 K. The solvent residual peak of the respective solvent was used as standard.

Size Exclusion Chromatography: SEC measurements in THF were performed on an Agilent system equipped with G1310A pump, a G1362A refractive index detector, and both a PSS Gram30 and a PSS Gram1000 column in series. THF was applied as eluent at 1 mL min^{-1} flow rate and the column oven was set to 40 °C. For the calibration a poly(methyl methacrylate) standard was used.

SEC measurements in DMSO were performed on a Jasco instrument using DMSO + 0.5% LiBr as eluent at a flow rate of 0.5 mL min^{-1} at 70 °C and a Pullulan calibration (Polymer Standards Service GmbH, Germany). The instrument was equipped with PSS NOVEMA 3000 Angsröm/300 Angström columns, a RI-930 detector, as well as a PU-980 pump.

Monomer Synthesis: *Benzyl 2-tert-Butoxycarbonylaminoacrylate (tBABA)*: *Benzyl tert-Butoxycarbonylserinate*: To a solution of *N*-(*tert*-butoxycarbonyl)-D-serine (8.5 g, 41.4 mmol) in 250 mL DMF was added cesium carbonate (14.17 g, 43.5 mmol) and the reaction mixture was stirred for 30 min at room temperature. Then, benzyl bromide (8.5 g, 49,7 mmol) was added, and the resulting solution was stirred for 12 h at room temperature. The reaction mixture was then diluted with ethyl acetate and washed with a saturated aqueous lithium bromide solution, a saturated aqueous $NaHCO_3$ solution, and brine. The organic layer was dried with Na_2SO_4 and the solvents were removed under reduced pressure. The crude product was purified by silica column chromatography with dichloromethane,

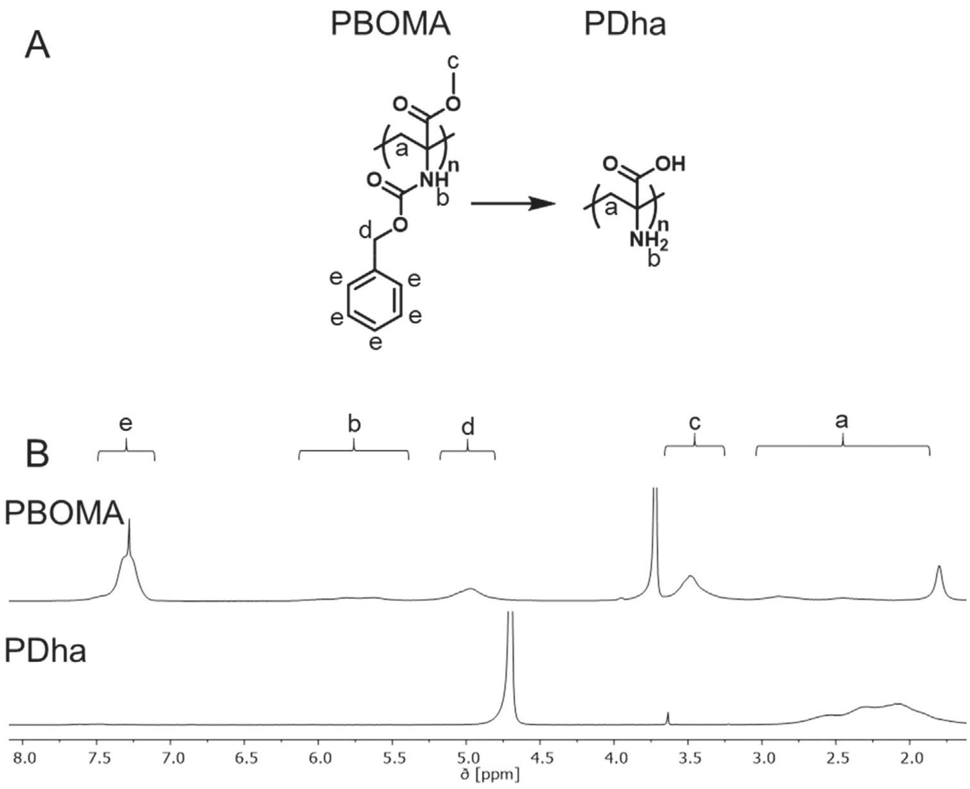

Figure 4. A) Overview of deprotection steps of PBOMA, B) ^{1}H-NMR of PBOMA ($CDCl_3$) and PDha (D_2O).

followed by a mixture of dichloromethane and methanol (9:1), as eluent (yield: 10.15 g, 83%).[24]

^{1}H NMR (250 MHz, Chloroform-*d*) δ 7.26–7.54 (m, 5H, Ar-H), 5.58 (d, *J* = 8.3 Hz, 1H, Ser-H), 5.21 (s, 2H, CH_2 (OBn)), 4.03–3.81 (m, 2H, Ser-H), 1.44 (s, 9H, O*t*Bu).

Benzyl 2-tert-Butoxycarbonylaminoacrylate (*t*BABA): Benzyl *N*-(*tert*-butoxycarbonyl)-D-serinate (8 g, 27.1 mmol) was dissolved in 120 mL dichloromethane. To this solution methanesulfonyl chloride (3.15 mL 40.56 mmol) was added. The reaction mixture was cooled down to 0 °C with an ice bath and 12.30 mL (88.9 mmol) triethylamine were added dropwise over a period of 30 min. After 20 min the solution turned orange. After finishing the addition, the solution was stirred for 1 h at 0 °C, allowed to warm up to room temperature, and afterward the solution was stirred for another 2 h. The reaction mixture was washed four times with an 1% aqueous solution of potassium bisulfate. The organic phase was dried with $MgSO_4$ and the solvent was removed under reduced pressure. The crude product was purified via silica gel column chromatography with a mixture of ethyl acetate and *n*-hexane (1:4) as eluent. Additionally, a recrystallization with a mixture of ethyl acetate and *n*-hexane (9:1) was conducted (yield 8.8 g, 93%).[14]

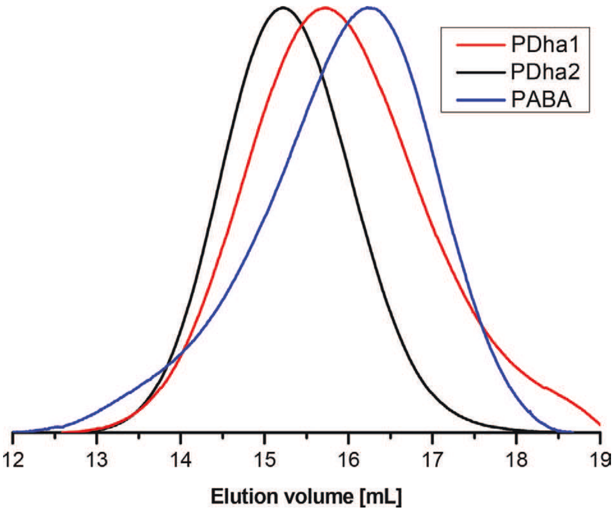

Figure 5. SEC elution traces of PDha1 (received through deprotection of P*t*BABA), PDha2 (received through deprotection of PBOMA) and PABA (intermediate step during the deprotection of P*t*BABA) (DMSO-SEC, PMMA calibration).

^{1}H NMR (300 MHz, Chloroform-*d*) δ 7.53–7.28 (m, 5H, Ar-H), 6.18 (s, 1H, DB), 5.79 (d, *J* = 1.6 Hz, 1H, DB), 5.26 (s, 2H, CH_2(OBn)), 1.48 (s, 9H, O*t*Bu).

Methyl 2-Benzyloxycarbonylaminoacrylate (BOMA): *Methyl Benzyloxycarbonylserinate*: D-serine methyl ester hydrochloride (4.22 g, 27.1 mmol) was dissolved in 35 mL ethyl acetate and 35 mL saturated aqueous sodium bicarbonate solution at 0 °C. To this solution benzyl chloroformate (3.78 g, 27.1 mmol) was added dropwise, and the resulting mixture was stirred for 3 h at room temperature. Subsequently, the mixture was extracted with diethyl ether (4 × 50 mL). The combined organic layers were washed with 1 M hydrochloric acid (4 × 50 mL). Finally, the crude product was purified by silica column chromatography with a mixture of hexane and ethyl acetate as eluent (1:1), which yielded the product (5.17 g, 89%).[27]

^{1}H NMR (300 MHz, Chloroform-*d*) δ 7.52–7.26 (m, 5H, Ar-H), 5.88 (s, 1H, NH), 5.14 (s, 2H, CH_2(OBn)), 4.47 (s, 1H, Ser-H), 3.96 (dd, *J* = 16.4, 3.6 Hz, 2H, Ser-H), 3.78 (s, 3H, OMe).

Methyl 2-Benzyloxycarbonylaminoacrylate (BOMA): The *N*-benzyloxycarbonyl-D-serine methyl ester (5.17 g, 20,4 mmol) and methanesulfonyl chloride (3 mL) were dissolved in 10 mL dichloromethane. The solution was cooled to 0 °C and 11.5 mL triethylamine were added dropwise. Afterward, the solution was stirred for 1 h at 0 °C and for another 2 h at room temperature. The reaction mixture was washed with a 1% solution of potassium hydrogen sulfate in water (4 × 50 mL). The organic phase was dried over $MgSO_4$ and the solvent was removed under reduced pressure. The crude product was purified via silica column chromatography and a mixture of ethyl acetate and hexane (1:4) as eluent (yield: 3.80 g, 74%).[14]

^{1}H NMR (300 MHz, Chloroform-*d*) δ 7.40 (m, 5H, Ar-H), 6.27 (s, 1H, DB), 5.81 (s, 1H, DB), 5.19 (s, 2H, CH_2 (OBn)), 3.85 (s, 3H, OMe).

Polymerization: *Poly(benzyl 2-tert-butoxycarbonylaminoacrylate) (PtBABA)*: In a typical procedure, benzyl 2-*tert*-butoxycarbonylaminoacrylate (1.5 g, 5.4 mmol) was dissolved in 1.46 mL dioxane. The photoinitiator TPO (18.8 mg, 54 µmol) was added and the reaction mixture was stirred under UV-irradiation in an UV-cube for 10 min. The reaction was quenched by the addition of methanol. The resulting polymer was precipitated in cold hexane. To remove the remaining monomer, the polymer was dissolved in CH_2Cl_2 and subsequently precipitated twice in cold hexane.[14]

^{1}H NMR (300 MHz, Chloroform-*d*) δ 7.94–6.85 (m, 5H, Ar-H), 6.35–4.24 (s, 2H, CH_2(OBn)), 2.21–3.52 (d, 2H, backbone), 1.91–0.62 (m, 9H, O*t*Bu).

Poly(methyl 2-benzyloxycarbonylaminoacrylate) (PBOMA): In a typical procedure, methyl 2-benzyloxycarbonylaminoacrylate (350 mg 1.5 mmol) was dissolved in 0.3 mL dioxane. The photoinitiator TPO (1.3 mg, 3.75 µmol) was added and the reaction mixture was stirred under UV-irradiation in an UV-cube for 10 min. The reaction was quenched by the addition of methanol. The resulting polymer was precipitated in cold hexane. To remove the remaining monomer, the polymer was dissolved in CH_2Cl_2 and subsequently precipitated twice in cold hexane.[14]

Deprotection: *Poly(benzyl tert-butoxycarbonylaminoacrylate) (PtBABA)*: *Synthesis of Poly(tert-butoxycarbonylaminoacrylate) (PtBAA)*: P*t*BABA (85 mg) was dissolved in 6 mL dioxane and a saturated aqueous solution of LiOH (3 mL) was added. The resulting mixture was refluxed for 4 h and after reducing the solution volume under reduced pressure, the polymer was precipitated in cold hexane.

^{1}H NMR (300 MHz, Deuterium Oxide) δ 1.90–2.67 (m, 2H, backbone), 1.24–1.43 (m, 9H, O*t*Bu).

Synthesis of Poly(benzyl aminoacrylate) (PABA): P*t*BABA (200 mg) was dissolved in 25 mL CH_2Cl_2 and $SiCl_4$ (1.68 mL, 14.4 mmol) and phenol (2 g, 21.25 mmol) was added. The reaction mixture was stirred for 30 min and the polymer was subsequently precipitated in cold hexane.[26]

^{1}H NMR (300 MHz, Deuterium Oxide) δ 7.76–7.13 (m, 5H, OBn), 1.92–2.61 (m, 2H, backbone).

Poly(methyl benzyloxycarbonylaminoacrylate) (PBOMA): *Synthesis of Polydehydroalanine (PDha)*: PBOMA (0.5 g) was dissolved in 20 mL dioxane. Then, a saturated aqueous solution of LiOH (20 mL) was added. The resulting mixture was refluxed for 3 h. Subsequently, the polymer was precipitated by acidification with 5% HCl solution and afterward washed several times with distilled water. The NMR showed complete deprotection.[14]

^{1}H NMR (300 MHz, Deuterium Oxide) δ 1.90–2.67 (m, 2H, backbone).

Supporting Information

Supporting Information is available from the Wiley Online Library or from the author.

Acknowledgements

The authors are grateful for financial support through the Deutsche Forschungsgemeinschaft (DFG, SCHA1640/12-1 to F.H.S. and P.B. as well as TRR234 "CataLight", Project B03). P.B. is grateful for a fellowship (Landesgraduiertenstipendium of the Friedrich Schiller University Jena). The authors further ackonwledge the NMR department at the Friedrich-Schiller-University for continuous support.

Conflict of Interest

The authors declare no conflict of interest.

Keywords

polyampholytes, polymer-analogous reactions, radical polymerization

Received: November 23, 2018
Revised: December 26, 2018

[1] A. Laschewsky, *Polymers* **2014**, *6*, 1544.
[2] D. A. Mortimer, *Polym. Int.* **1991**, *25*, 29.
[3] K. Petrak, J. Bioact. *J. Bioact. Compat. Polym.* **1986**, *1*, 202.
[4] G. Petzold, A. Nebel, H. M. Buchhammer, K. Lunkwitz, *Colloid Polym. Sci.* **1998**, *276*, 125.
[5] P. Bertrand, A. Jonas, A. Laschewsky, R. Legras, *Macromol. Rapid. Commun.* **2000**, *21*, 319.
[6] K. Jasmeet, S. L. Harikumar, K. Amanpreet, *J. Pharm. Pharm. Sci.* **2012**, *3*, 58.
[7] J. Choi, M. F. Rubner, *Macromolecules* **2005**, *38*, 116.
[8] P. K. Singh, V. K. Singh, M. Singh, *e-Polymers* **2007**, *7*, 1.
[9] A. B. Lowe, C. L. McCormick, *Chem. Rev.* **2002**, *102*, 4177.
[10] T. Nakaya, *Prog. Polym. Sci.* **1999**, *24*, 143.
[11] H. H. Hub, B. Hupfer, H. Koch, H. Ringsdorf, *Angew. Chem., Int. Ed. Engl.* **1980**, *19*, 938.
[12] S. Jiang, Z. Cao, *Adv. Mater.* **2010**, *22*, 920.
[13] P. Lin, C. W. Lin, R. Mansour, F. Gu, *Biosens Bioelectron.* **2013**, *47*, 451.
[14] U. Günther, L. V. Sigolaeva, D. V. Pergushov, F. H. Schacher, *Macromol. Chem. Phys.* **2013**, *214*, 2202.
[15] M. Billing, F. H. Schacher, *Macromolecules* **2016**, *49*, 3696.
[16] M. Billing, G. Festag, P. Bellstedt, F. H. Schacher, *Polym Chem.* **2017**, *8*, 936.
[17] M. von der Lühe, U. Günther, A. Weidner, C. Gräfe, J. H. Clement, S. Dutz, F. H. Schacher, *RSC Adv.* **2015**, *5*, 31920.
[18] Q. A. Pankhurst, J. Connolly, S. K. Jones, J. Dobson, *J. Phys. D: Appl. Phys.* **2003**, *36*, R167.
[19] P. Biehl, M. von der Lühe, S. Dutz, F. Schacher, *Polymers* **2018**, *10*, 91.
[20] P. Biehl, M. von der Lühe, F. H. Schacher, *Macromol. Rapid. Commun.* **2018**, *39*, 1800017.
[21] M. von der Lühe, A. Weidner, S. Dutz, F. H. Schacher, *ACS Appl. Nano Mater.* **2018**, *1*, 232.
[22] L. Krasemann, J. Membr. *Sci. Technol.* **2001**, *181*, 221.
[23] P. G. M. Wuts, T. W. Greene, in *Greene's Protective Groups in Organic Synthesis*, 4th ed., Wiley & Sons Inc., Hoboken **2006**, p. 1022.
[24] K. Lynch, T. L. MacDonald, *WO 2005/041899 A2*, **2005**.
[25] M. Ginisty, C. Gravier-Pelletier, Y. Le Merrer, *Tetrahedron: Asymmetry* **2006**, *17*, 142.
[26] K. M. Sivanandaiah, V. V. Suresh Babu, B. P. Gangadhar, *Tetrahedron Lett.* **1996**, *37*, 5989.
[27] L. Navarre, R. Martinez, J. P. Genet, S. Darses, *J. Am. Chem. Soc.* **2008**, *130*, 6159.

Supporting Information

for *Macromol. Rapid Commun.,* DOI: 10.1002/marc.201800857

Different Routes to Ampholytic Polydehydroalanine: Orthogonal versus Simultaneous Deprotection

Jan-Hendrik Kruse, Philip Biehl, and Felix Helmut Schacher*

Supporting Information

Different routes to ampholytic polydehydroalanine - orthogonal vs. simultaneous deprotection

J. Kruse[a,b], P. Biehl[a,b] and F. H. Schacher[a,b] *

[a]Institute of Organic Chemistry and Macromolecular Chemistry (IOMC), Friedrich-Schiller-University
Jena, Humboldtstraße 10, D-07743 Jena, Germany
[b]Jena Center for Soft Matter (JCSM), Friedrich-Schiller-Universität Jena, Philosophenweg 7, 07743
Jena, Germany

Email: felix.schacher@uni-jena.de

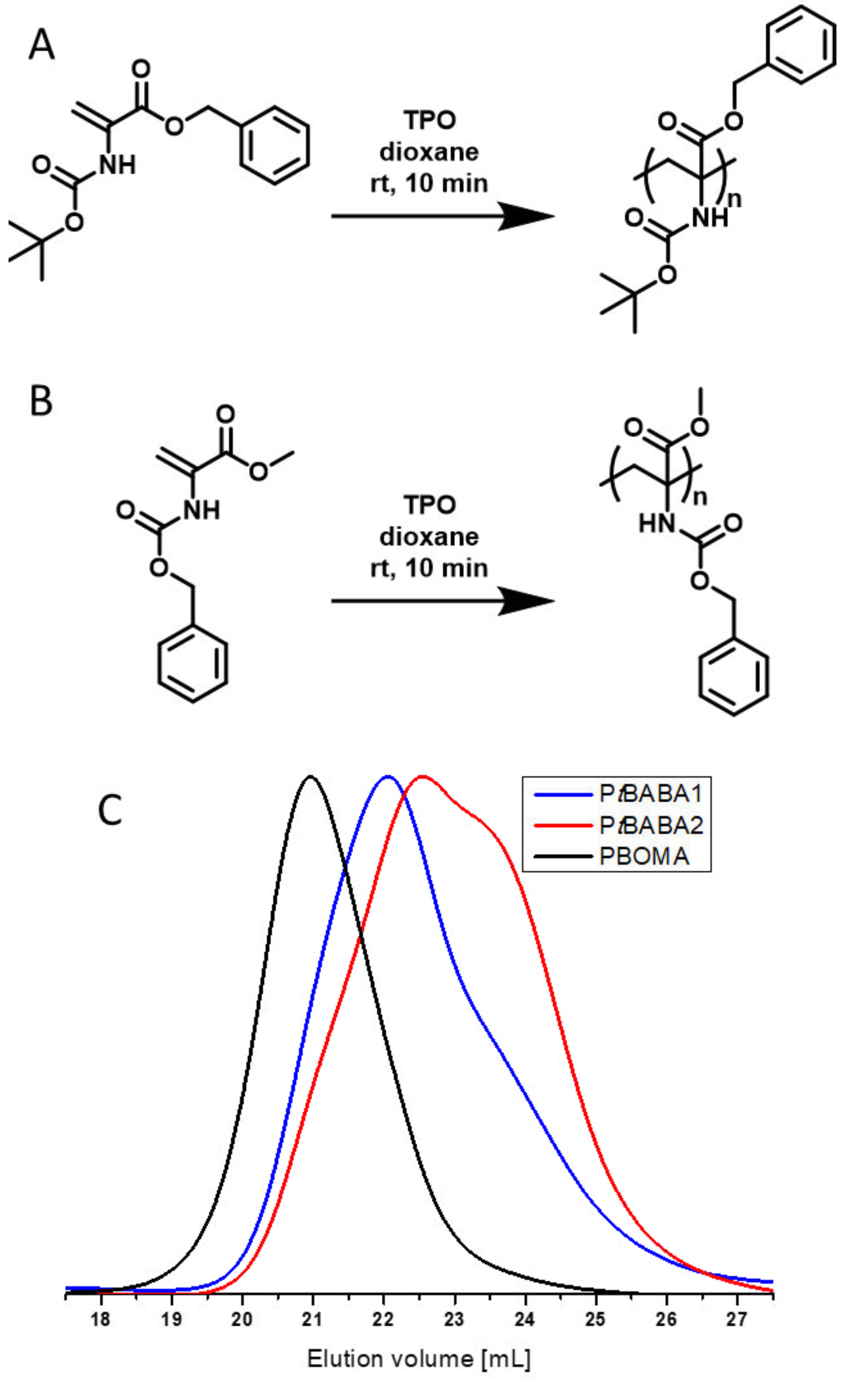

Figure S1: **A:** FRP of *t*BABA, **B:** FRP of BOMA, **C:** SEC elution traces of P*t*BABA1 (deprotected to PABA), P*t*BABA2 (deprotected to PDha) and PBOMA (deprotected to PDha) (THF-SEC, PS calibration).

Publication P5

“Surface Functionalization of Magnetic Nanoparticles Using a Thiol-Based Grafting-Through Approach”

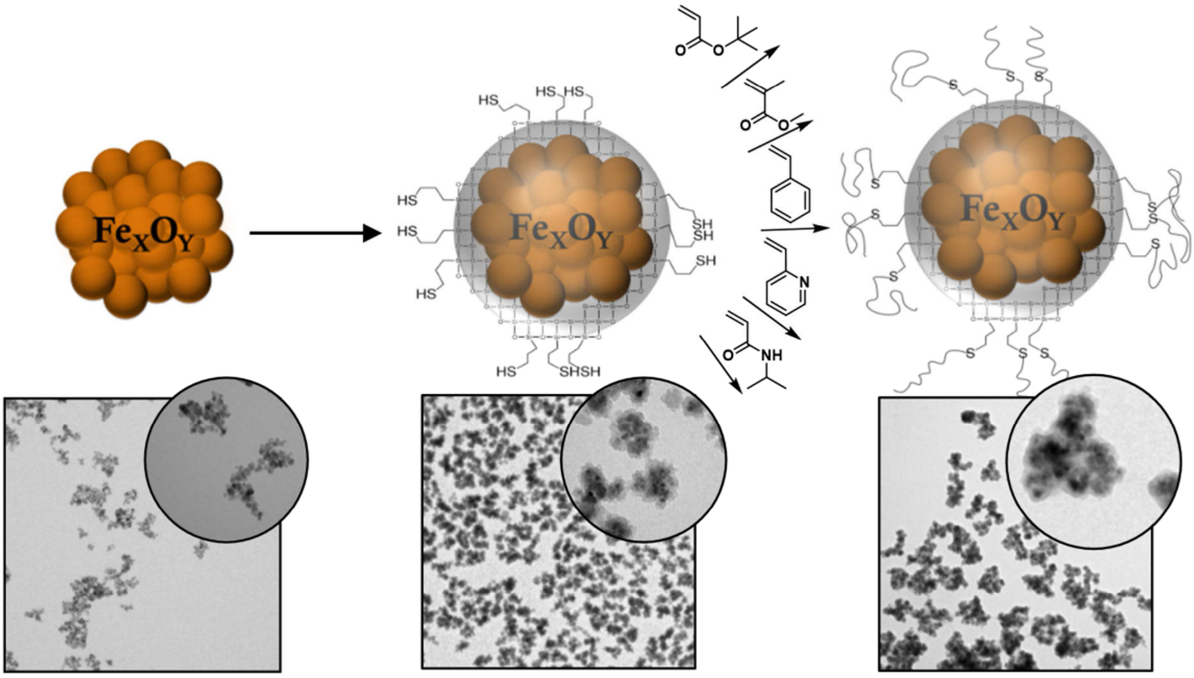

P. Biehl, F. H. Schacher

Surfaces **2020**, *3,* 116-131

surfaces

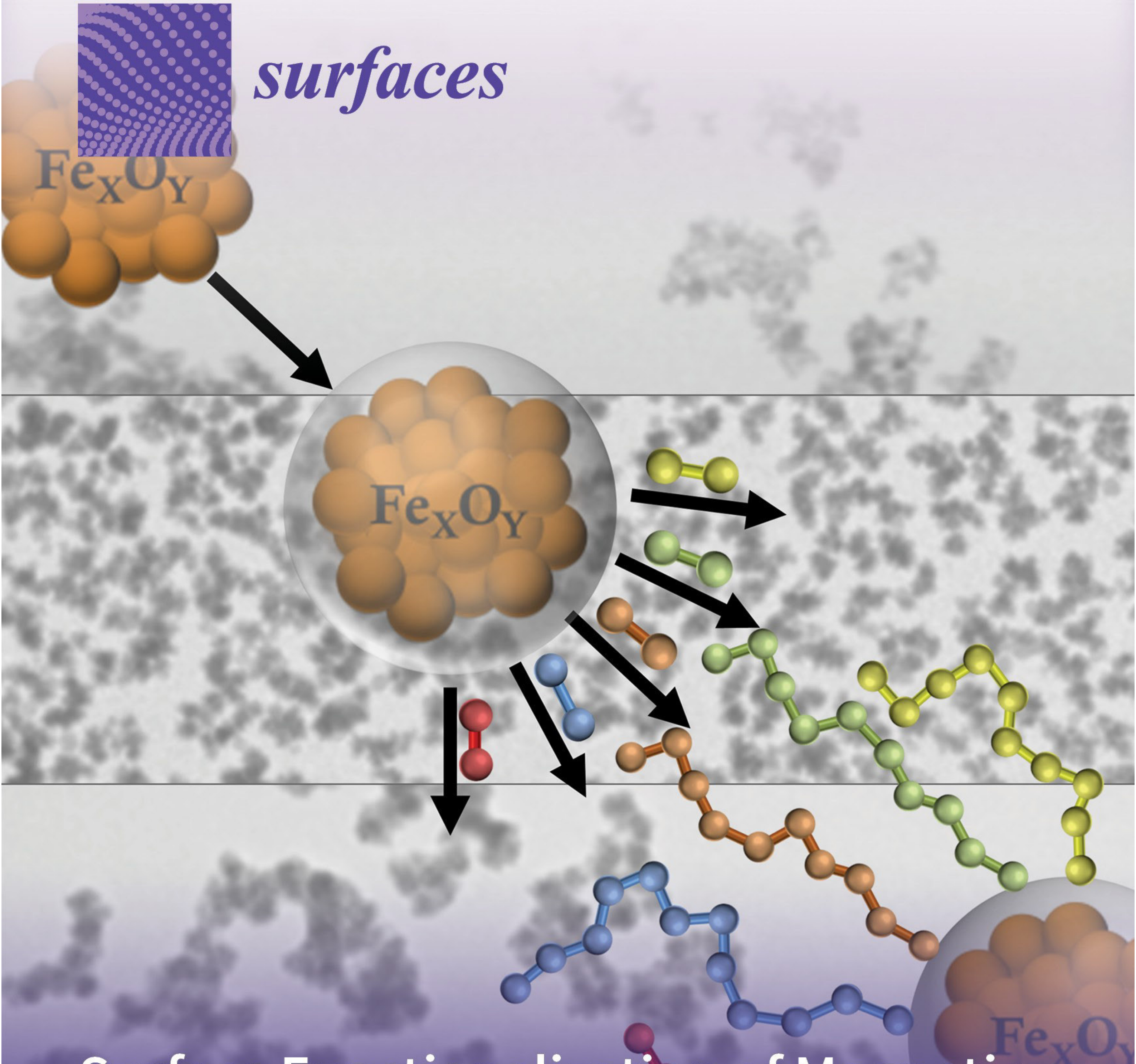

Surface Functionalization of Magnetic Nanoparticles Using a Thiol-based Grafting Through Approach

Volume 3 · Issue 1 | March 2020

MDPI

mdpi.com/journal/surfaces
ISSN 2571-9637

surfaces

Article

Surface Functionalization of Magnetic Nanoparticles Using a Thiol-Based Grafting-Through Approach

Philip Biehl and Felix H. Schacher *

Laboratory for Organic and Macromolecular Chemistry, Institut für Organische Chemie und Makro-molekulare Chemie, Friedrich-Schiller-Universität, Jena IOMC Humboldtstr. 10, D-07743 Jena, Germany; philip.biehl@uni-jena.de

* Correspondence: felix.schacher@uni-jena.de

Received: 20 February 2020; Accepted: 9 March 2020; Published: 18 March 2020

Abstract: Here we describe a simple and straightforward synthesis of different multifunctional magnetic nanoparticles by using surface bound thiol-groups as transfer agents in a free radical polymerization process. The modification includes a first step of surface silanization with (3-mercaptopropyl)trimethoxysilane to obtain thiol-modified nanoparticles, which are further used as a platform for modification with a broad variety of polymers. The silanization was optimized in terms of shell thickness and particle size distribution, and the obtained materials were investigated by dynamic light scattering (DLS), thermogravimetric analysis (TGA), transmission electron microscopy (TEM), and energy-dispersive X-ray spectroscopy (EDX). Subsequently, the free radical polymerization of different monomers (*tert*-butyl acrylate (*t*BA), methyl methacrylate (MMA), styrene, 2-vinyl pyridine (2VP), and *N*-isopropylacrylamide (NIPAAm)) was examined in the presence of the thiol-modified nanoparticles. During the process, a covalently anchored polymeric shell was formed and the resulting core–shell hybrid materials were analyzed in terms of size (DLS, TEM), shell thickness (TGA, TEM), and the presence of functional groups (attenuated total reflectance Fourier-transform infrared spectroscopy (ATR-FT-IR)). Hereby, the shell leads to a different solution behavior of the particles and in some cases an increased stability towards acids. Moreover, we examined the influence of the nanoparticle concentration during polymerization and we found a significant influence on dispersity of the resulting polymers. Finally, we compared the characteristics of the surface bound polymer and polymer formed in solution for the case of polystyrene. The herein presented approach provides straightforward access to a wide range of core–shell nanocomposites.

Keywords: magnetic multicore nanoparticles; surface modification; organic–inorganic nanocomposites; grafting-through

---

1. Introduction

Magnetic nanoparticles (MNPs) are discussed for a rather broad variety of applications such as magnetic resonance imaging (MRI) [1], as drug delivery systems [2,3], for tumor hyperthermia [4], bio separation [5–7], water purification systems [8–10], and as catalytic supports [11,12]. All these fields require well-controlled surface functionalization and a defined MNP morphology to ensure certain physical characteristics like magnetic properties or nanoparticle size while at the same presenting the desired chemical functionality at the surface. Especially the latter depending on the environment in which the particles will be applied and, here, the range includes highly saline aqueous media [7] as well as organic solvents [13]. Therefore, surface modification of MNPs can be regarded as one of the key elements for all applications being discussed. Here, the introduction of polymer surface coatings has been proven to impart enhanced suspension stability [14], protein repellence [15], solubility in a diverse set of environments [13,16], and adjustable surface charge [17]. For instance, both shielding and anti-fouling can be ascribed to poly(ethylene glycol)-based (PEG) surfaces as they are able to bind large amounts of water [18]. Control over any type of interactions with other molecules are another aspect for choosing a suitable surface coating as for example in biomedical applications a binding of biomolecules can be undesirable [19], while during bio sorting selective binding of certain partners is crucial [20].

There are several strategies for the immobilization of polymers at the surface of MNPs which can roughly be divided into adsorptive or covalent binding [21]. Whereby covalent binding itself can be subdivided into grafting-to, grafting-from, and grafting-through approaches, in any case the surface needs to be equipped with suitable binding motifs. In this regard, silane coupling agents are one of the most prominent ways to install certain functional groups, ranging from thiols over amines to vinyl moieties [7,22–26]. Among those, thiols are of interest for subsequent protein binding, with regard to thiol-ene chemistry but also in the context of radical polymerization techniques. They are widely employed as chain transfer agents in reversible addition fragmentation chain transfer polymerization RAFT [27] or the Strathclyde method [28,29] and typically exhibit rather high transfer rates. Such strategies have already been employed for the formation of polymer coatings at surfaces [30–35]. Here, mostly silica is used as starting material, either as macroscopic glass slides or as nanoparticles [30,32,34,35], and only few studies investigate MNP as starting material [31,33]. Whereas the general concept of immobilizing polymeric surface coatings using thiol moieties as anchoring points is known, our aim was to use this as a general strategy for the preparation of core–shell nanomaterials with a broad variety of surface functionality. Hence, we present a straightforward method to access MNP with different polymeric shells (poly(*tert*-butyl acrylate) (P*t*BA), poly(methyl methacrylate) (PMMA), polystyrene (PS), poly(2-viylpyridine) (P2VP), and poly(*N*-isopropyl acrylamide) (PNIPAAm)) starting from thiol-functionalized MNP as reactive platform. In a first step, pristine MNP are modified using silanization to immobilize thiol-groups and these particles are subsequently used as chain transfer agents in free radical polymerization (FRP) of different monomers. As a side effect, some polymers will be covalently linked to the particle surface, representing a simple one-step surface modification where the obtained nanocomposites can be magnetically separated from the reaction solution. Besides surface anchorage, this strategy also allows for a rapid polymer characterization in terms of dispersity and molecular weight as we assume that both polymers formed in solution and immobilized at the surface feature comparable molecular characteristics.

2. Materials and Methods

2.1. Instruments

Dynamic light scattering: DLS measurements were performed using an ALV Laser CGS 3 goniometer equipped with a 633 nm HeNe Laser (Langen, Germany) at 25 °C and at a detection angle of 90°. The CONTIN algorithm was used to evaluate the obtained data.

Thermogravimetric analysis: The samples (prepared and washed as described in the Nanoparticle Coating section) were magnetically separated and freeze-dried for 72 h. TGA measurements were carried out from 30 to 800 °C under synthetic air within a heating range of 10 K/min in a PerkinElmer TGA8000 device (Waltham, MA, USA).

Transmission electron microscopy: For TEM from aqueous solutions, copper grids were rendered hydrophilic by argon plasma cleaning for 120 s (Diener Electronics, Ebhausen, Germany). A total of 15 µL of the respective sample solution was applied to the grid, and excess sample was blotted away with a filter paper. TEM images were acquired with a 200 kV FEI Tecnai G 2 20 microscope equipped with a 4 K × 4 K Eagle HS CCD and a 1 K × 1 K Olympus MegaView camera for overview images (Hillsboro, OR, USA).

Size exclusion chromatography: SEC measurements were performed on an Agilent system (Santa Clara, CA, USA) equipped with G1310A pump, a G1362A refractive index detector, and both a PSS Gram30 and a PSS Gram1000 column in series (Mainz, Germany). DMAc + 0.21 wt % LiCl was applied as eluent at 1 mL min^{-1} flow rate and the column oven was set to 40 °C. For the calibration a PMMA or PS standard was used.

ATR-IR-spectroscopy: Measurements were performed on a PerkinElmer Frontier FT-IR, NIR, and FIR Spectrometer equipped with Golden Gate Single Reflection spectrometer (Waltham, MA, USA).

Ultrasonication: Ultrasonication was performed using an ElmaSonic S30H ultrasonic unit (Singen, Germany) and by using an ultrasound processor: Sonics VibraCell VC505 (Newtown, CT, USA).

Syringe pump: For defined addition of liquids, a Landgraf Laborsysteme HLL LA-30 syringe pump (Langenhagen, Germany) was used.

2.2. Materials

Sodiumhydrogencarbonate, iron(II) chloride, iron(III) chloride, sodium hydroxide, and potassium hydroxide were obtained from Roth in p.a. grade and used without further purification. MPTS, guanidine hydrochloride, 2-vinylpyridine, methyl methacrylate, *tert*-butyl acrylate, and styrene were purchased from Merck and all monomers were purified by column chromatography (AlOx) to detach stabilizer prior to use. 1 M solution of hydrogen chloride in ethyl acetate, absolute ethanol were purchased from Thermo Fisher Scientific and used as received. Tetrahydrofuran was of technical grade and distillated prior to use. The photoinitiator Lucirin-TPO was kindly provided by BASF.

2.3. Synthesis

Synthesis of MCNP: Multicore iron oxide nanoparticles were prepared according to previous work by Dutz et al. [36]. Briefly, the particles were synthesized by slowly adding a 1 M $NaHCO_3$ solution to a $FeCl_2$/$FeCl_3$ solution (total iron concentration 1.25 M; Fe^{2+}/Fe^{3+} ratio = 1/1.3) at a rate of 0.9 mL/min under permanent stirring up to pH 8, leading to the formation of a brownish precipitate. Afterward, the solution was boiled for 5 min to form an almost black precipitate. The MCNP were then magnetically washed with distilled water until a conductivity below 10 µS/cm (room temperature) was reached.

Synthesis of MPTS@MCNP: In a typical procedure MCNP (100 mg) were suspended in 500 mL water (0.2 mg mL^{-1}) with a pH of 11 (adjusted by NaOH) in a two neck round bottom flask. An ultra-sonication finger (1 min with 30% intensity) was used to suspend the particles and the suspension was directly stirred mechanically with 250 rpm by a Teflon stirrer and treated with an ultra-sonication bath. An amount of MPTS (100, 200, 300, or 400 µL) was dissolved in dry ethanol with a final concentration of 90 mmol/L. The solution was added with a constant drop rate of 50 µL/min to the nanoparticle suspension. Subsequently, the suspension was stirred for 19 h and the particles were afterwards separated magnetically followed by four washing steps with 40 mL water.

Synthesis of Polymer@MPTS@MCNP: In a typical procedure MPTS@MCNP (10 mg) were separated from solution and treated with 1 M guanidine hydrochloride solution (1 mL) for one hour. Afterwards, the particles were washed three times with THF. A microwave vial was charged with the respective monomer (48 mmol), TPO (13.5 mg), and 20 mL THF, sealed and degassed for 20 min before the suspension was treated with ultrasonication. The reaction vial was exposed to intense UV-irradiation for 15 min without stirring, to avoid unwanted magnetic precipitation. The obtained particles were separated magnetically and the supernatant was kept for further analysis. The particles were washed three times with THF to remove any unbound polymer and dried under vacuum.

Detachment of PS from Particles: 5 mg PS@MPTS@MCNP were suspended in a 1 M solution of hydrogen chloride in ethyl acetate. After several minutes the dissolving of particles was observed and a yellow solution (Fe^{3+}) was obtained. The yellow solution was separated from a resulted precipitate by centrifugation. A 1 M aqueous solution of KOH was added to the precipitate and sonicated for 30 min. After separation of the solution from the precipitate the obtained PS was dissolved in DMAc and measured by SEC.

3. Results and Discussion

3.1. MPTS@MCNP

In this study, we used multicore magnetic nanoparticles (MCNP) which were synthesized by coprecipitation of a Fe^{2+}/Fe^{3+}-solution as described earlier by Dutz et al. [36,37]. The particles exhibited a radius of 26 nm and consisted of several primary cores of about 11 nm which build up a cluster-like structure (multicore particle). This structure was already present before any coating process (TEM micrographs Figure S1, Supplementary Materials) and the average particle size was just below the single domain radius of iron oxides (Dc (Fe_3O_4) = 128 nm) [38]. Both size and magnetic properties of the MCNP used here would be favorable for an application in the field of hyperthermia or any strategy aiming for heat generation or rapid magnetic separation [39]. As MCNP tend to undergo secondary aggregation due to strong magnetic dipolar–dipolar interactions [40], the first challenge was the introduction of a defined silane coating while maintaining a well-dispersed system. The formation of a silica shell around MNPs is well-studied and already shown for many different systems [22,25,41–43]. However, we found that several protocols are difficult to adopt if the nanoparticles change in size or from single to multicore character or in chemical composition which made it necessary to optimize the coating procedure for the herein used particles. Several protocols suggest a two-step route for surface functionalization using 3-(mercaptopropyl)trimethoxysilane (MPTS, Scheme 1) [24,44,45] by applying first tetraethyl orthosilicate, followed by the functional silane. Nevertheless, in our case a straightforward one-step procedure turned out to lead to well-defined core–shell nanoparticles. Therefore, a diluted suspension of MCNP (0.2 mg/mL) at a pH of 11 (adjusted with KOH) was stirred mechanically and MPTS in dry ethanol was added at a constant flow rate of 50 μL min^{-1}. Higher concentrations of nanoparticles led to aggregation and thus to enclosure of bigger agglomerates within the same siloxane shell. Dilution was the only way we found to avoid larger aggregates during the coating process. After addition of the silane, the mixture was allowed to react for 18 h. The particles were then magnetically separated and washed three times with water. After application of the siloxane shell, the suspension changed color from dark to lighter brown, a phenomenon which is also described for similar coating procedures in the literature [41].

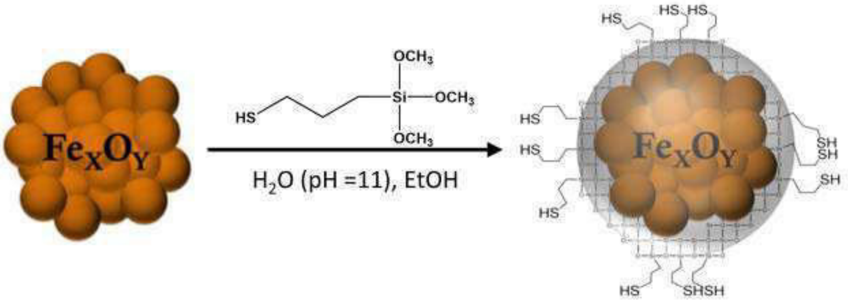

Scheme 1. Surface functionalization of magnetic multicore nanoparticles (MCNP) with (3-mercaptopropyl) trimethoxysilane (MPTS).

The ratio of MCNP to MPTS was optimized in order to control both size and shell thickness of the siloxane shell. By varying the amount of MPTS we were able to obtain different shell thicknesses and a rather good control about the overall size of the resulting nanoparticles. Figure 1A shows the size distribution measured by dynamic light scattering (DLS) prior to and after the coating process in water. The formation of a siloxane shell led to an increased hydrodynamic radius and clearly broadened the size distribution. While the pristine particles had a hydrodynamic radius of 26 nm, the core–shell particles exhibited an increasing hydrodynamic radius from 50 up to 100 nm as the ratio of MPTS to MCNP was increased from 1:1 to 4:1. Furthermore, we used thermogravimetric analysis (TGA) to quantify the amount of MPTS at the nanoparticle surface (Figure 1B) due to the presence of organic compounds (–$(CH_2)_3$–SH groups). The pristine MCNP showed a weight (wt) loss of 2.6% which is attributed to remaining carbonates which were used during the MCNP synthesis. The organic compounds in MPTS@MCNP led to an additional weight loss between 200 °C and 700 °C. With an increasing amount of MPTS the weight loss increased from 8.2% (ratio 1:1) up to 27.8% (ratio 4:1). This is a strong indication for the presence of a siloxane shell at the nanoparticle surface.

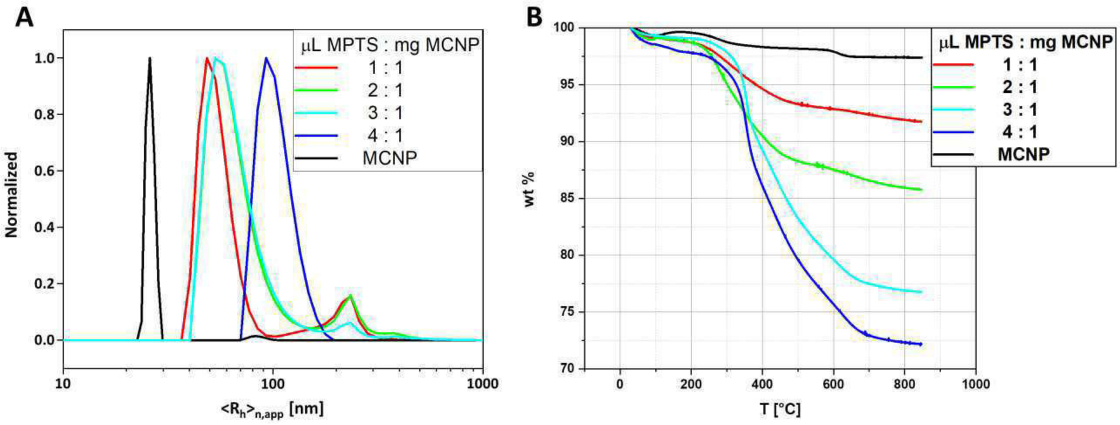

Figure 1. (**A**) Number-weighted DLS CONTIN plots of pristine MCNP (black line, $\langle R_h \rangle_{n,app}$ = 26 nm), and MPTS@MCNP obtained for varying ratios of MPTS to MCNP of 1:1 (red line, $\langle R_h \rangle_{n,app}$ = 48 nm), 2:1 (green line, $\langle R_h \rangle_{n,app}$ = 53 nm), 3:1 (cyan line, $\langle R_h \rangle_{n,app}$ = 52 nm), 4:1 (blue line, $\langle R_h \rangle_{n,app}$ = 93 nm). (**B**) Thermograms of MCNP (black line, 2.6% overall weight loss), MPTS@MCNP obtained from a ratio of MPTS to MCNP of 1:1 (red line, 8.2% overall weight loss), 2:1 (green line, 14.2% overall weight loss), 3:1 (cyan line, 23.2% overall weight loss), 4:1 (blue line, 27.8% overall weight loss).

Transmission electron microscopy (TEM) was used to confirm the mean size of the MPTS@MCNP nanoparticles (Figure 2), resulting in approximately 100–200 nm diameter which is in good agreement with the results from DLS measurements. With an increasing amount of MPTS a light grey shell becomes visible around the MCNP core, mainly evident for MPTS:MCNP ratios of 3:1 and 4:1. It was further possible to adjust different shell thicknesses, e.g., around 5 nm for the 3:1 ratio while about 15 nm were found in case of 4:1. As according to this data the MPTS@MCNP using a 3:1 ratio exhibited a defined and reasonably thin shell, these samples were chosen for further modifications.

In addition, scanning transmission electron microscopy/energy-dispersive X-ray spectroscopy (STEM-EDX) mapping was performed to verify the presence of thiols. The sample was analyzed towards iron-, silica-, sulfur-, and oxygen-content and—as can be seen from Figure 3—all elements are relatively homogeneously distributed. Here, we analyzed a rather large particle agglomerate as the performance of STEM-EDX measurements is improved—however, the data confirms successful immobilization of thiol-groups at the surface of MPTS@MCNP.

3.2. *Polymer@MPTS@MCNP*

The thiols at the surface of MPTS@MCNP enable further functionalization as they can be used as chain transfer agents in radical polymerization processes [28,46,47]. As side reaction, some polymer chains will be covalently linked to the MPTS@MCNP surface. Prior to use, MPTS@MCNP were treated with an aqueous solution of 1 M guanidine hydrochloride to activate the thiols followed by three washing steps with THF (the solvent for all polymerizations). THF was chosen as it is a suitable solvent for all investigated monomers/polymers and furthermore allowed a well dispersed nanoparticle suspension without aggregation occurring (Figure S2A, Supplementary Materials). It was possible to polymerize a broad variety of vinyl monomers (*t*BA, MMA, styrene, 2VP, NIPAAm) in the presence of the particles (Scheme 2). We chose polymer coatings with different properties in order to show the broad applicability of our strategy. All polymerizations were carried out under comparable conditions concerning monomer concentration and monomer to initiator ratio. Thus, each attempt consisted of 10 mg nanoparticles in 20 mL THF, diphenyl(2,4,6-trimethylbenzoyl)phosphine oxide (TPO) as photo-initiator with a concentration of 1.9 mmol L^{-1} and the respective monomer at a concentration of 2.4 mol L^{-1} (Table 1).

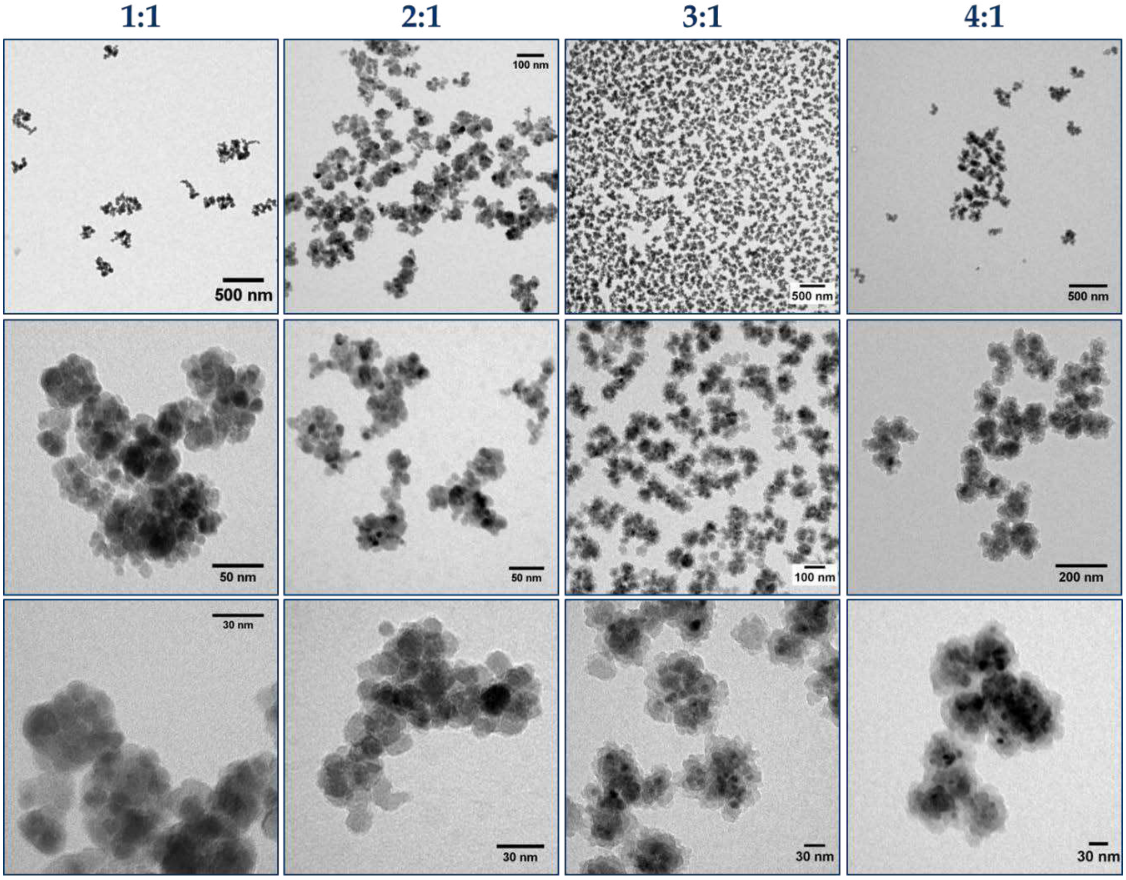

Figure 2. TEM micrographs of MPTS@MCNP obtained from different ratios of MPTS to MCNP at different magnifications.

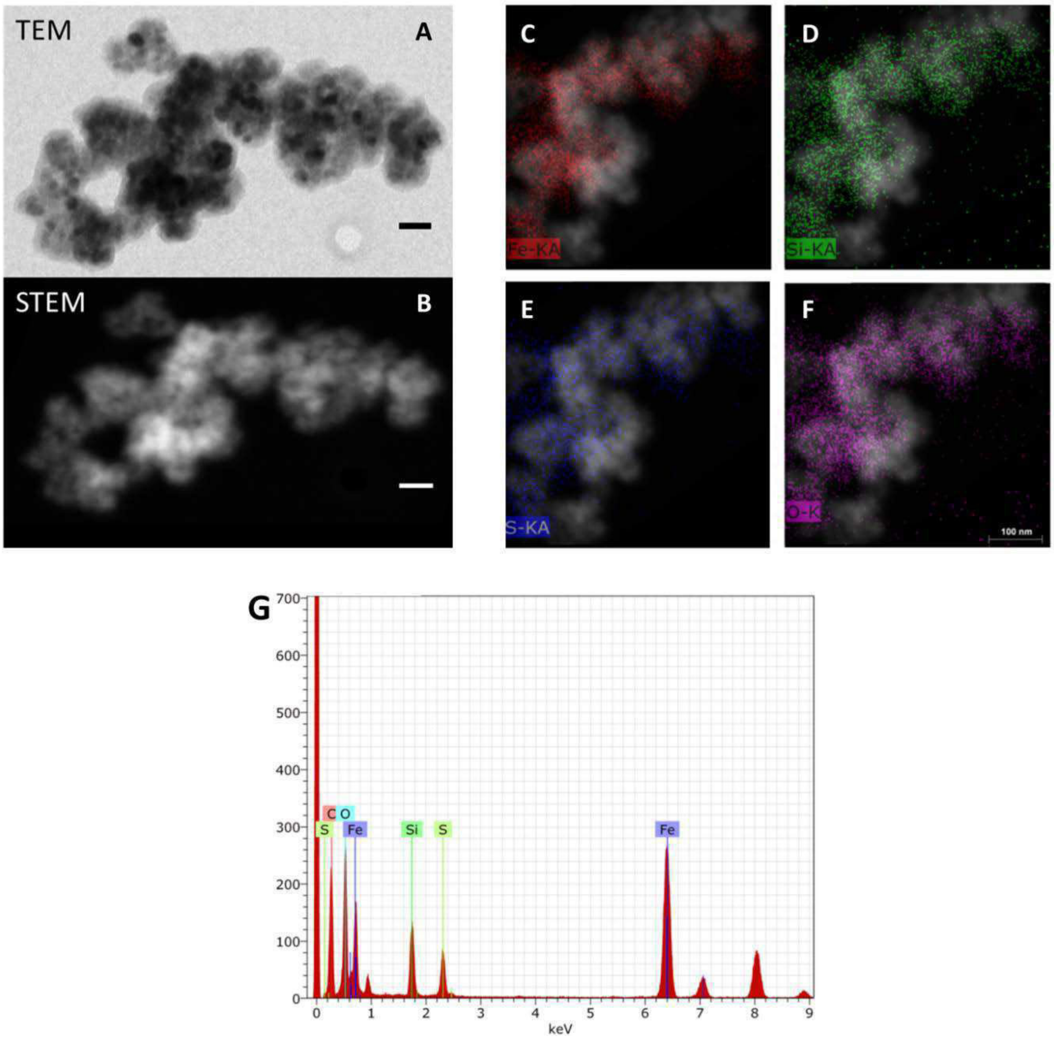

Figure 3. (**A**) TEM image of MPTS@MCNP (scale bar 100 nm); (**B**) STEM image of MCNP@MPTS (scale bar 100 nm); (**C–F**) EDX mapping of Fe, Si, S, and O obtained from the respective particles; (**G**) EDX analysis of MPTS@MCNP.

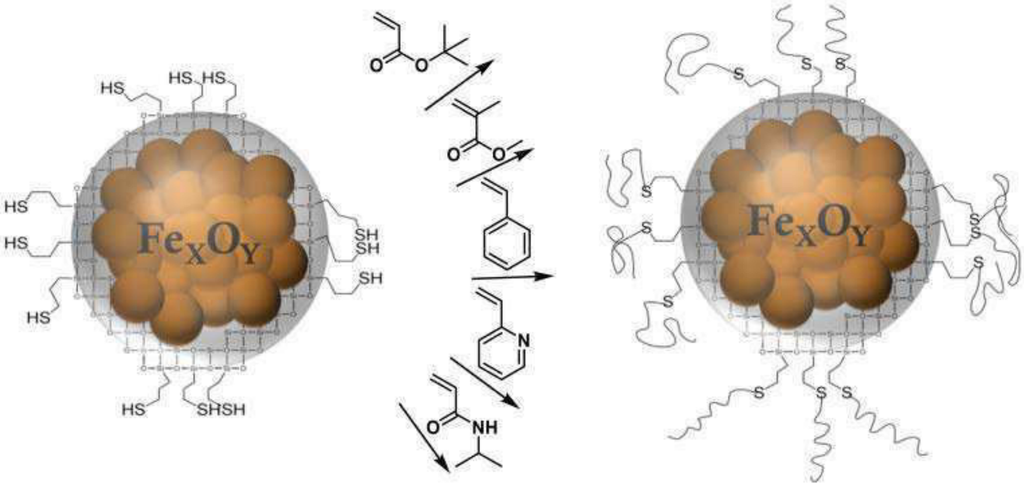

Scheme 2. Polymerization of different monomers in the presence of MPTS@MCNP.

By using a photo-initiator (TPO) it was possible to achieve rather short polymerization times of about 20 min. The particles were subsequently magnetically separated from the reaction mixture and the polymers in solution were further analyzed. The SEC traces shown in Figure 4 exhibited a rather broad distribution and the obtained molar masses varied between 9 kg mol^{-1} (P2VP) and 141 kg mol^{-1} (PMMA), depending on the respective monomer. The dispersity was around 2 for all polymers which is typical for a free radical polymerization process.

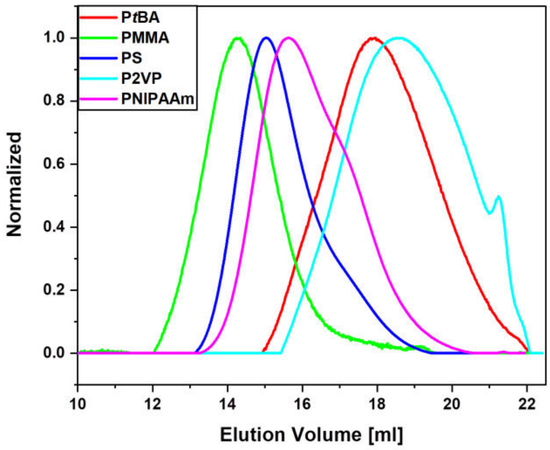

Figure 4. SEC elution traces (DMAc/LiCl) of polymers synthesized by free radical polymerization in the presence of MPTS@MCNP as chain transfer agent: red line: P*t*BA (M_n = 8.900 kg mol^{-1}; $Đ$ = 2.2); green line: PMMA (M_n = 141.200 kg mol^{-1}; $Đ$ = 2.1); blue line: PS (M_n = 58.500 kg mol^{-1}; $Đ$ = 1.9); cyan line: P2VP (M_n = 5.600 kg mol^{-1}; $Đ$ = 2.3); pink line: PNIPAAM (M_n = 35.400 kg mol^{-1}; $Đ$ = 2.0).

Table 1. Composition of different reaction mixtures for the free radical polymerization of different monomers in the presence of MPTS@MCNP as chain transfer agent, and SEC-results for the obtained polymers.

Monomer	**Molar Ratios**		**Monomer/MPTS@MCNP**	$\bar{M}_n$ **(kg mol^{-1})**	**$Đ$**
	Monomer	**TPO**			
***t*BA**	74	0.06	6.15 g/10 mg	8.900 (a)	2.2 (a)
MMA	74	0.06	4.8 g/10 mg	141.200 (a)	2.1 (a)
Styrene	74	0.06	5 g/10 mg	58.500 (b)	1.9 (b)
P2VP	74	0.06	5.05 g/10 mg	5.600 (b)	2.3 (b)
NIPAAm	74	0.06	5.43 g/10 mg	35.400 (a)	2.0 (a)

(a) Determined by SEC using DMAc/LiCl SEC as eluent and calibrated against PMMA standards; (b) Determined by SEC using DMAc/LiCl SEC as eluent and calibrated against PS standards.

The obtained particles were subsequently washed five times with THF to remove any loosely bound or adsorbed polymer. DLS was used to investigate how the size distribution of MPTS@MCNP changed after the polymerization (Figure 5). The initial radius of 51 nm of MPTS@MCNP in THF increased to values between 174 and 224 nm. We explain this rather drastic size increase by a combination of the polymer shell being formed together with a potential incorporation of several nanoparticles within one polymer shell, e.g., by recombination reactions occurring during radical polymerization. In addition, PMMA@MPTS@MCNP and P2VP@MPTS@MCNP showed a shoulder to higher hydrodynamic radii, which also hint towards some secondary aggregation taking place.

Thermogravimetric analysis (TGA) was performed to quantitatively analyze the amount of bound polymer (Figure 5). The thiol-functionalized particles showed a mass loss of 23.2% attributed to the organic compounds of the siloxane shell. The main weight loss for the particles after application of a polymer coating was obtained in the temperature range of 230–600 °C. Compared to MPTS@MCNP, the onset of the decomposition was shifted to lower temperatures, also indicating the presence of a polymer shell. One exception was observed for PNIPAAm where the main decomposition occurred between 250–620 °C. In comparison to the thermogravimetric measurement of MPTS@MCNP, we were able to estimate the relative amount of polymer which was between 31% (PMMA) and 21% (P*t*BA) for the majority of polymers. Again, PNIPAAm@MPTS@MCNP presented an exception as here only 11 wt % were found. We used the values derived from TGA measurements to calculate a theoretical shell thickness for each polymer coating. The formula used is given in the Supporting Information and the calculated thicknesses were between 7 nm (PNIPAAm) and 19 nm (PMMA). Please note that the calculated values are based on several assumptions, e.g., the presence of only spherical particles and a mixed core density composed of the MPTS shell and the Fe_2O_3 core–hence, these values should be treated as rough estimates. However, TGA confirmed successful immobilization for all polymers at the nanoparticle surface. A control reaction using pristine MCNP and *t*BA as monomer resulted in no observable polymer shell (Figure S2B, Supplementary Materials) indicating that a MPTS shell is mandatory for a successful polymer immobilization.

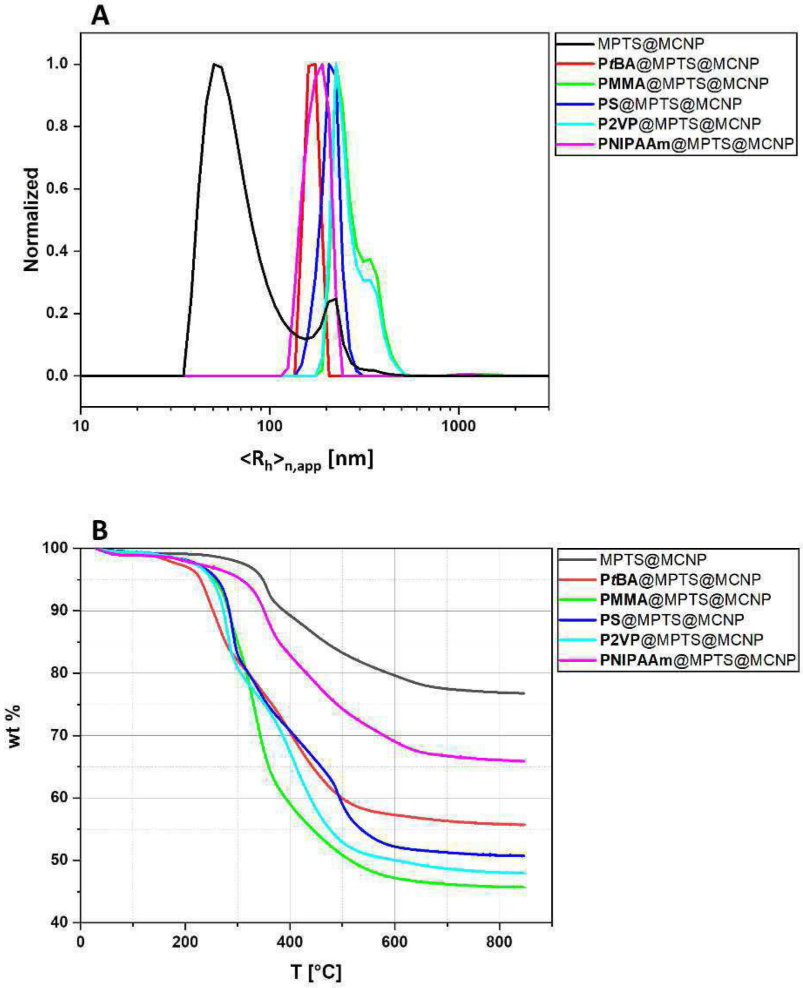

Figure 5. (**A**) Number-weighted DLS CONTIN plots of MPTS@MCNP (black line, $\langle R_h \rangle_{n,app}$ = 51 nm), P*t*BA@MPTS@MCNP (red line, $\langle R_h \rangle_{n,app}$ = 174 nm), PMMA@MPTS@MCNP (green line, $\langle R_h \rangle_{n,app}$ = 224 nm), PS@MPTS@MCNP (blue line, $\langle R_h \rangle_{n,app}$ = 206 nm), P2VP@MPTS@MCNP (cyan line, $\langle R_h \rangle_{n,app}$ = 224 nm), PNIPAAm@MPTS@MCNP (pink line, $\langle R_h \rangle_{n,app}$ = 190 nm). (**B**) Thermograms between 50 °C and 850 °C under synthetic air of MPTS@MCNP (black line, 23.2% overall weight loss), P*t*BA@MPTS@MCNP (red line, 44.3% overall weight loss), PMMA@MPTS@MCNP (green line, 54.3% overall weight loss), PS@MPTS@MCNP (blue line, 49.3% overall weight loss), P2VP@MPTS@MCNP (cyan line, 52.0% overall weight loss); PNIPAAm@MPTS@MCNP (pink line, 34.1% overall weight loss).

The TEM micrographs in Figure 6 show the MPTS-coated particles and the core–shell-shell nanoparticles obtained after polymerization. It is evident that the radius of the particles increased after modification, which we explain by partial aggregation and the presence of a thicker shell. However, it is difficult to see any difference in contrast between both shells. Nevertheless, the overall size of the aggregates in the TEM micrographs is within the same range as the values obtained from DLS measurements (between 200 and 400 nm) (Table 2).

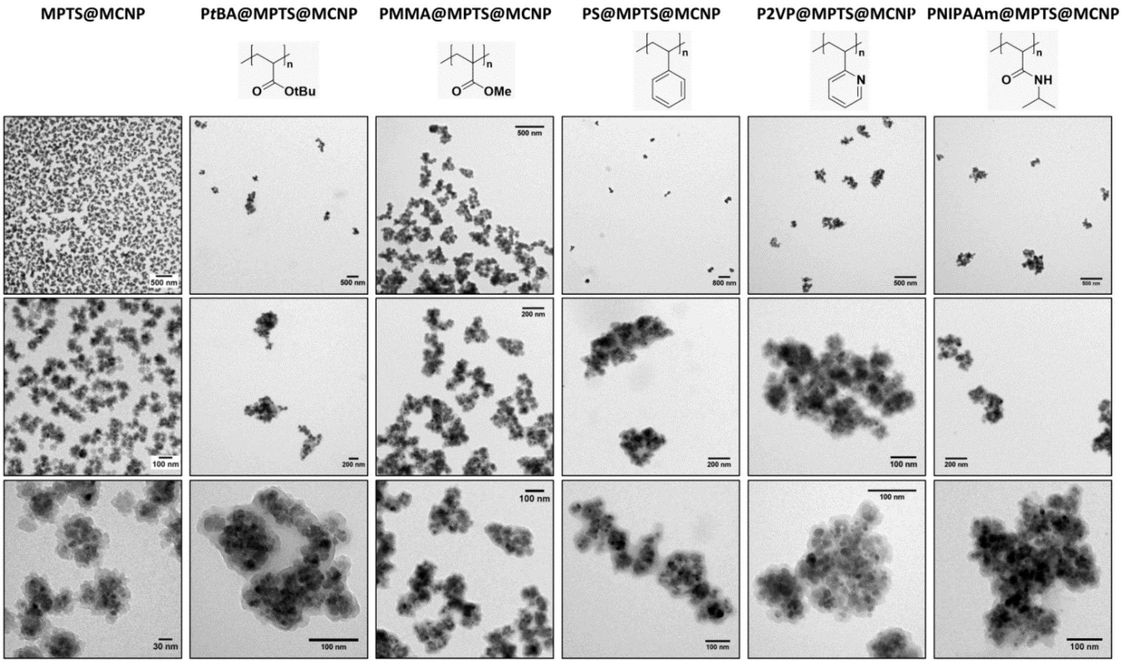

Figure 6. TEM micrographs of different polymer@MPTS@MCNP obtained from polymerizations in the presence of MPTS@MCNP as chain transfer agent at different magnification.

Table 2. Mass loss between 200 and 800 °C under synthetic air and hydrodynamic radius of Polymer@MPTS@MCNP.

Sample	wt Loss (%)	$\langle R_h \rangle_{n,app\ max}$ (nm)	Calculated Polymer Shell Thickness (nm)
MPTS@MCNP	23.2	51	
P*t*BA@MPTS@MCNP	44.3 (Δ = 21.1)	174	14 (a)
PMMA@MPTS@MCNP	54.3 (Δ = 31.1)	224	19 (a)
PS@MPTS@MCNP	49.3 (Δ = 26.1)	206	17 (a)
P2VP@MPTS@MCNP	52.0 (Δ = 28.8)	224	18 (a)
PNIPAAm@MPTS@MCNP	34.1 (Δ = 10.9)	190	7 (a)

(a) Calculated according to Equation S1, Supplementary Materials.

As another method to probe the chemical composition, ATR FT-IR measurements were performed to analyze the functional groups for MPTS@MCNP and polymer@MPTS@MCNP (Figure 7). Whereas MPTS@MCNP did not show any characteristic bands, specific signals for the surface immobilized polymer were observed in all other cases (Table 3). Particles functionalized with carbonyl containing polymers showed characteristic bands around 1720 cm^{-1}, while bands for the aromatic ring system (between 1600–1570 cm^{-1} and 1500–1470 cm^{-1}) appeared for P2VP and PS. In addition, after immobilization of PNIPAAm an additional band around 1550 cm^{-1} was evident, which can be assigned to the amide functionality. Altogether, both TGA as well as ATR FT-IR confirmed the successful formation of different polymer shells.

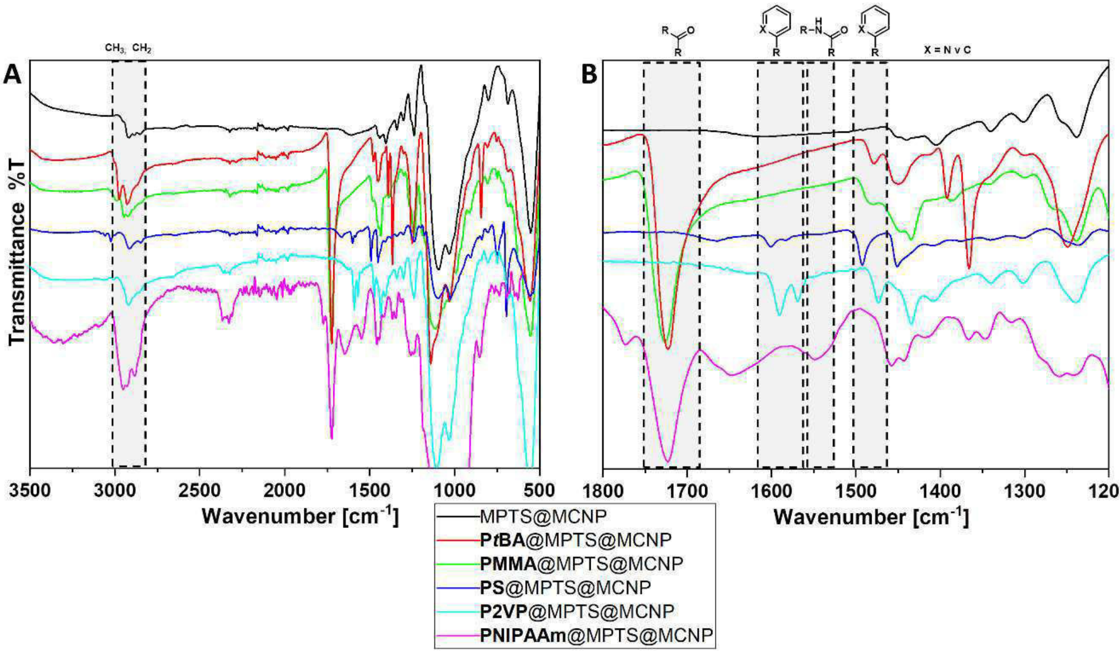

Figure 7. (**A**) ATR-FTIR spectra—black line: MPTS@MCNP; red line: P*t*BA@MPTS@MCNP; green line: PMMA@MPTS@MCNP; blue line: PS@MPTS@MCNP; cyan line: P2VP@MPTS@MCNP; pink line: PNIPAAm@MPTS@MCNP. (**B**) Enlargement of the region within the spectra where functional groups can be assigned.

Table 3. Assignment of selected IR-bands of polymer@MPTS@MCNP

Band Assignment	**Wavenumbers in cm^{-1} Surface Coating**				
	P*t*BA	**PMMA**	**PS**	**P2VP**	**PNIPAAm**
ν_{as} (CH$_3$, CH$_2$)	2975 ms	2993 m	-	2926 s	2953 s
ν_{as} (CH$_3$, CH$_2$)	2924 ms	2950 ms	2912 m	2336 w	2882 s
ν (C=O)	1722 s	1725 s	-	-	1721 s
δ (CO–N–H)	-	-	-	-	1549 m
ν (C–C in–ring)	-	-	1603 w	1591 m/1569 s	-
ν (C–C in–ring)	-	-	1493 ms/1451 ms	1473 ms	-

Vibrational mode: ν_{as}—asymmetric stretching vibration; ν—stretching vibration; δ—deformation vibration; Intensities: w—weak; m—medium, ms—medium strong, s—strong.

It could further be observed that the nanoparticles exhibited different solution properties after coating. For example, PNIPAAm/P2VP@MPTS@MCNP were well-dispersed in THF and water, whereas all other particles could mainly be dispersed in THF and other organic solvents. However, an expected temperature response of PNIPAAm@MPTS@MCNP could not be observed. Whereas this was initially surprising, similar findings were made by Wang et al. who synthesized magnetic nanoparticles with a coating of P(PEGMA-co-NIPAAm). Here, also no thermo-responsive behavior was observed, which was explained by aggregation hindrance due to sterical constraints of the polymer chains after surface immobilization [31].

3.3. Influence of Particle Concentration on the Polymerization

As the surface bound thiols act as chain transfer agents during the radical polymerization step it can be expected that the nanoparticle concentration has an influence on the polymerization. Therefore, the amount of MPTS@MCNP during a styrene polymerization was varied between 5 and 50 mg and the resulting polymers were investigated by SEC (Figure 8). As expected, the dispersity was decreasing from 9.6 to 2.8 with an increasing amount of MPTS@MCNP, while at the same time the M_n

was increasing, both effects of the chain transfer agent concentration. However, taking into account the shape of the SEC elution traces and the fact that the maximum in the elution curve is not constantly decreasing leads us to the conclusion that the influence on the overall dispersity is more pronounced (Table 4).

Table 4. SEC results for PS obtained by free radical polymerization in the presence of different amounts of MPTS@MCNP as chain transfer agent

MPTS@MCNP (mg)	M_n (a) (kg mol^{-1})	$Đ$ (a)
5	6.900	9.6
10	12.800	5.2
20	13.300	4.5
50	62.600	2.8

(a) Determined by SEC using DMAc/LiCl SEC as eluent and calibrated against PS standards.

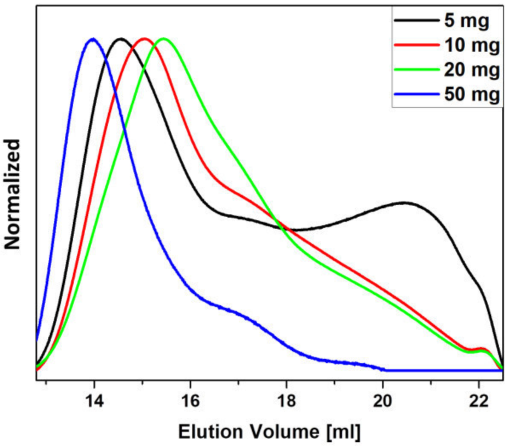

Figure 8. SEC elution traces (DMAc/LiCl) of PS synthesized by free radical polymerization in the presence of different amounts of MPTS@MCNP as chain transfer agent: black line: PS obtained in the presence of 5 mg (M_n = 6.900 kg mol^{-1}; $Đ$ = 9.6); red line: PS (10 mg, M_n = 12.800 kg mol^{-1}; $Đ$ = 5.2); green line: PS (20 mg, M_n = 13.300 kg mol^{-1}; $Đ$ = 4.5); blue line: PS (50 mg, M_n = 62.600 kg mol^{-1}; $Đ$ = 2.8).

3.4. Comparison of Polymer Formed at the Nanoparticle Surface vs. in Solution

We were interested in comparing the characteristics of polymer formed in solution to the material covalently immobilized at the surface of MPTS@MCNP. We therefore exemplarily investigated PS@MPTS@MCNP obtained in the presence of 50 mg MPTS@MCNP where according to TGA data the thickest polymer shell was formed (Figure S3, Supplementary Materials). TEM images show that the particles indeed exhibit a thick shell and form large aggregates (Figure 9A–D), which we so far attribute to the increased concentration of MPTS@MCNP during polymerization. PS@MPTS@MCNP were poorly water soluble and exhibited a foil-like structure upon drying, as well as increased resistance towards 1 M aq. HCl as the formation of an organic shell with increased hydrophobicity reduces the accessibility of the magnetic core. While the pristine particles dissolved within seconds, ultrasonication for several minutes was necessary in case of coated particles.

After PS@MPTS@MCNP were exposed to 1 M HCl/ethyl acetate solution to dissolve the iron oxide core, the siloxane shell was dissolved in a second step using 1 M aq. KOH. The obtained polymer was precipitated and investigated via SEC (Figure 9E). Both elution curves of PS obtained in the polymerization solution and from PS@MPTS@MCNP matched well although at higher elution volumes a shoulder was visible for PS from solution. This is an indication that polymers with lower molar masses might be less represented on the particle surface.

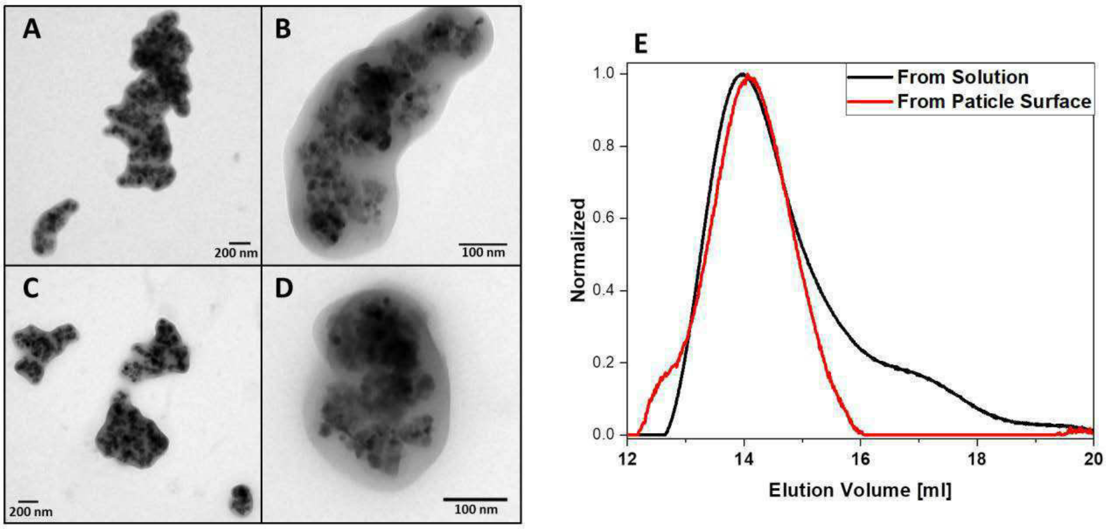

Figure 9. (**A–D**) TEM micrographs of PS@MPTS@MCNP; (**E**) SEC elution traces (DMAc/LiCl) of PS synthesized by free radical polymerization in the presence of MPTS@MCNP: black line: PS from reaction solution (M_n = 62.600 kg mol^{-1}; $Đ$ = 2.78); red line: PS obtained from the particle surface (M_n = 165 kg mol^{-1}; $Đ$ = 1.80).

4. Conclusions

We demonstrated a simple and straightforward method to covalently immobilize different polymers at the surface of iron oxide MNPs. The obtained hybrid materials were synthesized in a two-step coating process: silanization was first used to immobilize thiol-groups which were used in a second coating step for a grafting through approach in a free radical polymerization. The silanization was optimized in terms of shell thickness and size distribution of the nanoparticles and allowed access to defined nanomaterials which served as a platform for further surface modification. We examined several monomers (MMA, *t*BA, sytrene, 2VP, and NIPAAm) as potential polymer coatings and were able to show that this method allows the formation of a broad variety of polymer shells. The resulting materials exhibited a polymer content of 10–30 wt % and the amount of thiol-functionalized MCNP had a direct effect on the polymerization process. Finally, the mean molecular weight of the surface-immobilized polymer in case of polystyrene corresponded quite well to the material formed in solution during the polymerization. In conclusion, we present a straightforward, time- and cost-efficient method to access a broad variety of covalently anchored polymeric coatings for magnetic nanoparticles.

Supplementary Materials: The following are available online at http://www.mdpi.com/2571-9637/3/1/11/s1: Figure S1: TEM micrographs of pristine MCNP, Figure S2: Number-weighted DLS CONTIN plots of MPTS@MCNP in different solvents and thermograms for a control experiment using pristine MCNP for grafting attempts; Figure S3: Thermograms between 50 °C and 850 °C under synthetic air of MPTS@MCNP (black line, 19% overall weight loss), PS@MPTS@MCNP (red line, 50% overall weight loss); Equation S1: Formula used for the calculation of shell thickness according to TGA.

Author Contributions: P.B. and F.H.S. conceived this work. P.B. carried out the synthesis, physico chemical characterization, and data analysis. P.B. and F.H.S. jointly discussed results and wrote the manuscript. All authors have read and agreed to the published version of the manuscript.

Funding: This research was funded by the Deutsche Forschungsgemeinschaft (DFG, SCHA1640/12-1).

Acknowledgments: The authors are grateful to Andreas Weidner (TU Ilmenau) for providing the multicore magnetic nanoparticles. F.H.S. and P.B. gratefully acknowledge financial support through the Deutsche Forschungsgemeinschaft (DFG, SCHA1640/12-1). The TEM facilities of the Jena Center for Soft Matter (JCSM) were established with a grant from the German Research Council (DFG) and the European Fonds for Regional Development (EFRE).

Conflicts of Interest: The authors declare no conflict of interest.

References

1. Ito, A.; Shinkai, M.; Honda, H.; Kobayashi, T. Medical Application of Functionalized Magnetic Nanoparticles. *J. Biosci. Bioeng.* **2005**, *100*, 1–11. [CrossRef] [PubMed]
2. Song, L.; Ho, V.H.B.; Chen, C.; Yang, Z.; Liu, D.; Chen, R.; Zhou, D. Efficient, pH-Triggered Drug Delivery Using a pH-Responsive DNA-Conjugated Gold Nanoparticle. *Adv. Healthc. Mater.* **2013**, *2*, 275–280. [CrossRef] [PubMed]
3. Mochalin, V.N.; Pentecost, A.; Li, X.-M.; Neitzel, I.; Nelson, M.; Wei, C.; He, T.; Guo, F.; Gogotsi, Y. Adsorption of Drugs on Nanodiamond: Toward Development of a Drug Delivery Platform. *Mol. Pharm.* **2013**, *10*, 3728–3735. [CrossRef]
4. Hergt, R.; Dutz, S.; Müller, R.; Zeisberger, M. Magnetic Particle Hyperthermia: Nanoparticle Magnetism and Materials Development for Cancer Therapy. *J. Phys. Condens. Matter* **2006**, *18*, S2919–S2934. [CrossRef]
5. Chen, Y.; Xiong, Z.; Zhang, L.; Zhao, J.; Zhang, Q.; Peng, L.; Zhang, W.; Ye, M.; Zou, H. Facile Synthesis of Zwitterionic Polymer-Coated Core-Shell Magnetic Nanoparticles for Highly Specific Capture of N-Linked Glycopeptides. *Nanoscale* **2015**, *7*, 3100–3108. [CrossRef]
6. Yeh, C.-H.; Chen, S.-H.; Li, D.-T.; Lin, H.-P.; Huang, H.-J.; Chang, C.-I.; Shih, W.-L.; Chern, C.-L.; Shi, F.-K.; Hsu, J.-L. Magnetic Bead-Based Hydrophilic Interaction Liquid Chromatography for Glycopeptide Enrichments. *J. Chromatogr. A* **2012**, *1224*, 70–78. [CrossRef]
7. Urena-Benavides, E.E.; Lin, E.L.; Foster, E.L.; Xue, Z.; Ortiz, M.R.; Fei, Y.; Larsen, E.S.; Kmetz, A.A., II; Lyon, B.A.; Moaseri, E.; et al. Low Adsorption of Magnetite Nanoparticles with Uniform Polyelectrolyte Coatings in Concentrated Brine on Model Silica and Sandstone. *Ind. Eng. Chem. Res.* **2016**, *55*, 1522–1532. [CrossRef]
8. Yagub, M.T.; Sen, T.K.; Afroze, S.; Ang, H.M. Dye and its Removal from Aqueous Solution by Adsorption: A Review. *Adv. Colloid Interface Sci.* **2014**, *209*, 172–184. [CrossRef]
9. Ozay, O.; Ekici, S.; Baran, Y.; Kubilay, S.; Aktas, N.; Sahiner, N. Utilization of Magnetic Hydrogels in the Separation of Toxic Metal Ions from Aqueous Environments. *Desalination* **2010**, *260*, 57–64. [CrossRef]
10. Dutta, K.; De, S. Smart Responsive Materials for Water Purification: An Overview. *J. Mater. Chem. A* **2017**, *5*, 22095–22112. [CrossRef]
11. Fidale, L.C.; Nikolajski, M.; Rudolph, T.; Dutz, S.; Schacher, F.H.; Heinze, T. Hybrid Fe_3O_4@Amino Cellulose Nanoparticles in Organic Media–Heterogeneous Ligands for Atom Transfer Radical Polymerizations. *J. Colloid Interface Sci.* **2013**, *390*, 25–33. [CrossRef] [PubMed]
12. Stevens, P.D.; Fan, J.; Gardimalla, H.M.R.; Yen, M.; Gao, Y. Superparamagnetic Nanoparticle-Supported Catalysis of Suzuki Cross-Coupling Reactions. *Org. Lett.* **2005**, *7*, 2085–2088. [CrossRef]
13. Cai, J.; Miao, Y.Q.; Yu, B.Z.; Ma, P.; Li, L.; Fan, H.M. Large-Scale, Facile Transfer of Oleic Acid-Stabilized Iron Oxide Nanoparticles to the Aqueous Phase for Biological Applications. *Langmuir* **2017**, *33*, 1662–1669. [CrossRef] [PubMed]
14. Billing, M.; Gräfe, C.; Saal, A.; Biehl, P.; Clement, J.H.; Dutz, S.; Weidner, S.; Schacher, F.H. Zwitterionic Iron Oxide (γ-Fe_2O_3) Nanoparticles Based on P(2VP-grad-AA) Copolymers. *Macromol. Rapid Commun.* **2017**, *38*, 1600637. [CrossRef] [PubMed]
15. Zhao, T.; Chen, K.; Gu, H. Investigations on the Interactions of Proteins with Polyampholyte-Coated Magnetite Nanoparticles. *J. Phys. Chem. B* **2013**, *117*, 14129–14135. [CrossRef]
16. Debnath, K.; Mandal, K.; Jana, N.R. Phase Transfer and Surface Functionalization of Hydrophobic Nanoparticle using Amphiphilic Poly(amino acid). *Langmuir* **2016**. [CrossRef]
17. Von der Lühe, M.; Günther, U.; Weidner, A.; Grafe, C.; Clement, J.H.; Dutz, S.; Schacher, F.H. SPION@Polydehydroalanine Hybrid Particles. *RSC Adv.* **2015**, *5*, 31920–31929. [CrossRef]
18. Keefe, A.J.; Jiang, S. Poly(zwitterionic)protein Conjugates Offer Increased Stability without Sacrificing Binding Affinity or Bioactivity. *Nat. Chem.* **2012**, *4*, 59–63. [CrossRef]
19. Gong, Y.-K.; Winnik, F.M. Strategies in Biomimetic Surface Engineering of Nanoparticles for Biomedical Applications. *Nanoscale* **2012**, *4*, 360–368. [CrossRef]
20. Mazzucchelli, S.; Colombo, M.; De Palma, C.; Salvade, A.; Verderio, P.; Coghi, M.D.; Clementi, E.; Tortora, P.; Corsi, F.; Prosperi, D. Single-Domain Protein A-Engineered Magnetic Nanoparticles: Toward a Universal Strategy to Site-Specific Labeling of Antibodies for Targeted Detection of Tumor Cells. *ACS Nano* **2010**, *4*, 5693–5702. [CrossRef]

21. Biehl, P.; von der Lühe, M.; Dutz, S.; Schacher, F.H. Synthesis, Characterization, and Applications of Magnetic Nanoparticles Featuring Polyzwitterionic Coatings. *Polymers* **2018**, *10*, 91. [CrossRef] [PubMed]
22. McCarthy, S.A.; Davies, G.-L.; Gun'ko, Y.K. Preparation of Multifunctional Nanoparticles and their Assemblies. *Nat. Protoc.* **2012**, *7*, 1677–1693. [CrossRef] [PubMed]
23. Kumar, R.; Roy, I.; Ohulchanskyy, T.Y.; Goswami, L.N.; Bonoiu, A.C.; Bergey, E.J.; Tramposch, K.M.; Maitra, A.; Prasad, P.N. Covalently Dye-Linked, Surface-Controlled, and Bioconjugated Organically Modified Silica Nanoparticles as Targeted Probes for Optical Imaging. *ACS Nano* **2008**, *2*, 449–456. [CrossRef] [PubMed]
24. Chekina, N.; Horak, D.; Jendelova, P.; Trchova, M.; Benes, M.J.; Hruby, M.; Herynek, V.; Turnovcova, K.; Sykova, E. Fluorescent Magnetic Nanoparticles for Biomedical Applications. *J. Mater. Chem.* **2011**, *21*, 7630–7639. [CrossRef]
25. Kyeong, S.; Jeong, C.; Kim, H.Y.; Hwang, D.W.; Kang, H.; Yang, J.-K.; Lee, D.S.; Jun, B.-H.; Lee, Y.-S. Fabrication of Mono-Dispersed Silica-Coated Quantum Dot-Assembled Magnetic Nanoparticles. *RSC Adv.* **2015**, *5*, 32072–32077. [CrossRef]
26. Cui, Y.; Zheng, X.-S.; Ren, B.; Wang, R.; Zhang, J.; Xia, N.-S.; Tian, Z.-Q. Au@Organosilica Multifunctional Nanoparticles for the Multimodal Imaging. *Chem. Sci.* **2011**, *2*, 1463–1469. [CrossRef]
27. Chiefari, J.; Chong, Y.K.; Ercole, F.; Krstina, J.; Jeffery, J.; Le, T.P.T.; Mayadunne, R.T.A.; Meijs, G.F.; Moad, C.L.; Moad, G.; et al. Living Free-Radical Polymerization by Reversible Addition−Fragmentation Chain Transfer: The RAFT Process. *Macromolecules* **1998**, *31*, 5559–5562. [CrossRef]
28. O'Brien, N.; McKee, A.; Sherrington, D.C.; Slark, A.T.; Titterton, A. Facile, Versatile and Cost Effective Route to Branched Vinyl Polymers. *Polymer* **2000**, *41*, 6027–6031. [CrossRef]
29. Eckardt, O.; Wenn, B.; Biehl, P.; Junkers, T.; Schacher, F.H. Facile Photo-Flow Synthesis of Branched Poly(butyl acrylate)s. *React. Chem. Eng.* **2017**, *2*, 479–486. [CrossRef]
30. Zhou, F.; Liu, W.; Chen, M.; Sun, D.C. A Novel Way to Prepare Ultra-Thin Polymer Films Through Surface Radical Chain-Transfer Reaction. *Chem. Commun.* **2001**, 2446–2447. [CrossRef]
31. Wang, S.; Zhou, Y.; Guan, W.; Ding, B. One-Step Copolymerization Modified Magnetic Nanoparticles via Surface Chain Transfer Free Radical Polymerization. *Appl. Surf. Sci.* **2008**, *254*, 5170–5174. [CrossRef]
32. Chen, J.-J.; Struk, K.N.; Brennan, A.B. Surface Modification of Silicate Glass Using 3-(Mercaptopropyl)trimethoxysilane for Thiol–Ene Polymerization. *Langmuir* **2011**, *27*, 13754–13761. [CrossRef] [PubMed]
33. Bach, L.G.; Islam, M.R.; Kim, J.T.; Seo, S.; Lim, K.T. Encapsulation of Fe_3O_4 Magnetic Nanoparticles with Poly(methyl methacrylate) via Surface Functionalized Thiol-Lactam Initiated Radical Polymerization. *Appl. Surf. Sci.* **2012**, *258*, 2959–2966. [CrossRef]
34. Liu, P.; Liu, W.M.; Xue, Q.J. In Situ Radical Transfer Addition Polymerization of Styrene from Silica Nanoparticles. *Eur. Polym. J.* **2004**, *40*, 267–271. [CrossRef]
35. Liu, S.; Zhou, F.; Di, D.; Jiang, S. Surface-Confined Radical Chain Transfer: The Intermediate Reaction for Chemically Attaching Polymer Films on Porous Silica for Chromatographic Application. *Colloids Surf. A Physicochem. Eng. Asp.* **2004**, *244*, 87–93. [CrossRef]
36. Dutz, S.; Clement, J.H.; Eberbeck, D.; Gelbrich, T.; Hergt, R.; Müller, R.; Wotschadlo, J.; Zeisberger, M. Ferrofluids of Magnetic Multicore Nanoparticles for Biomedical Applications. *J. Magn. Magn. Mater.* **2009**, *321*, 1501–1504. [CrossRef]
37. Dutz, S.; Andrä, W.; Hergt, R.; Müller, R.; Oestreich, C.; Schmidt, C.; Töpfer, J.; Zeisberger, M.; Bellemann, M.E. Influence of Dextran Coating on the Magnetic Behaviour of Iron Oxide Nanoparticles. *J. Magn. Magn. Mater.* **2007**, *311*, 51–54. [CrossRef]
38. Lu, A.-H.; Salabas, E.L.; Schüth, F. Magnetic Nanoparticles: Synthesis, Protection, Functionalization, and Application. *Angew. Chem. Int. Ed.* **2007**, *46*, 1222–1244. [CrossRef]
39. Tong, S.; Quinto, C.A.; Zhang, L.; Mohindra, P.; Bao, G. Size-Dependent Heating of Magnetic Iron Oxide Nanoparticles. *ACS Nano* **2017**. [CrossRef]
40. Gao, J.; Gu, H.; Xu, B. Multifunctional Magnetic Nanoparticles: Design, Synthesis, and Biomedical Applications. *Acc. Chem. Res.* **2009**, *42*, 1097–1107. [CrossRef]
41. Rho, W.-Y.; Kim, H.-M.; Kyeong, S.; Kang, Y.-L.; Kim, D.-H.; Kang, H.; Jeong, C.; Kim, D.-E.; Lee, Y.-S.; Jun, B.-H. Facile Synthesis of Monodispersed Silica-Coated Magnetic Nanoparticles. *J. Ind. Eng. Chem.* **2014**, *20*, 2646–2649. [CrossRef]

42. Vogt, C.; Toprak, M.S.; Muhammed, M.; Laurent, S.; Bridot, J.-L.; Müller, R.N. High Quality and Tuneable Silica Shell–Magnetic Core Nanoparticles. *J. Nanopart. Res.* **2010**, *12*, 1137–1147. [CrossRef]
43. Yi, D.K.; Selvan, S.T.; Lee, S.S.; Papaefthymiou, G.C.; Kundaliya, D.; Ying, J.Y. Silica-Coated Nanocomposites of Magnetic Nanoparticles and Quantum Dots. *J. Am. Chem. Soc.* **2005**, *127*, 4990–4991. [CrossRef] [PubMed]
44. Viltužnik, B.; Košak, A.; Zub, Y.L.; Lobnik, A. Removal of Pb(II) Ions from Aqueous Systems using Thiol-Functionalized Cobalt-Ferrite Magnetic Nanoparticles. *J. Sol-Gel Sci. Technol* **2013**, *68*, 365–373. [CrossRef]
45. Shahverdi, N.; Heydarinasab, A.; Panahi, H.A.; Moniri, E. Synthesis and Evaluation of Enalapril-Loaded PVA/PMC Modified Magnetic Nanoparticles as a Novel Efficient Nano-Carrier. *Chem. Sel.* **2019**, *4*, 5246–5250. [CrossRef]
46. Forster, D.J.; Heuts, J.P.A.; Davis, T.P. Conventional and Catalytic Chain Transfer in the Free-Radical Polymerization of 2-Phenoxyethyl Methacrylate. *Polymer* **2000**, *41*, 1385–1390. [CrossRef]
47. Eckardt, O.; Seupel, S.; Festag, G.; Gottschaldt, M.; Schacher, F.H. Synthesis and Degradation of Branched, Photo-Labile Poly(acrylic acid) and Polystyrene. *Polym. Chem.* **2019**, *10*, 593–602. [CrossRef]

Supplementary Materials

Surface functionalization of magnetic nanoparticles using a thiol-based grafting through approach

Philip Biehl, F. H. Schacher

Institute of Organic and Macromolecular Chemistry (IOMC), Friedrich Schiller University Jena, Humboldtstraße 10, D-07743 Jena, Germany

E-mail: felix.schacher@uni-jena.de

Jena Center for Soft Matter (JCSM), Friedrich Schiller University Jena, Philosophenweg 7, D-07743 Jena, Germany

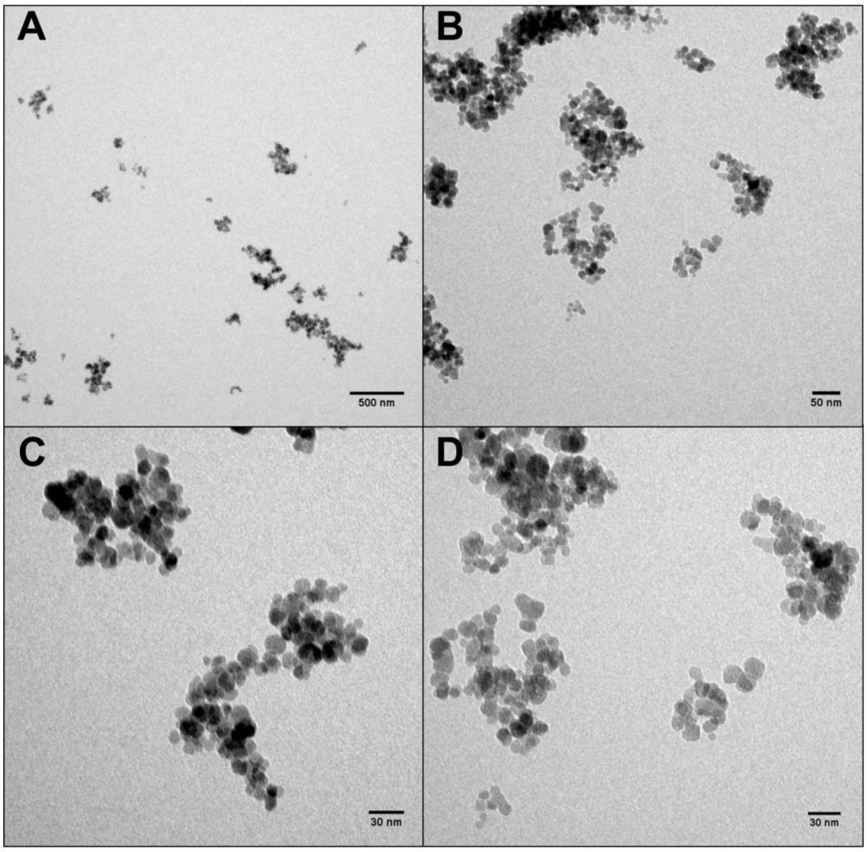

Figure S1: TEM micrographs of pristine MCNP (A-D, different magnifications).

The control sample was treated exactly like MPTS@MCNP. The polymerization of P*t*BA was in both cases successful but according to TGA results no polymer was anchored to the MCNP surface in case of the pristine MCNP.

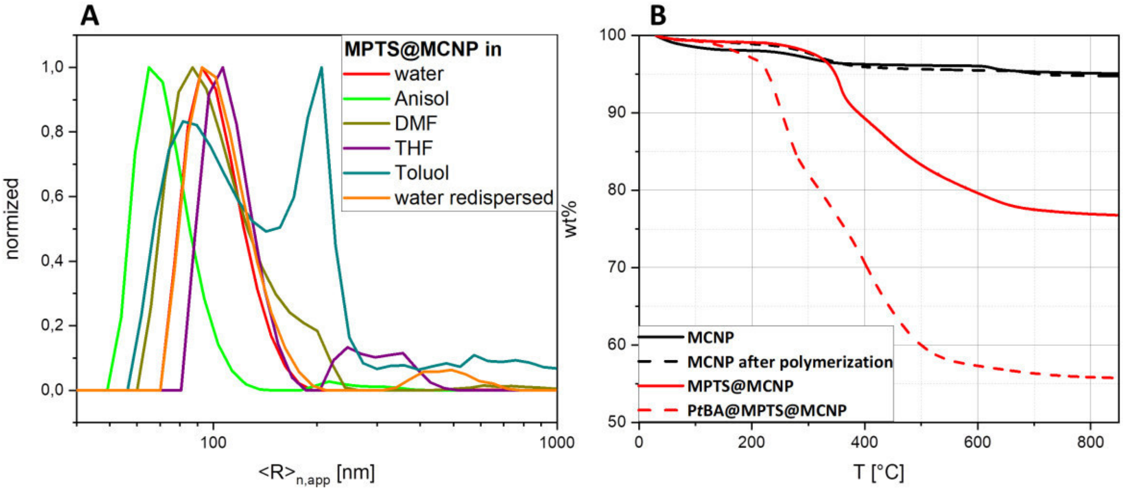

Figure S2: (A) Number-weighted DLS CONTIN plots of MPTS@MCNP obtained from a ratio MPTS:MCNP 4:1 in water (red line, $\langle R_h \rangle_{n,app}$ = 93 nm and diameter of 186 nm), MPTS@MCNP in anisol (green line, $\langle R_h \rangle_{n,app}$ = 65 nm and diameter of 130 nm), MPTS@MCNP in DMF (brown line, $\langle R_h \rangle_{n,app}$ = 87 nm and diameter of 174 nm), MPTS@MCNP in THF (purple line, $\langle R_h \rangle_{n,app}$ = 106 nm and diameter of 212 nm); MPTS@MCNP in toluol (turquoise line, $\langle R_h \rangle_{n,app}$ = 82 and 207 nm and diameter of 164 respectively 414 nm), MPTS@MCNP redispersed in water (orange line, $\langle R_h \rangle_{n,app}$ = 93 nm and diameter of 186 nm) (B) Thermograms between 50°C and 850°C under synthetic air of MCNP (black line, 5 % overall weight loss), MCNP after polymerization attempt with *t*BA as monomer(black dashed line, 5.3% overall weight loss), MPTS@MCNP (red line, 23.2% overall weight loss), P*t*BA@MPTS@MCNP (red dashed line, 44.3% overall weight loss).

Equation S1: Formula used for the calculation of shell thickness according to TGA

$$r_s = \sqrt[3]{r_c^3 + \left(r_c^3 \left(\frac{\rho_c}{\rho_s}\right)\left(\frac{WL}{RM}\right)\right)} - r_c$$

r_s …shell thickness

r_c … core radius (from DLS: MPTS@MCNP $\langle R_h \rangle_{n,app}$ = 52 nm)

ρ_c … core density (approx. 3.88 g/cm^3) →

$\rho(SiO_2)$[1] = 2.19 g/cm^3

ρ(Magnetite(5.1 g/cm^3) /Maghemite(5.24 g/cm^3))[2] = 5.17 g/cm^3

$\rho((SiO_2)_{0.4}/(\text{Magnetite/Maghemite})_{0.6})$ = 3.98g/cm^3 [a]

ρ_s … density of shell material ρ(P*t*BA)[3] = 1 g/cm^3

ρ(PMMA)[4] = 1.18 g/cm^3

ρ(PS)[5] = 1.06 g/cm^3

ρ(P2VP)[6] = 1.16 g/cm^3

ρ(PNIPAM)[7] = 1.1 g/cm^3

WL … weight loss

RM … residual mass

[a] The density of the core is based on the assumption that it contains 60% iron oxide, which consists to 50% of Magnetite and 50% Maghemite, and 40% condensed MPTS, which has a similar density as silica. The ratio for MPTS/iron oxide is based on the thermo gravimetric measurements showing a weight loss of 23.6% attributed to the MPTS shell. As The MPTS shell consists of 59% thermo degradable organic compounds and 41% non-degradable silica the 23.6% weight loss in TGA measurements lead to approximately 40% MPTS-shell in the particles.

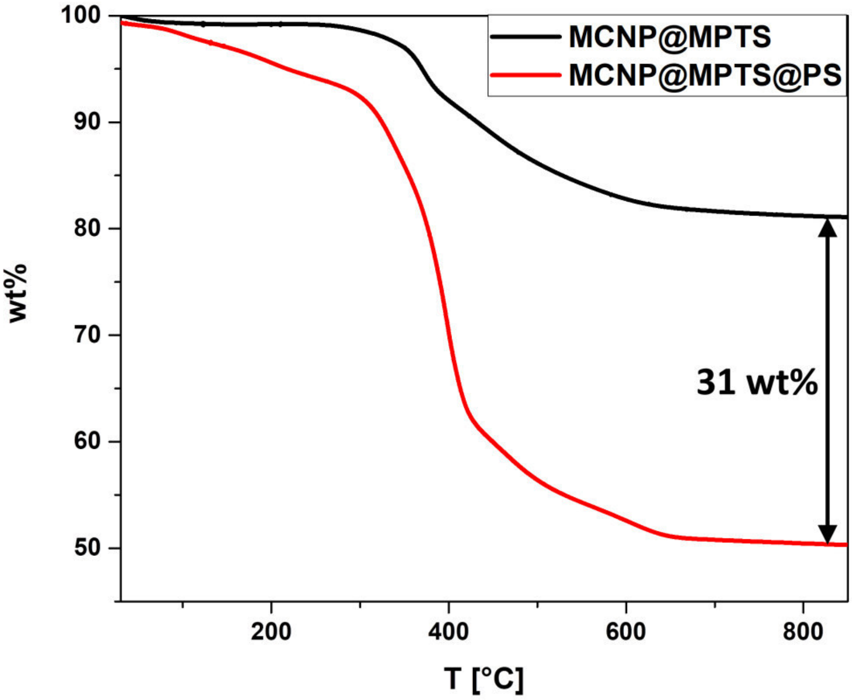

FigureS3: Thermograms between 50°C and 850°C under synthetic air of MPTS@MCNP (black line, 19 % overall weight loss), PS@MPTS@MCNP (red line, 50% overall weight loss).

References

1. Harald, F.; Hartmann-Schreier, J. Siliciumdioxid. RÖMPP [Online], Stuttgart, Georg Thieme Verlag: 2016.
2. Redaktion; Sitzmann, H. Eisenoxide. RÖMPP [Online], Stuttgart, Georg Thieme Verlag: 2013.
3. Miller, M.L.; Rauhut, C.E. Crystalline Poly(tert-butyl acrylate). *J. Polym. Sci.* **1959**, *38*, 63-72, doi:10.1002/pol.1959.1203813307.
4. Kaiser, W. Kunststoffchemie für Ingenieure : von der Synthese bis zur Anwendung. *Carl Hanser, München* **2011**, 353f.
5. Wang, C.; Hsu, C.-H.; Lin, J.-H. Scaling Laws in Electrospinning of Polystyrene Solutions. *Macromolecules* **2006**, *39*, 7662-7672, doi:10.1021/ma060866a.
6. Urakawa, O.; Yasue, A. Glass Transition Behaviors of Poly (Vinyl Pyridine)/Poly (Vinyl Phenol) Revisited. *Polymers* **2019**, *11*, 1153.
7. Sbeih, S.; Mohanty, P.S.; Morrow, M.R.; Yethiraj, A. Structural Parameters of Soft PNIPAM Microgel Particles as a Function of Crosslink Density. *J. Colloid Interface Sci.* **2019**, *552*, 781-793, doi:https://doi.org/10.1016/j.jcis.2019.05.047.

Publication P6

“Weak Polyampholytes at the Interface of Magnetic Nanocarriers: A Facile Catch and Release Platform for Dyes”

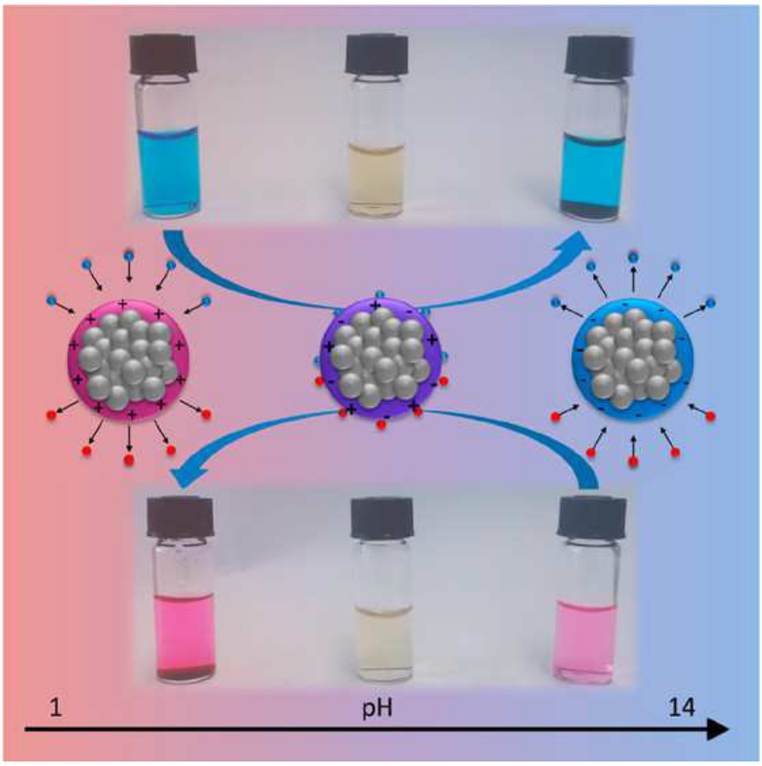

P. Biehl, P. Wiemuth, J. G. Lopez, M.-C. Barth, A. Weidner, S. Dutz, K. Peneva, F. H. Schacher

Langmuir **2020**, *36,* 6095–6105

LANGMUIR

pubs.acs.org/Langmuir Article

Weak Polyampholytes at the Interface of Magnetic Nanocarriers: A Facile Catch-and-Release Platform for Dyes

P. Biehl, P. Wiemuth, J. Garcia Lopez, M.-C. Barth, A. Weidner, S. Dutz, K. Peneva, and F. H. Schacher*

Cite This: *Langmuir* 2020, 36, 6095−6105

Read Online

ACCESS | Metrics & More | Article Recommendations | SI Supporting Information

ABSTRACT: We present a platform of charge-invertible core−shell hybrid particles for the selective and reversible adsorption of small charged molecules as model systems. The herein employed carrier systems consist of an iron oxide core coated with different pH-responsive polyampholytes which exhibit varying surface charge depending on the surrounding pH value. The resulting materials were used for electrostatically mediated catch-and-release experiments of either cationic or anionic dyes with the perspective to allow the pH-dependent magnetically guided transport of suitable cargo. The use of three different polyampholyte coatings (poly(2-(imidazol-1-yl)acrylic acid) (PImAA), poly(dehydroalanine) (PDha), and poly(*N*,*N*-diallylglutamate) (PDAGA)) enables a deeper understanding about how the surface net charge in combination with the charge and charge density of any cargo influences such processes. The size, surface charge, and aggregation behavior of the herein described particles were investigated via dynamic light scattering (DLS), transmission electron microscopy (TEM), and pH-dependent ζ-potential measurements, whereas adsorption and release studies were investigated via UV−vis.

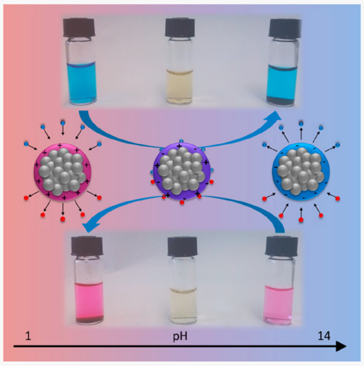

■ INTRODUCTION

The defined and ideally reversible adsorption (or chemisorption) of small organic molecules to any type of interface is of interest with regard to drug delivery systems,[1,2] wastewater treatment,[3−5] and the deposition of catalysts on a suitable support.[6,7] Such processes are interfacial effects and rely on different interactions between the surface and the respective cargo molecules. The underlying driving forces include van der Waals, hydrophobic, dipole−dipole, hydrogen bonding, and electrostatic interactions. Among those, electrostatic interactions are the strongest and can be regarded as the main directing force, if present.

Polyelectrolytes are macromolecules that feature high charge density and are often employed as coating materials for planar surfaces or nanoparticles, in the latter case often imparting significantly increased solution stability to the respective nanomaterial.[8] Polyampholytes, as a subclass of polyelectrolytes, contain both positive and negative charges, and if charge density depends on the pH value, then such materials can exhibit drastic shifts in net charge. Naturally occurring systems with a zwitterionic surface can be found in protein structures, cell walls, and betaines.[8] The similarity of artificial zwitterionic surfaces to their natural counterparts is reflected in good biocompatibility and potential antibiofouling properties which reduce unwanted interactions with biomolecules.[8−10] A majority of polyzwitterionic structures found in the literature exhibit permanent charge over a broad pH range by using sulfate or phosphonic acid groups on one side and quaternary amines on the other side. There are several examples of polyampholytes which find applications in drug delivery and as surface coatings for various biomaterials.[11−14] Typical examples are poly(carbobetaine)s,[15] poly(sulfobetaine)s,[15] and poly(phosphobetaine)s[15] as well as copolymers such as poly(4-vinylpyridine-*co*-acrylic acid),[16,17] poly(*N*,*N*-dimethylaminoethyl methacrylate-*co*-methacrylic acid),[18] and poly(sodium styrenesulfonate-*co*-4-vinylpyridine).[19] However, most of these systems show limited changes in net charge or charge density with varying pH value. Applied as coatings for magnetic nanoparticles, the resulting hybrid materials can be directed by an external magnetic field. This has already been used for the rapid, selective, and complete removal of pollutants from solutions.[20] Regarding drug delivery, the magnetic targeting of organs or tissues by such nanocarriers has been demonstrated, and subsequent hyperthermia treatment has shown great potential for damaging and killing cancer cells.[21,22] In addition, charge-tunable polyelectrolytes have been used for the adsorption of mainly cationic small molecules in the field of wastewater remediation.[23−26]

Although typical immobilization strategies (e.g., catalysts) demand a permanent binding of a specific moiety to the substrate, reversible binding events are of particular interest in the case of wastewater treatment or drug delivery, also in terms

Received: February 18, 2020
Revised: May 12, 2020
Published: May 12, 2020

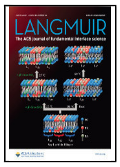

https://dx.doi.org/10.1021/acs.langmuir.0c00455
Langmuir 2020, 36, 6095−6105

of an efficient recycling of the carrier system. One way to tackle this are pH-responsive coating materials, where binding (strength) is altered by changes in the pH value, as shown for the release of drugs due to a significantly lowered pH in cancer cells.[27] It has been shown that pH within cancer cells can be as low as 5−5.5, whereas healthy cells typically exhibits a pH value of 7.4.[28] This renders the use of weak polyzwitterionic or polyampholytic coatings highly interesting. Such materials are also described as annealed polyampholytes ("acid−base monomers that are ionized depending on the pH of the solution"[29]) and open up a way to impart pH-dependent adsorption/release.[29,30] At different pH values, suitable polyampholytes can present polyanionic, polyzwitterionic, or polycationic character,[31] enabling complete charge inversion at the surface of carrier materials.

We have reported previously on the synthesis of polydehydroalanine (PDha) as one example of a weak polyampholyte, including the synthesis of block and graft copolymers containing PDha.[32,33] This material has also been used for the coating of magnetic nanoparticles, and the pH-dependent (surface) charge inversion could be used to reversibly adsorb/desorb the cationic dye methylene blue (MB), polyelectrolytes, and BSA as a model protein.[26,34] In all cases, desorption required changes in pH and occurred close to the apparent isoelectric point. We were therefore interested in understanding how pH-dependent surface charge and charge density affect the adsorption and release of small (charged) molecules to the surface of magnetic core−shell hybrid materials. We selected three polyampholytic coating materials featuring varying isoelectric points, poly(2-(imidazol-1-yl)acrylic acid) (PImAA), poly(dehydroalanine) (PDha), and poly(*N*,*N*-diallylglutamate) (PDAGA). These materials serve as a small platform for catch-and-release experiments using a selection of charged dye molecules as model pollutants, aiming at a deeper understanding of how structure and charge characteristics of the surface coating in combination with different dyes affect adsorption and release. In that regard, fast and convenient quantification could be achieved using UV−vis spectroscopy. We first started using a range of model dyes with varying net charge before comparing different polyampholytic coatings using two dyes of similar chemical structure but featuring opposite charge.

■ EXPERIMENTAL SECTION

Materials and Instruments. *Chemicals.* Cesium carbonate (99%), benzyl bromide (98%), benzyl chloroformate (98%), silicon tetrachloride (99%), and methanesulfonyl chloride (≥99.7%) were purchased from Sigma-Aldrich. TFA (≥99.9%) was purchased from Roth, triethylamine (≥99.0%) was purchased from CHEMSOLUTE, and *N*-(*tert*-butoxycarbonyl)-L-serine (98%) was purchased from Carbolution Chemicals. The UV photoinitiator, Lucirin-TPO ((diphenylphosphoryl)(mesityl)methanone), was kindly provided by BASF. All chemicals were used as received.

Nuclear Magnetic Resonance Spectroscopy (NMR). ^{1}H NMR spectra were recorded on a 300 MHz Bruker AVANCE spectrometer using $CDCl_3$, DMSO-d_6, and D_2O with NaOD as deuterated solvents at a temperature of 298 K. The solvent residual peak of the respective solvent was used as a standard.

Size-Exclusion Chromatography (SEC). SEC measurements in THF were performed on an Agilent system equipped with a G1310A pump, a G1362A refractive index detector, and both a PSS Gram30 and a PSS Gram1000 column in series. THF was applied as an eluent at a 1 mL min^{-1} flow rate, and the column oven was set to 40 °C. For the calibration, a poly(methyl methacrylate) standard was used.

SEC measurements in DMSO were performed on a Jasco instrument using DMSO + 0.5% LiBr as the eluent at a flow rate of 0.5 mL min^{-1} at 65 °C and a Pullulan calibration (Polymer Standards Service GmbH, Germany). The instrument was equipped with PSS NOVEMA 3000 Angström/300 Angström columns, a RI-930 detector, and a PU-980 pump.

Dynamic Light Scattering. DLS measurements were performed using an ALV Laser CGS 3 goniometer equipped with a 633 nm HeNe laser at 25 °C and at a detection angle of 90°. The CONTIN algorithm was used to evaluate the obtained data.

Transmission Electron Microscopy. For TEM from aqueous solutions, copper grids were rendered hydrophilic by argon plasma cleaning for 30 s (Diener Electronics). A total of 15 μL of the respective sample solution was applied to the grid, and excess sample was blotted with filter paper. TEM images were acquired with a 200 kV FEI Tecnai G2 20 microscope equipped with a 4K × 4K Eagle HS CCD and a 1K × 1K Olympus MegaView camera for overview images.

Ultrasonication was performed using an ElmaSonic S30H ultrasonic unit.

Thermogravimetric Analysis. The samples (prepared and washed as described in the Nanoparticle Coating section) were magnetically separated and freeze-dried for 72 h. TGA measurements were carried out from 30 to 800 °C under synthetic air with a heating rate of 10 °C/min in a PerkinElmer TGA8000 device.

Synthesis of Polydehydroalanine (PDha). PDha was synthesized as reported by Günther et al.[31] A total of 250 mg of poly(aminomethyl acrylate) (PAMA) was dissolved in 10 mL of 1,4-dioxane, and 10 mL of a saturated solution of LiOH was added. The mixture was stirred at 100 °C for 3 h and neutralized with diluted HCl(aq). During neutralization, PDha precipitated. Yield: 97%. ^{1}H NMR (300 MHz, D_2O/NaOD, pH 8): δ 2.6 (CH_2).

Synthesis of Poly(2-(imidazol-1-yl)acrylic Acid) (PImAA). PImAA was synthesized as reported elsewhere.[35] Briefly, DMSO (1.75 M EImA) and AIBN (0.5 mol %) were added to a flask charged with ethyl 2-(imidazol-1-yl)acrylate (EImA). The mixture was degassed by three freeze−pump−thaw cycles and held at 65 °C for 48 h. The resulting polymer was precipitated afterward in EtOAc (45 mL), centrifuged, and dried under vacuum. The obtained PEImA (101.7 mg) was dissolved in methanol (2 mL), and a solution of lithium hydroxide monohydrate (162.3 mg, 3.87 mmol, 5 equiv per monomer unit) in water (2 mL) was added. The reaction mixture was held at 65 °C for 48 h and dialyzed against water. The aqueous solution of the polymer was freeze-dried and afforded 75.7 mg of PImAA as a white solid.

^{1}H NMR (400 MHz, D_2O): δ = 2.5−3.5 (backbone), 6.5−8.5 (imidazole group) ppm.

Synthesis of Poly(N,N-diallylglutamate) (PDAGA). PDAGA was synthesized as reported elsewhere.[36] Briefly, HCl was introduced into a suspension of glutamic acid (59 g, 0.4 mol) in methanol (500 mL) at 0 °C until a clear solution was obtained. The solution was then stirred at room temperature for 3 days. After removal of the solvent at 25 °C, the obtained product was dissolved in water (100 mL) and carefully neutralized with K_2CO_3 at 0 °C; the aqueous mixture was then saturated with anhydrous K_2CO_3 and immediately extracted with $CHCl_3$ (5 × 100 mL). After drying and concentration, the residual product (61 g, 87%) was dissolved in anhydrous K_2CO_3 (87 g, 0.63 mol) in acetonitrile (300 mL) at 40−50 °C. Allyl bromide (85 g, 0.70 mol) was added dropwise to the mixture for a period of 30 min under stirring. The resulting mixture was then stirred at 60 °C for 18 h. After removal of the solvent, the residue was taken up in water (200 mL) and extracted with ether (3 × 100 mL). The organic layer was dried, concentrated, and distilled using a vigreux distilling column to obtain the corresponding diallylamine derivative as a colorless liquid. This liquid (5.4 g) was treated with NaOH (2 g) in 15 mL of water. After 1 day, the dispersion had become a clear solution and was adjusted to a pH of 3 with concentrated HCl. The viscous solution was then freeze-dried. The obtained solid was extracted with 30 mL of acetone, and the suspension was stirred at 60 °C and rapidly filtered. The

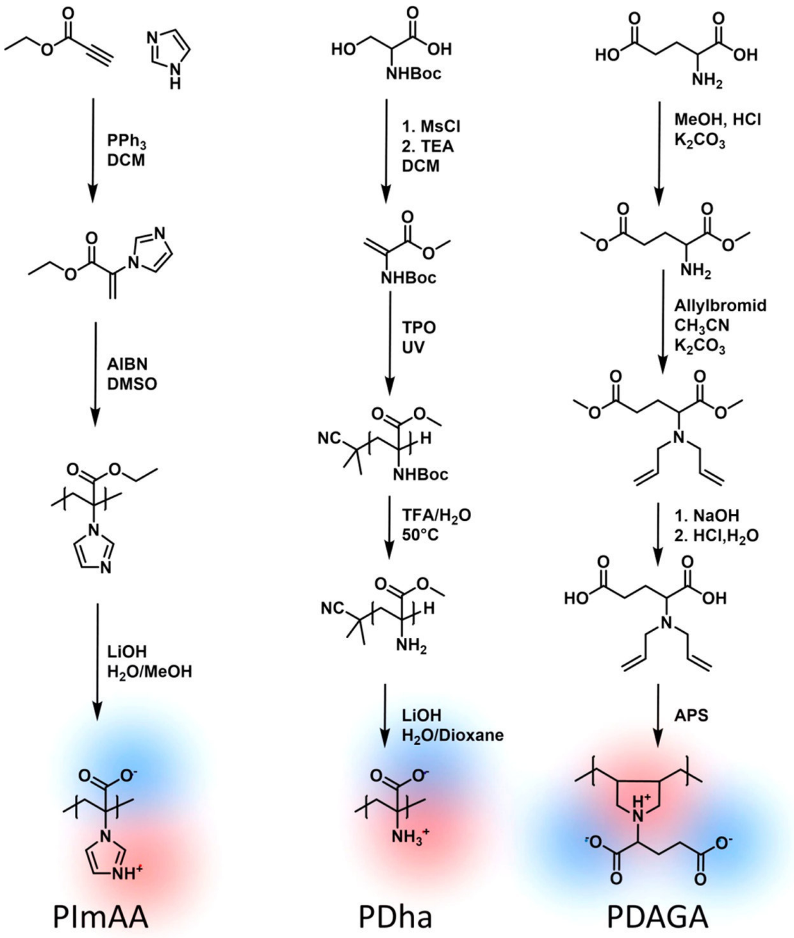

Figure 1. Synthetic pathway and structure of weak polyampholytes used in this work, shown in their charged state: poly(2-(imidazol-1-yl)acrylic acid) (PImAA), poly(dehydroalanine) (PDha), and poly(*N*,*N*-diallylglutamate) (PDAGA).

remaining solid in the filter was washed with acetone. After the evaporation of acetone, the monomer was obtained as white flakes.

The following cyclopolymerization was carried out by dissolving 1.44 g of the monomer in 0.5 mL of water. The solution was degassed and heated to 85 °C. APS (133 μg) was added to the solution while stirring and left for 15 min. The mixture was subsequently cooled to room temperature, and the obtained polymer was dialyzed against water for 3 days. Freeze-drying gave a white powder.

Synthesis of MCNP. Multicore iron oxide nanoparticles were prepared according to previous work by Dutz et al.[21] Briefly, the particles were synthesized by slowly adding a 1 M $NaHCO_3$ solution to a $FeCl_2/FeCl_3$ solution (total iron concentration 1.25 M; Fe^{2+}/Fe^{3+} ratio = 1/1.3) at a rate of 0.9 mL/min under permanent stirring up to pH 8, leading to the formation of a brownish precipitate. Afterward, the solution was boiled for 5 min to form an almost black precipitate. The MCNPs were then magnetically washed with distilled water until a conductivity of <10 μS/cm (room temperature) was reached.

Synthesis of PDI-4Pyl. Fluorescent dye *N*,*N*′-bis(2,6-diisopropylphenyl)-1,6,7,12-tetra-[3-(*N*-methylpyridinium)oxy] perylene-3,4,9,10-tetracarboxylic acid diimide iodide was synthesized according to the procedure previously published by Kohl et al.[37]

Synthesis of PDI-4S. Fluorescent dye PDI-4S (*N*,*N*′-bis(2,6-diisopropylphenyl)-1,6,7,12-tetra-[(4-sulfuric acid)phenoxy] perylene-3,4,9,10-tetracarboxylic acid diimide) was synthesized according to the procedure previously published by Kohl et al.[37]

Nanoparticle Coating. *PDha@MCNP.* A total of 100 mg of PDha was dissolved in 100 mL of water (pH = 12). The solution was carefully titrated with diluted hydrochloric acid to a pH of 7. To this solution was added 100 mL of a dispersion of MCNP (1 g/L). The mixture was stirred at 50 °C for 1 h. The dispersion was separated magnetically, and the supernatant was removed. The particles were redispersed in Milli-Q water using ultrasonication. This procedure was repeated five times.

PImAA@MCNP. PImAA (100 mg) was dissolved in 100 mL of water (pH = 12). The solution was carefully titrated with diluted hydrochloric acid to a pH of 8. To this solution was added 100 mL of a dispersion of MCNP (1 g/L). The mixture was stirred at 50 °C for 1 h. The dispersion was separated magnetically, and the supernatant was removed. The particles were redispersed in Milli-Q water using ultrasonication. This procedure was repeated five times.

PDAGA@MCNP. PDAGA (100 mg) was dissolved in 100 mL of Milli-Q water (pH = 6) with the additional help of salt. To this solution was added 40 mL of a dispersion of MCNP (1 g/L). The mixture was stirred at 50 °C for 1 h. The dispersion was separated magnetically, and the supernatant was removed. The particles were redispersed in Milli-Q water using ultrasonication. This procedure was repeated five times.

Adsorption and Desorption Studies. An aqueous dye solution (1 mL) was added to 2 mg of nanoparticles that were magnetically separated from solution. The resulting suspension was shaken intensively and kept overnight. The following day the particles were removed magnetically, and the supernatant was investigated by UV–vis spectroscopy. In case of solutions that were too concentrated, a 10-fold dilution was carried out. The particles were then washed at least 3 times with 1 mL of solution per washing step to remove unbound dye. Afterward, they were exposed to 1 mL of aqueous solutions with different pH values, and the supernatant was investigated.

■ RESULTS AND DISCUSSION

We showed earlier that polydehydroalanine (PDha) is a polyampholyte with pH-dependent charge characteristics and that a defined layer of PDha can be used as a coating for magnetic nanoparticles. The resulting hybrid materials are responsive to magnetic fields and changes in the pH value of the surrounding medium.[34] Upon adjusting suitable pH values, the reversible adsorption/desorption of polyelectrolytes in a layer-by-layer approach[38] as well as a cationic model dye (methylene blue) could be demonstrated.[26] In the latter case, the catch and release of methylene blue over multiple cycles could be demonstrated, which in our opinion is an important feature in view of the possible application of such systems in wastewater treatment. The main hypothesis for the reported adsorption behavior relied on the (apparent) isoelectric point of the PDha shell and, with that, the pH-dependent adsorption and subsequent release of different types of charged cargo upon inversion of the surface charge.

We were interested in whether this system can serve as a general platform for reversible charge-mediated adsorption processes and its application as a general nanocarrier system. We therefore extend this approach to different polyampholytic coatings based on poly(2-(imidazol-1-yl)acrylic acid) (PImAA), poly(dehydroalanine) (PDha), and poly(*N*,*N*-diallylglutamate) (PDAGA), which are shown in Figure 1 for the surface modification of magnetic multicore nanoparticles (MCNP). In all cases, carboxylic acid moieties lead to the efficient formation of a polymeric shell and the resulting coatings differ in basicity (imidazole and primary and tertiary amines) and in the number of carboxylic acid groups per monomer unit. Therefore, the isoelectric point (IEP) of these polymers and the resulting hybrid materials will change and allow a broader pH range for the adsorption and the release of charged molecules. Although often the term “point of neutral charge” is found in the literature, we will herein use the term IEP to describe charge neutrality and we assume a zwitterionic state of the polyampholytic shell around the IEP (Figure 1).

Synthesis of Polyampholytes@MCNP. The magnetic nanoparticles were synthesized by coprecipitation of a Fe^{2+}/Fe^{3+} solution as described earlier by Dutz et al.[21,39] The particles consist of primary cores of about 11 nm (X-ray diffraction, XRD), which form clusters of about 45 nm in radius. Note that the cluster structure (multicore particle) is already present before the coating process (TEM micrographs in Figure S1).

The surface coating of the magnetic nanoparticles was varied by using three different polyampholytes. The molecular weight and distribution of the polyampholytes were determined by SEC measurements (Table 1, Figure S2).

Table 1. Molecular Characteristics of the Used Polyampholytes as Determined by SEC Measurements

sample	M_n [g mol^{-1}]	M_w [g mol^{-1}]	$Đ$
PDAGA	2100[a]	8100[a]	3.8[a]
PImAA	2700[a]	3800[a]	1.4[a]
PDha	13 700[b]	27 300[b]	2.0[b]

[a] Determined by SEC using 0.1 M Na_2HPO_4/0.05% NaN_3 pH 9 as the eluent and calibrated against PAA standards [b] Determined by SEC using DMAc/LiCl SEC as the eluent and calibrated against PMMA standards.

The polymers were first dissolved in water, and then MCNPs were added under mechanical stirring and ultrasonication. After coating, the particles were magnetically separated, washed five times to remove loosely bound polymer, and subsequently characterized by TGA, TEM, and DLS measurements (Figure 2). In case of PImAA and PDha, the polymers were first dissolved under basic conditions and subsequently titrated with diluted hydrochloric acid. It was observed that the pH of the reaction solution is crucial for the successful adsorption of the respective polymer to the MCNP surface. Thermogravimetric analysis of the pristine MCNP under synthetic air revealed that between 30 and 100 °C a mass loss occurs which is related to attached water and then an increasing mass loss at around 200 °C was observable due to the incomplete oxidation of iron oxides (Fe^{2+} to Fe^{3+}, conversion of magnetite to maghemite). Furthermore, an additional mass loss of about 1−2% at higher temperatures was ascribed to unreacted carbonates which are involved in the synthesis process. PImAA showed adsorption at pH values of <10, and it was observed that a lowering of the pH was accompanied by higher amounts of PImAA being adsorbed (approximately 3 wt % at pH = 8 and about 8 wt % at pH = 7, Figure S3). However, PImAA shows a solubility gap below pH 6.8, which limited the conditions suitable for coating.[35] In case of PDha, a shell of 7.6 wt % was deposited at pH = 7, and the same pH value in the presence of 10 wt % sodium chloride (referring to the amount of polymer) was optimum for the deposition of PDAGA, leading to PDAGA@MCNP with a total polymer content of 8 wt %. The pH stability of the polyampholytic shells was exemplarily investigated for PImAA@MCNP, which showed a sufficient stability in a pH range between 2 and 10 (Figure S4A), while the long-term stability over at least half a year was proven for PDha@MCNP (Figure S4B).

TEM micrographs for the resulting polyampholyte@MCNP hybrid nanoparticles are shown in Figure 2. In the overview in Figure 2A, no larger agglomerates are observed, while Figure 2B−D shows representative micrographs for PDAGA@MCNP, PImAA@MCNP, and PDha@MCNP at higher magnification. Both the inorganic (multi)core and the organic layer are visible, and the diameter of the aggregates is between 150 and 200 nm with an organic shell of between 2 and 5 nm. The images presented here are dry-state TEM micrographs where both the shell thickness and the aggregation state might differ from the solution state. The amount of adsorbed polymer obtained from TGA measurements and the hydrodynamic radius from DLS measurements were used to calculate a theoretical shell thickness. The formula is shown in eq S1, and the calculation results in shell thicknesses of 5 nm for PDAGA, 5 nm for PDha, and 6 nm for PImAA, which is in accordance with the data obtained from TEM measurements.

DLS was used to determine the hydrodynamic radius, and Figure 2 shows a value of about 45 nm for pristine MCNP. After coating with the different polyampholytes, the radii increase to 75 nm (PDAGA@MCNP) and 100 nm (both PDha@MCNP and PImAA@MCNP), indicating that some aggregation is occurring. It also cannot be excluded that aggregates of a few MCNPs are enclosed within one polyampholyte shell during the coating process. The signals at higher hydrodynamic radii (around 200 nm) are an additional indication of partial aggregation. In addition, we investigated the hydrodynamic size of two systems (PDha@MCNP and PDAGA@MCNP) as a function of the pH value

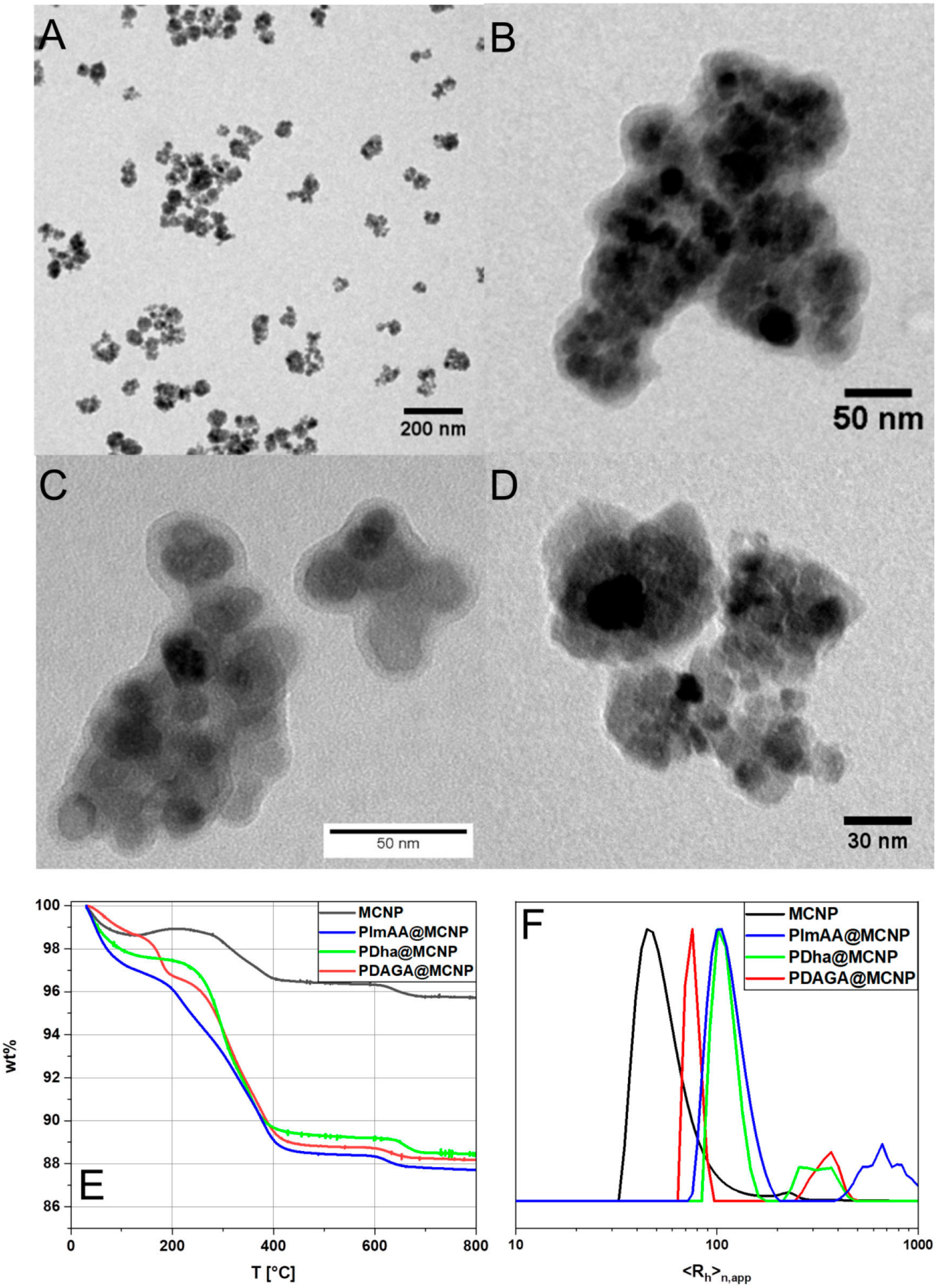

Figure 2. TEM micrographs of (A) PDAGA@MCNP (overview) and higher magnifications of (B) PDAGA@MCNP, (C) PImAA@MCNP, and (D) PDha@MCNP. (E) Thermograms of pristine MCNP (black line, 4% overall weight loss), PDAGA@MCNP (red line, 11.9%), PDha@MCNP (blue line, 11.6%), and PImAA@MCNP (green line, 12.2%). (F) Number-weighted DLS CONTIN plots of pristine MCNP (black line, $\langle R_h \rangle_{n,app}$ = 45 nm), PImAA@MCNP (blue line, $\langle R_h \rangle_{n,app}$ = 100 nm), PDAGA@MCNP (red line, $\langle R_h \rangle_{n,app}$ = 75 nm), and PDha@MCNP (green line, $\langle R_h \rangle_{n,app}$ = 100 nm).

(Figures S5 and S6), and in both cases, an increase in R_H could be observed at lower pH.

Zeta potential measurements were used to determine the surface charge at different pH values. Therefore, aqueous dispersions were prepared at pH 10 and subsequently titrated with hydrochloric acid, and samples were taken at every pH (Figure 3). The pristine MCNPs show a zeta potential of about −30 mV at high pH values with an IEP of pH 4 to 5, and the

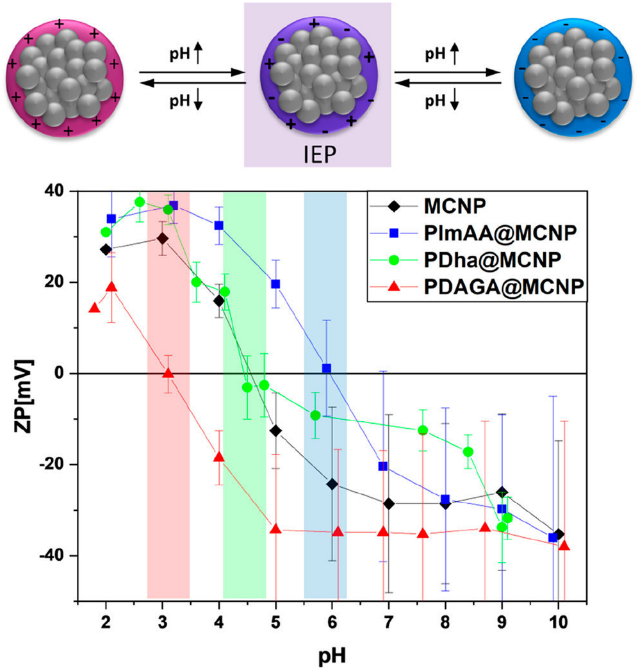

Figure 3. pH-dependent ζ potentials of pristine MCNP (black diamonds), PImAA@MCNP (blue squares), PDha@MCNP (green spots), and PDAGA@MCNP (red triangles).

Scheme 1. Graphical Representation of the pH-Dependent Adsorption and Release of Charged Small Molecules (Model Dyes) Using PDha@MCNP Hybrid Nanoparticles

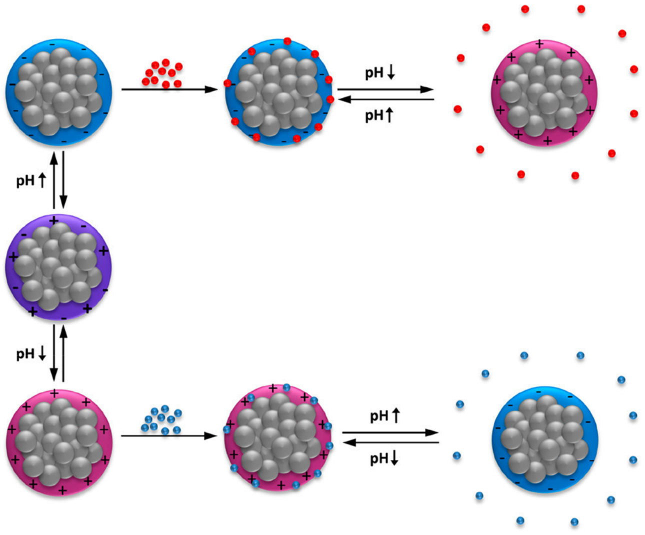

values increase to +30 mV at low pH. After coating, the general trend in net charge as a function of the pH value is comparable, although the apparent IEP shifts to 6 for PImAA@MCNP, remains at pH 4 to 5 for PDha@MCNP, and is around pH 3 for PDAGA@MCNP. Hence, the polyampholytic coatings allow the apparent IEP to be shifted, whereby each polyampholyte can be assigned to an amino acid analogue (glutamic acid is comparable to PDAGA (pH = 3.08[40]), alanine is comparable to PDha (pH = 6.11[40]), and histidine is comparable to PImAA (pH = 7.64[40])).

Reversible Adsorption of Charged Small Molecules to PDha@MCNP. Scheme 1 shows the general workflow we used and our proposed mechanism for adsorption and release experiments using different charged model dyes.

We first used PDha@MCNP to investigate the reversible adsorption and pH-dependent release of different model dyes with varying charge under two different adsorption conditions (pH = 7, where the nanoparticles exhibit a negative surface charge, and pH = 2, where a positive surface charge is expected). The corresponding dyes are shown in Figure 4 and were selected on the basis of availability and net charge (e.g., their amount of sulfonates (brilliant blue vs trypan blue)). Exceptions are PDI-4PyI (*N*,*N*′-bis(2,6-diisopropylphenyl)-1,6,7,12-tetra-[3-(*N*-methylpyridinium)oxy]perylene-3,4,9,10-tetracarboxylic acid diimide iodide) and PDI-4S (*N*,*N*′-bis(2,6-diisopropylphenyl)-1,6,7,12-tetra-[(4-sulfuric acid)phenoxy] perylene-3,4,9,10-tetracarboxylic acid diimide),[37,41] which have chemical similar structures but opposite charge.

For adsorption experiments, the model dyes were dissolved at a concentration of 10 μg/mL and then added to 2.5 mg of PDha@MCNP which had just been magnetically separated from their stock solution. After shaking, the particles were separated magnetically, and then the supernatant was analyzed (selected examples are shown in Figure 5). We observed that the adsorption process is rather fast and complete within a few minutes, as already described for comparable systems.[42] However, to avoid any kinetic contribution to the overall adsorption process, we left all samples overnight before separation. Under neutral conditions, cationic dyes showed fast adsorption to PDha@MCNP, whereas no adsorption could be seen under acidic conditions (Table 2). This is in contrast to pristine MCNP, which showed a negligible adsorption capability for cationic dyes at neutral pH (Figure S7A). We qualitatively rated adsorption so that (++) describes systems where all dye was removed according to UV−vis measurements, partial removal was observed (+), or no adsorption occurred (0). Under the conditions reported here, the amount of adsorbed dye seems to be decoupled from its net charge as both neutral red and PDI-4PyI with respective charges of +1 and +4 per dye molecule could be removed completely. In comparison, malachite green and fuchsine showed rather low adsorption, presumably due to the delocalized cationic charge and additional steric hindrance by the three phenyl groups. Similar results regarding the adsorption behavior of bulky dyes were already observed and discussed by Meng et al.[43] In contrast to our system, their adsorption process is mainly driven by van der Waals forces, and thus the triphenyl-substituted samples adsorbed well while azobenzene dyes seemed to be adsorbed less effectively.[43] As we assume that the main driving forces in our case are attractive electrostatic interactions, delocalized charges explain a lower adsorption tendency.

The release of both neutral red and PDI-4S at a pH of 2 led to over 90% desorption, while in the case of malachite green and fuchsine only low release was observed. This is expected as both dyes, malachite green and fuchsine, did not bind sufficiently to the particles before release. As we initially anticipated, all negatively charged dyes showed no adsorption at pH = 7. Nevertheless, by lowering the pH to 2 the surface charge of PDha@MCNP is inverted and quantitative adsorption occurred, followed by subsequent release upon increasing the pH to 8 (Table 2). Please note that PDI-4S also adsorbed to pristine MCNP under acidic conditions and could be quantitatively released at pH = 8 (Figure S7B).

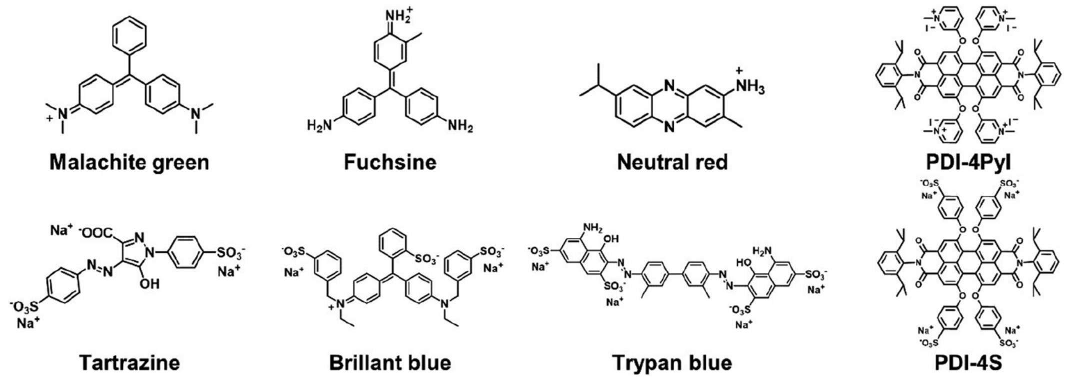

Figure 4. Structure of charged model dyes investigated in this work: malachite green, fuchsine, neutral red, PDI-4PyI, tartrazine, brillant blue, trypan blue, and PDI-4S.

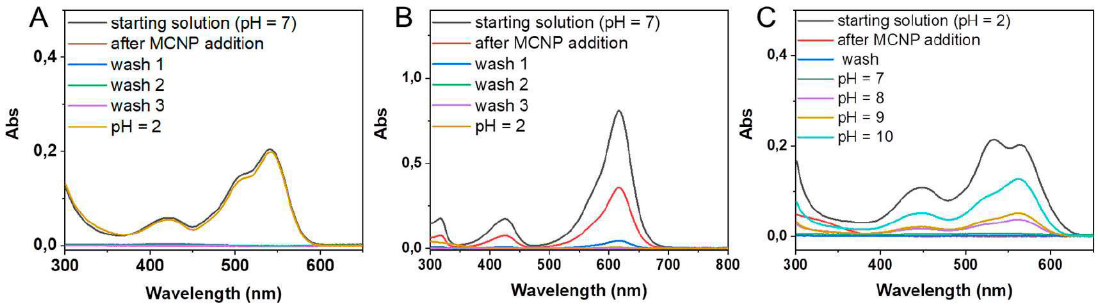

Figure 5. UV–vis spectra of adsorption and release experiments of PDha@MCNP with (A) PDI-4PyI (full adsorption and full release), (B) malachite green (partial adsorption and no release), and (C) PDI-4S (full adsorption under acidic conditions) using PDha@MCNP.

Table 2. Adsorption and Release of Different Charged Dyes Using PDha@MCNP[a]

			adsorp	desorption			
dye (net charge)	adsorp pH = 7	desorp pH = 2	pH = 2	pH = 7	pH = 8	pH = 9	pH = 10
malachite green (+1)	+	0	0	0	–	–	–
fuchsine (+1)	+	0	0	0	–	–	–
neutral red (+1)	++	++	0	0	–	–	–
PDI-4PyI (+4)	++	++	0	0	–	–	–
tartrazine (−2)	0	0	++	0	+	+	+
brillant blue (−2)	0	0	++	0	+	+	+
trypan blue (−4)	0	0	++	0	+	+	+
PDI-4S (−4)	0	0	++	0	+	+	+

[a] ++, full adsorption; +, partial adsorption; 0, no adsorption; –, not carried out.

Comparative Adsorption/Release of Two Structurally Similar Dyes. After investigating a range of different model dyes using PDha@MCNP, we also investigated effects of the underlying polyampholytic shell featuring different IEPs as described earlier for PDAGA@MCNP, PDha@MCNP, and PImAA@MCNP. We used two perylene-based dyes (PDI-4Pyl and PDI-4S) with similar structure but opposite charge because PDI-4PyI contains four positively charged pyridinium groups whereas PDI-4S features four negatively charged sulfonates. Both systems are fully charged over the entire pH range employed in this study.

Adsorption and Release of PDI-4Pyl. A solution of PDI-4Pyl in Milli-Q water was added to all three core–shell nanoparticles, redispersed by vortex mixing, and the particles were separated afterward with a magnet. After being washed, the loaded particles were exposed stepwise to aqueous solutions with different pH values in a way in which the pH was lowered in steps of 1 (pH 6 to 2) and the sum of released dye was determined (Figure 6). PImAA@MCNP showed poor adsorption properties and no significant release under acidic conditions, which we attribute to the fact that adsorption is carried out rather close to the IEP of the PImAA shell. On the other hand, both PDha@MCNP and PDAGA@MCNP showed complete adsorption according to UV–vis and release in the pH range between 4 and 5, while this is exactly the pH range in which the isoelectric point of PDha@MCNP is located (IEP = 4.5, which is a release of 87%). In the case of PDAGA@MCNP, the IEP is shifted toward lower values.

For the latter two cases, we further investigated the maximum loading capacity and assumed a Langmuir isotherm for the adsorption process. The plot of C_e/q vs C_e yielded for both systems a straight line (C_e is the equilibrium chromophore concentration in solution, q is the equilibrium adsorption amount of the chromophore) (Figure S9). From the slope, the value of q_m (the maximum adsorption amount of chromophore per milligram of adsorbent) was estimated, which is 11.4 μg/mg for PDha@MCNP and 18.4 μg/mg for PDAGA@MCNP, respectively. The loading capacity of

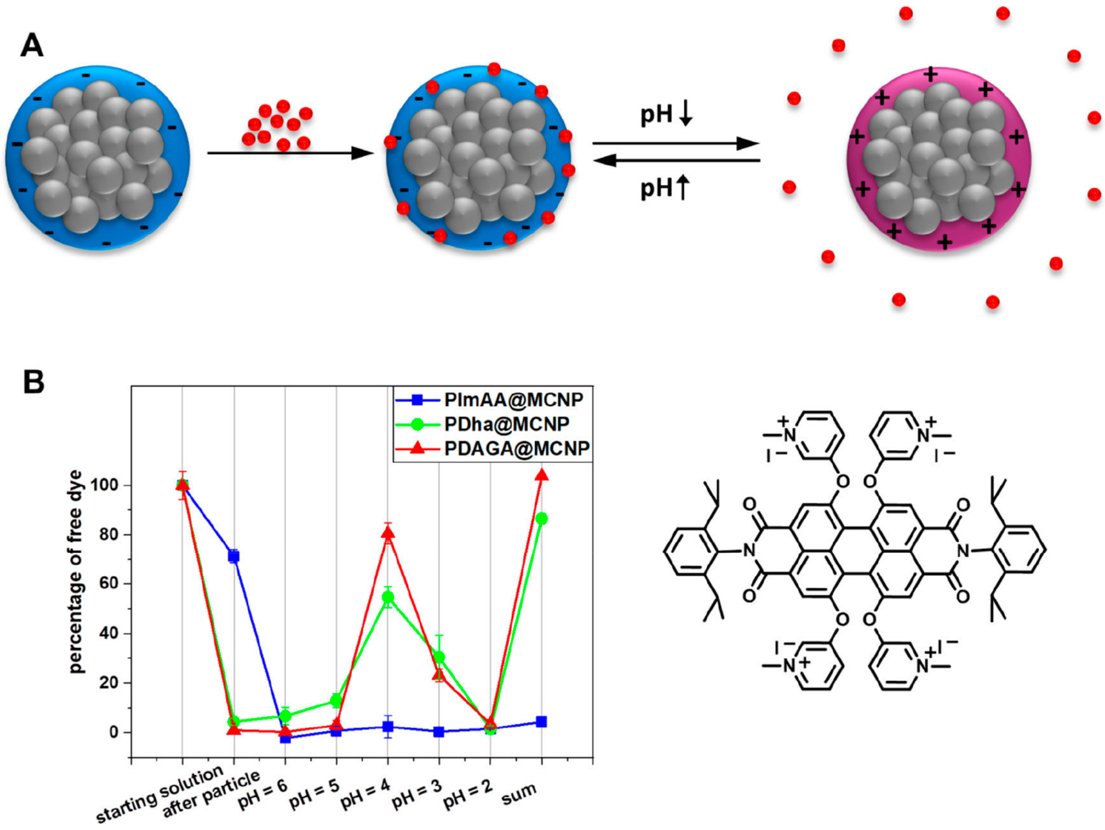

Figure 6. (A) Graphical representation of the adsorption/desorption process. (B) Percentage of the PDI-4PyI main absorbance band (542 nm) before and after the dispersion of coated particles and solutions at different pH values. (Right) Chemical structure of PDI-4PyI.

PDAGA-functionalized particles is significantly higher, which might be attributed to the additional carboxylic acid functionality in each repeat unit.

Adsorption and Release of Anionic PDI-4S. Next, we used acidic conditions (pH = 2) to adsorb PDI-4S, followed by several washing steps under the same condition. As described before, the pH was subsequently changed in steps of 1 pH unit (pH 4−10). PDI-4S adsorbed completely to PImAA@MCNP without any noticeable release during subsequent washing steps. An increase in the pH led to a first release at pH 7, followed by additional release if the pH was further increased, resulting in a cumulative release of 83%. In the case of PDha@MCNP, complete adsorption could also be observed, and release started at pH 8, which in summary also led to 83% released dye. Finally, PDAGA@MCNP exhibited release at pH = 5, and up to 73% of the initially applied dye was released in total. Here, the observed release is shifted if compared to expectations based on the isoelectric points discussed earlier. All systems investigated show release at pH values higher than the respective IEP, where in case of PDAGA@MCNP 2 pH units, for PImAA@MCNP 1 pH unit, and for PDha@MCNP a release about 3.5 pH units above the IEP was found.

We also determined the maximum loading capacity of all systems toward PDI-4S assuming a Langmuir adsorption isotherm, and in all cases, the plot of C_e/q vs C_e yielded a straight line (Figure S10), revealing values of q_m which are 47.3 μg/mg for PDAGA@MCNP, 15.6 μg/mg for PDha@MCNP, and 50.5 μg/mg for PImAA@MCNP, respectively. The maximum loading capacity for the PImAA coating material resembled the capacity of PDAGA well, whereas it was significantly lower in the case of PDha.

The adsorption experiments of both PDI dyes show a reproducible adsorption and release behavior of the respective dye with each hybrid system. Depending on the polyampholytic shell, different pH values were required for a successful release, and individual loading capacities were found, which shows that the respective polyampholyte influences the catch-and-release behavior qualitatively and quantitatively.

Fluorescent Magnetic Nanoparticles via Dye Adsorption. Fluorescence spectroscopy investigations of the adsorption process showed that the removal of the dye from the initially used aqueous solutions is indeed quantitative, as shown in Figure 8. No fluorescence of a 10 μg/mL PDI-4PyI solution could be detected after the addition of PDha@MCNP and subsequent removal by an external magnetic field. Further investigations of the resulting PDI-4Pyl@PDha@MCNP particles revealed fluorescence (Figure 8c), which also decreased if the particles were again removed by an external magnetic field. This gives clear evidence that the dye maintains its fluorescence properties after attachment to the nanoparticle surface. The resulting fluorescent nanosensors are, in our opinion, very interesting for potential application in bioimaging. Fluorescence microscopy as one of the more powerful techniques available for biological studies features high resolution, sensitivity, and selectivity.[44] A pH-dependent release of the cargo molecules might be tracked by means of fluorescence, while the nanoparticles at the same time are detectable on a separate channel by MRI techniques. Rather few examples in the literature describe a noncovalent fluorescent labeling of magnetic nanoparticles. In one case, π−π interactions were used to immobilize dyes for bioimaging.[45] Our method, on the other hand, allows a rapid

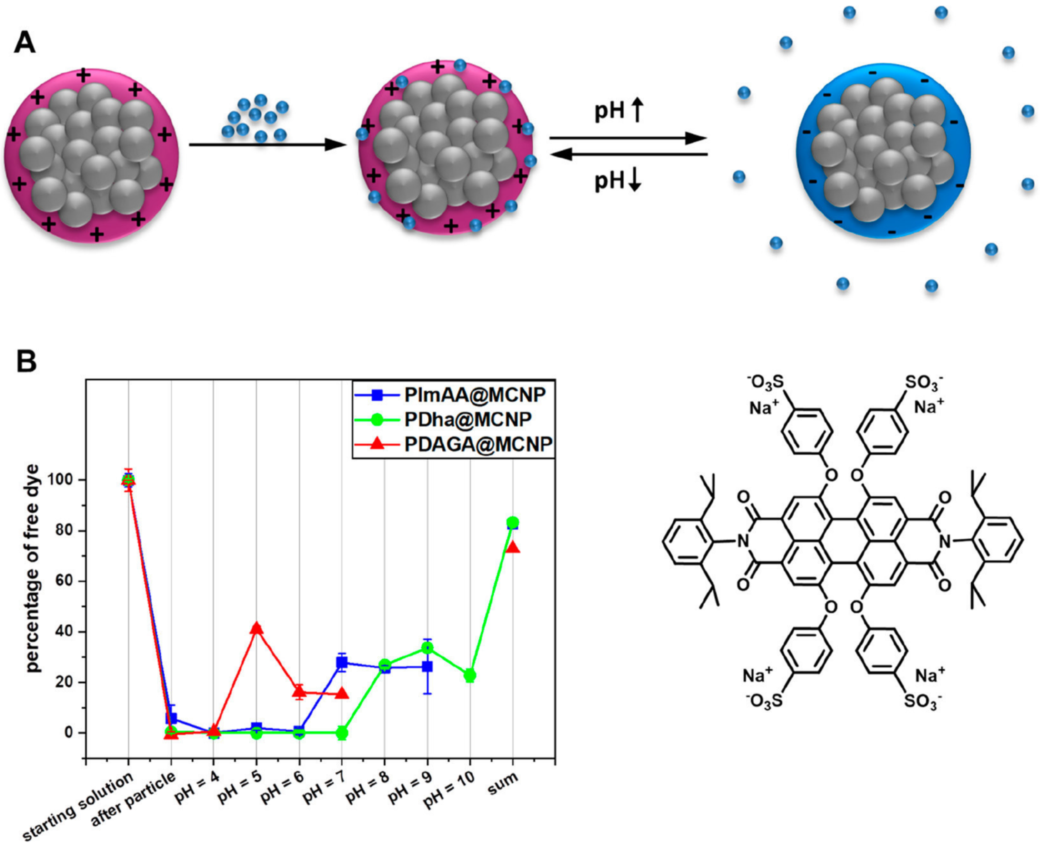

Figure 7. (A) Graphical representation of the investigated adsorption/desorption process. (B) Intensities of the PDI-4S main absorbance band (564 nm) before and after the dispersion of coated particles and solutions at different pH values. (Right) Chemical structure of PDI-4S.

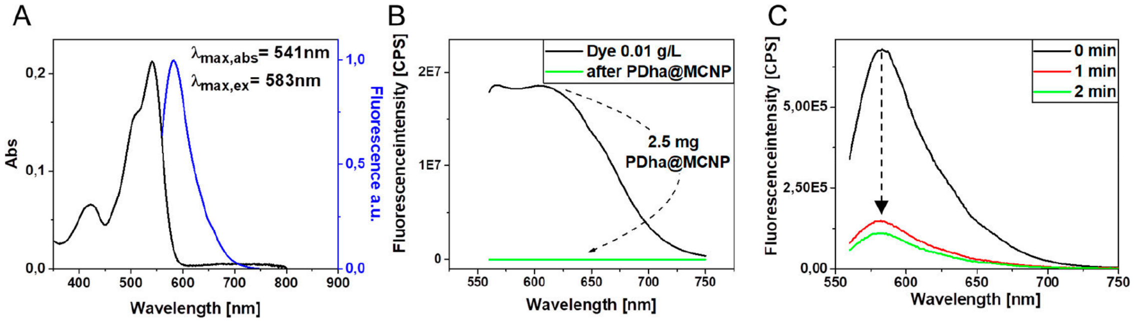

Figure 8. (A) Absorption (solid black line) and fluorescence spectra (solid blue line) of PDI-4PyI in aqueous solution. (B) Fluorescence intensity of PDI-4PyI solution before (black line) and after (green line) 2.5 mg of PDha@MCNP has been applied to the solution. (C) Fluorescence spectra of a 0.1 mg/mL suspension of PDha@MCNP which has been exposed to PDI-4PyI as a function of an applied magnetic field.

and facile way to produce fluorescent hybrid magnetic nanoparticles with a straightforward workup procedure.

■ CONCLUSIONS

The aim of this work was to elucidate general trends in the adsorption and release of small charged molecules from the surface of magnetic nanoparticles featuring a polyampholytic coating. With this, we started out using three different weak polyampholytes as coating materials (PDha, PDAGA, and PImAA) in combination with a range of model dyes of different charge density and net charge. Hereby, different shell materials exhibit varying IEP, and this is translated to the surface charge of the core–shell hybrid nanoparticles. In general, positively charged dyes adsorbed well under neutral conditions and were successfully released upon acidification. On the other hand, negatively charged dyes adsorbed only under acidic conditions and were released by an increase in pH. Interestingly, triarylmethane-based dyes showed distinctly lower adsorption, which we so far attribute to rather delocalized charges and to the bulky phenyl groups. This shows that such adsorption processes depend not only on the net charge of any cargo but also on the chemical structure in general as well as potential steric constraints. By comparison of the three different polyampholytic coatings, it became evident that the adsorption itself depends on the coating material (and the respective IEP) whereas the subsequent release is mainly influenced by the pH value. In the case of negatively charged dyes, our data suggests that other parameters (such as the presence of additional functional groups) play an important role in the quantitative understanding of these processes.

https://dx.doi.org/10.1021/acs.langmuir.0c00455
Langmuir 2020, 36, 6095−6105

Nevertheless, we can show that a small platform of polyampholytic core−shell nanoparticles can be used to tailor the adsorption and release of small molecule cargo. Besides this, the presented approach is also an efficient method for the preparation of fluorescently labeled magnetic nanoparticles, although the stability window of any adsorbed chromophore has to be taken into account. We foresee further applications for such fluorescent magnetic nanoprobes in the area of biomedical research because these materials enable imaging and release studies via a diverse range of techniques.

■ ASSOCIATED CONTENT

Supporting Information

The Supporting Information is available free of charge at https://pubs.acs.org/doi/10.1021/acs.langmuir.0c00455.

> TEM micrographs of pristine MCNP; SEC elution traces of the used polyampholytes; thermograms of polyampholytes@MCNP under different coating conditions, under a varying pH environment, and for the long-term stability test of the shell; formula used for the calculation of the shell thickness according to TGA; pH-dependent number-weighted DLS CONTIN plots for PDha@MCNP and PDAGA@MCNP; adsorption and release experiments of PDI-4PYL and PDI-4S with pristine MCNPs; calibration curves for the determination of PDI-4PYL and PDI-4S concentrations; and determination of the saturation concentration of PDI-4PYL and PDI-4S for PDha@MCNP, PImAA@MCNP, and PDAGA@MCNP (PDF)

■ AUTHOR INFORMATION

Corresponding Author

F. H. Schacher − *Institute of Organic Chemistry and Macromolecular Chemistry (IOMC), Friedrich-Schiller-University Jena, D-07743 Jena, Germany; Jena Center for Soft Matter (JCSM), Friedrich-Schiller-Universität Jena, 07743 Jena, Germany;* orcid.org/0000-0003-4685-6608; Email: felix.schacher@uni-jena.de

Authors

P. Biehl − *Institute of Organic Chemistry and Macromolecular Chemistry (IOMC), Friedrich-Schiller-University Jena, D-07743 Jena, Germany; Jena Center for Soft Matter (JCSM), Friedrich-Schiller-Universität Jena, 07743 Jena, Germany*

P. Wiemuth − *Institute of Organic Chemistry and Macromolecular Chemistry (IOMC), Friedrich-Schiller-University Jena, D-07743 Jena, Germany; Jena Center for Soft Matter (JCSM), Friedrich-Schiller-Universität Jena, 07743 Jena, Germany*

J. Garcia Lopez − *Institute of Organic Chemistry and Macromolecular Chemistry (IOMC), Friedrich-Schiller-University Jena, D-07743 Jena, Germany; Jena Center for Soft Matter (JCSM), Friedrich-Schiller-Universität Jena, 07743 Jena, Germany*

M.-C. Barth − *Institute of Inorganic and Analytical Chemistry, Friedrich-Schiller University Jena, 07743 Jena, Germany*

A. Weidner − *Institute of Biomedical Engineering and Informatics, Technische Universität Ilmenau, 98693 Ilmenau, Germany*

S. Dutz − *Institute of Biomedical Engineering and Informatics, Technische Universität Ilmenau, 98693 Ilmenau, Germany; Department of Nano Biophotonics, Leibniz Institute of Photonic Technology, 07745 Jena, Germany*

K. Peneva − *Institute of Organic Chemistry and Macromolecular Chemistry (IOMC), Friedrich-Schiller-University Jena, D-07743 Jena, Germany; Jena Center for Soft Matter (JCSM), Friedrich-Schiller-Universität Jena, 07743 Jena, Germany;* orcid.org/0000-0001-5578-3266

Complete contact information is available at: https://pubs.acs.org/10.1021/acs.langmuir.0c00455

Notes

The authors declare no competing financial interest.

■ ACKNOWLEDGMENTS

The authors are grateful for financial support through the Deutsche Forschungsgemeinschaft (DFG, SCHA1640/12-1: F.H.S. and P.B.). The TEM facilities of the Jena Center for Soft Matter (JCSM) were established with a grant from the German Research Council (DFG) and the European Fonds for Regional Development (EFRE).

■ REFERENCES

(1) Song, L.; Ho, V. H. B.; Chen, C.; Yang, Z.; Liu, D.; Chen, R.; Zhou, D. Efficient, pH-Triggered Drug Delivery Using a pH-Responsive DNA-Conjugated Gold Nanoparticle. *Adv. Healthcare Mater.* **2013**, *2* (2), 275−280.

(2) Mochalin, V. N.; Pentecost, A.; Li, X.-M.; Neitzel, I.; Nelson, M.; Wei, C.; He, T.; Guo, F.; Gogotsi, Y. Adsorption of Drugs on Nanodiamond: Toward Development of a Drug Delivery Platform. *Mol. Pharmaceutics* **2013**, *10* (10), 3728−3735.

(3) Yagub, M. T.; Sen, T. K.; Afroze, S.; Ang, H. M. Dye and its Removal from Aqueous Solution by Adsorption: A Review. *Adv. Colloid Interface Sci.* **2014**, *209*, 172−184.

(4) Dutta, K.; De, S. Smart Responsive Materials for Water Purification: An Overview. *J. Mater. Chem. A* **2017**, *5* (42), 22095−22112.

(5) Ozay, O.; Ekici, S.; Baran, Y.; Kubilay, S.; Aktas, N.; Sahiner, N. Utilization of Magnetic Hydrogels in the Separation of Toxic Metal Ions from Aqueous Environments. *Desalination* **2010**, *260* (1), 57−64.

(6) Fidale, L. C.; Nikolajski, M.; Rudolph, T.; Dutz, S.; Schacher, F. H.; Heinze, T. Hybrid Fe_3O_4@Amino Cellulose Nanoparticles in Organic Media − Heterogeneous Ligands for Atom Transfer Radical Polymerizations. *J. Colloid Interface Sci.* **2013**, *390* (1), 25−33.

(7) Stevens, P. D.; Fan, J.; Gardimalla, H. M. R.; Yen, M.; Gao, Y. Superparamagnetic Nanoparticle-Supported Catalysis of Suzuki Cross-Coupling Reactions. *Org. Lett.* **2005**, *7* (11), 2085−2088.

(8) Laschewsky, A. Structures and Synthesis of Zwitterionic Polymers. *Polymers* **2014**, *6* (5), 1544.

(9) Singh, P. K.; Singh, V. K.; Singh, M. Zwitterionic Polyelectrolytes: A Review. *e-Polym.* **2007**, *7* (1), DOI: 10.1515/epoly.2007.7.1.335.

(10) Lowe, A. B.; McCormick, C. L. Synthesis and Solution Properties of Zwitterionic Polymers. *Chem. Rev.* **2002**, *102* (11), 4177−4190.

(11) Nakaya, T. Phospholipid Polymers. *Prog. Polym. Sci.* **1999**, *24* (1), 143−181.

(12) Hub, H. H.; Hupfer, B.; Koch, H.; Ringsdorf, H. Polymerizable Phospholipid Analogues–New Stable Biomembrane and Cell Models. *Angew. Chem., Int. Ed. Engl.* **1980**, *19* (11), 938−40.

(13) Jiang, S.; Cao, Z. Ultralow-fouling, Functionalizable, and Hydrolyzable Zwitterionic Materials and their Derivatives for Biological Applications. *Adv. Mater.* **2010**, *22* (9), 920−32.

(14) Lin, P.; Lin, C. W.; Mansour, R.; Gu, F. Improving Biocompatibility by Surface Modification Techniques on Implantable Bioelectronics. *Biosens. Bioelectron.* **2013**, *47*, 451−60.

(15) Kudaibergenov, S.; Jaeger, W.; Laschewsky, A. Polymeric Betaines: Synthesis, Characterization, and Application. *Supramolecular Polymers, Polymeric Betains, Oligomers*; Advances in Polymer Science; Springer: Berlin, 2006; pp 157−224.

(16) Masuda, S.; Minagawa, K.; Tsuda, M.; Tanaka, M. Spontaneous Copolymerization of Acrylic Acid with 4-Vinylpyridine and Microscopic Acid Dissociation of the Alternating Copolymer. *Eur. Polym. J.* **2001**, *37* (4), 705−710.

(17) Billing, M.; Gräfe, C.; Saal, A.; Biehl, P.; Clement, J. H.; Dutz, S.; Weidner, S.; Schacher, F. H. Zwitterionic Iron Oxide (γ-Fe_2O_3) Nanoparticles Based on P(2VP-grad-AA) Copolymers. *Macromol. Rapid Commun.* **2017**, *38* (4), 1600637.

(18) Merle, Y. Synthetic Polyampholytes. 5. Influence of Nearest-Neighbor Interactions on Potentiometric Curves. *J. Phys. Chem.* **1987**, *91* (11), 3092−3098.

(19) Lica, C.; Segarceanu, M.; Plesca, M.; Rikabi, A.; Nechifor, G. Synthesis of a new Polymer Poly(Styrene Sulfonic Acid-co-4-Vinylpyridine) for Proton Exchange Membrane for Fuel Cell. *U.P.B. Sci. Bull., Ser. B* **2014**, *76*, 151−158.

(20) Mohammed, L.; Gomaa, H. G.; Ragab, D.; Zhu, J. Magnetic Nanoparticles for Environmental and Biomedical Applications: A Review. *Particuology* **2017**, *30*, 1−14.

(21) Dutz, S.; Clement, J. H.; Eberbeck, D.; Gelbrich, T.; Hergt, R.; Müller, R.; Wotschadlo, J.; Zeisberger, M. Ferrofluids of Magnetic Multicore Nanoparticles for Biomedical Applications. *J. Magn. Magn. Mater.* **2009**, *321* (10), 1501−1504.

(22) Hergt, R.; Dutz, S.; Müller, R.; Zeisberger, M. Magnetic Particle Hyperthermia: Nanoparticle Magnetism and Materials Development for Cancer Therapy. *J. Phys.: Condens. Matter* **2006**, *18* (38), S2919−S2934.

(23) Mak, S.-Y.; Chen, D.-H. Fast Adsorption of Methylene Blue on Polyacrylic Acid-Bound Iron Oxide Magnetic Nanoparticles. *Dyes Pigm.* **2004**, *61* (1), 93−98.

(24) Pandey, G.; Singh, S.; Hitkari, G. Synthesis and Characterization of Polyvinyl Pyrrolidone (PVP)-Coated Fe_3O_4 Nanoparticles by Chemical co-Precipitation Method and Removal of Congo Red Dye by Adsorption Process. *Int. Nano Lett.* **2018**, *8* (2), 111−121.

(25) Shen, D.; Fan, J.; Zhou, W.; Gao, B.; Yue, Q.; Kang, Q. Adsorption Kinetics and Isotherm of Anionic Dyes onto Organo-Bentonite from Single and Multisolute Systems. *J. Hazard. Mater.* **2009**, *172* (1), 99−107.

(26) Biehl, P.; Lühe, M. v. d.; Schacher, F. H. Reversible Adsorption of Methylene Blue as Cationic Model Cargo onto Polyzwitterionic Magnetic Nanoparticles. *Macromol. Rapid Commun.* **2018**, *39* (14), 1800017.

(27) Zhu, Y.-J.; Chen, F. pH-Responsive Drug-Delivery Systems. *Chem. - Asian J.* **2015**, *10* (2), 284−305.

(28) Lee, E. S.; Oh, K. T.; Kim, D.; Youn, Y. S.; Bae, Y. H. Tumor pH-Responsive Flower-Like Micelles of Poly(l-Lactic Acid)-b-Poly(Ethylene Glycol)-b-Poly(l-Histidine). *J. Controlled Release* **2007**, *123* (1), 19−26.

(29) Kudaibergenov, S. E.; Nuraje, N. Intra- and Interpolyelectrolyte Complexes of Polyampholytes. *Polymers* **2018**, *10* (10), 1146.

(30) Choi, J.; Rubner, M. F. Influence of the Degree of Ionization on Weak Polyelectrolyte Multilayer Assembly. *Macromolecules* **2005**, *38* (1), 116−124.

(31) Günther, U.; Sigolaeva, L. V.; Pergushov, D. V.; Schacher, F. H. Polyelectrolytes with Tunable Charge Based on Polydehydroalanine: Synthesis and Solution Properties. *Macromol. Chem. Phys.* **2013**, *214* (19), 2202−2212.

(32) Max, J. B.; Pergushov, D. V.; Sigolaeva, L. V.; Schacher, F. H. Polyampholytic Graft Copolymers Based on Polydehydroalanine (PDha) − Synthesis, Solution Behavior and Application as Dispersants for Carbon Nanotubes. *Polym. Chem.* **2019**, *10*, 3006.

(33) Billing, M.; Schacher, F. H. ATRP of *tert*-Butoxycarbonylaminomethyl Acrylate (*t*BAMA): Well-Defined Precursors for Polyelectrolytes of Tunable Charge. *Macromolecules* **2016**, *49* (10), 3696−3705.

(34) von der Lühe, M.; Günther, U.; Weidner, A.; Gräfe, C.; Clement, J. H.; Dutz, S.; Schacher, F. H. SPION@Polydehydroalanine Hybrid Particles. *RSC Adv.* **2015**, *5* (40), 31920−31929.

(35) Rössel, C.; Billing, M.; Görls, H.; Festag, G.; Grube, M.; Bellstedt, P.; Nischang, I.; Schacher, F. H. Synthesis and Modification of Poly(Ethyl 2-(Imidazol-1-yl)Acrylate) (PEImA). *Polymer* **2017**, *127*, 182−191.

(36) Jamiu, Z. A.; Al-Muallem, H. A.; Ali, S. A. A Glutamic Acid-Based Polymer Keeping Intact the Integrity of all the Three Original Functionalities of the Amino Acid. *Des. Monomers Polym.* **2016**, *19* (2), 128−137.

(37) Kohl, C.; Weil, T.; Qu, J.; Müllen, K. Towards Highly Fluorescent and Water-Soluble Perylene Dyes. *Chem. - Eur. J.* **2004**, *10* (21), 5297−5310.

(38) von der Lühe, M.; Weidner, A.; Dutz, S.; Schacher, F. H. Reversible Electrostatic Adsorption of Polyelectrolytes and Bovine Serum Albumin onto Polyzwitterion-Coated Magnetic Multicore Nanoparticles: Implications for Sensing and Drug Delivery. *ACS Appl. Nano Mater.* **2018**, *1* (1), 232−244.

(39) Dutz, S.; Andrä, W.; Hergt, R.; Müller, R.; Oestreich, C.; Schmidt, C.; Töpfer, J.; Zeisberger, M.; Bellemann, M. E. Influence of Dextran Coating on the Magnetic Behaviour of Iron Oxide Nanoparticles. *J. Magn. Magn. Mater.* **2007**, *311* (1), 51−54.

(40) Liu, H. X.; Zhang, R. S.; Yao, X. J.; Liu, M. C.; Hu, Z. D.; Fan, B. T. Prediction of the Isoelectric Point of an Amino Acid Based on GA-PLS and SVMs. *J. Chem. Inf. Model.* **2004**, *44* (1), 161−167.

(41) Weil, T.; Vosch, T.; Hofkens, J.; Peneva, K.; Müllen, K. The Rylene Colorant Family—Tailored Nanoemitters for Photonics Research and Applications. *Angew. Chem., Int. Ed.* **2010**, *49* (48), 9068−9093.

(42) Nassar, N. N. Kinetics, Mechanistic, Equilibrium, and Thermodynamic Studies on the Adsorption of Acid Red Dye from Wastewater by γ-Fe_2O_3 Nanoadsorbents. *Sep. Sci. Technol.* **2010**, *45* (8), 1092−1103.

(43) Meng, L.; Zhang, X.; Tang, Y.; Su, K.; Kong, J. Hierarchically Porous Silicon−Carbon-Nitrogen Hybrid Materials Towards Highly Efficient and Selective Adsorption of Organic Dyes. *Sci. Rep.* **2015**, *5*, 7910.

(44) Leung, B. O.; Chou, K. C. Review of Super-Resolution Fluorescence Microscopy for Biology. *Appl. Spectrosc.* **2011**, *65* (9), 967−980.

(45) Kainz, Q. M.; Schätz, A.; Zöpfl, A.; Stark, W. J.; Reiser, O. Combined Covalent and Noncovalent Functionalization of Nanomagnetic Carbon Surfaces with Dendrimers and BODIPY Fluorescent Dye. *Chem. Mater.* **2011**, *23* (16), 3606−3613.

Supporting Information

Weak polyampholytes at the interface of magnetic nanocarriers: A facile catch and release platform for dyes

P. Biehl[a,b], P. Wiemuth[a,b], J. Garcia Lopez[a,b], M.-C. Barth[c], A. Weidner[d], S. Dutz[d,e], K. Peneva[a,b], and F. H. Schacher[a,b] *

[a]Institute of Organic Chemistry and Macromolecular Chemistry (IOMC), Friedrich-Schiller-University Jena, Humboldtstraße 10, D-07743 Jena, Germany
[b]Jena Center for Soft Matter (JCSM), Friedrich-Schiller-Universität Jena, Philosophenweg 7, 07743 Jena, Germany
[c]Institute of Inorganic and Analytical Chemistry, Friedrich-Schiller UniversityJena, Germany
[d]Institute of Biomedical Engineering and Informatics, Technische Universität Ilmenau, 98693 Ilmenau, Germany
[e]Department of Nano Biophotonics, Leibniz Institute of Photonic Technology, 07745 Jena, Germany

number of pages: 7

number of figures: 10

number of equations: 1

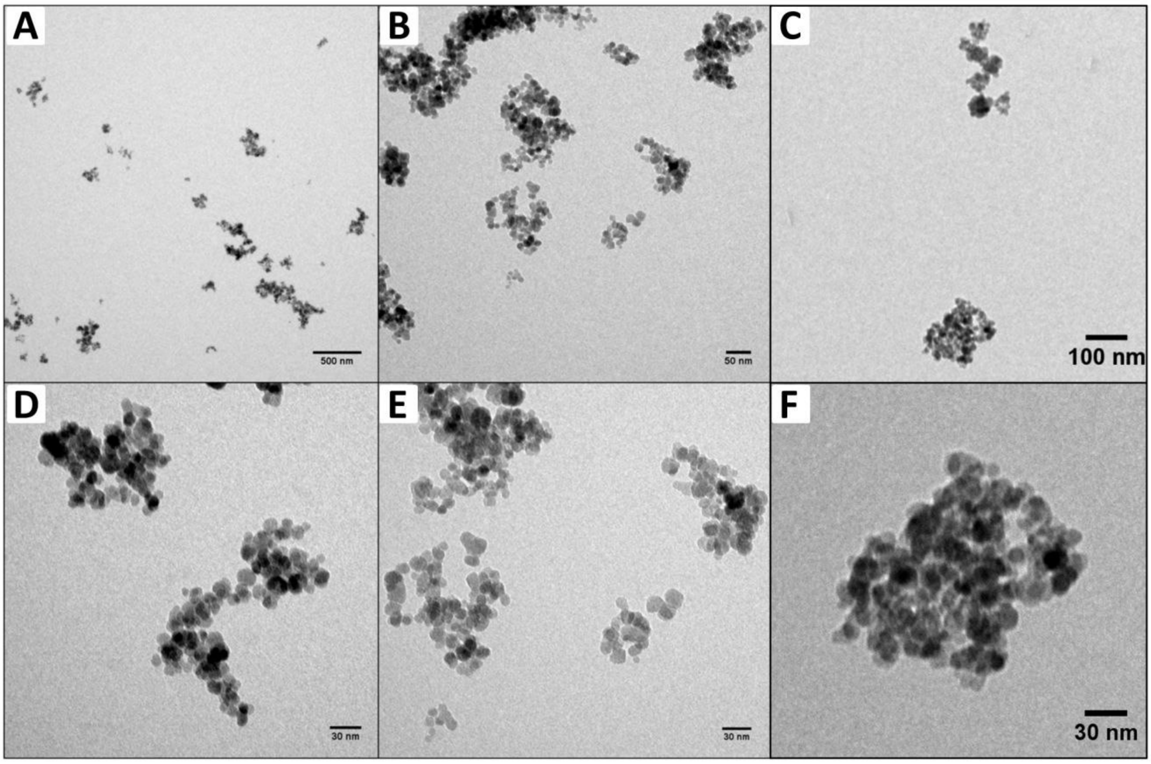

Figure S1: A-F: TEM micrographs of pristine MCNP.

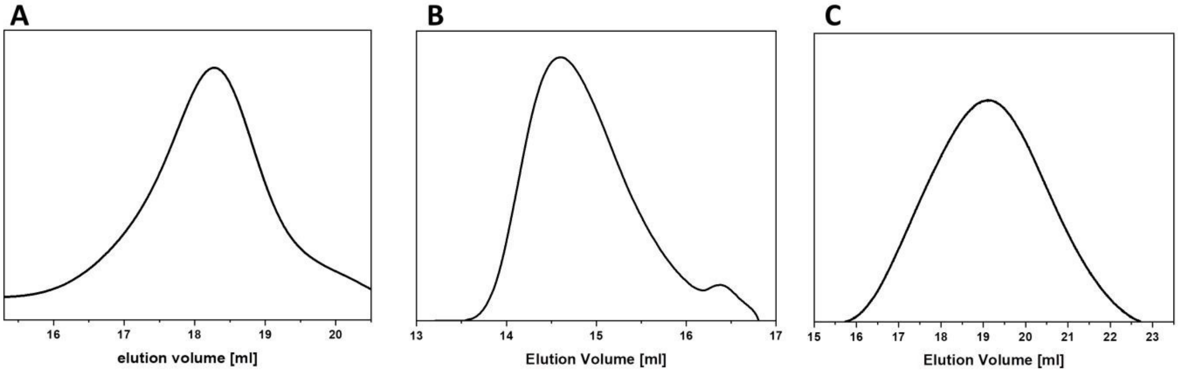

Figure S2: SEC elution traces of the used polyampholytes A) PDAGA (0,1 M Na_2HPO_4/0,05% NaN_3 pH 9, PAA calibration), B) PImAA (0,1 M Na_2HPO_4/0,05% NaN_3 pH 9, PAA calibration), C) PDha (DMAc/LiCl SEC, PMMA calibration).

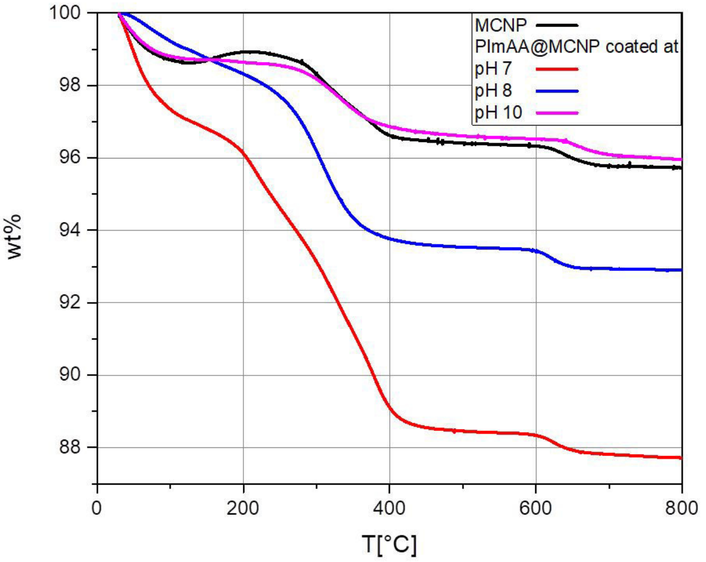

Figure S3: Thermograms of PImAA@MCNP after coating at different pH values.

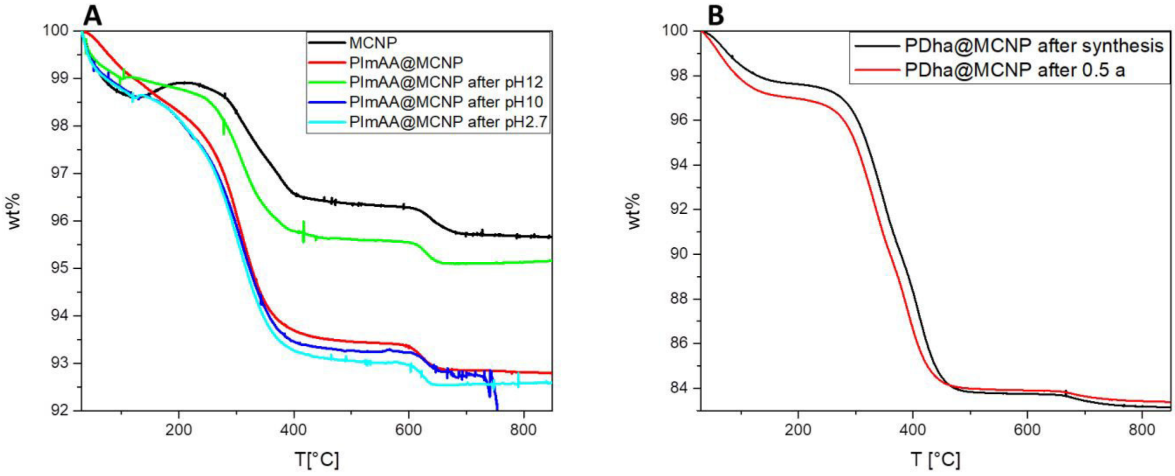

Figure S4: A) Thermograms of MCNP (black line) and PImAA@MCNP after synthesis (red line) and after exposure to different pH values: after exposure to pH 12 (green line), after exposure to pH 10 (blue line), after exposure to pH 2.7 (cyan line), B) thermograms of PDha@MCNP directly after synthesis (black, line) and after 0.5 years of storage (red, line).

Equation S1: Formula used for the calculation of shell thickness according to TGA

$$r_s = \sqrt[3]{r_c^3 + \left(r_c^3\left(\frac{\rho_c}{\rho_s}\right)\left(\frac{WL}{RM}\right)\right)} - r_c$$

r_s …shell thickness

r_c … core radius (from DLS: MCNP $\langle R_h \rangle_{n,app}$ = 45 nm)

ρ_c … core density (approx. 5.2 g/cm3)

ρ_s … density of shell material (approx. 1.1 g/cm3)

WL … weight loss

RM … residual mass

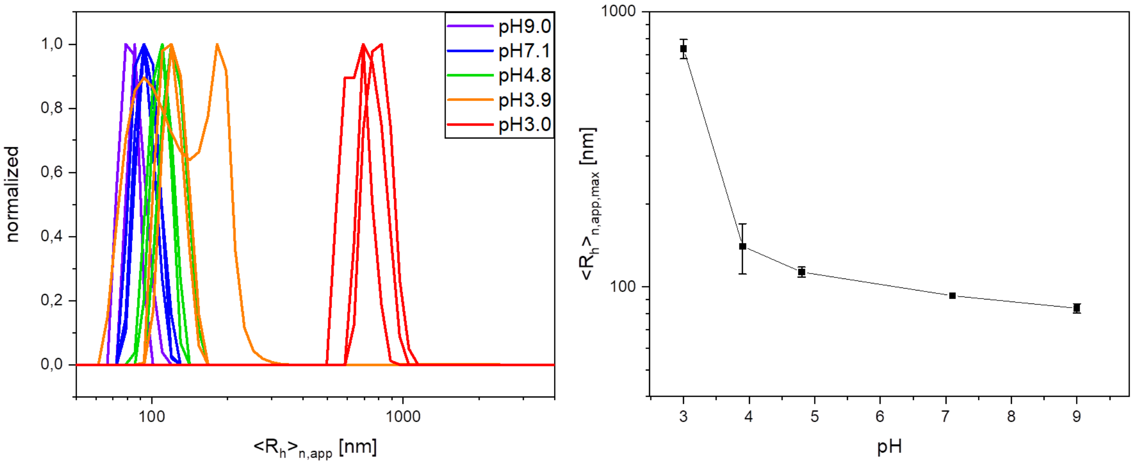

Figure S5: A) number-weighted DLS CONTIN plots of PDha@MCNP at different pH values; B) Hydrodynamic maxima of number-weighted DLS CONTIN plots of PDha@MCNP at different pH values.

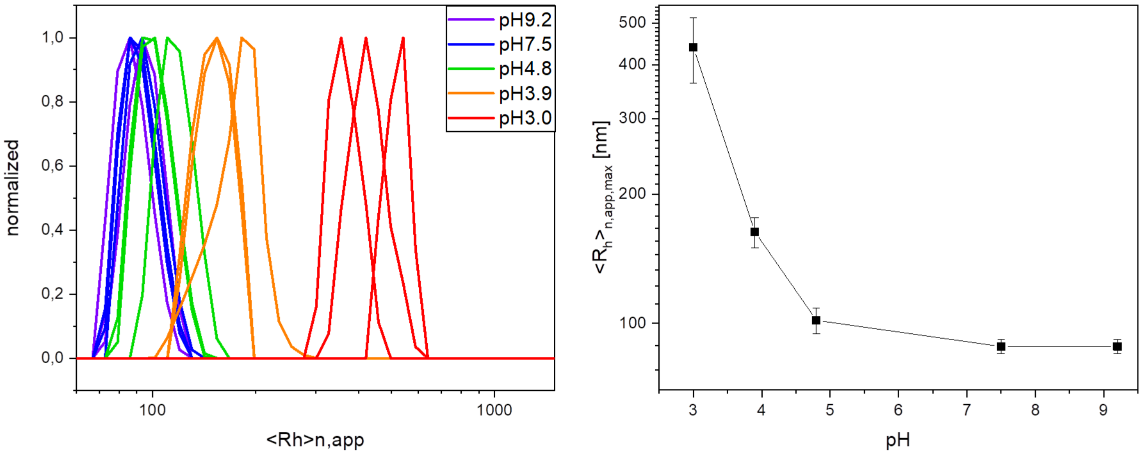

Figure S6: A) PDAGA@MCNP at different pH values; B) Hydrodynamic maxima of number-weighted DLS CONTIN plots of PDAGA@MCNP at different pH values.

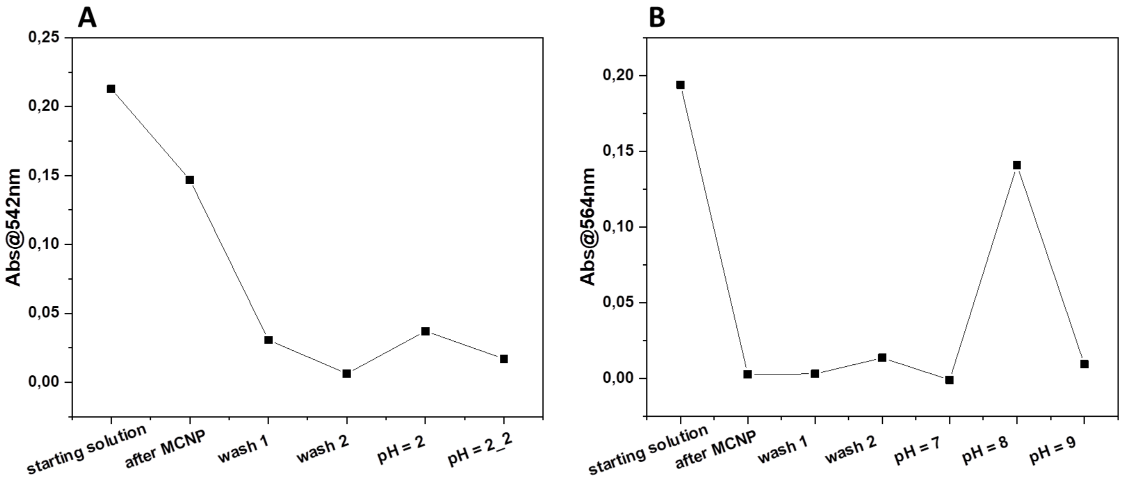

Figure S7: A) intensities of the PDI-4PyI main absorbance band (542 nm) before and after dispersion of pristine MCNP, washing steps, and release solutions at pH = 2, B) intensities of the PDI-4S main absorbance band (564 nm) before and after dispersion of pristine MCNP, washing steps, and solutions at different pH-values.

Concentration calibration curves of PDI-4Pyl (pH = 7) and PDI-4S (pH = 2)

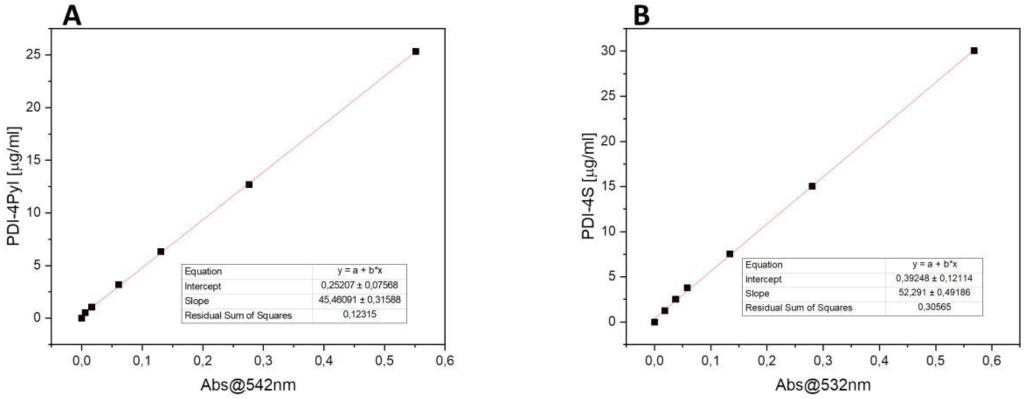

Figure S8: Calibration curves for concentration calculation of A) PDI-4Pyl (pH = 7) and B) PDI-4S (pH = 2).

Saturation concentration of PDI-4Pyl on different systems at pH = 7

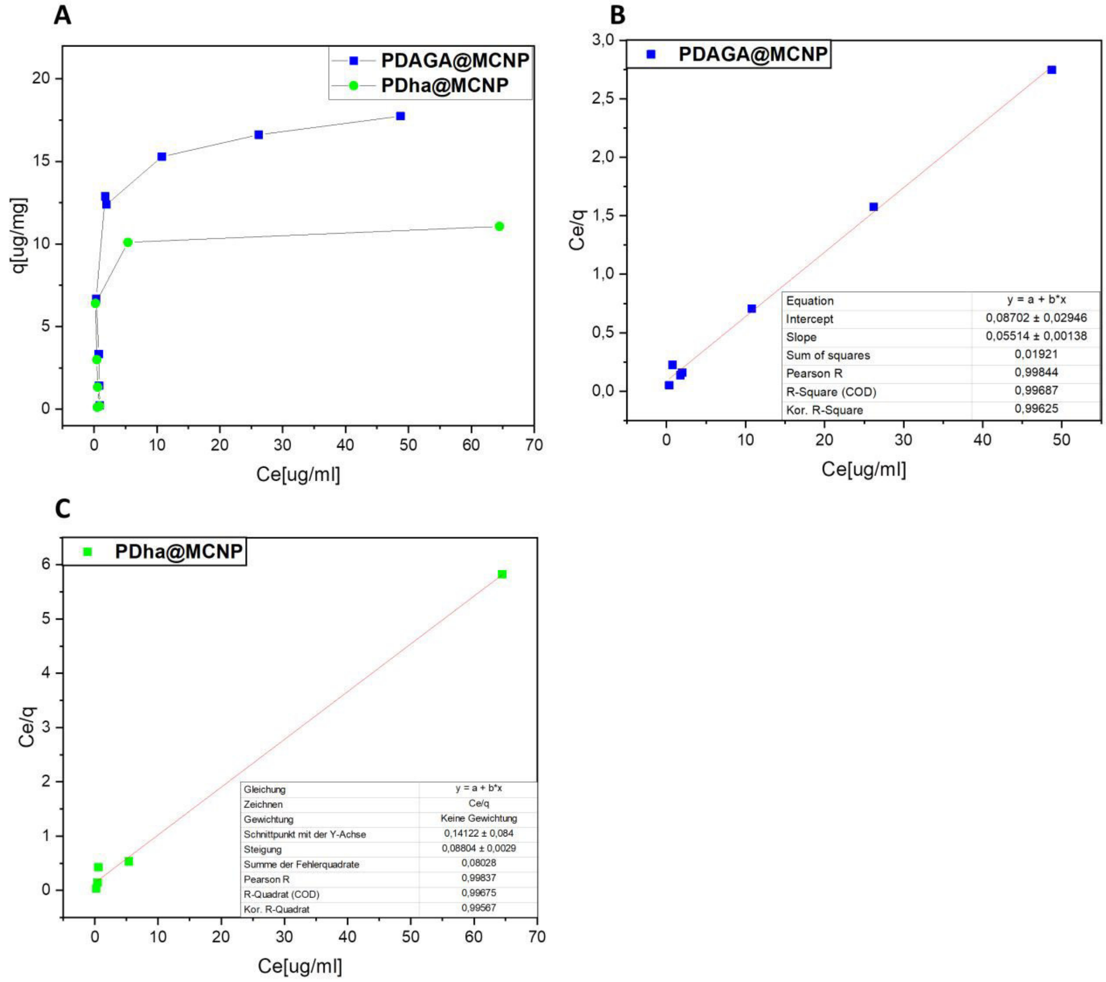

Figure S9: A) Adsorption isotherm of PDI-4Pyl to PDAGA@MCNP and PDha@MCNP. Conditions: Particles: 2 mg/ml; PDI-4Pyl: 1–50 µg/ml; temperature: 25 °C; pH: 7 B) A plot of C_e/q against C_e for the adsorption of PDI-4Pyl on PDAGA@MCNP resulting in a value for q_m = 18.14 µg/mg C) A plot of C_e/q against C_e for the adsorption of PDI-4Pyl on PDha@MCNP resulting in a value for q_m = 11.36 µg/mg.

Saturation concentration of PDI-4S on different systems at pH = 2

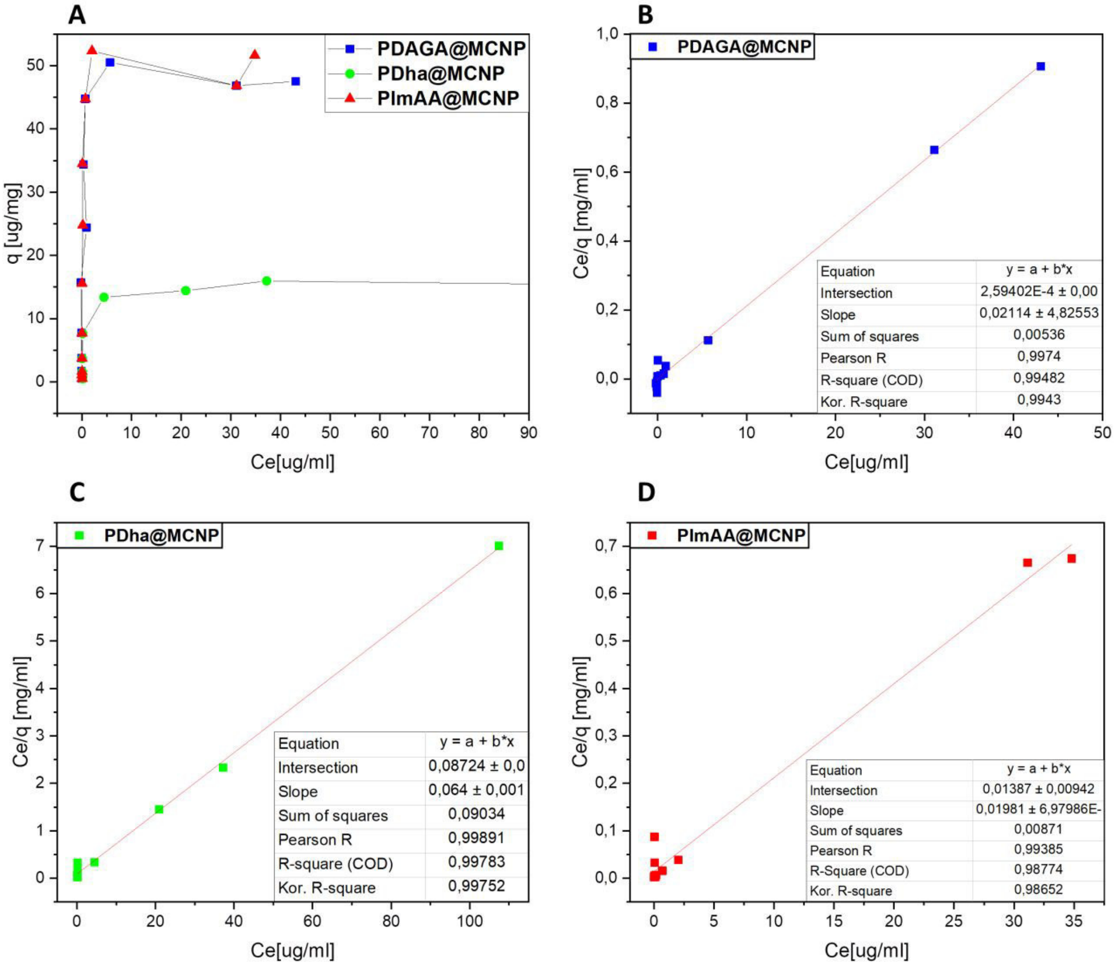

Figure S10: A) Adsorption isotherm of PDI-4S to PDAGA@MCNP, PDha@MCNP, and PImAA@MCNP. Conditions: Particle concentration 2 mg/ml; PDI-4S: 1–50 µg/ml; temperature: 25 °C; pH: 2 B) A plot of C_e/q against C_e for the adsorption of PDI-4S on PDAGA@MCNP resulting in a value for q_m = 47.30 µg/mg C) A plot of C_e/q against C_e for the adsorption of PDI-4S on PDha@MCNP resulting in a value for q_m = 15.63 µg/mg D) A plot of C_e/q against C_e for the adsorption of PDI-4S on PImAA@MCNP resulting in a value for q_m = 50.48 µg/mg.